



TECHNICAL REPORT RDMR-AF-10-01
NASA/TP-2010-216380

FLIGHT TEST RESULTS FOR THE MOTIONS AND AERODYNAMICS OF A CARGO CONTAINER AND A CYLINDRICAL SLUNG LOAD

Jeffery A. Lusardi and LTC Dwight E. Robinson

Aeroflightdynamics Directorate
Aviation and Missile Research, Development, and Engineering Center
at Ames Research Center, Moffett Field, California

Luigi S. Cicolani

San Jose State University Research Foundation
Aeroflightdynamics Directorate
Aviation and Missile Research, Development, and Engineering Center
at Ames Research Center, Moffett Field, California

Lloyd D. Greaves

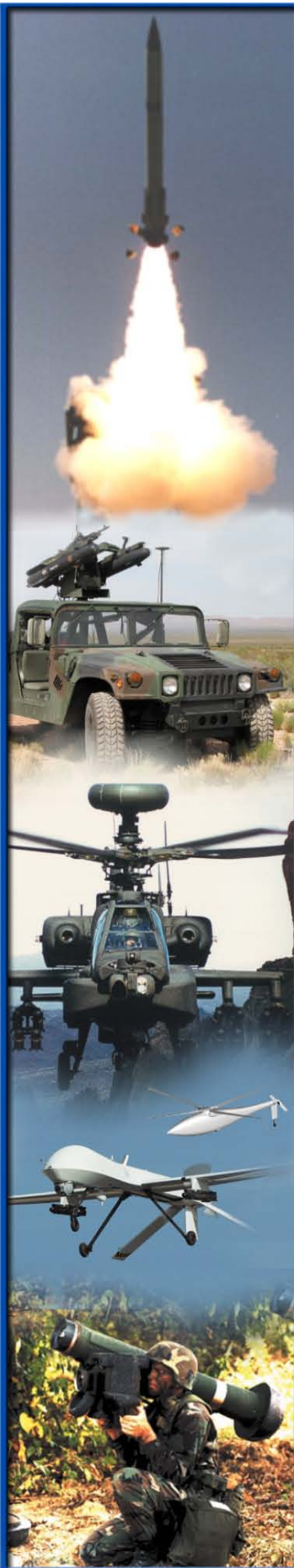
Ames Research Center
Moffett Field, California

Aviv Rosen and Rueben Raz

Israel Technion Institute of Technology
Haifa, Israel

April 2010

Approved for public release; distribution is unlimited.



Report Documentation Page				Form Approved OMB No. 0704-0188	
Public reporting burden for the collection of information is estimated to average 1 hour per response, including the time for reviewing instructions, searching existing data sources, gathering and maintaining the data needed, and completing and reviewing the collection of information. Send comments regarding this burden estimate or any other aspect of this collection of information, including suggestions for reducing this burden, to Washington Headquarters Services, Directorate for Information Operations and Reports, 1215 Jefferson Davis Highway, Suite 1204, Arlington VA 22202-4302. Respondents should be aware that notwithstanding any other provision of law, no person shall be subject to a penalty for failing to comply with a collection of information if it does not display a currently valid OMB control number.					
1. REPORT DATE APR 2010		2. REPORT TYPE		3. DATES COVERED 00-00-2010 to 00-00-2010	
4. TITLE AND SUBTITLE Flight Test Results for the Motions and Aerodynamics of a Cargo Container and a Cylindrical Slung Load				5a. CONTRACT NUMBER	
				5b. GRANT NUMBER	
				5c. PROGRAM ELEMENT NUMBER	
6. AUTHOR(S)				5d. PROJECT NUMBER	
				5e. TASK NUMBER	
				5f. WORK UNIT NUMBER	
7. PERFORMING ORGANIZATION NAME(S) AND ADDRESS(ES) Ames Research Center, Moffett Field, CA				8. PERFORMING ORGANIZATION REPORT NUMBER	
9. SPONSORING/MONITORING AGENCY NAME(S) AND ADDRESS(ES)				10. SPONSOR/MONITOR'S ACRONYM(S)	
				11. SPONSOR/MONITOR'S REPORT NUMBER(S)	
12. DISTRIBUTION/AVAILABILITY STATEMENT Approved for public release; distribution unlimited					
13. SUPPLEMENTARY NOTES					
14. ABSTRACT					
15. SUBJECT TERMS					
16. SECURITY CLASSIFICATION OF:			17. LIMITATION OF ABSTRACT Same as Report (SAR)	18. NUMBER OF PAGES 81	19a. NAME OF RESPONSIBLE PERSON
a. REPORT unclassified	b. ABSTRACT unclassified	c. THIS PAGE unclassified			

DESTRUCTION NOTICE

FOR CLASSIFIED DOCUMENTS, FOLLOW THE PROCEDURES IN DoD 5200.22-M, INDUSTRIAL SECURITY MANUAL, SECTION II-19 OR DoD 5200.1-R, INFORMATION SECURITY PROGRAM REGULATION, CHAPTER IX. FOR UNCLASSIFIED, LIMITED DOCUMENTS, DESTROY BY ANY METHOD THAT WILL PREVENT DISCLOSURE OF CONTENTS OR RECONSTRUCTION OF THE DOCUMENT.

DISCLAIMER

THE FINDINGS IN THIS REPORT ARE NOT TO BE CONSTRUED AS AN OFFICIAL DEPARTMENT OF THE ARMY POSITION UNLESS SO DESIGNATED BY OTHER AUTHORIZED DOCUMENTS.

TRADE NAMES

USE OF TRADE NAMES OR MANUFACTURERS IN THIS REPORT DOES NOT CONSTITUTE AN OFFICIAL ENDORSEMENT OR APPROVAL OF THE USE OF SUCH COMMERCIAL HARDWARE OR SOFTWARE.



Flight Test Results for the Motions and Aerodynamics of a Cargo Container and a Cylindrical Slung Load

*Luigi S. Cicolani
San Jose State University Research Foundation
Army Aeroflightdynamics Directorate
Ames Research Center, Moffett Field, California*

*Jeffery Lusardi
Army Aeroflightdynamics Directorate
Ames Research Center, Moffett Field, California*

*Lloyd D. Greaves
Ames Research Center, Moffett Field, California*

*LTC Dwight Robinson
Army Aeroflightdynamics Directorate
Ames Research Center, Moffett Field, California*

*Aviv Rosen and Rueben Raz
Israel Technion Institute of Technology
Haifa, Israel*

The NASA STI Program Office . . . in Profile

Since its founding, NASA has been dedicated to the advancement of aeronautics and space science. The NASA Scientific and Technical Information (STI) Program Office plays a key part in helping NASA maintain this important role.

The NASA STI Program Office is operated by Langley Research Center, the Lead Center for NASA's scientific and technical information. The NASA STI Program Office provides access to the NASA STI Database, the largest collection of aeronautical and space science STI in the world. The Program Office is also NASA's institutional mechanism for disseminating the results of its research and development activities. These results are published by NASA in the NASA STI Report Series, which includes the following report types:

- **TECHNICAL PUBLICATION.** Reports of completed research or a major significant phase of research that present the results of NASA programs and include extensive data or theoretical analysis. Includes compilations of significant scientific and technical data and information deemed to be of continuing reference value. NASA's counterpart of peer-reviewed formal professional papers but has less stringent limitations on manuscript length and extent of graphic presentations.
 - **TECHNICAL MEMORANDUM.** Scientific and technical findings that are preliminary or of specialized interest, e.g., quick release reports, working papers, and bibliographies that contain minimal annotation. Does not contain extensive analysis.
 - **CONTRACTOR REPORT.** Scientific and technical findings by NASA-sponsored contractors and grantees.
 - **CONFERENCE PUBLICATION.** Collected papers from scientific and technical conferences, symposia, seminars, or other meetings sponsored or cosponsored by NASA.
 - **SPECIAL PUBLICATION.** Scientific, technical, or historical information from NASA programs, projects, and missions, often concerned with subjects having substantial public interest.
 - **TECHNICAL TRANSLATION.** English-language translations of foreign scientific and technical material pertinent to NASA's mission.
- Specialized services that complement the STI Program Office's diverse offerings include creating custom thesauri, building customized databases, organizing and publishing research results . . . even providing videos.

For more information about the NASA STI Program Office, see the following:

- Access the NASA STI Program Home Page at <http://www.sti.nasa.gov>
- E-mail your question via the Internet to help@sti.nasa.gov
- Fax your question to the NASA Access Help Desk at (301) 621-0134
- Telephone the NASA Access Help Desk at (301) 621-0390
- Write to:
NASA Access Help Desk
NASA Center for AeroSpace Information
7115 Standard Drive
Hanover, MD 21076-1320



Flight Test Results for the Motions and Aerodynamics of a Cargo Container and a Cylindrical Slung Load

Luigi S. Cicolani

San Jose State University Research Foundation

Army Aeroflightdynamics Directorate

Ames Research Center, Moffett Field, California

Jeffery Lusardi

Army Aeroflightdynamics Directorate

Ames Research Center, Moffett Field, California

Lloyd D. Greaves

Ames Research Center, Moffett Field, California

LTC Dwight Robinson

Army Aeroflightdynamics Directorate

Ames Research Center, Moffett Field, California

Aviv Rosen and Rueben Raz

Israel Technion Institute of Technology

Haifa, Israel

National Aeronautics and
Space Administration

Ames Research Center
Moffett Field, California 94035-1000

Available from:

NASA Center for AeroSpace Information
7115 Standard Drive
Hanover, MD 21076-1320
(301) 621-0390

National Technical Information Service
5285 Port Royal Road
Springfield, VA 22161
(703) 487-4650

TABLE OF CONTENTS

LIST OF FIGURES	v
LIST OF TABLES	vi
NOMENCLATURE	vii
ABBREVIATIONS AND ACRONYMS	viii
SUMMARY	1
INTRODUCTION	2
FLIGHT TEST SETUP	4
Test configurations	4
Slings	7
Instrumentation	9
Flight test summary	10
Conduct of flight tests	10
CONEX FLIGHT CHARACTERISTICS	12
Yaw degree of freedom	13
Pendulum degrees of freedom	17
Load motions with offset cg	24
Hook force and sling-leg tensions	27
Summary	32
AERODYNAMICS OF THE SPINNING CONEX	33
Equations	33
Aerodynamic angles	33
Drag	35
Side force	37
Lift	37
Z-Moment	37
Aerodynamics with offset cg	42
ENGINE CANISTER FLIGHT CHARACTERISTICS	45
Load motions	45
Principal frequencies	46
Motion figures	47
Motion summary	48
Trail angle	50

TABLE OF CONTENTS (cont.)

ENGINE CANISTER AERODYNAMICS.....	52
Aerodynamics	53
Aerodynamic summary	58
Predictability of the engine canister aerodynamics	58
Reynolds number effects	59
CONCLUSIONS	62
REFERENCES	64
APPENDIX A. PHYSICAL PROPERTIES OF THE LOADS AND SLINGS	67
APPENDIX B. INSTRUMENTATION AND SIGNAL CHARACTERISTICS	75
APPENDIX C. COMPENDIUM OF FLIGHT TESTS	81
APPENDIX D. EQUATIONS FOR CABLE ANGLES AND LOAD AERODYNAMICS AND AN ANALYSIS OF ERRORS	115
APPENDIX E. CONEX STATIC AERODYNAMICS TABLES	133
APPENDIX F. ENGINE CANISTER STATIC AERODYNAMICS TABLES.....	163

LIST OF FIGURES

Figure 1. Test configurations.	5
Figure 2. CONEX cargo container test load	6
Figure 3. Engine-canister test load.....	6
Figure 4. Standard 4-legged military sling.....	8
Figure 5. Sling windup.....	9
Figure 6. Load instrumentation.	9
Figure 7. Cable angles.....	12
Figure 8. Yaw rate; 4000-lb CONEX; swiveled sling.	13
Figure 9. Mean steady-state spin rate; swiveled sling.....	14
Figure 10. 4000-lb CONEX, swiveled sling: Yaw-rate reversals at high speeds.	15
Figure 11. Yaw DOF; 4000-lb CONEX; no swivel.....	16
Figure 12. Trail angle.....	17
Figure 13. Mean lateral cable angle; swiveled sling	18
Figure 14. Pendulum motions: Cable-angle extremes; 2000-lb CONEX; and swiveled sling.	19
Figure 15. Cable-angle ranges (maximum–minimum).	20
Figure 16. Cable angles; 4000-lb CONEX; swiveled sling.	21
Figure 17. Cable angles; 4000-lb CONEX; no swivel.....	22
Figure 18. Cable-angle time histories; 4000-lb CONEX.....	23
Figure 19. Principal pendulum motion frequencies; 4000-lb CONEX; swiveled sling.....	24
Figure 20. Pendulum frequency: 2000- and 4000-lb CONEX; swivel and no swivel.....	24
Figure 21. CONEX ballasted for offset cg.....	25
Figure 22. Load yaw motions with offset cg; 4000-lb CONEX; swiveled sling.	25
Figure 23. Pendulum motions with offset cg; 4000-lb CONEX; swiveled sling.....	26
Figure 24. Yaw behavior vs. cg offset and airspeed; 4000-lb CONEX.....	27
Figure 25. Extremes of hook force and cable tensions; 4000-lb CONEX; swiveled sling.	28
Figure 26. Sling-leg tensions and hook force; 4000-lb CONEX; swiveled sling; 70 kias; Spin = -164.3 deg/sec.....	28
Figure 27. Sling-leg tensions and hook-force autocorrelations; 4000-lb CONEX; swiveled sling; 70 kias; Spin = 164 deg/sec.	30
Figure 28. Hook-force principal frequencies; 4000-lb CONEX; swiveled sling.....	30
Figure 29. Sling-leg tensions; 4000-lb CONEX; no swivel; 80 kias.	31
Figure 30. Sling-leg tension autocorrelations; 4000-lb CONEX; no swivel; 80 kias.....	32
Figure 31. Aerodynamic angles; definitions.	34
Figure 32. Aerodynamic angles; 4000-lb CONEX; swiveled sling (units: kts, deg, sec).....	34
Figure 33. Drag; 4000-lb CONEX; swiveled sling (units: ft, kts, deg, sec).	36
Figure 34. Averaged flight and static drag; 4000-lb CONEX; swiveled sling.	37

LIST OF FIGURES (cont.)

Figure 35. Side force; 4000-lb CONEX; swiveled sling (units: kts, deg, sec).....	38
Figure 36. Lift; 4000-lb CONEX; swiveled sling.....	39
Figure 37. Z-Moment; 4000-lb CONEX; swiveled sling (units in subplot titles are kts, deg/sec, and deg).....	39
Figure 38. Autocorrelations; z-moment; 50 kias; Spin = -122 deg/sec.....	40
Figure 39. Frequency response at 50 kias; $MAZ_{flight}/MAZ_{static}$	41
Figure 40. Magnitude and phase at discrete frequencies; 50 kias; $MAZ_{flight}/MAZ_{static}$	41
Figure 41. Aerodynamic angles; offset cg; 80 kias.....	43
Figure 42. Moment about the spin axis; offset cg; 80 kias.	43
Figure 43. Drag and side force; offset cg; 80 kias.	44
Figure 44. X- and y-moments; offset cd; 80 kias.....	44
Figure 45. Engine-canister motions.	46
Figure 46. Engine-canister motions: Principal frequencies.	47
Figure 47. Engine-canister pendulum motions.	48
Figure 48. Engine-canister lateral-directional motions.	49
Figure 49. Engine-canister trail angle.	50
Figure 50. Engine-canister mean specific drag and lift.....	51
Figure 51. Engine-canister aerodynamic angle coverage in the flight data.	52
Figure 52. Engine-canister aerodynamics; 75 kias.....	53
Figure 53. Engine-canister drag.	54
Figure 54. Engine-canister lift.....	55
Figure 55. Engine-canister side force.....	56
Figure 56. Engine-canister yaw moment.....	57
Figure 57. Prediction of engine-canister aerodynamics.	59
Figure 58. Engine-canister aerodynamics: effects of Reynolds number.....	60

LIST OF TABLES

Table 1. Summary of slung-load test flights 20056 – 2008	11
--	----

NOMENCLATURE

A more complete notation is given in appendix D with the equations needed for the calculations of this report. The following list suffices for the remainder of the text.

D	drag, lb
doq	drag divided by dynamic pressure, ft ²
g , g	gravity vector, gravity magnitude, 32.17 ft/sec ²
K _D , K _L	drag, lift divided by dynamic pressure, ft ²
ka_j	unit direction vector of cable j, j = 1, 2, 3, 4
K _s	Spring stretching constant, lbs per ft of stretch
L	lift, lb; cable length, ft; or reference length, ft; depending on context
loq	lift divided by dynamic pressure, ft ²
q	dynamic pressure, lb/ft ²
MA _z	load aerodynamic moment about the load body z-axis, ft-lb
Mc	torsional resistance at the hook, ft-lb
p, q, r	body axes components of rigid body angular velocity, rad/sec
Re	Reynolds number, V L/ν
u, v, w	Body-axes components of velocity
V	airspeed, kts or ft/sec
W, W ₁ , W ₂	weight, helicopter weight, or load weight, lb
x, y, z	axes of a reference frame
Y	side force
α	angle of attack
β	sideslip angle
φ _C	cable lateral direction angle relative to level heading axes
Δφ _C	cable lateral direction angle relative to helicopter body axes
φ _T	lateral trail angle (mean lateral cable angle for a trim record)
θ _C	cable longitudinal direction angle relative to level heading axes
Δθ _C	cable longitudinal direction angle relative to helicopter body axes
θ _T	longitudinal trail angle (mean longitudinal cable angle for a trim record)
σ	standard deviation
τ _j	cable tension in cable j, j = 1, 2, 3, 4
ν	viscosity of air at sea level standard day, 1.61 e-4 ft ² /sec
ω, ω _p , ω _s	angular velocity, pendulum natural frequency, stretching natural frequency
ψ ₁ , ψ ₂	helicopter heading, load heading
⊗	vector cross product

ABBREVIATIONS AND ACRONYMS

ADS	aircraft data system
AED	Army Aviation Engineering Directorate
AFDD	Aeroflightdynamics Directorate
AOA	angle of attack
CFD	computational fluid dynamics
cg	center of gravity
CONEX	<u>CON</u> tainer <u>Ex</u> press_cargo container
CW, CCW	clockwise, counterclockwise
DGPS	Differential Global Positioning
DOFs	degrees of freedom
EEL	Engineering Evaluation Laboratory, Ames Research Center
EGI	embedded GPS/INU
gc	geometric center
GPS	Global Positioning System
Hz	hertz; cycles per second
IAS	indicated airspeed
IIT	Israel Institute of Technology
INU	inertial navigation unit
kias	IAS in knots
LDAS	load data-acquisition system
ODE	ordinary differential equation
PC	personal computer
stdv	standard deviation
UTC	Universal Time, coordinated
VAC	volts, AC
VDC	volts, DC
VME	Virtual Machine Environment (computer)

FLIGHT TEST RESULTS FOR THE MOTIONS AND AERODYNAMICS OF A CARGO CONTAINER AND A CYLINDRICAL SLUNG LOAD

Luigi S. Cicolani¹, Jeffery Lusardi², Lloyd D. Greaves³, LTC Dwight Robinson², Aviv Rosen⁴,
and Reuben Raz⁴

Ames Research Center

SUMMARY

The stability of loads slung beneath a helicopter has been an ongoing problem since the beginnings of slung-load operations. Many loads are limited by stability to speeds well below the power-limited speed of the helicopter-slung-load configuration. Load motions are forced by steady and unsteady aerodynamics and are rich in complex interactions between the dynamics and aerodynamics. The present report examines the motions and aerodynamics of a cargo container and a cylindrical engine-canister slung load using a flight database accumulated over the past decade at the Army Aeroflightdynamics Directorate, Moffett Field, California. The loads were instrumented with a military-grade inertial navigation unit and Global Positioning System and with sling-leg load cells to measure cable tensions. Data were collected for various load weights, sling configurations, slings suspended with and without a swivel, and for both offset and centered center of gravity in forward flight out to the limiting airspeed for all configurations.

Load motions are analyzed for the directional and pendulum degrees of freedom. A variety of steady-state behaviors were found, depending on configuration. When suspended without a swivel, the cargo-container sling winds up and pendulum excursions limit operational speeds to 60 kts. With a swivel, the cargo container spun up to a steady yaw rate and the spin suppressed the pendulum motions and allowed the load to be carried to the power limit of the configuration. The spin also produced a small but measurable Magnus effect. An extreme cg offset produced stability around small end into the wind. The engine canister generally oscillated around broadside to the wind.

Cable tensions and hook force are analyzed for both the swiveled and unswiveled slings. For the swiveled sling, the sling-leg tension variations occurred at harmonics of the spin rate and the harmonics were cancelled or reinforced when summed into the hook force. For the unswiveled sling, cable tension variations are dominated by the windup cycle.

¹ San Jose State University Research Foundation, Army Aeroflightdynamics Directorate, Ames Research Center, Moffett Field, CA.

² Army Aeroflightdynamics Directorate, Ames Research Center, Moffett Field, CA.

³ Ames Research Center, Moffett Field, CA.

⁴ Israel Technion Institute of Technology, Haifa, Israel.

Equations to derive the load aerodynamics from the flight data are given. The aerodynamics of the steadily spinning cargo container were obtained for the combinations of airspeed, spin rate, and trail angle obtained in flight, and the results were compared to the static aerodynamics from wind tunnel data to obtain the effects of spin. The cylindrical load was previously undocumented, and its static aerodynamics were obtained for the available range of attitude in the flight data.

INTRODUCTION

Slung load research has been conducted by the Army Aeroflightdynamics Directorate (AFDD) at NASA Ames Research Center since the mid-1990's based on flight tests with an instrumented load, wind tunnel tests, and computational-fluid-dynamics (CFD) simulations. The general objectives of this work were to improve load envelope clearance testing, to model the unsteady aerodynamics that account for the instabilities of many difficult loads, and to develop simulations that can be used for stability prediction, control system design, and simulation certification of new, previously untested, loads. The flight testing with an instrumented Black Hawk test aircraft and instrumented load provided a data base that has been used variously to validate dynamic simulations at AFDD and the Army Aviation Engineering Directorate (AED), to validate CFD codes being developed to study cargo container aerodynamics, and to validate dynamic wind tunnel tests with a suspended load.

The objective of the present report is to present an analysis of the flight data for the motion and aerodynamics of a cargo container and a cylindrical slung load. The container is a 6- by 6- by 8-ft-long cargo box, also called a CONEX (CONTainer EXpress). It is subject to significant aerodynamic forces and moments in forward flight that limit its operational speed envelope to 60 kts because of aerodynamic instability. While it is no longer a standard military container, it was selected in the mid-1990s as a test load because it is typical of the class of cargo containers and box-shaped loads with speed envelopes limited well below the power limit of the helicopter-load configuration and because its weight could be carried by the Black Hawk test aircraft. The cylindrical load is a 9- by 5-ft-diameter engine canister selected in 2005 to provide a load distinct from cargo containers and with unknown flight characteristics that could be used to test the capability of the AED simulation to predict flight behavior of new loads in advance of flight tests.

The present report is thus a comprehensive flight test report. Previous publications from this body of work have dealt with the larger objectives of the research (refs. 1–13). The material of the present report has appeared partially in some of these publications as needed.

Much of the early literature on cargo container slung loads focused on the 8- by 8- by 20-ft MILVAN, which was the standard difficult load in research on the Heavy Lift Helicopter in the 1970s (refs. 14–19). An important distinction from the MILVAN studies is that the MILVAN is carried in a two-point suspension. Flight test and dynamic wind tunnel tests of the CONEX were conducted in the study reported in reference 20, which established the critical airspeed and described the instability of the CONEX along with several other types of slung loads.

The present study is aimed at single-point suspensions and takes advantage of modern high-accuracy instrumentation to obtain and document details of the load dynamics over the complete forward-flight envelope. The CONEX tests were conducted both with and without a swivel at the hook, which significantly affects the load directional motion, and with an offset-load cg, which has an unexpected effect on load behavior. The principal innovation of the present work is the extraction of load aerodynamics from flight measurements. This task was simplified by using a swivel to prevent the variable sling geometry that ensues from sling windup in the absence of a swivel. The CONEX with a swivel spun up to a steady-state spin rate, so that the aerodynamics obtained are those of a spinning box. It was found that the data are sufficiently accurate to measure and describe the effects of spin on the aerodynamics. The engine canister was found to oscillate slowly around broadside to the wind, allowing extraction of tabulated aerodynamics in the region around broadside. In addition, the sensors measured the sling-leg tensions and hook force, and these parameters are examined in detail.

The technical material is organized into five sections covering (1) flight test setup and summary, (2) CONEX flight characteristics, (3) CONEX aerodynamics, (4) engine canister flight characteristics, and (5) engine canister aerodynamics. In addition, several appendices provide more details on (A) physical description of the loads and slings, (B) load instrumentation and signal characteristics, (C) a compendium of flight tests, (D) equations to derive the load aerodynamics from the flight data and an error analysis, (E) tabulated wind tunnel data for the CONEX static aerodynamics, and (F) a partial tabulation of the engine-canister aerodynamics from flight test data.

The slung load research at AFDD, including the work of the present report, was conducted as Tasks 14 and 21 under the United States/Israel memorandum of agreement for cooperative research on "Rotorcraft Aeromechanics and Man-Machine Integration Technology." In addition, this study makes use of several flights conducted as part of a simulation development project at AED. Among the coauthors of this report, Prof. Rosen and Dr. Raz generated the wind tunnel test data that appears at many points in the text; LTC Robinson was the chief test pilot and flew the load to its limiting conditions (power, stability, or trail angle); Mr. Greaves designed and built the advanced load data-acquisition system based on a GPS/INU unit and load cells in the sling legs that provided slung-load data of unprecedented accuracy and comprehensiveness; and Dr. Lusardi was involved in all parts of the flight testing as test engineer and onboard data-acquisition-system operator, and in the data processing. In addition, the ground crew, crew chief, load handlers, avionics technicians, and telemetry engineers who made numerous and essential contributions to the conduct of the work should be recognized.

FLIGHT TEST SETUP

Slung-load flight tests with the UH-60 Black Hawk and an instrumented load have been conducted at Moffett Field at various times in the last decade with a 6- by 6- by 8-ft CONEX cargo container as the principal test load. Initial flight test efforts (refs. 1–3) and the summarizing article (ref. 21) focused on evaluation of the principal dynamic characteristics of the two-body slung-load system (stability margins, handling-qualities parameters, and load pendulum modes) and on development of a capability for rapid identification of these parameters during clearance flight tests between test points.

Recent tests (2005 to 2008) with improved load instrumentation focused on documenting load motions in forward flight out to the verge of instability and extracting the load aerodynamics from the flight data. The previous and current tests together provide a database that has been used for simulation development and validation (refs. 3, 4, 6, and 8) and validation of CFD computations (ref. 7) and wind tunnel scale-model studies (ref. 13).

Test configurations. The test configurations consisted of an EH-60L Black Hawk helicopter carrying a cargo container or a cylindrical engine canister load suspended with a standard 4-legged military sling set or the sling set plus a 65-ft pendant (fig. 1). In most cases a swivel was included at the hook or at the connection of the sling set to the pendant, allowing free rotation of the load to avoid the windup of the sling at the hook that occurs in the absence of a swivel. However, tests were flown without a swivel, and the behavior of the container without a swivel is also discussed.

The cargo container test load was a CONEX (fig. 2). It is a rectangular box, 8.48 ft wide by 6.11 ft long by 6.41 ft high, with skids along the long sides, indentations along the top edges, and corrugations along the sides and bottom. These departures from the geometry of a simple smooth-sided sharp-edged box are small, and they produce small to moderate changes from the aerodynamics of a simple box, principally from the skids. The corrugations are 2 in. wide with 2-in. separations and 1.5-in. deep. These are under 2% of full-scale dimensions. The wind tunnel literature (refs. 18 and 24) indicate that corrugations produce small effects, under 5% in drag and under 10% in other components. The skids are 6 in. high by 3 in. wide with four foot-long forklift holes, and they produce moderate changes in the aerodynamic symmetries of a simple box, principally in the symmetry of drag about $\alpha = 0$, where there is a 24% difference between skids full forward and skids full back for the broadside CONEX (ref. 24). Among cargo containers and box-shaped loads, the CONEX is moderately elongated (scale = 1 x 1 x 1.4) compared to a cubic container and much less elongated than the MILVAN container (scale = 1 x 1 x 2.4). Like other cargo containers it has significant aerodynamics in forward flight and is limited to 60 kts in military operations (ref. 22) because of aerodynamic stability considerations.

The cylindrical test load was a Lycoming F102 turbofan engine canister (fig. 3) measuring 5.0 ft in diameter by 9.0 ft long together with skids, supports, rings, and a center-plane flange. As is shown in the present results, these appendages produce significant departures from the expected symmetries in the aerodynamics of a simple cylinder. This load is not a certified military load, and its flight behavior and speed envelope were unknown prior to the tests.



a) CONEX, sling set



b) Engine canister, sling set



c) Long line

Figure 1. Test configurations.

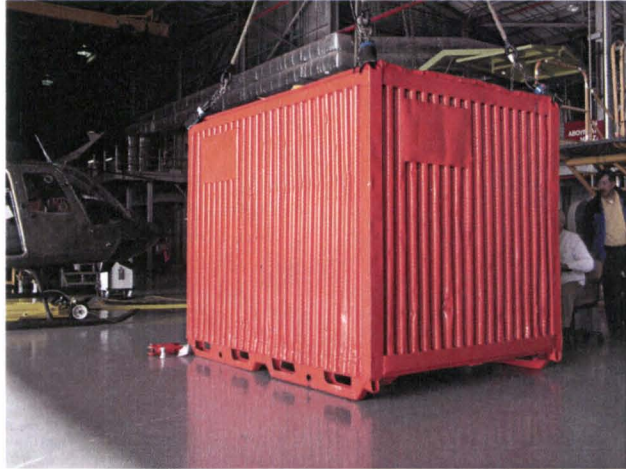


Figure 2. CONEX cargo container test load.



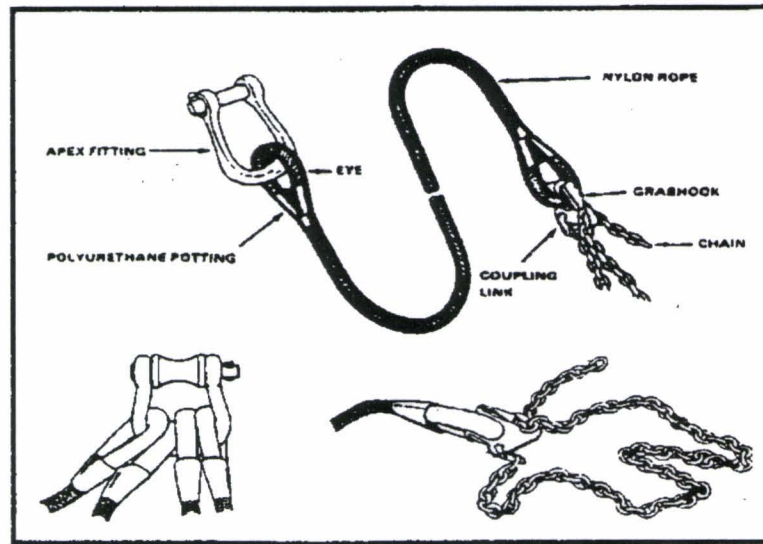
Figure 3. Engine-canister test load.

Dimensions, weights, inertias, and cg locations for the test loads are summarized in appendix A. The CONEX was flown empty (2000 lb) and ballasted with 1 and 2 tons of 100-lb sand bags. The engine canister was flown without ballast (2000 lb). The ballast and instrumentation system were placed in the loads to maintain the load cg close to the geometric center in x and y. In one test the CONEX was ballasted with 1 ton of lead plates placed near the door to obtain an extreme offset of the cg. The sensors were located close to the geometric center. Weights and locations were measured for the constituent masses of these loads, and then inertias and cg locations were computed by summing the contributions of the constituent masses. Each constituent mass was approximated to have uniform density over its volume in these calculations.

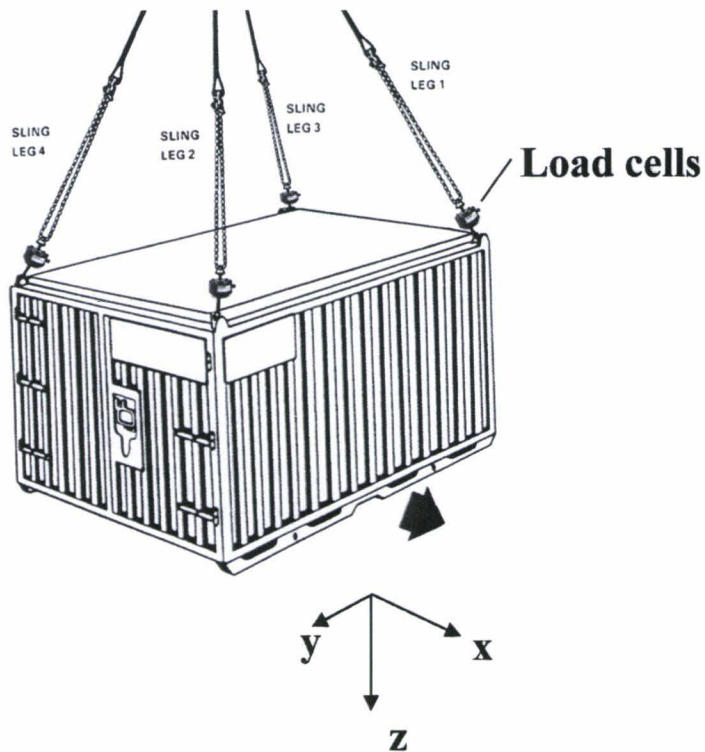
Slings. A 4-legged standard military sling set rated at 10,000 lb was used in all tests. Each leg consisted of a 12-ft nylon rope followed by 8 ft of chain passed through the lift points and doubled back to the third link (fig. 4(a)), following rigging instructions in reference 22. Figure 4(b) shows the enumeration of the sling legs and lift points along with the directions of the load body axes (the x-axis is perpendicular to a long side). The load is rigged to lift off in a broadside orientation with sling legs 1 and 2 being the forward legs. The sling legs are attached to a clevis at the apex of the sling and inserted in the clevis with the forward sling legs on the outside and the rear sling legs on the inside (fig. 4(a)). The length of the unloaded sling leg, when rigged to the load, measured 15.833 ft. Rigging details and the body axes for the engine canister are similar; that is, the canister is rigged for broadside lift-off and the body x-axis is perpendicular to the long side of the canister.

The stretching constant of the sling set was measured at 38580 lb per foot of stretch, or, equivalently, the stretching constant for each sling leg was 9645 lb/ft. The corresponding stretch of the sling due to static load weights is under 0.2 ft, and additional variations during flight due to load drag or excitation of the stretching modes is under 0.1 ft. In some tests a 65-ft long-line military sling was added to the sling configuration. The load was attached at the bottom with the 4-legged sling set and the swivel (fig. 1). The stretching constant of the long-line sling was measured at 36723 lb per foot of stretch. Sling stretching properties are discussed further in appendix A.

A swivel at the hook was used in most tests with the sling set (fig. 4(c)). The U.S. Army normally does not use a swivel, in which case the sling set winds up and unwinds at the hook. The number of turns of windup depends on airspeed and load weight. Up to five turns were observed without a swivel in the current tests with the sling wound up a third of the way down the sling (fig. 5). The swivel allows the load-sling subsystem to rotate freely and maintain constant sling geometry. In the case of the CONEX, the container spins up to a steady rate that represents a balance between the mean yaw moment around a rotation and the swivel friction. Laboratory tests indicated that swivel friction depends on weight only, is independent of spin rate, and is very small, under 10 ft-lb for the swivel used in these tests (appendix A). The spin stabilizes the CONEX out to higher airspeeds and also simplifies the motion context in which the aerodynamics derived from the flight data are to be understood; that is, they are the aerodynamics of a spinning box.



a) Sling-set details



b) Rigging and body axes



c) Sling apex and swivel

Figure 4. Standard 4-legged military sling.



Figure 5. Sling windup.

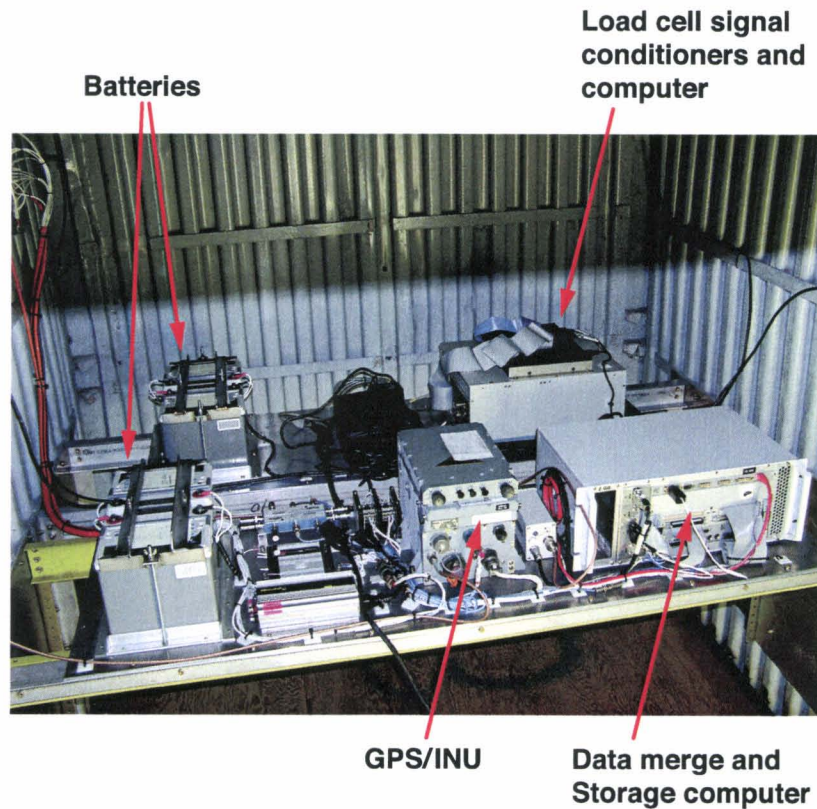


Figure 6. Load instrumentation.

Instrumentation: The load was instrumented with an embedded GPS/INU (EGI) that provided high-accuracy load dynamic data. A photograph of the complete load data acquisition system (LDAS) installed in the CONEX is shown in figure 6. In addition, load cells (strain gages) rated at 5000 lb were inserted in the sling legs at the lift points (fig. 4(b)) to measure sling-leg tensions, and these data were acquired in the LDAS and merged with the EGI data. Together, the EGI and load cells provided sufficient information to extract the aerodynamics from the flight data.

A flow chart of the LDAS is given in appendix B along with a list of signals from the system and a review of signal characteristics (measurement range, data rates, and noise properties). The system is powered by four 12-volt dry marine batteries that sufficed for 2 hours of flight before recharging. The system includes signal conditioners for the load-cell analog data; a computer to sample, digitize, and average the data; and a main computer to merge the EGI and the load-cell data, store the data on board the load at 100 Hz, and telemeter data up to the aircraft at 60 Hz via a radio modem. The entire system was mounted on two pallets that could be ported between the test loads; together they weighed 309 lb. The EGI was located within 6 in. of the geometric center of the load for both the CONEX and the engine canister. The load instrumentation was sufficient for the dynamic range of the load motions as well as accurate for all states and degrees of freedom (DOFs) of the load-rigid body dynamics.

The aircraft was well-instrumented, and data were collected and recorded by the aircraft data system (ADS). A schematic and brief description of the ADS are included in appendix B along with a list of signals from aircraft sensors (control-system sensors, ship's INU/GPS, boom pressure head and alpha-beta vanes, Differential Global Positioning (DGPS), and miscellaneous analog sensors). A flat-panel display was programmed with multiple selectable screens to display system status and modes as well as digital readout and moving-window time-history strip plots of various subsets of the sensors. Data were recorded on board at 100 Hz (regardless of actual data rate for any particular sensor, which ranged from 10 to 200 Hz, depending on the sensor), and selected data was telemetered to a ground station at 50 Hz using a 150 Kbaud radio modem pair with about a 20-mile range. In addition, a camera was mounted in the hatch looking down at the load to record load-motion video.

Flight test summary. The slung-load flight tests conducted from 2005 to 2008 are summarized in table 1. These tests are archived as a database in AFDD's TRENDS flight-data archive system. A compendium of flights and data records is given in appendix C.

Conduct of flight tests. Safety limits of 95% power, ± 30 deg lateral pendulum excursion, and longitudinal swing to -45 deg relative to the helicopter were adopted for the flight tests. Loads were flown at increasing speed until one of these limits was encountered. Load motions were monitored visually from a chase plane and by the crew chief looking down through a hatch hole, and quantitatively at a telemetry ground station.

Trim records are the principal source of data for this report, where "trim" means that the test pilot maintained the aircraft centered in straight level flight at the test indicated airspeed (IAS) while the load moved autonomously as driven by the aerodynamics and restrained by the sling. However, load pendulum swinging is coupled to helicopter attitude via moments applied to the aircraft by the hook-force vector. This swinging caused variations in helicopter attitude at the pendulum frequency, principally in roll, and the pilot was asked to fly the trim records with lateral stick fixed to avoid pilot excitation of the lateral pendulum mode.

TABLE 1. SUMMARY OF SLUNG-LOAD TEST FLIGHTS 2005–2008^{1, 2, 3, 4}

Flight No.	Date	Load	Sling	No. of Records	Reference Speed (kts)	Control Axes	Test Events
81	8 Jul 05	engine can	long line	7	0 to 30	lat, lon,	trims, doublets
82	12 Jul 05	engine can	long line	51	0 to 80	lat, lon	trims, doublets
85	26 Jul 05	6K CONEX	long line	31	0, 50	lat, lon	sweeps, doublets
86	2 Aug 05	6K CONEX	long line	29	0 to 95		trims
88	22 Sept 05	2K CONEX	sling set	22	40 to 70	lat, lon	trims, doublets
89	3 Sept 05	4K CONEX	sling set	32	40 to 100	lat, lon	trims, doublets
90	6 Oct 05	4K CONEX	sling set	32	0, 30, 60	lon, lat	trims, sweeps, dblts
91	14 Oct 05	engine can	sling set	52	0, 30 to 80 kts	lon, lat	trims, doublets, sweeps at 0.30 kts
107	16 Feb 06	engine can	sling set	43	50, 70	lon, lat	sweeps at 50, 70 kts, maneuvers
108	12 Feb 07	2K CONEX	sling set	8	0 to 40		trims
109	13 Feb 07	2K CONEX	sling set	31	40 to 100		trims
110	15 Feb 07	2K CONEX	sling set no swivel	12	40 to 70		trims
116	11 Apr 07	4K CONEX	sling set no swivel	13	40 to 105		trims
132	13 Aug 07	4K CONEX	sling set	12	40 to 107		trims
133	7 Nov 07	2K CONEX	long line	8	40 to 100		trims
134	7 Nov 07	4K CONEX	sling set	9	80 to 105		trims
135	21 Jan 08	4K CONEX offset cg	sling set	17	40 to 110		trims

1. All flights except 110 and 116 were flown with a swiveled sling.
2. Flights from 88 on were flown with load cells in the sling legs. Prior flights were flown without.
3. Boom pressure head and some load EGI data items are unavailable in flights 108 and 109.
4. The reference speed refers to the cockpit indicated airspeed above 35 kts and to the inertial ground speed below 35 kts.

CONEX FLIGHT CHARACTERISTICS

This section describes the motions of the load-sling subsystem. The three principal degrees of freedom are yaw and the longitudinal and lateral pendulum motions. The pendulum degrees of freedom can be represented by longitudinal and lateral cable angles measured as the direction angles of the hook-to-load-cg line segment (fig. 7). This definition of “cable angles” applies whether the suspension is a single or multicable sling. The cable angles can be measured in any reference frame. In this work these angles are measured in level heading axes, which are local vertical axes with the x-axis along the direction of flight. The longitudinal cable angle is measured from the local vertical to the projection of the hook-to-load-cg line segment onto the x-z plane of these axes (positive forward). The lateral cable angle is the angle between the line segment and this projection (positive for load swinging left). Cable angles relative to aircraft body axes are also of interest in some contexts (relative longitudinal cable angle is measured in the helicopter x-z plane). Equations for the computation of these cable angles from the flight data are given in appendix D.

For the multi-cable sling, the remaining three rigid body degrees of freedom can be represented as sling stretching motions (collective stretch and two asymmetric stretching modes) or, alternatively, as collective stretch and load pitch and roll DOFs. The cable stretch motions can be neglected in this discussion of flight characteristics because of the stiffness of the sling and the corresponding high frequency and negligible amplitudes of the stretching motions. However, some results are given in this section for sling-leg tensions. These tensions can vary significantly at the stretching frequencies as well as at the frequencies of the load motions.

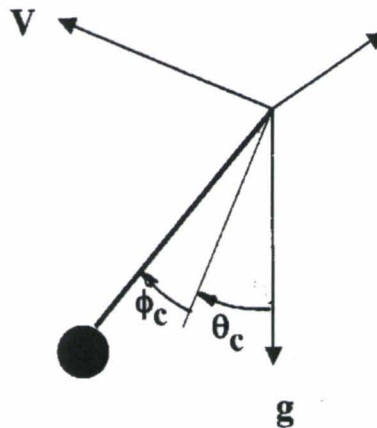


Figure 7. Cable angles.

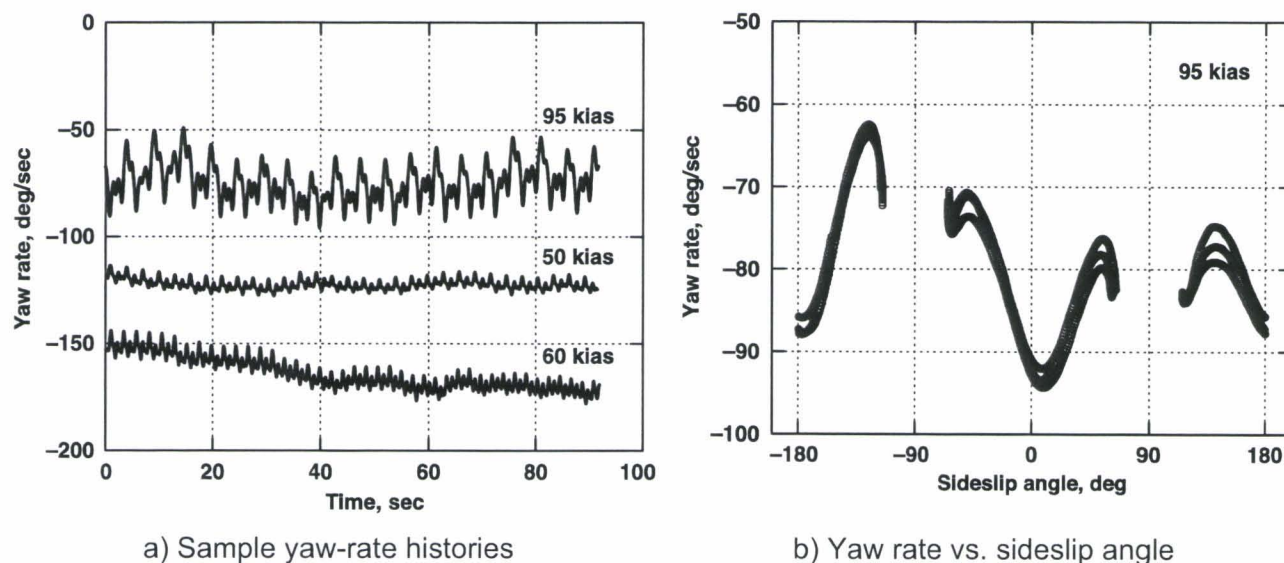


Figure 8. Yaw rate; 4000-lb CONEX; swiveled sling.

The analysis focuses on the trim records, where "trim" means that the aircraft is centered in straight and level flight at the test IAS while the load moves autonomously relative to the aircraft as forced by the load aerodynamics and constrained by the sling. The load was allowed to settle into its steady-state yaw motion after changing the test speed and before taking a trim record. A complicating factor is that the load motions are coupled to aircraft attitude, principally in roll, and sometimes the pilot reacted to the aircraft roll variations in an effort to maintain helicopter attitude, thus adding pilot excitations to the load pendulum motions. The pilot was requested to fly with the lateral stick fixed if possible.

In the presentation of results, airspeeds are given as indicated airspeed (labeled "IAS") or true airspeed (labeled "airspeed"). The indicated airspeed is the reference IAS tracked by the pilot using the ship's indicator, and true airspeed is derived from the boom air data. True airspeed is 5 to 10 kts higher than IAS.

Yaw degree of freedom. The CONEX was suspended with a swivel at the hook for all of the flight tests except two. The swivel allowed the load to rotate, and it was found to spin up to a steady-state spin that varied with airspeed and load weight. Sample time histories for the swiveled sling are given in figure 8(a); they show a mean steady-state value with small variations around the mean. These variations are periodic and repeat themselves every revolution, as seen in the plot of several revolutions vs. sideslip angle in figure 8(b). The results in figure 8 for the 4000-lb CONEX are typical of the time histories at all the test weights. (Notes: 1. $\beta = 0$ corresponds to long side into the wind (broad side load). 2. In figure 8(b) there are gaps in β without any data around $\beta = \pm 90$ deg because the map from continuously varying velocity components, u , v , w , to the aerodynamic angles, α , β , (see appendix D) is discontinuous near these points.)

The variation of the mean steady-state yaw rate of the swiveled sling with airspeed for several load weights is shown in figure 9(a). The variation follows the same pattern at all load weights, increasing to an extreme at some airspeed, and then declining as airspeed increases further. The extreme spin rate increases with load weight, reaching 197 deg/sec (about half a revolution per sec) for the heaviest test weight, and it occurs at different airspeeds depending on weight. The data go well beyond the 60 kias operational limit of the CONEX, in part because the spin acts to stabilize the CONEX and maintain small pendulum excursions out to higher airspeeds, and in part because increased weight is a stabilizing factor that reduces the relative size and effect of the aerodynamics at each airspeed. The empty CONEX continued spinning as speed increased past 60 kias and remained stable out to near the power limit of the configuration where excessive trail angle developed. The data in the figure for the empty CONEX are for cases using the sling set only. In flight 133 with the long-line sling configuration, the empty CONEX stopped spinning at 100 kias and pendulum amplitude increased. For the 4000-lb CONEX there is a steady spin rate up to 95 kias. At 100 kias this spinning turns into reversals between clockwise (CW) and counterclockwise (CCW) spinning. Several samples of this behavior are shown in figure 10. In these samples the spin reverses direction in the vicinity of small end into the wind. As is shown in the discussion of pendulum motions, the breakup of the steady spin is associated with a sharp increase in pendulum excursions.

The spin rate data are plotted vs. trail angle in figure 9 (b), where trail angle is the angle by which the load trails the local vertical due to drag. Both spin rate and trail angle are principally functions of airspeed and weight. The variation with trail angle is similar to the variation with airspeed; that is, spin rate increases to a maximum magnitude at some trail angle and then reverses. These reversals occur in a small range of trail angle between -10 and -15 deg, and suggest that the aerodynamic cause of the reversal occurs at a common trail angle.

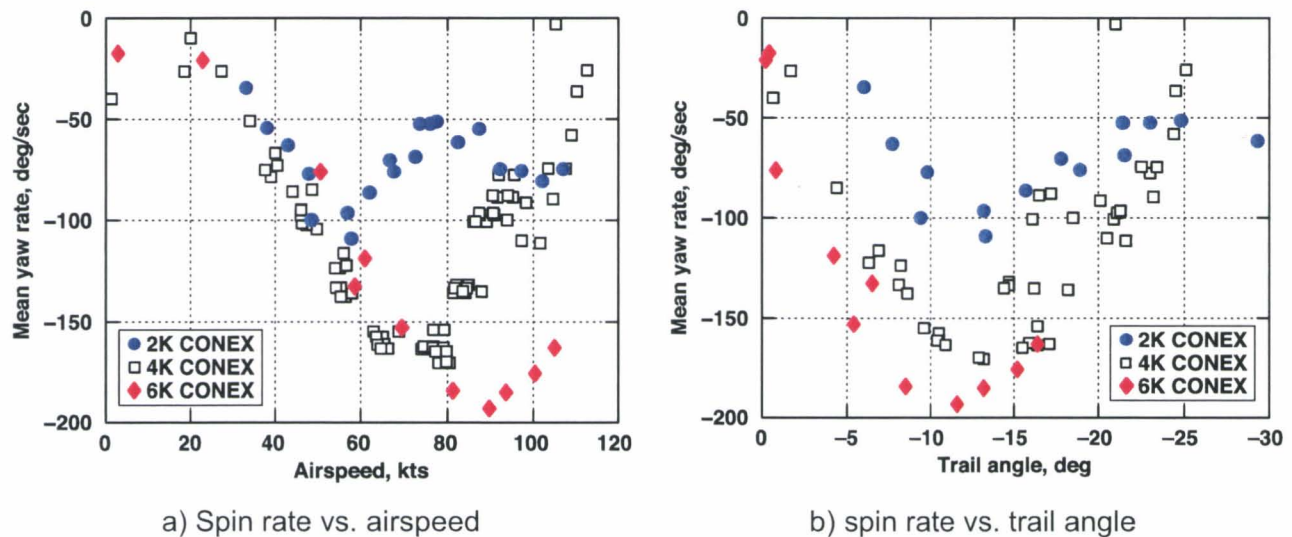


Figure 9. Mean steady-state spin rate; swiveled sling.

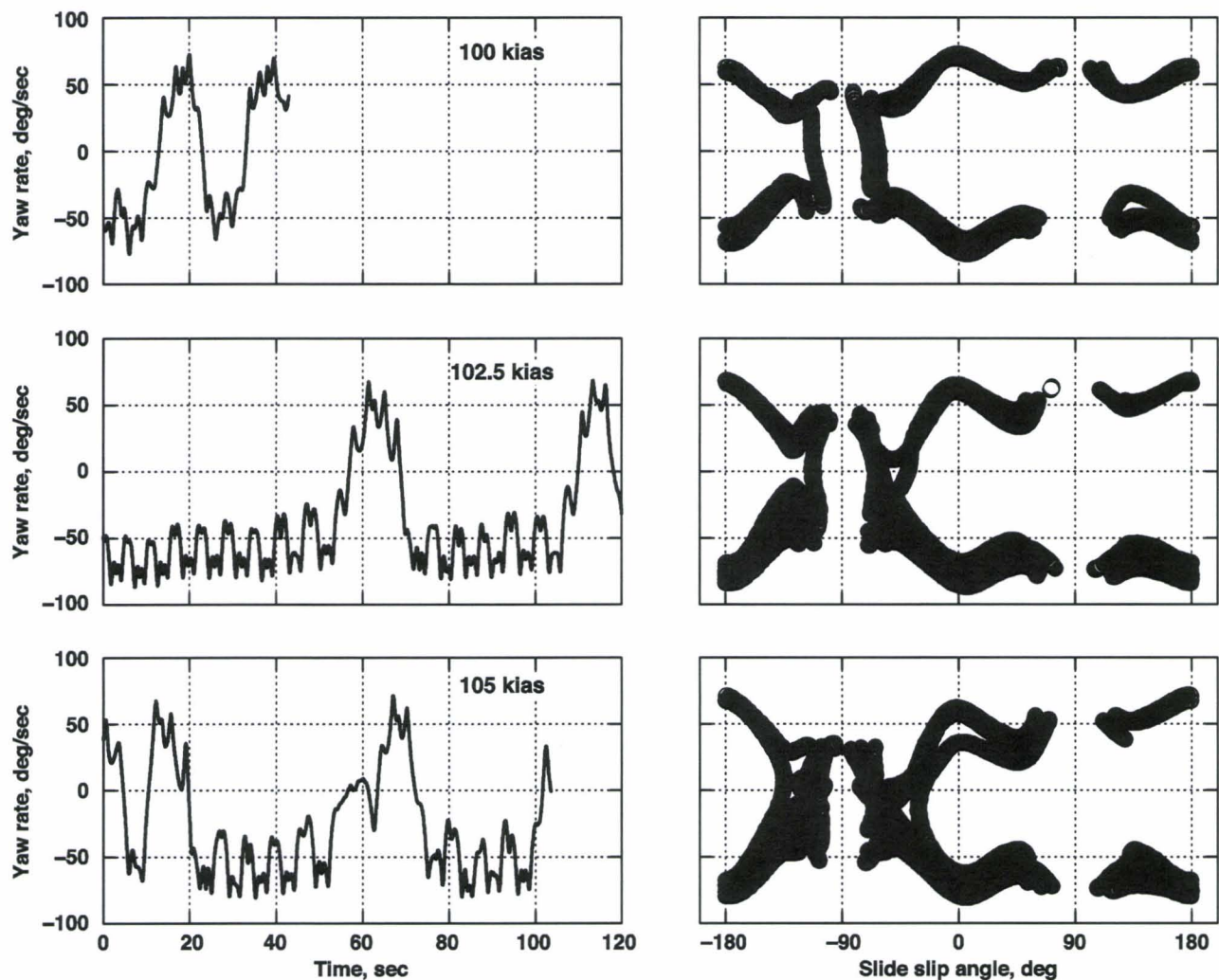
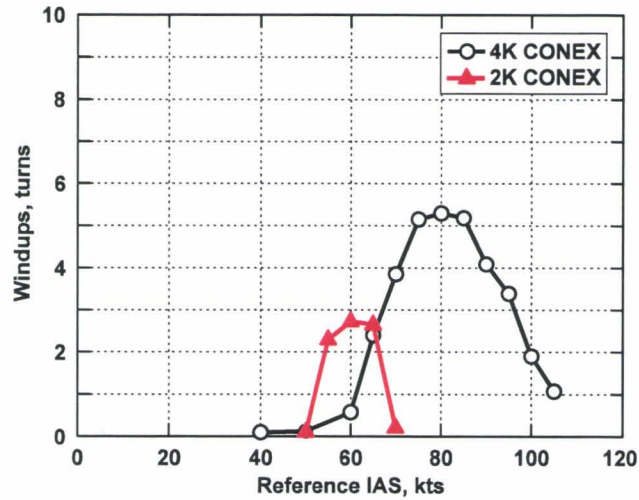


Figure 10. 4000-lb CONEX, swiveled sling: Yaw-rate reversals at high speeds.

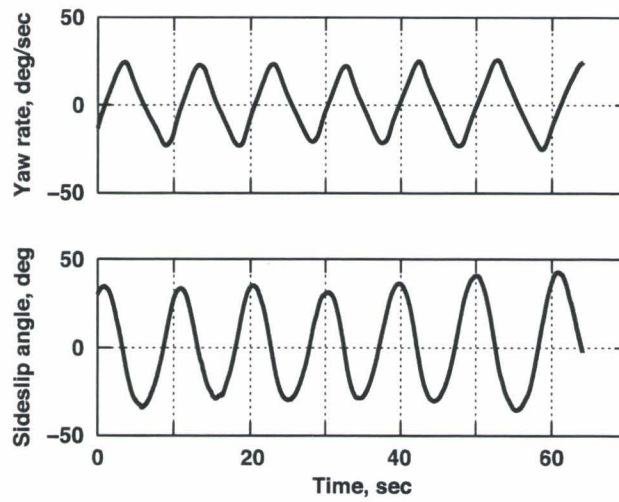
The mean steady-state spin rate of the swiveled sling represents a balance between the swivel friction and the mean value of the aerodynamic moment about the cable direction around a rotation. Swivel friction is very small for the swivel used in these tests, around 4 ft-lb for the 4000-lb load (appendix A). Thus the spin rate variation with airspeed depends in part on the friction characteristics of the swivel.

For the swiveled sling the load can spin in either direction, depending on the direction of rotation when the steady spin is initialized. Normally, spin is initialized in hover in the CCW direction by the swirl in the rotor downwash, and it continues in that direction for the entire flight.

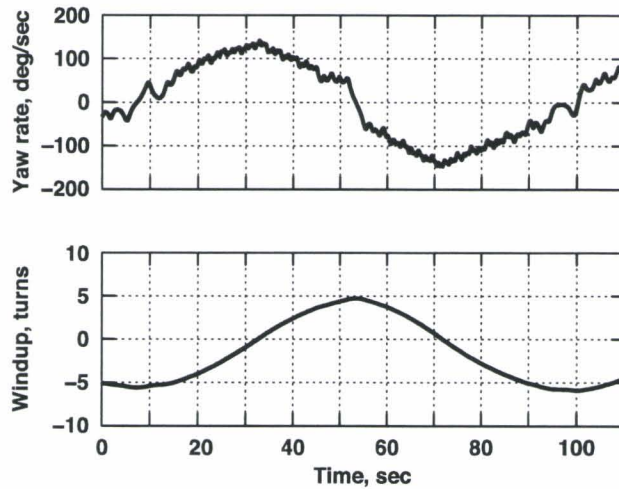
Without a swivel the sling continually winds up and unwinds between CW and CCW extremes. Figure 11(a) shows the number of turns of windup vs. airspeed for the 2000- and 4000-lb CONEX containers. For the 4000-lb CONEX there is little windup at speeds up to 60 kias and then windup increases to ± 5 turns in each direction at 80 kias. Above 85 kias windup decreases rapidly. Windup for the 2000-lb CONEX follows the same pattern but with half the maximum windup. Evidently,



a) Windup vs. airspeed



b) Yaw DOF; 40 kias; 4000-lb CONEX



c) Yaw DOF; 80 kias; 4000-lb CONEX

Figure 11. Yaw DOF; 4000-lb CONEX; no swivel.

windup increases with load weight. Pendulum excursions also increase dramatically with the drop-off in windup (shown in the next subsection). For the 4000-lb CONEX the test sequence of airspeeds was stopped at the power limit without reaching excessive pendulum excursions; that is, increased weight stabilizes the unswiveled container. At 40 kias (fig. 11(b)) sideslip angle and yaw rate are periodic, and oscillate within ± 45 deg around broadside and ± 30 deg/sec. At 80 kias where windup peaks, they are similarly periodic (fig. 11(c)), except that the amplitudes in windup and yaw rate are much larger and the period is much longer (90 sec).

Pendulum degrees of freedom. The pendulum degrees of freedom are represented by the longitudinal and lateral cable angles (previously defined in fig. 7), or, equivalently, the x and y motion of the load cg. The mean value of the longitudinal cable angle is nonzero, and it increases with airspeed with the load trailing the hook. This trail angle is due to load drag in the case that lift is negligible, and it can be approximated for such loads by:

$$\theta_T = -\tan^{-1}\left(\frac{D}{W}\right)$$

Figure 12 shows the trail angle for all test weights along with least-squares fits of the formula to the data to show the trend. The plot includes data for all sling configurations.

The trail angle depends on and increases in magnitude with the specific drag (drag divided by weight). At a given airspeed, trail angle is smaller for larger weights; e.g., the ballasted 4000-lb CONEX has half the specific drag at each airspeed as the empty CONEX, and a correspondingly smaller trail angle. Specific drag reflects the relative size of the load aerodynamic forces in g's. The trail angles corresponding to 0.5g and 1g are 26.6 and 45 deg, respectively. The empty CONEX reaches 0.5g at 75 kts (65 kias), while the 4000-lb load reaches this specific drag at 104 kts (95 kias).

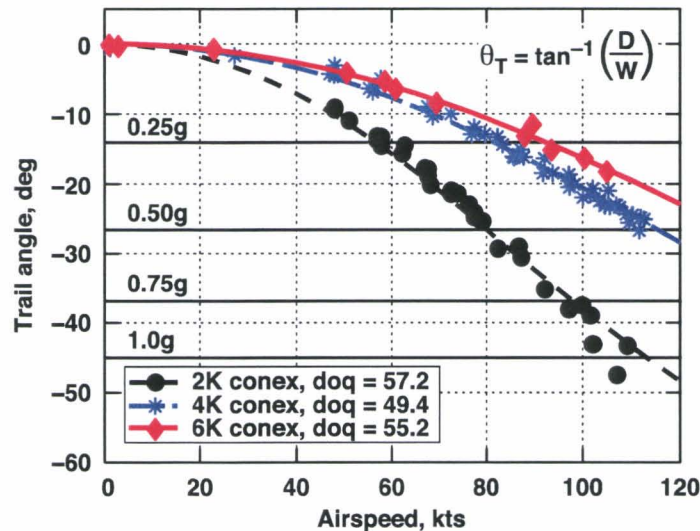


Figure 12. Trail angle.

For the swiveled sling the mean lateral cable angle data showed small nonzero values, up to 6 deg, where zero was expected. If we assume the flight data for cable angles are accurate to a fraction of a degree, then a Magnus effect similar to that found for spinning cylinders is suspected to account for the lateral offset. A simple model of the Magnus effect (ref. 23) indicates that it generates force perpendicular to the plane of the spin axis and the velocity vector in the direction of and proportional to $\omega \otimes V$. For the CONEX spinning CCW about its vertical axis, a Magnus effect would generate a small steady negative side force, ΔY , and a corresponding small positive mean lateral cable angle:

$$\phi_T = -\tan^{-1}\left(\frac{\Delta Y}{W}\right)$$

CW spin would generate negative mean lateral cable angle. The mean lateral cable angle is shown in figure 13(a) and (b) vs. rV for two weights. The plots are augmented with data from a related wind tunnel study of the suspended CONEX in which the model could be initialized in CW or CCW spin. These data are closely approximated by a linear fit. The linear fit differs with weight, but when the data are mapped to the corresponding mean side force the results align closely with a linear trend independent of weight (fig. 13(c)). These data from two independent sources are consistent with the hypothesis that a Magnus effect accounts for the lateral cable-angle offset.

The load is in constant motion around the mean longitudinal and lateral cable angles. Figure 14 shows the extreme cable angles relative to the helicopter for the empty CONEX with swiveled sling. The empty CONEX was (unexpectedly) well-behaved out to 100 kias, evidently because of a stabilizing effect of spin. The longitudinal cable-angle limit was exceeded at 100 kias and the lateral cable angles were well within the 30-deg limit at all airspeeds.

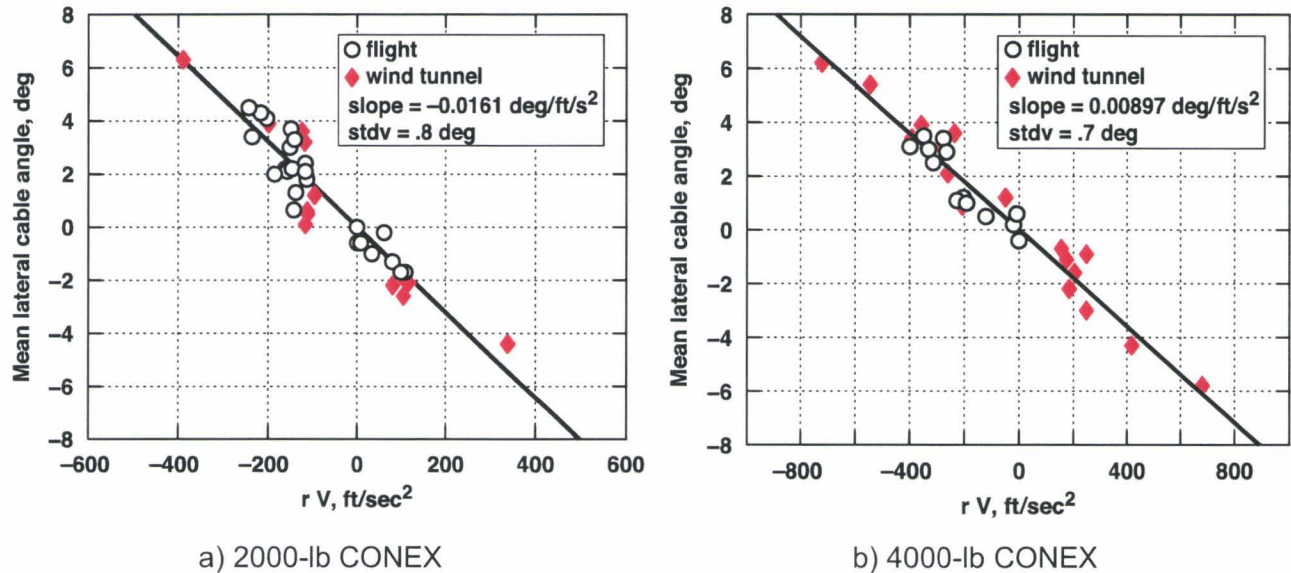
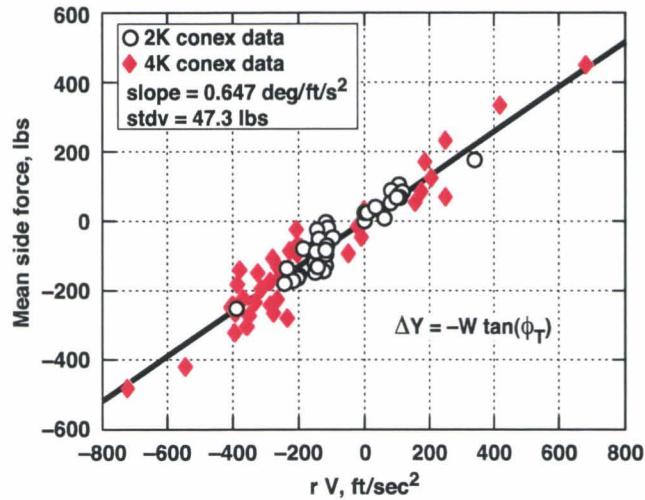


Figure 13. Mean lateral cable angle; swiveled sling.



c) Estimated mean side force

Figure 13. Mean lateral cable angle; swiveled sling (continued).

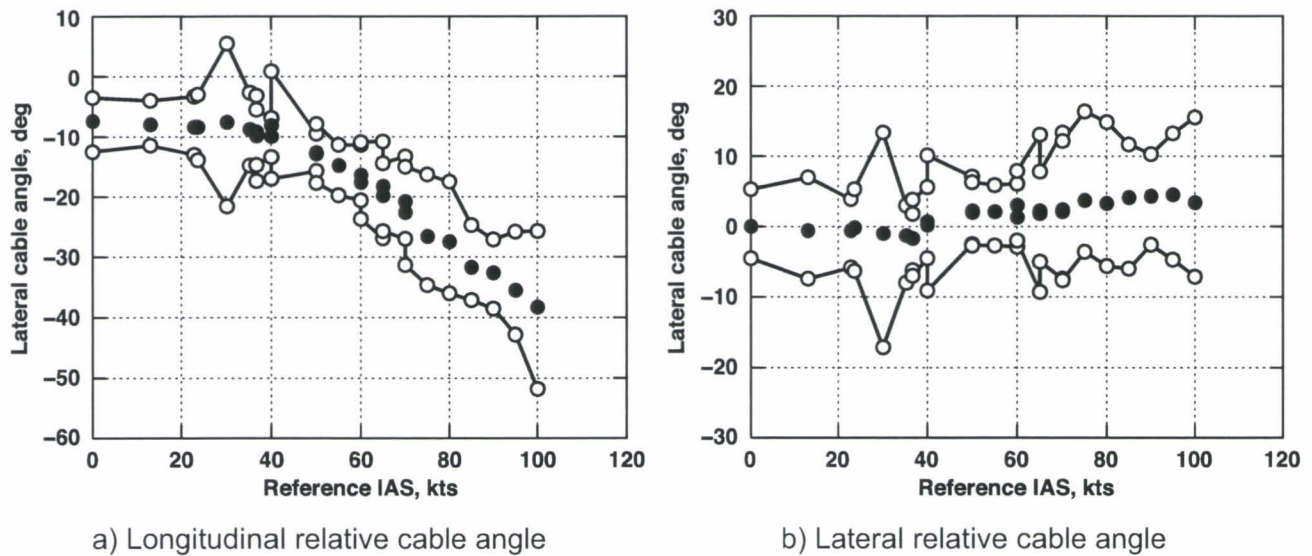
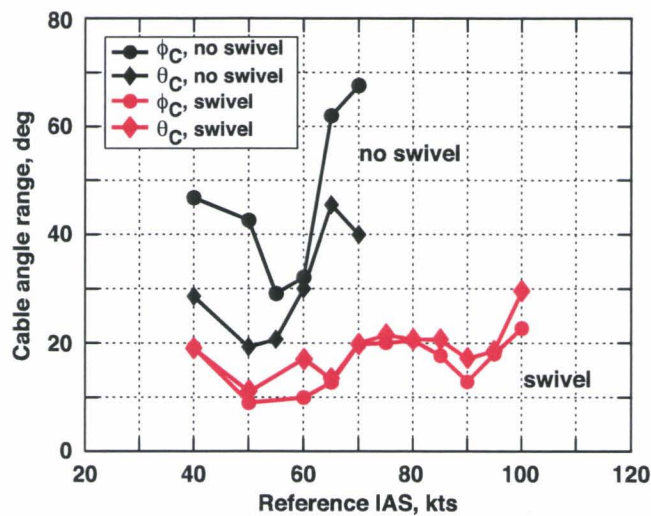


Figure 14. Pendulum motions: Cable-angle extremes; 2000-lb CONEX; and swiveled sling.

Figure 15(a) compares the cable-angle ranges (maximum–minimum) for the 2000-lb CONEX suspended with and without a swivel. Without a swivel, excursions are larger at all airspeeds and become excessive at 65 kias, exceeding the ± 30 -deg lateral cable-angle limit; this result is consistent with the operational limit of 60 kias for the CONEX. This case is illustrated in figure 15(b). With a swivel the load maintained a steady spin at all airspeeds and excursions were small (below ± 10 deg) out to 100 kias, where excursions increase somewhat and the trail angle reaches a safety limit.

Figure 15(c) makes the same comparison for the 4000-lb CONEX. With a swivel, there is a surge in excursions around 40 kias, and above that the steady spin maintains very small pendulum excursions (± 5 deg) out to 95 kias. At 100 kias the steady spin breaks up (fig. 10) and the pendulum excursions increase by a factor of three. The test was stopped at this airspeed because of the sudden increase in excursions and the possibility that the excursions would diverge further. Excursions without a swivel are larger than with a swivel above 60 kts but not excessive, and the configuration was flown out past 100 kias to the power limit.

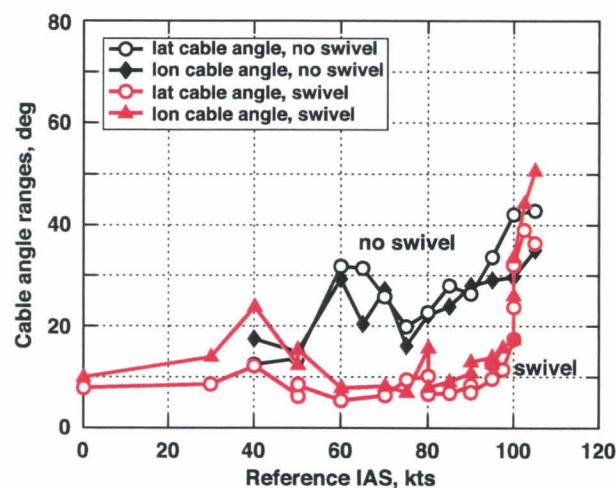
In figures 15 (a) and (c), lateral and longitudinal pendulum excursions are present at roughly equal amplitudes at most test points, and neither direction of swing dominates the motion. For the 4000-lb CONEX with swivel the longitudinal excursions are larger at low speeds, up to twice the size of the lateral (fig. 15 (c)). For the 2000-lb CONEX without a swivel, lateral excursions are larger at most test speeds (fig. 15(a)).



a) 2000-lb CONEX



b) 2000-lb CONEX; no swivel; 70 kias



c) 4000-lb CONEX

Figure 15. Cable-angle ranges (maximum–minimum).

Figures 16 and 17 show the pendulum motion figures of the 4000-lb CONEX with and without a swivel plotted as lateral vs. longitudinal cable angle. These plots are the cg motions as seen through the hook hatch scaled to angles. All plots are at the same scale for comparison. These plots echo the results in figure 15(c); that is, with a swivel, excursions surge at 40 and 100 kias, and are very small for speeds in between; and, without a swivel, excursions surge at 60 kias and increase above 80 kias but are moderate, within ± 20 deg at all test airspeeds. Similar plots for the 2000-lb CONEX show the same consistency with the results in figure 15(a) and are omitted. A closer inspection of the figures shows they are approximately elliptical with shifting amplitude and axis orientation, the result of simple pendulum motions at slightly different lateral and longitudinal frequencies and driven by forces that vary with the yawing motion of the box due to spin.

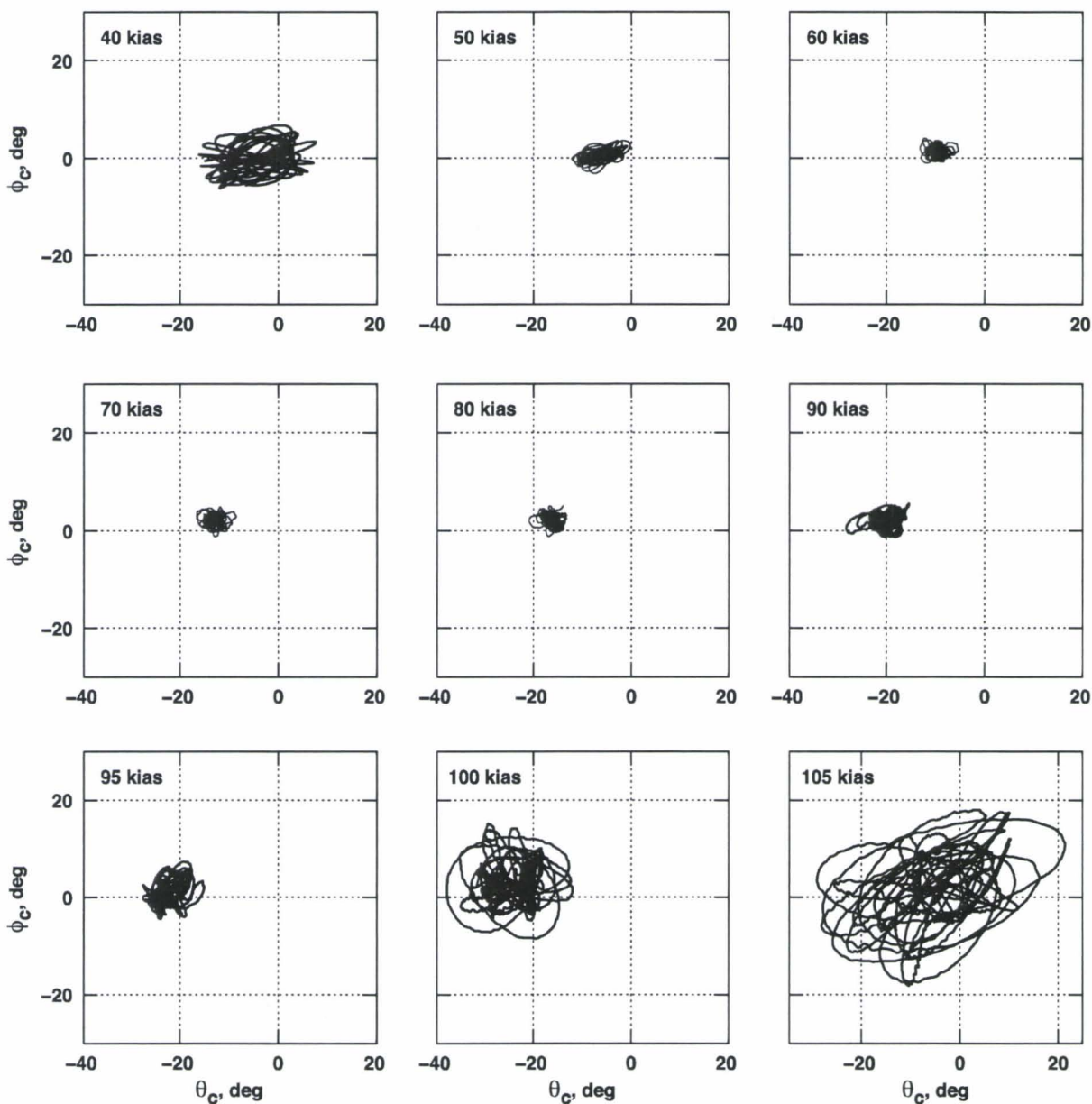


Figure 16. Cable angles; 4000-lb CONEX; swiveled sling.

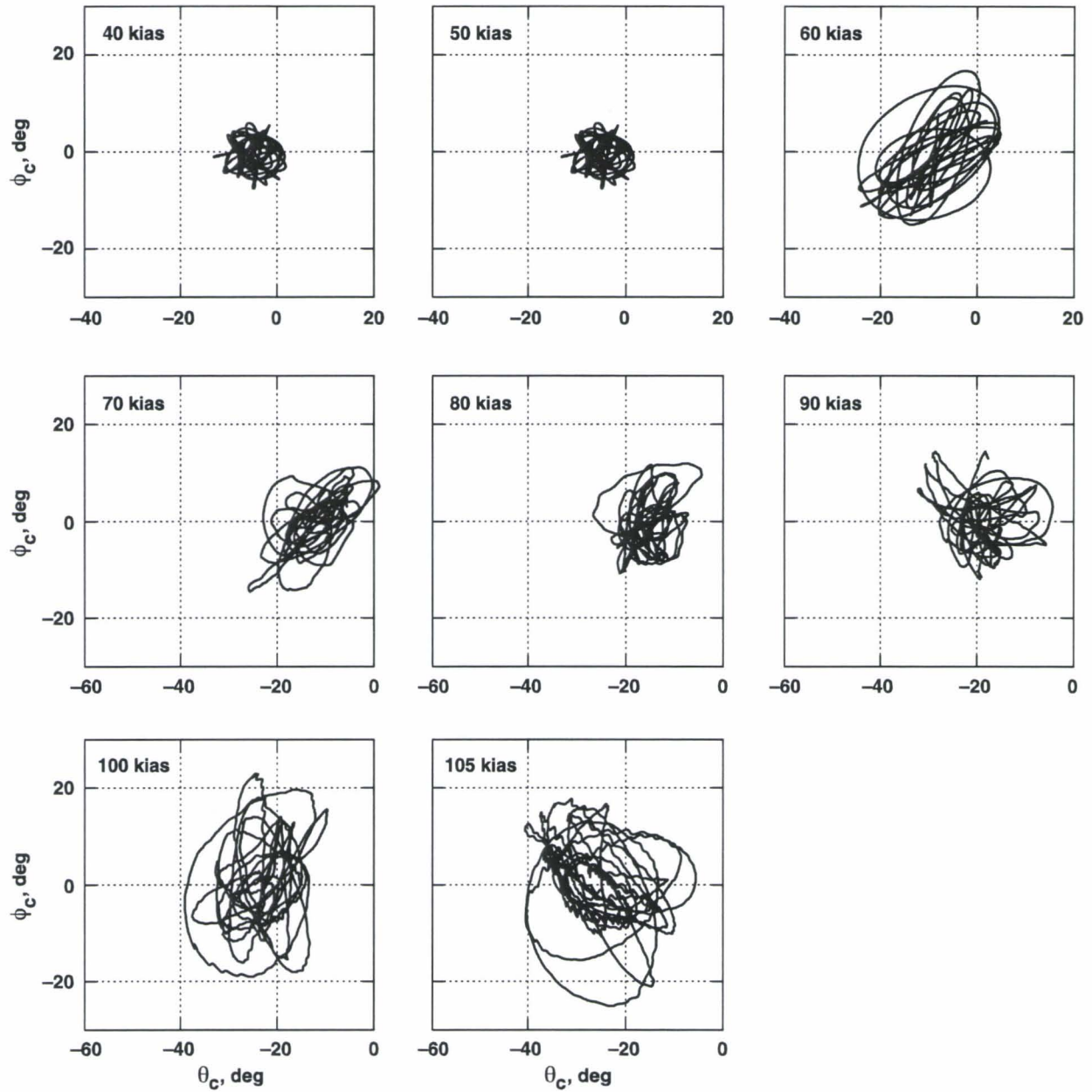


Figure 17. Cable angles; 4000-lb CONEX; no swivel.

Figure 18 shows some sample cable-angle time histories. The first case (40 kias, swiveled sling) has sinusoidal longitudinal and lateral motions. The longitudinal cable angle amplitude is visibly larger than the lateral. The relative phase of the cable angles changes slowly during the record, as seen in the relative times of the extremes, and this change indicates slightly different frequencies. In addition, amplitudes vary during the record. These features result in the complex but bounded figures seen in figures 16 and 17. The second case (70 kias, swiveled sling) corresponds to the maximum spin rate. Pendulum excursions are very small. The third case (60 kias, no swivel) is sinusoidal with a single frequency; this sample is typical of the pendulum excursions without a swivel at all airspeeds.

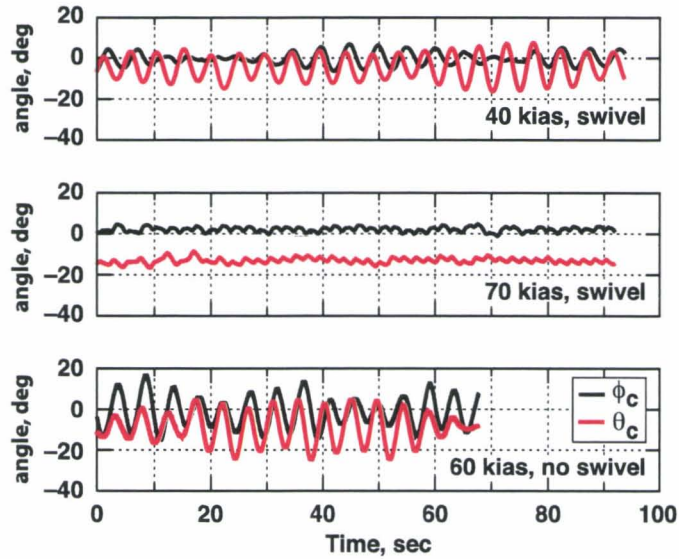
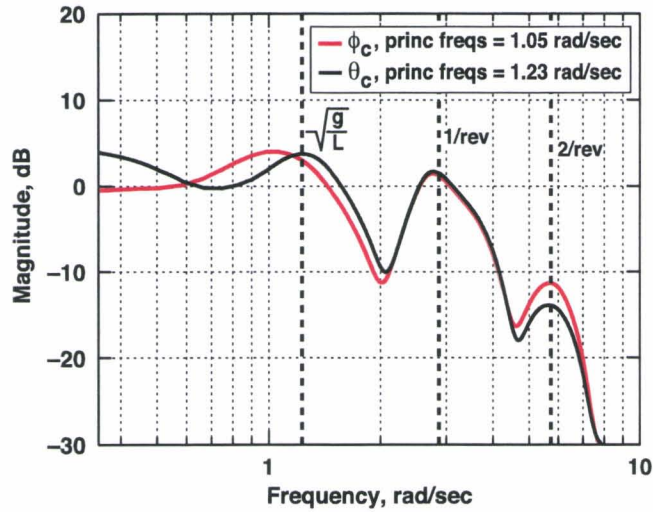


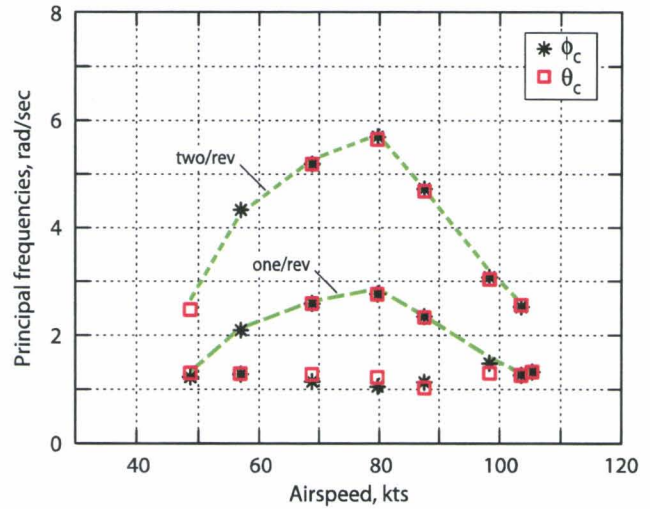
Figure 18. Cable-angle time histories; 4000-lb CONEX.

The principal frequencies of the pendulum motion are of interest. Figure 19(a) shows autocorrelations for the cable angles for a sample case for the 4000-lb CONEX with swiveled sling. The case is at 70 kias, where the spin rate is largest. The autocorrelations are nearly identical for longitudinal and lateral pendulum motions. There are three principal frequencies that correspond to the simple pendulum frequency and to one and two per revolution of the spinning container. Note the small difference between the lateral and longitudinal pendulum frequencies. These peaks of the autocorrelations are well-defined despite the very small excursion amplitudes seen in figure 18 for this case. Autocorrelations were obtained for all records with similar results. Figure 19(b) shows the variation of the principal frequencies with airspeed. The lowest principal frequency varies only a little with airspeed (the data are in the range of 1 to 1.5 rad/sec) and are close to the simple pendulum frequency, $\omega_p = \sqrt{g/L} = 1.23$ rad/sec. The spin-rate variation with airspeed is included as dashed lines in the figure; it is apparent that the second and third principal frequencies follow the spin rate and twice the spin rate closely. The pendulum motions related to spin rate are due to periodic variations in the aerodynamics around a revolution. Generally, the magnitudes at the pendulum frequency and at 1/rev are about the same size (plot omitted). At 50 and 103 kts (40 and 95 kias) the spin rate is close to the pendulum frequency. Autocorrelations for the 4000-lb CONEX without a swivel were obtained. The only principal frequency is the pendulum frequency.

Pendulum frequencies for the swiveled and unswiveled sling and for the 2000 and 4000-lb weights are collected in figure 20, including some low-speed data from reference 1. The data without a swivel are nearly invariant with airspeed with a mean pendulum frequency of 1.3 rad/sec and nearly identical for lateral and longitudinal motions. The data with a swivel vary over the range of 1 to 1.5 rad/sec and are close to the results without a swivel. Thus the pendulum frequencies are approximately unaffected by the swivel or its absence, and the aerodynamics and trail angle have, at most, weak effects on the pendulum frequency.



a) Sample cable-angle autocorrelations; 80 kts (70 kias); Spin = 164 deg/sec



b) Principal frequencies

Figure 19. Principal pendulum motion frequencies; 4000-lb CONEX; swiveled sling.

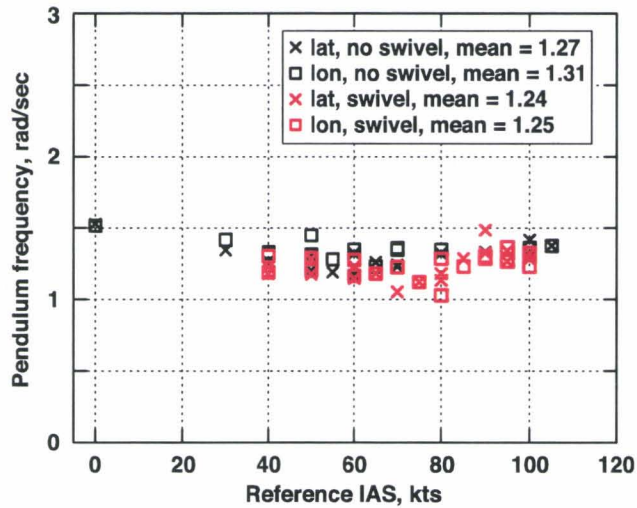


Figure 20. Pendulum frequency: 2000- and 4000-lb CONEX; swivel and no swivel.

Load motions with offset cg. The flight test loads were configured with some attention to centering the cg in x, y. However, cargo containers are loaded in the field without attention to cg location, and it was of interest to determine the effect of offset cg, if any, on the steady-state motions of the load. The CONEX was ballasted with 2140 lb of lead plates installed next to the door (small end of the CONEX) for maximum cg offset from the geometric x-y center (fig. 21). An offset of 1.54 ft along the y-axis was obtained, and it was equivalent to 4.1-deg offset of the hook-to-load-cg axis of rotation from the load vertical axis.

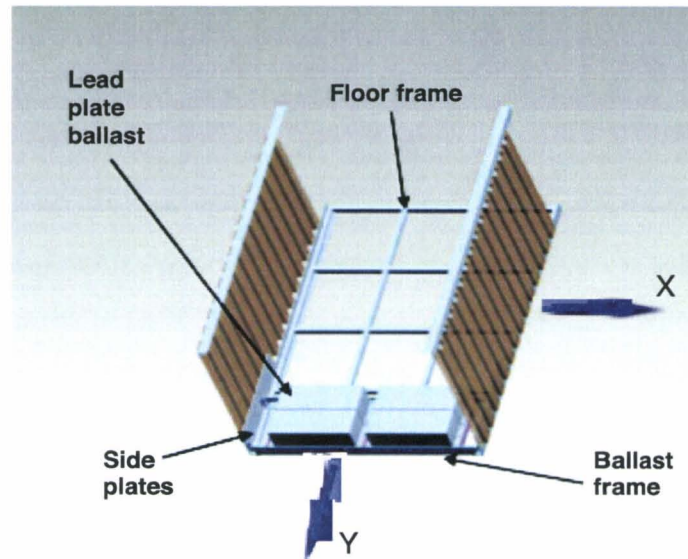


Figure 21. CONEX ballasted for offset cg.

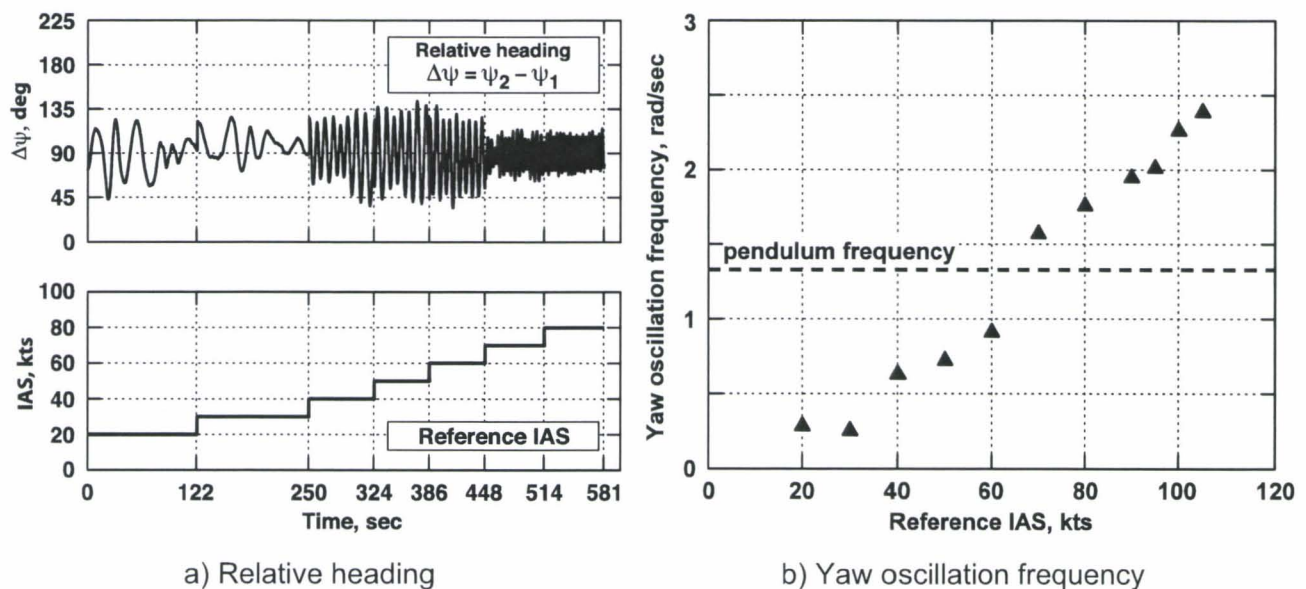


Figure 22. Load yaw motions with offset cg; 4000-lb CONEX; swiveled sling.

In the result the load stabilized in yaw around small heavy end into the wind and was well behaved. Figure 22(a) shows the relative heading (load heading minus helicopter heading). The load oscillates continually in yaw around 90-deg relative heading, and within a region of stabilizing restoring moment with neutral damping. Trim records at all speeds out to 80 kts are concatenated in the figure. The data system failed at higher speeds, but the video recording showed that the load was similarly stable around small side into the wind out to the power limit. Figure 22(b) shows the frequency of the yaw oscillations estimated from the time histories and from the video recording. It increases with airspeed over the range of the data and is disjoint from the pendulum motions except at about 65 kias.

Figure 23 shows the corresponding pendulum motions. These motions are small, under 10-deg amplitude, with a surge in lateral cable-angle amplitude at 70 kts.

This steady-state behavior with cg offset along the y-axis is different from that observed previously for centered cg, with and without a swivel, and has the favorable property of stabilizing around a minimum-drag orientation. The test-case offset was the extreme that can be obtained with 2000 lb of ballast, and is not a practical approach for stabilization in the field.

To determine sensitivity of yaw behavior to cg offset, wind tunnel tests with the load suspended in the tunnel were conducted at the Israel Institute of Technology (IIT) low-speed tunnel using the same dynamic test rig described in references 11 and 13. Several cg offsets were tested corresponding to full-scale offsets from the geometric center along the long axis of 0.27, 0.50, 0.80, 1.10, and 1.35-ft full scale. Records were taken at various fixed speeds from about 40 to 130 kts full scale. The results for yaw behavior were:

- At 0.27-ft cg offset, the load spun up at all airspeeds.
- At 0.50-ft cg offset, the load spun up for speeds up to 90 kts and oscillated in yaw about the small heavy end into the wind at higher airspeeds.
- At 0.80-ft cg offset and all larger offsets, the load oscillated in yaw about the small heavy end into the wind.

The wind tunnel test points are summarized in figure 24 to show the cg-airspeed boundary between spinning and oscillating steady-state yaw behavior. The boundary occurs between 0.5 and 0.8 ft cg offset (full scale) at all airspeeds up to 90 kts and at lower cg offsets above 90 kts. The flight case (1.54-ft offset) is well outside this boundary.

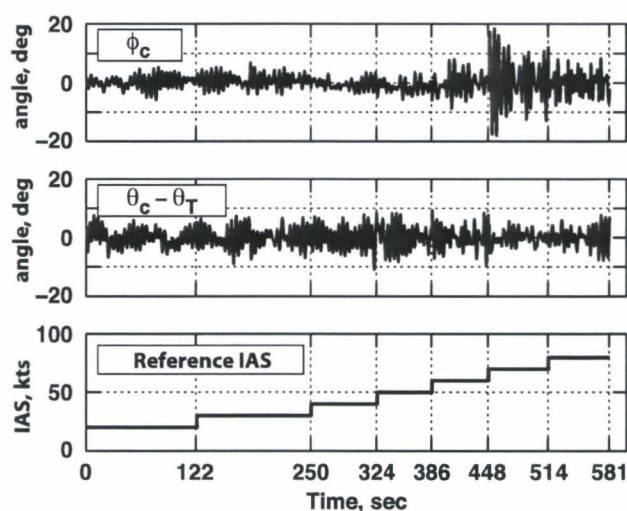


Figure 23. Pendulum motions with offset cg; 4000-lb CONEX; swiveled sling.

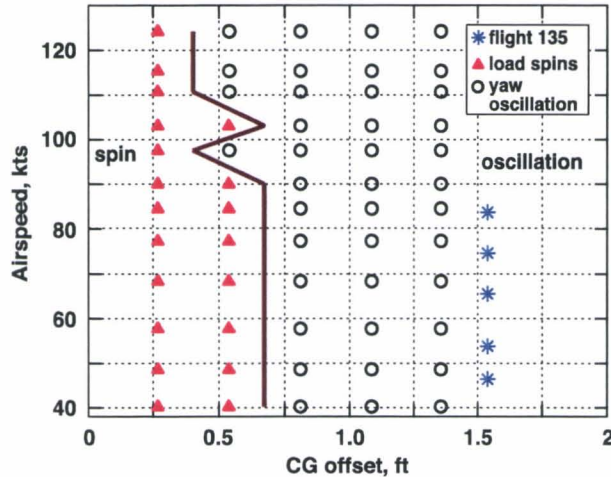


Figure 24. Yaw behavior vs. cg offset and airspeed; 4000-lb CONEX.

In the wind tunnel tests, yaw oscillation amplitudes were below 45 deg for the larger cg offsets beyond the boundary, similar to the flight 135 data, seemingly captured in a region of static stability in yaw. Closer to the spin/oscillation boundary, yaw excursions were larger, above 135deg, before reversing the direction of rotation to return towards small heavy end into the wind and inside the boundary, the load continues rotating with no tendency to return to small end into the wind.

Pendulum oscillations in the wind tunnel tests were very small for all cases with continual spin, similar to the flight cases with centered cg and continual spin. In the region with oscillatory yaw angle, there were cases with large pendulum excursions, in the range of 20 to 40 deg amplitude, sometimes predominantly lateral swing and sometimes predominantly longitudinal swing. The pendulum motions in the tunnel were not as well suppressed as in the flight case with extreme offset cg.

It is unknown how much cg offset occurs in field operations with cargo containers. The wind tunnel data indicate that the steady state spin condition is obtained for the cg within 6 to 10 inches of the geometric center in the case of the CONEX with 1 ton of cargo.

Hook-force and sling-leg tensions. Flight data on sling-leg tensions is available, probably for the first time, and results are given next.

If the load is suspended in the laboratory, the four sling legs are equally loaded assuming the cg is centered in x and y and the sling legs have identical lengths. This scenario is very nearly the case for the test load. In flight, tensions vary among the legs because of load motions and excitation of the sling stretching modes. The sling legs are enumerated 1, 2, 3, and 4 corresponding to the forward-left (1), forward-right (2), rear-left (3), and rear-right lift (4) points on the CONEX, where "forward" refers to the load-body axes positive x-direction (see fig. 4(b)).

Figures 25 to 28 present data for the 4000-lb CONEX and swiveled sling.

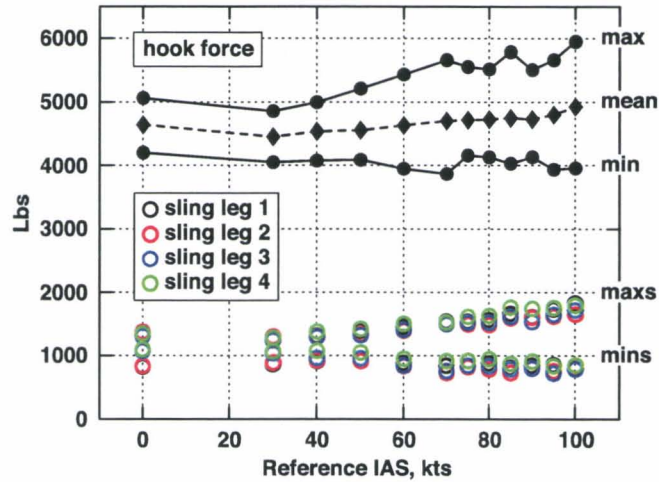


Figure 25. Extremes of hook force and cable tensions;4000-lb CONEX; swiveled sling.

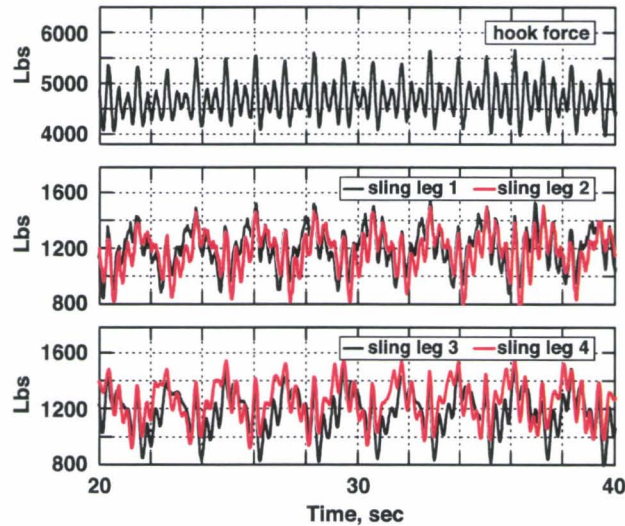


Figure 26. Sling-leg tensions and hook force; 4000-lb CONEX; swiveled sling; 70 kias;
Spin = -164.3 deg/sec.

Figure 25 shows the extremes of the hook-force magnitude and sling-leg tensions vs. airspeed. Hook force is in the range of 4000 to 6000 lb in the upper part of the figure and the sling-leg tensions are in the range of 500 to 2000 lb in the lower part of the figure. The mean hook force increases by 500 lb over the airspeed range, reflecting the increase in drag with airspeed. Hook force varies around the mean during a trim record, and the range of the variations increases from ± 400 lb at hover to ± 1000 lb at 100 kts. The extremes of the sling-leg tensions are about 25% of the hook force, as expected, and all 4 legs have similar extremes. Time histories show that the variations are continual. At hover these variations occur at the frequency of the collective stretching mode. In forward flight, frequencies related to spin appear strongly, as illustrated next.

Figure 26 shows time histories of the sling legs and hook force at 70 kias for the swiveled sling. At this airspeed, the spin rate is a maximum (164 deg/sec) and there is very little pendulum motion. The sling-leg tension histories show a large-scale periodic variation at the spin rate (Period = 2.2 sec) with smaller high-frequency variations superposed. The dominant variations in sling legs 1 and 2 are in phase with each other and 180 deg out of phase with legs 3 and 4. The hook force is the vector sum of the forces on the hook from the four sling legs. The dominant frequency in the sling legs is not visible in the hook-force time history in figure 26 because of cancellation in this sum.

Figure 27 shows the autocorrelations for the sling-leg tensions and hook force of figure 25. The sling-leg tension magnitudes in figure 27(a) approximately overlap and have their maxima at the same frequencies. For reference, the pendulum frequencies identified previously and the spin rate for this case are 1.05 (lateral pendulum), 1.23 (longitudinal pendulum), and 2.8 rad/sec (spin). For the sling-leg tensions the dominant peak occurs at 2.75 rad/sec corresponding to 1/rev of the spin and the next 3 peaks at 5.8, 8.8, and 11.7 rad/sec coincide with 2, 3, and 4/rev and are 8 to 15 dB smaller in magnitude than the 1/rev component. The data indicate that the dominant variation of the sling-leg tensions for the swiveled sling is associated with the spin, although it is uncertain how spin can induce such variations.

Linear analysis of the helicopter-slung load dynamics indicates that there are three lightly damped stretching modes: vertical, lateral, and longitudinal. The vertical mode is a collective stretch analogous to the stretch of a single cable sling. The lateral stretch mode consists of the left and right pairs of sling legs stretching 180 deg out of phase, and it appears as load roll variations in the mode shape. The longitudinal stretch mode consists of the forward and rear pairs of sling legs stretching 180 deg out of phase, and it appears as variations in load pitch angle.

The calculated values of the vertical and lateral stretching mode frequencies in the linear analysis, 18.8 and 18.2 rad/sec, respectively, are close to the peak in the autocorrelations at 17.5 rad/sec, and they may account for this peak. A magnified time history of the cable tensions shows that variations at this frequency are in phase among the 4 sling legs, implying that this frequency is a collective stretching frequency. The calculated value of the longitudinal stretch mode, 26.2 rad/sec, is close to the small-magnitude peak in the autocorrelations at 27.1 rad/sec.

The hook-force autocorrelation in figure 27 shows maxima at all the same frequencies as the sling legs, but the maxima at 1/rev and 3/rev have been suppressed, while the maxima at 2/rev and 4/rev have been reinforced and the vertical-stretch mode is a dominant frequency. The maximum at 17.5 rad/sec has been reinforced in the summation of sling-leg forces, confirming that this frequency is a collective stretching frequency.

The frequencies corresponding to well-defined peaks in the hook-force autocorrelations are collected in figure 28 for all airspeeds. The plot includes dashed lines to indicate the spin frequency and its harmonics at all airspeeds where the spin rate is well-defined. The data show that the frequencies at the autocorrelation peaks track the spin frequency and its harmonics. Generally, the 1/rev cable tensions cancel out in the hook-force autocorrelation but with small discernible peaks left over and the 3/rev tensions cancel out without discernible residual peaks. The highest two frequencies are associated with stretching and are nearly invariant with airspeed.

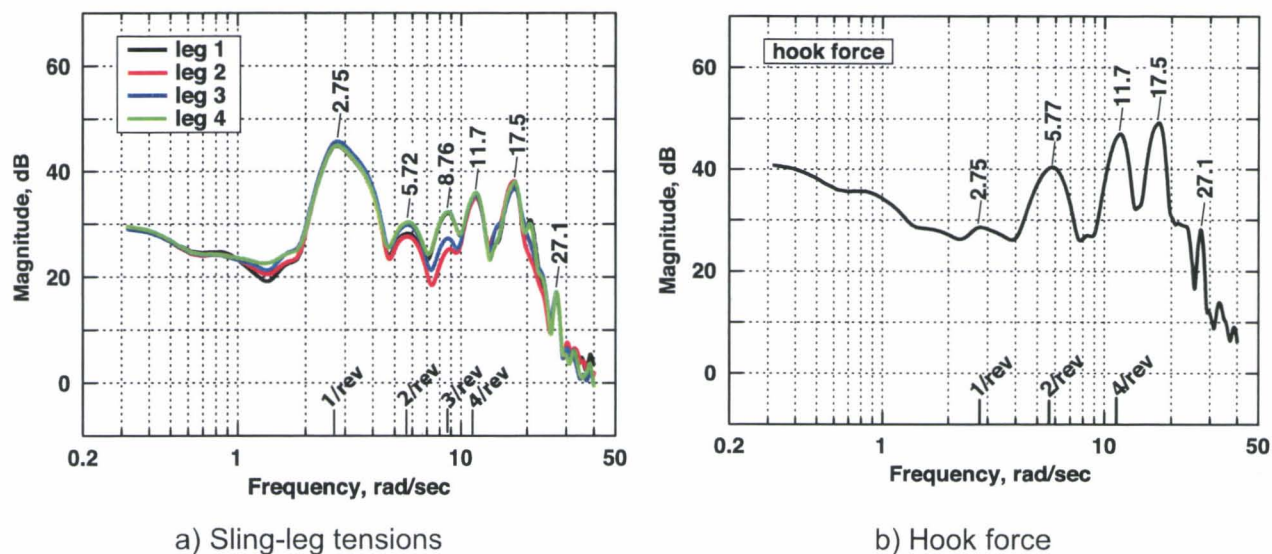


Figure 27. Sling-leg tensions and hook-force autocorrelations; 4000-lb CONEX; swiveled sling; 70 kias; Spin = 164 deg/sec.

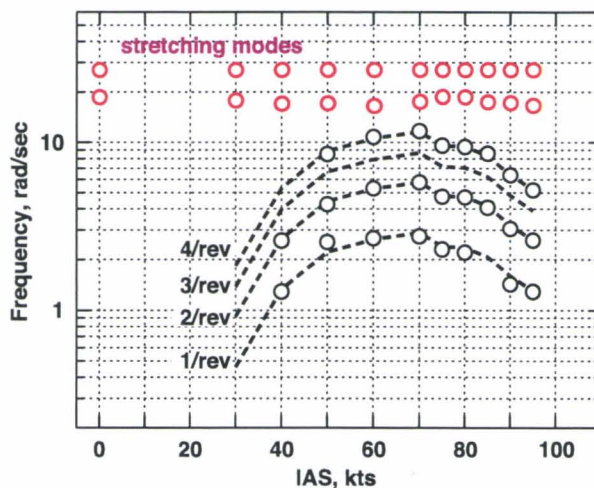


Figure 28. Hook-force principal frequencies; 4000-lb CONEX; swiveled sling.

Figures 29 and 30 present data for the 4000-lb CONEX without a swivel. In this case there are larger pendulum motions and yaw rate is periodic because of sling wind up.

Figure 29 shows cable-tension time histories at the airspeed for maximum windup (± 5 turns). The windup cycle (turns) is included in the figure for comparison. The largest amplitude variation in sling-leg tensions is periodic with very low frequency (0.07 rad/sec, period about 90 sec) and tracks the windup cycle. Excursions range down to 600 lb and up to 2100 lb. Smaller higher-frequency variations are superposed on that. The principal tension variations in sling legs 1 and 4 at opposite corners of the CONEX are in phase with each other and with the windup cycle so that tension is a maximum at maximum CW windup and a minimum at maximum CCW windup. Tensions in sling

legs 2 and 3 are 180 deg out of phase with tensions in legs 1 and 4, so that the load is not evenly distributed among the sling legs. The mechanism by which windup increases the load in one pair of sling legs while reducing the load in the other pair is unknown. Tension was expected to be a maximum at both the maximum CW and CCW windups in all sling legs because of the simultaneous shortening of the 4 sling legs. However, the data show an unexpected trend.

Autocorrelations of the four sling-leg tensions are shown in figure 30 for the same case shown in figure 29, and they are very nearly identical. The maximum magnitude occurs at the windup frequency (0.07 rad/sec). Magnitude at and around the pendulum frequency (1.3 rad/sec) is 20 dB smaller (20 dB corresponds to a factor of 10 difference in engineering units). Magnitude in this region is approximately fixed over a range of frequencies without a well-defined peak. The local peak at 13 rad/sec is 10 dB smaller than the magnitude at the pendulum frequency and may be the collective stretch mode, although at a lower frequency than expected from the sling stretch constant. Variations at the pendulum frequency and at the collective stretch frequency are readily seen in magnified time histories of the tension. The sharp peak at 27.1 rad/sec occurs at the same frequency previously seen for the swiveled sling and is the value expected for the longitudinal stretch mode.

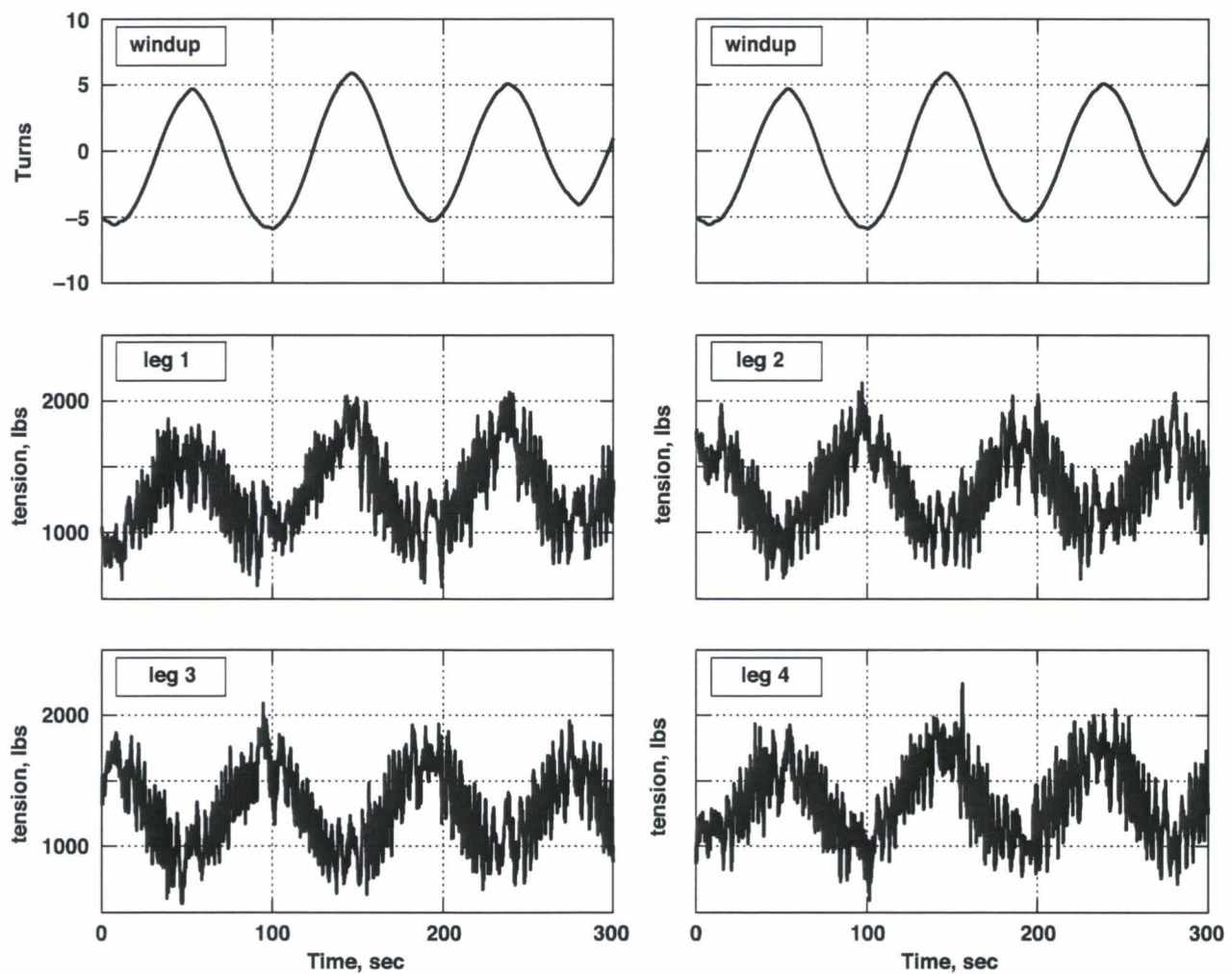


Figure 29. Sling-leg tensions; 4000-lb CONEX; no swivel; 80 kias.

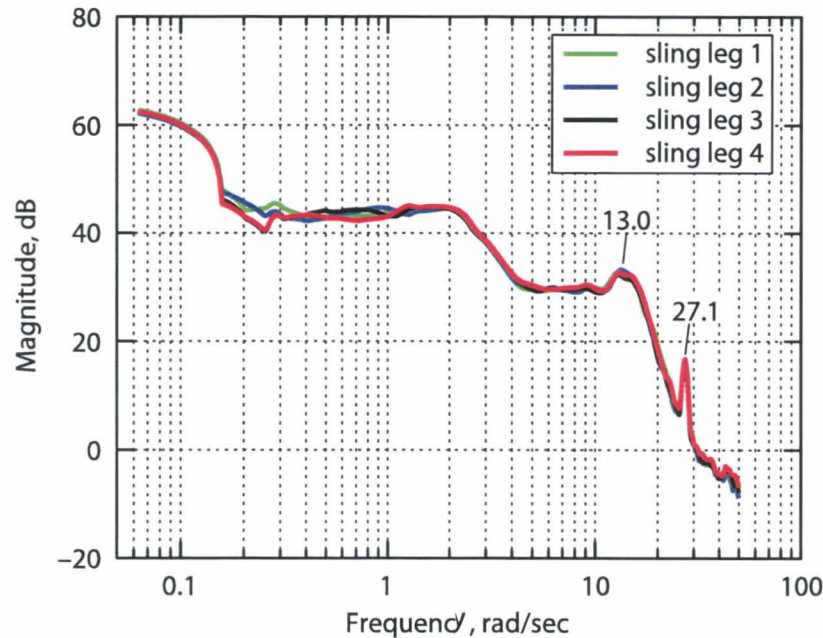


Figure 30. Sling-leg tension autocorrelations; 4000-lb CONEX; no swivel; 80 kias.

Summary. These data reveal three types of steady-state yawing motion; a steady spin rate with the use of a swivel, and with centered load cg; sling windup in the absence of a swivel and with centered cg; and oscillations centered around a trim heading if the cg is sufficiently offset from the x-y geometric center, where the trim heading is associated with the direction of the offset on the heavy side. For centered cg, it was found that steady spin, enabled by the swivel, suppresses the pendulum excursions and permits an expansion of the speed envelope of the CONEX out to near the power-limited speed of the configuration at all weights. Without a swivel, the empty CONEX becomes unstable above 60 kts, but stability and speed envelope improve significantly with ballasting.

Sling leg tensions and hook-force magnitude were documented. Results showed variations in sling leg tensions at the discrete frequencies of the collective and lateral stretching modes and at the frequencies of the load yaw motion; that is, at the harmonics of the spin rate for the swiveled sling and at the period of the windup oscillation for the sling without swivel. Sling leg tension variations at the motion frequencies were either in phase or pairwise out of phase. For the swiveled sling, the in-phase frequencies were reinforced in the hook force and the out-of-phase frequencies tended to cancel out, including the largest magnitude variation in the sling-leg tensions.

AERODYNAMICS OF THE SPINNING CONEX

This section reviews the extraction of load aerodynamics from flight data and compares the results with wind tunnel data for the static aerodynamics.

Equations. The method and equations used to extract the load aerodynamics and the aerodynamic angles from the flight data are given in detail in appendix D. Computations are based on the Newton–Euler force and moment balance equations for the load-sling subsystem. These equations are arranged to give the body-axes components of the aerodynamic force and cg moment in terms of the dynamic data (accelerations, attitude, angular rates, and sling-leg tensions) and parameters measured or estimated a priori (load weight, inertia, cg and EGI locations, sling geometry, and swivel friction). This process yields time histories of the aerodynamics from the flight data. The corresponding time histories of the aerodynamic angles, α , β , are computed from the air velocity vector at the load cg, which is determined from the EGI inertial velocity and wind information derived from the helicopter data. Finally, moments about the geometric center are computed for comparison with wind tunnel static aerodynamic data and body axes components are transformed to wind axes components.

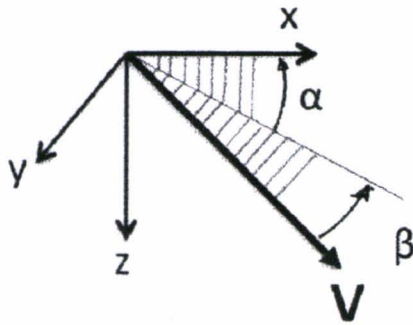
The aerodynamics that can be obtained from a sufficiently instrumented load are limited to the attitudes and motions adopted by the load autonomously in flight. Thus, this source of aerodynamic data does not lend itself to the systematic measurement of the load aerodynamics. However, in the present case with the use of a swivel the CONEX spins up to a steady spin rate and the aerodynamics are those of a spinning box at each recorded flight condition characterized by trail angle and spin rate (θ_T , Ω_{sp}). The effect of spin on the aerodynamics can be obtained by a comparison with the corresponding static aerodynamics obtained by interpolating the tabulated wind tunnel data from reference 24 for the same ($\alpha(t)$, $\beta(t)$) histories. Tables of wind tunnel data from reference 24 are documented in appendix E every 5 deg in α , β .

A question of interest is whether there is sufficient accuracy in the data to measure the effects of spin on the aerodynamics. The evidence that there is sufficient accuracy is discussed at the end of this section along with an error analysis in appendix D.

The results given in this section are for the 4000-lb CONEX with swiveled sling and centered cg with some additional results for the offset-cg configuration. All aerodynamics are given as force and moment divided by dynamic pressure.

Aerodynamic angles. The conventional aerodynamic angles, α , β , are the direction angles of the air velocity vector in load body axes. These angles are illustrated in figure 31. Figure 32 shows the locus of aerodynamic angles, $\alpha(\beta)$, for sample airspeeds over the speed range of the flight tests. The plots show data for all revolutions in each flight record, 20 to 40 revolutions depending on the record. As seen, $\alpha(\beta)$ is a repeating locus with a narrow range of α values at each β . The locus is more or less narrow, depending on the pendulum motions occurring simultaneously with the steady spin. Similar characteristics occur in all flight records for the spinning CONEX. As previously noted, there is a gap in the values of β obtained around $\beta = \pm 90$ deg (small side into the wind). This gap is due to discontinuities in both α and β in the map from continuous velocity component

histories, u , v , w , to the aerodynamic angles, and the β gap is related to the trail angle and increases with trail angle. Similarly there is a gap in the range of values of α that occur; it is also related to the trail angle; that is, values in $[-\theta_T, \theta_T]$ are not obtained except for some values inside this range because of pendulum swinging. Taking these records together (last plot in fig. 32), it is seen that only about a quarter of the complete domain of the aerodynamic angles was accessible in these flight tests.



β angle from V to its projection on the body x - z plane.

α angle from projection of V on body x - z plane to body x -axis

$$V_b = (u, v, w)^T$$

$$\alpha = \tan^{-1}\left(\frac{w}{u}\right), \quad -90 < \alpha < 90$$

$$\beta = \tan^{-1}\left(\frac{v}{u/\cos\alpha}\right), \quad -180 < \beta < 180$$

Figure 31. Aerodynamic angles; definitions.

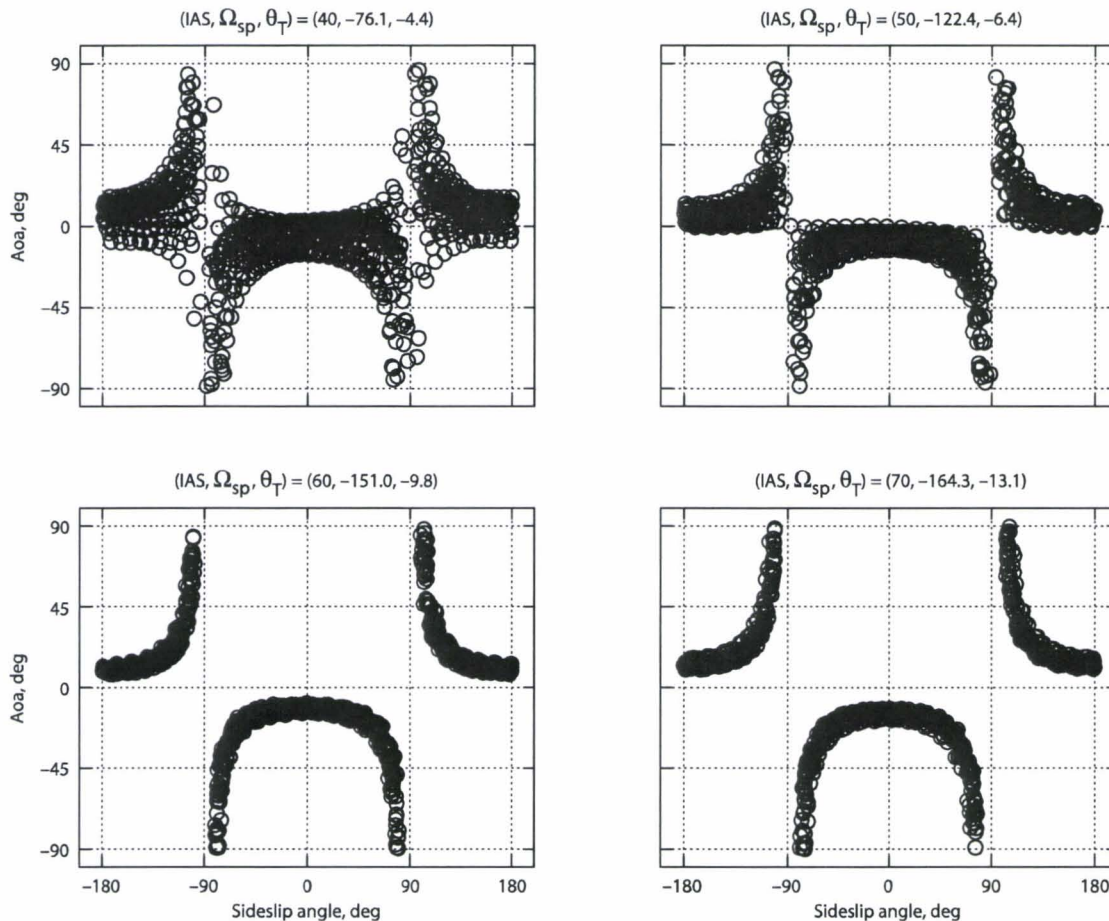


Figure 32. Aerodynamic angles; 4000-lb CONEX; swiveled sling (units: kts, deg, sec).

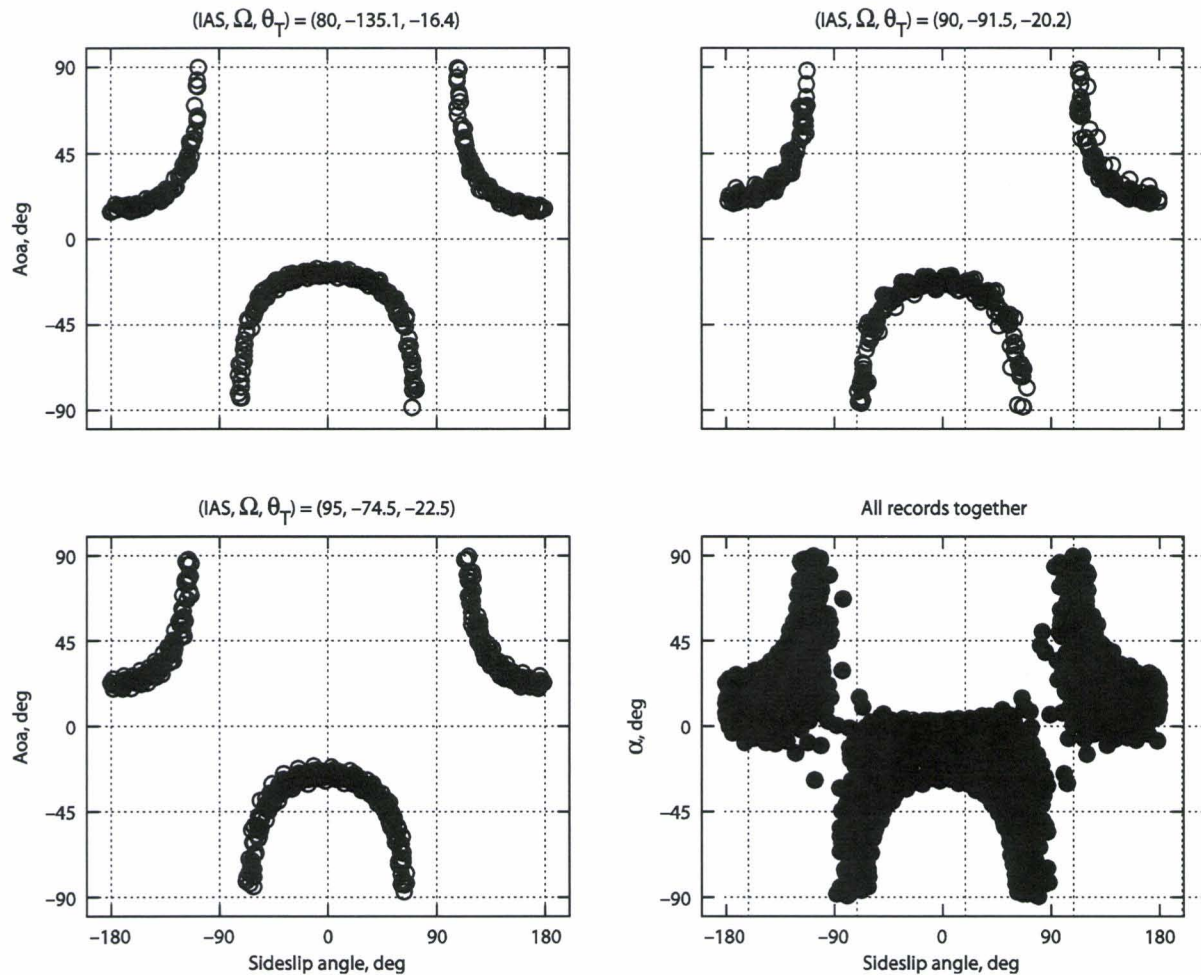


Figure 32. Aerodynamic angles; 4000-lb CONEX; swiveled sling (continued).

Drag. Figure 33 shows the drag parameter vs. sideslip angle for all revolutions in each flight record. The figure includes the static drag as obtained from wind tunnel measurements corresponding to the flight (α, β) history and the difference between the two. Note that, in principle, bluff-body aerodynamics are independent of Reynolds number so that the data from scale-model tunnel tests is an accurate measure of the full-scale data. This fact has been substantiated for the CONEX in CFD computations, (refs. 5 and 7), and evidence from the present flight test data indicates that it is true.

The principal difference between flight and static drag is that the flight drag is less than the static drag at all or nearly all points around a revolution. The mean drag around a revolution is shown in figure 34. The mean flight drag is less than the mean static drag at all airspeeds, and the reduction is 14 to 22% of the mean static drag. The reduction can be due to systematic tunnel error, systematic flight measurement errors, or the effect of spin on drag. There is some evidence that the flight data are accurate (the trail angle matches the flight drag estimate), leaving the other two possible explanations for the drag reduction.

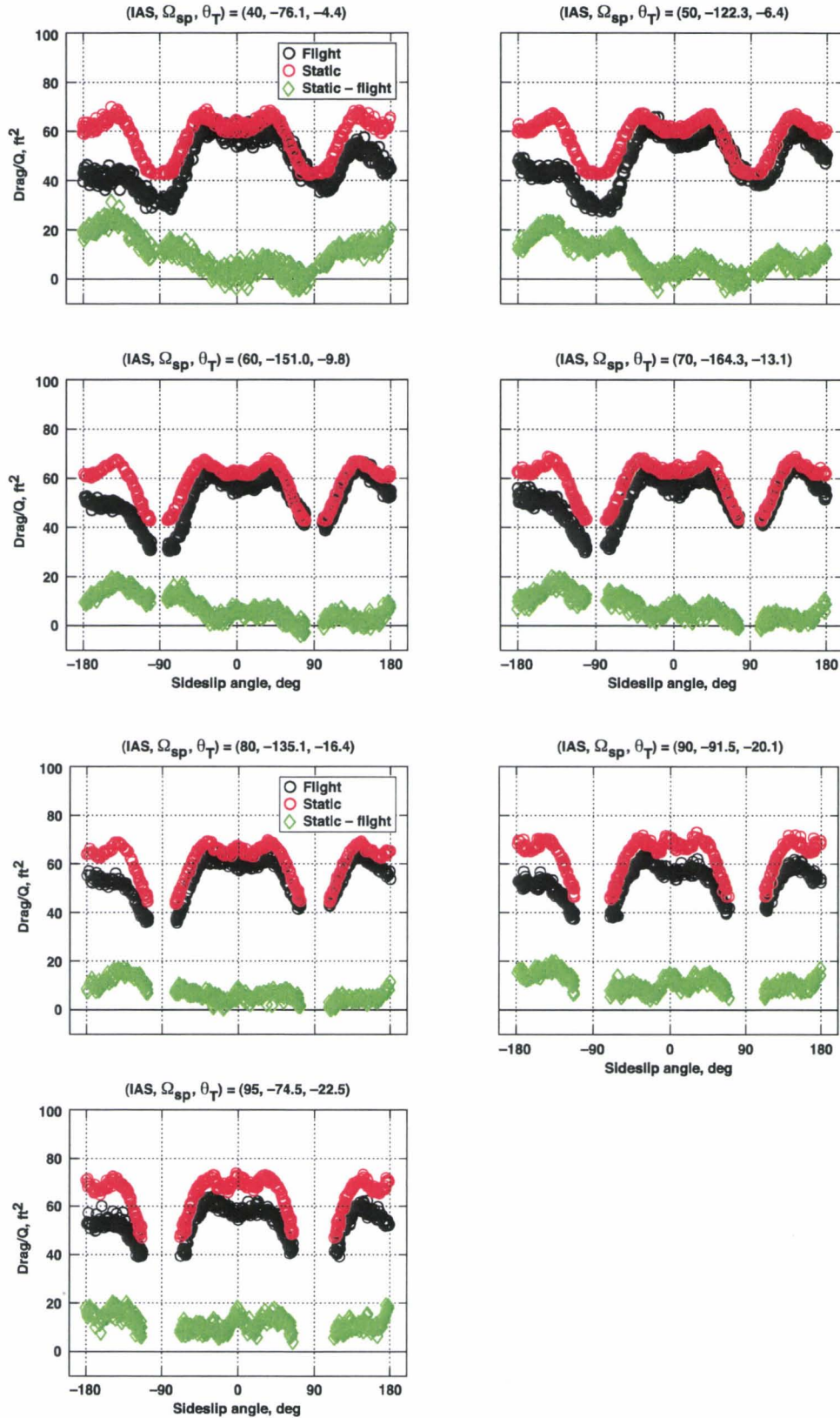


Figure 33. Drag; 4000-lb CONEX; swiveled sling (units: ft, kts, deg, sec).

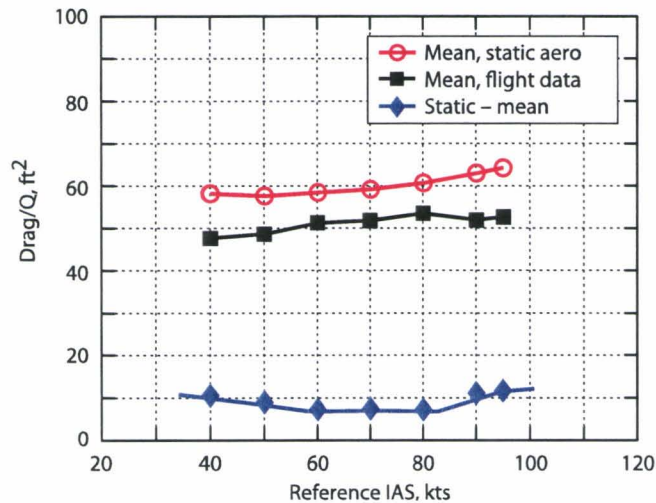


Figure 34. Averaged flight and static drag; 4000-lb CONEX; swiveled sling.

Side force. Figure 35 compares the flight and static side-force parameter. Counterclockwise (CCW) spin corresponds to increasing beta around a rotation. The principal effect of spin is a large reduction in slope after broadside into the wind (after $\beta = -180$ and 0 deg). The static side force is antisymmetric around a face flat to the wind, and the effects of spin distort this symmetry. Phase shift due to lags in the development of flow structures compared to the static flow structure are a factor in this difference. A visible trend is that the difference between static and flight reduces with increasing airspeed and nearly disappears at the highest airspeeds because of decreasing spin rate as expected. However, a comparison of the differences in the 40- and 95-kias plots suggest that factors associated with trail angle also affect the difference.

Lift. The presence of lift in the load flight aerodynamics is examined in figure 36 in a plot of specific lift (lift divided by weight) vs. airspeed. Mean values are negligible to $0.05g$ at the highest airspeed, and variations around the mean due to spin are under $0.1g$. For the 4000-lb CONEX lift has little effect on load motions or the trail angle. The mean specific drag is included in the plot for comparison.

Z-moment. Time histories of the z-axis component of the moment about the geometric center are shown in figure 37. The moment about this axis accounts for the load spin characteristics. In each case, the plot shows behavior for one period of rotation.

Comparison of flight and static aerodynamics in any sample record shows that both have the same frequencies with 4 pairs of extremes each revolution. The relation between the two can be characterized as lags in the zero crossings and extremes and changes in the magnitudes of the extremes, and these difference properties vary around a revolution. The frequency content of the time histories is shown in figure 38 for a sample record. The plot shows that both time histories have three principal frequencies that correspond to harmonics of the spin rate at 2, 4, and 8 per revolution; that is, the time histories are superpositions of periodic functions with these three frequencies. The lowest harmonic is related to the property of the static aerodynamics that all aerodynamic components repeat themselves every 180 deg of rotation about a fixed spin axis and therefore occur at $2/\text{rev}$. The autocorrelations seen in figure 38 are typical of all the flight records with the CONEX spinning.

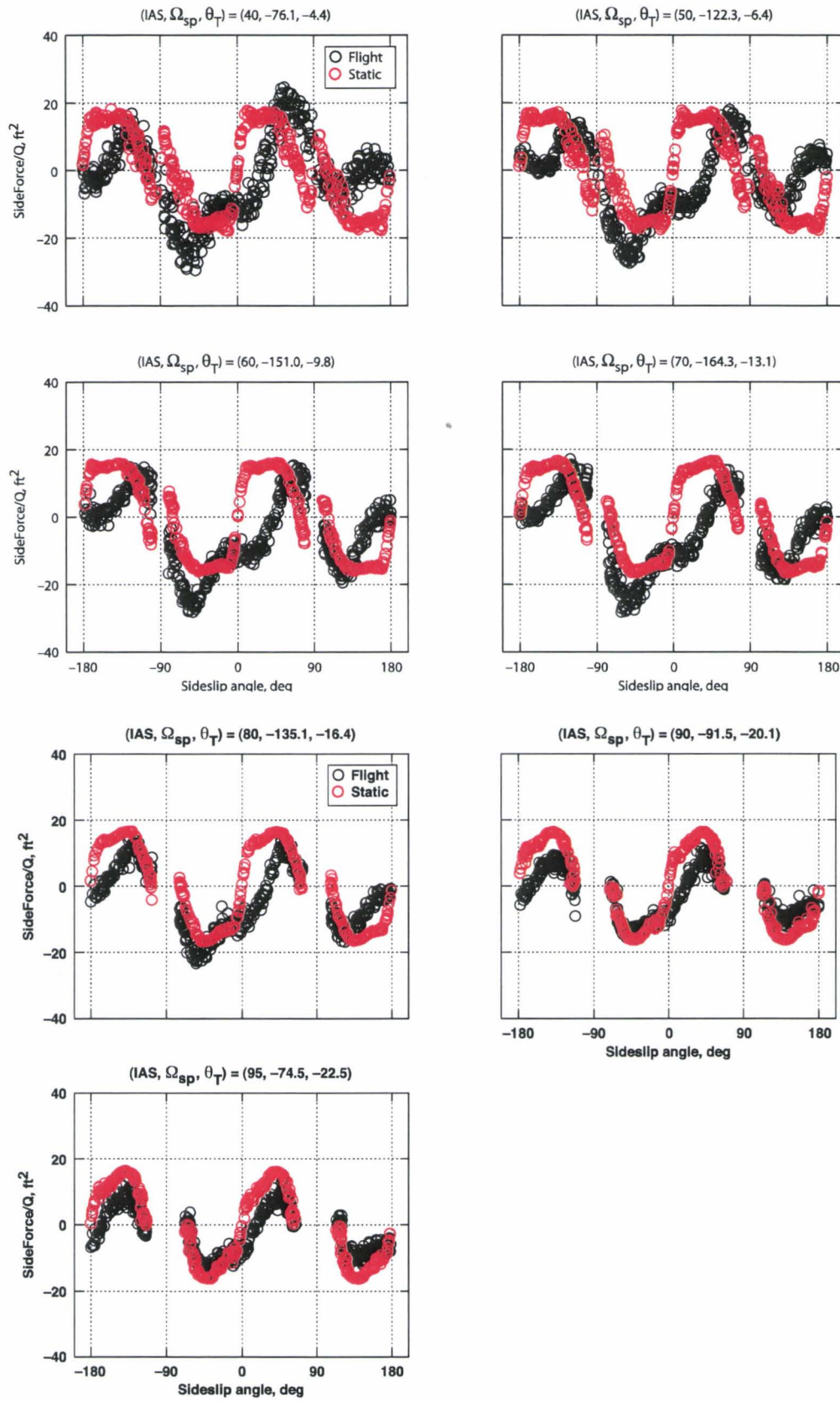


Figure 35. Side force; 4000-lb CONEX; swiveled sling (units: kts, deg, sec).

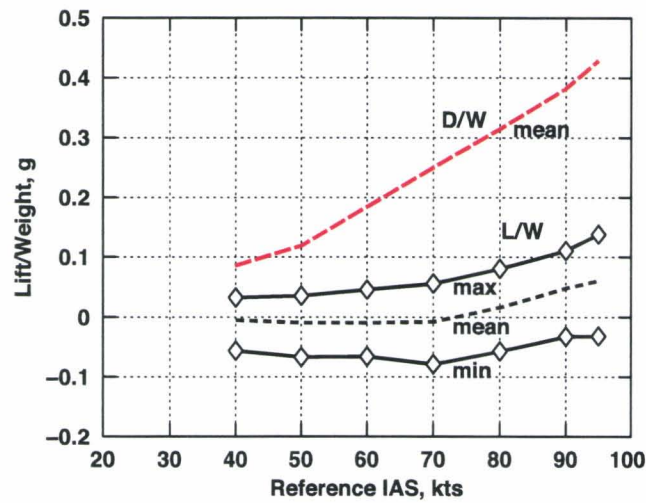


Figure 36. Lift; 4000-lb CONEX; swiveled sling.

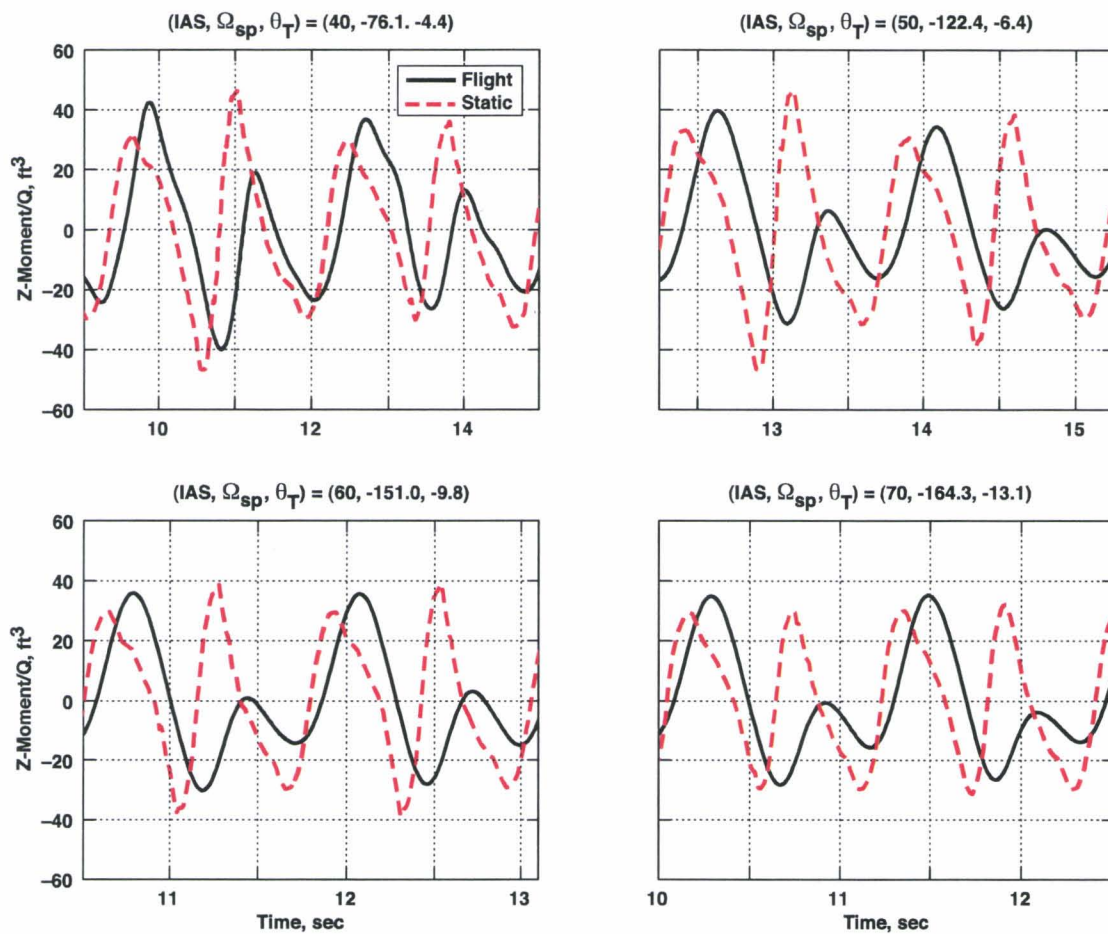


Figure 37. Z-Moment; 4000-lb CONEX; swiveled sling (units in subplot titles are kts, deg/sec, and deg).

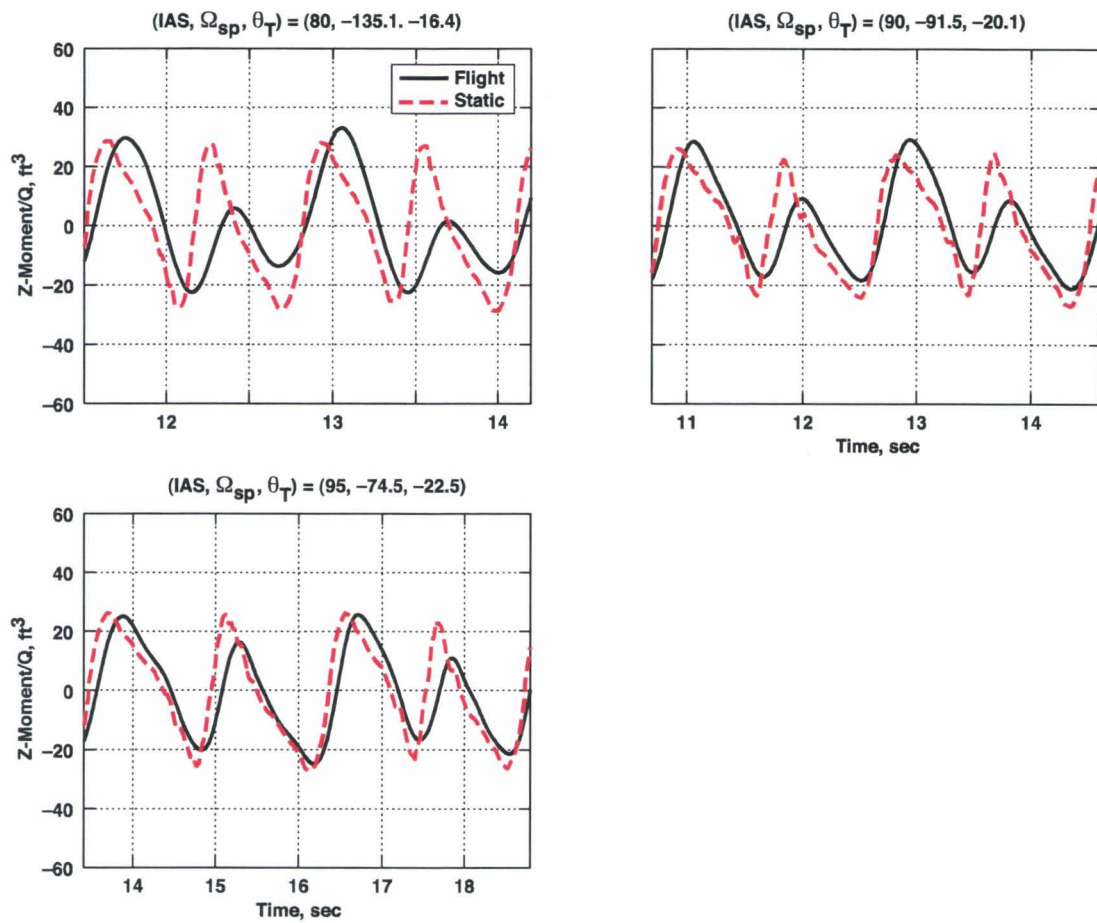


Figure 37. Z-Moment; 4000-lb CONEX; swiveled sling (continued).

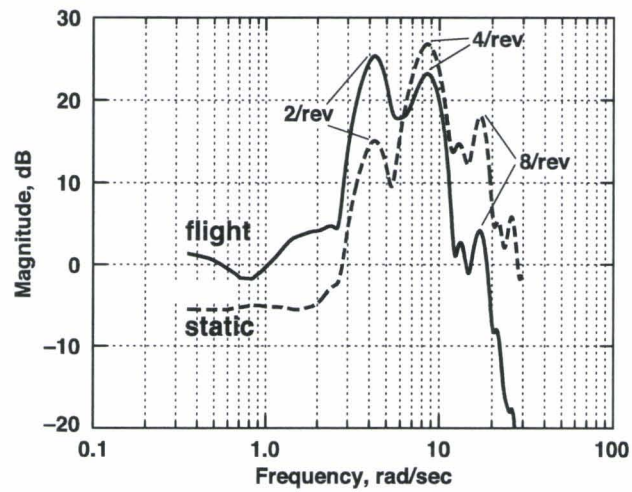


Figure 38. Autocorrelations; z-moment; 50 kias; Spin = -122 deg/sec.

The relation between the aerodynamics of the spinning CONEX and the corresponding static aerodynamics can be further characterized by the frequency response between the two. A sample case is shown in figure 39. The stair-step variation in magnitude and phase with frequency and the peaks of coherence at particular frequencies is typical of a system with discrete frequencies. Gain and phase at the discrete frequencies can be extracted from the frequency responses and these values are collected for all test airspeeds in figure 40. The largest gain reduction and phase shift of the spinning

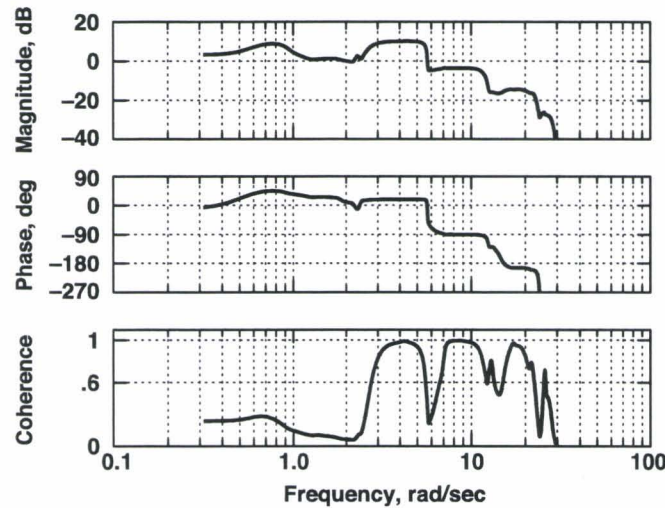


Figure 39. Frequency response at 50 kias; $\frac{MA_{z_{flight}}}{MA_{z_{static}}}$

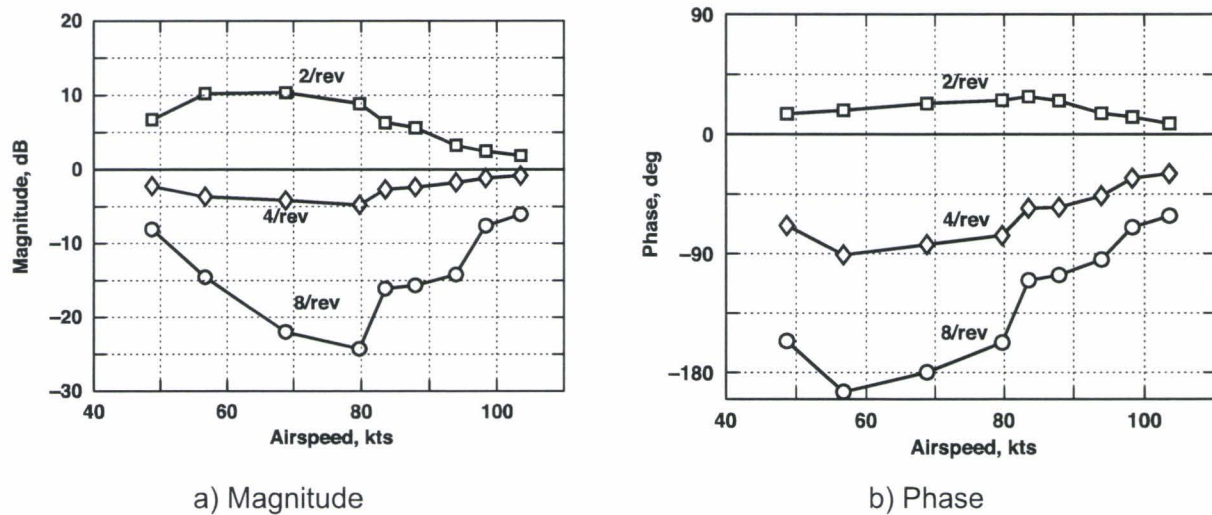


Figure 40. Magnitude and phase at discrete frequencies; 50 kias; $\frac{MA_{z_{flight}}}{MA_{z_{static}}}$

CONEX Z-moment relative to the static z-moment occur in the 8/rev component, with lesser attenuation and phase shift in the 4/rev component and some gain and lead in the lowest harmonic. An interesting trend is that the flight z-moment converges on the static z-moment at the highest airspeeds, similar to the expected trend seen above in the side force results. This trend is seen in the Z-moment time histories and again in figure 40, where the harmonic components converge toward 0 dB and zero phase shift.

It is possible to fit a transfer function through the frequency response that matches phase and magnitude at the discrete frequencies and also matches the static magnitude corresponding to the mean flight spin rate. This fitting was done for several airspeeds in a separate study reported in references 6 and 11 using frequency domain identification utilities from the literature (ref. 25). The transfer function can be transformed to an ordinary differential equation (ODE) in the time domain to model the effects of spin on the static aerodynamics. The ODE model was implemented in a simulation and the simulation reproduced the flight yaw motions accurately. This result confirms that the flight measurements were sufficiently accurate to capture the effects of spin on the aerodynamics.

Aerodynamics with offset cg. As previously discussed, the flight motions for the offset cg load configuration consisted of yaw oscillations around the small heavy end into the wind. The corresponding yaw rate was oscillatory with amplitudes up to 50 deg/sec. The data so far indicate that yaw rates of that magnitude have little effect on the aerodynamics. Consequently, the aerodynamics should be very close to the static aerodynamics, and a comparison with the static aerodynamics from the wind tunnel data will provide a further test of the accuracy of the flight data.

The following data were obtained at 80 kias. The load aerodynamic angles for this case, and, therefore, the scope of the comparison, are limited to a narrow but substantial region of the aerodynamic angle domain shown in figure 41.

Figure 42(a) shows the spin-axis component of the moment about the load gc vs. relative heading. This moment accounts for load yaw motions. It is seen that this moment is statically stable at almost all times (points in the upper-left and lower-right quadrants are restoring towards the central relative heading at 90 deg). A plot of the corresponding wind tunnel static aerodynamic data (fig 42(b)) shows close agreement with the principal features of the flight data. The data are from 18 cycles of the yaw oscillation. The average values vs. relative heading were computed, and good agreement between the flight and wind tunnel data was obtained (fig. 42(c)).

Figure 43 shows 20-second samples of the drag and side force. These components differ strongly in that drag is large with small oscillations at twice the frequency of the yaw oscillation while side force is small and oscillatory around zero at the yaw frequency. The flight data capture these distinct characteristics accurately, although with a moderate bias in the drag magnitude (under 10%).

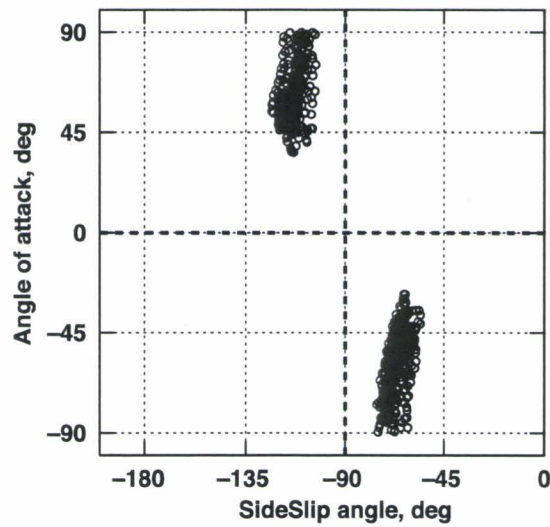
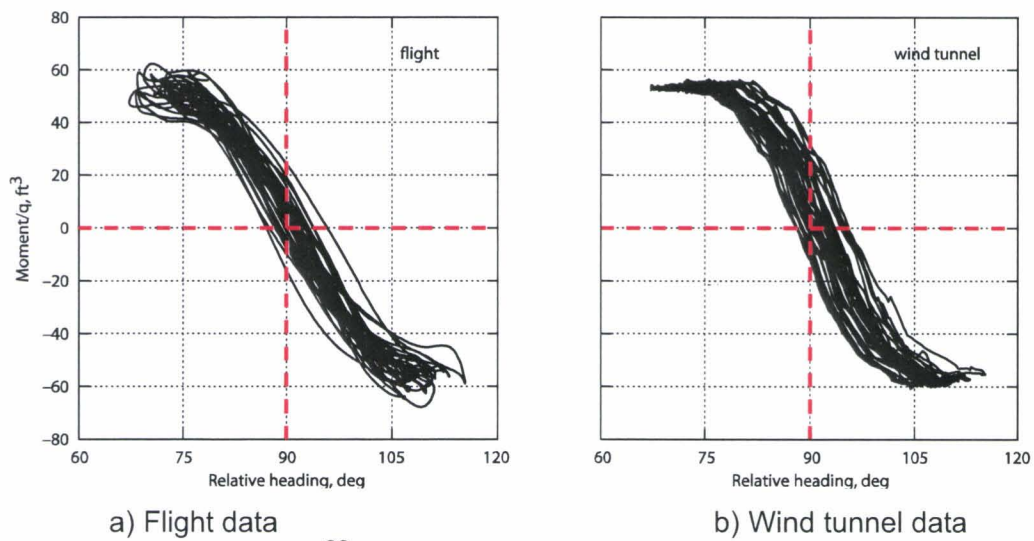
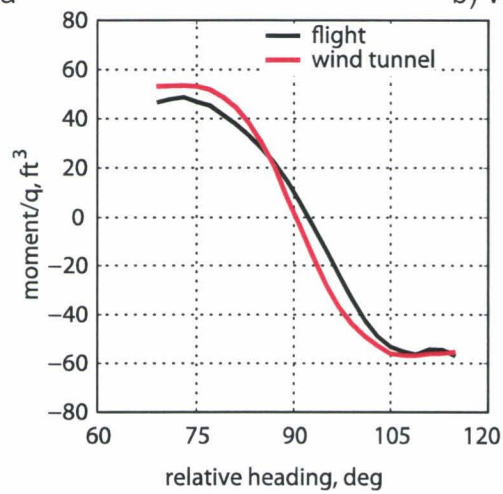


Figure 41. Aerodynamic angles; offset cg; 80 kias.



a) Flight data

b) Wind tunnel data



c) Comparison of means vs. $\Delta\psi$

Figure 42. Moment about the spin axis; offset cg; 80 kias.

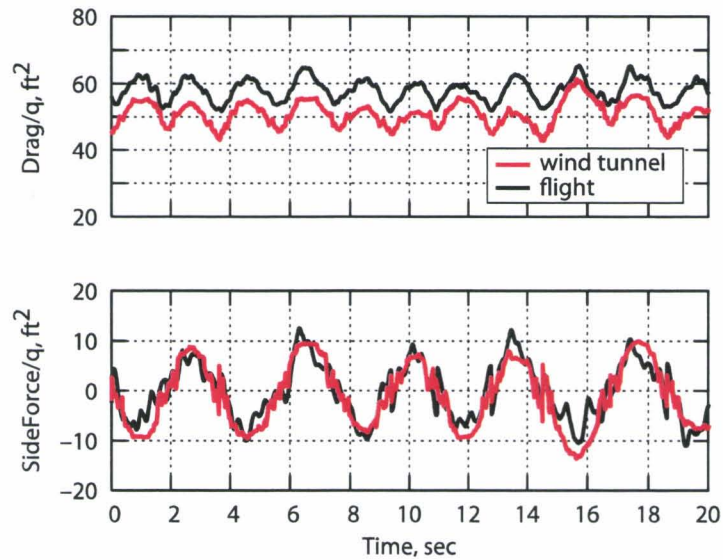


Figure 43. Drag and side force; offset cg; 80 kias.

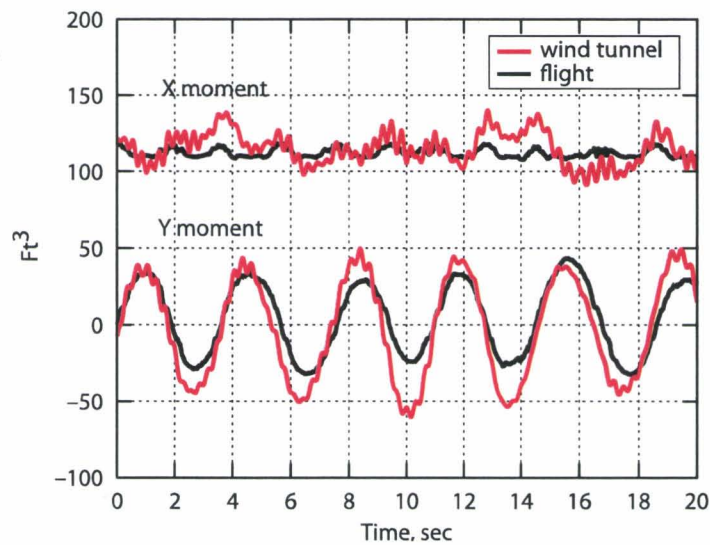


Figure 44. X- and y-moments; offset cd; 80 kias.

Figure 44 shows 20-second samples of the x and y body-axes moments about the cg. These two components, like drag and side force, have distinct characteristics, and they are accurately measured by the flight data.

The results in this section, for both the spinning CONEX and the nearly static CONEX, confirm that the load aerodynamics have been accurately extracted from the flight data using current state-of-the-art rigid-body dynamic sensors and system-parameter estimates (weight, inertia, etc.) of modest accuracy. In addition, the results tend to confirm the accuracy of the scale-model wind tunnel data in measuring the full-scale aerodynamics.

ENGINE CANISTER FLIGHT CHARACTERISTICS

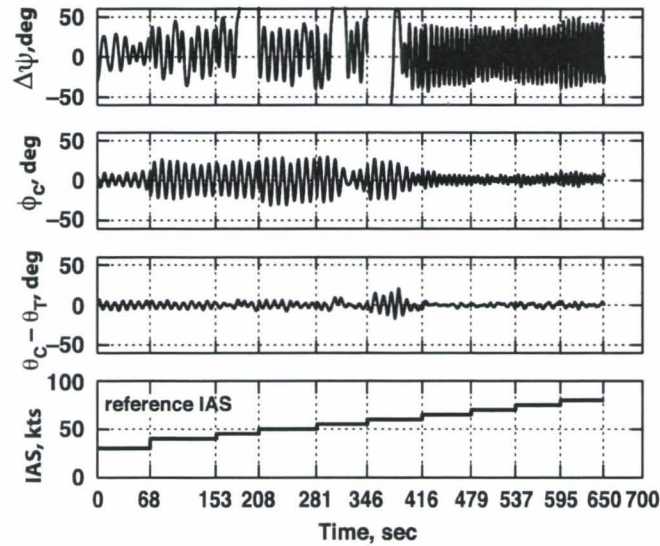
The engine canister was added to the flight test program to have a second, previously untested load to validate the ability of the simulation in references 8 and 10 to predict the motions of unknown loads. Its flight characteristics are sufficiently different from cargo containers to be of general interest. Data were obtained with a long-line sling (81 ft from hook to load cg) and the sling set (20 ft from hook to cg) at forward speeds from 30 to 80 kias. The suspension included a swivel in these tests.

Load motions. Load motion results for the long-line and sling-set suspensions are shown in figure 45 for all airspeeds concatenated together. Relative heading, $\Delta\psi$, (load heading minus helicopter heading) and the cable angles are shown. All angles are plotted to the same scale, and the trail angle has been subtracted from the longitudinal cable angle to facilitate comparison of motion amplitudes.

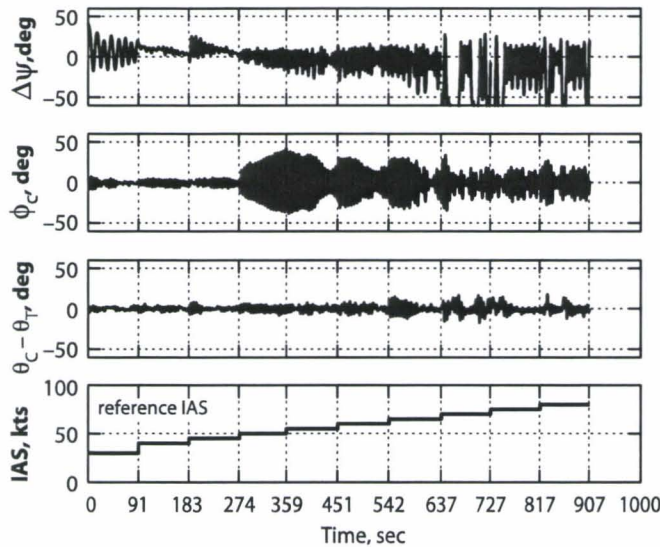
For the long-line sling (fig. 45(a)), the engine canister aligned broad side to the wind and oscillated in yaw within 45 deg of that orientation, except for occasional excursions out to small side into the wind or rotating by $n \times 180$ deg before resettling into oscillations around a broadside orientation. The yaw oscillation frequency is visibly higher for speeds greater than 60 kts than for lower speeds. Pendulum motions show oscillatory lateral oscillations at all airspeeds, and these oscillations continue through the periods where the directional oscillations are interrupted by rotational motion. Amplitude is small at 30 kts and then enlarges to 20 to 25 deg over the range of 40 to 60 kts and becomes small again at higher airspeeds. Longitudinal cable angle is oscillatory out to 60 kts, and then the longitudinal motions lapse into small nonperiodic variations above that airspeed. Its amplitude is much smaller than the lateral cable-angle amplitude at all airspeeds.

For the sling set (fig. 45(b)) the load again oscillates in yaw around broadside to the wind with some excursions out to the small side to the wind at the highest speeds, 70 to 80 kts. Details differ from the long-line suspension in that yaw oscillation amplitudes are well below 45 deg and irregular and the central heading is offset from broadside (e.g., at 40, 45, 75, and 80 kias). The lateral pendulum is small up to 45-kts airspeed, surges out to 40-deg amplitude at 50 kts, and then remains active at moderate to large amplitudes at all higher airspeeds. The surge to 40 deg is much larger than for the long-line sling and excessive for operational flight. The CONEX also exhibits a surge in pendulum amplitude at 50 to 60 kts, where load aerodynamics first become a significant forcing function on the load motions relative to gravitational forces. A similar surge was noted in recent flight tests of a nearly cubic load. Longitudinal swing is small with irregular amplitude at all airspeeds.

In summary, the principal motions of the engine canister are lateral pendulum oscillations and directional oscillations around broadside to the wind. Details of the motion differ significantly for two sling lengths.



a) Long-line sling



b) Sling set

Figure 45. Engine-canister motions.

Principal frequencies. The principal frequencies of the three load degrees of freedom (yaw and the two cable angles) are shown in figure 46 for all test airspeeds. These frequencies were determined from the magnitude peaks in the autocorrelations of the time histories. For the long-line sling (fig. 46(a)) the cable-angle frequencies match the simple pendulum frequency (0.63 rad/sec) up to 60 kts. In that speed range the lateral pendulum motions are moderately excited (fig. 45(a)) and the directional frequency is close to or matches the pendulum frequency. At higher airspeeds, the directional frequency rises to about 1 rad/sec and the side-force variations due to the yaw oscillation force a small-amplitude (5-deg) lateral oscillation at the same frequency while lateral oscillations at the pendulum frequency die out.

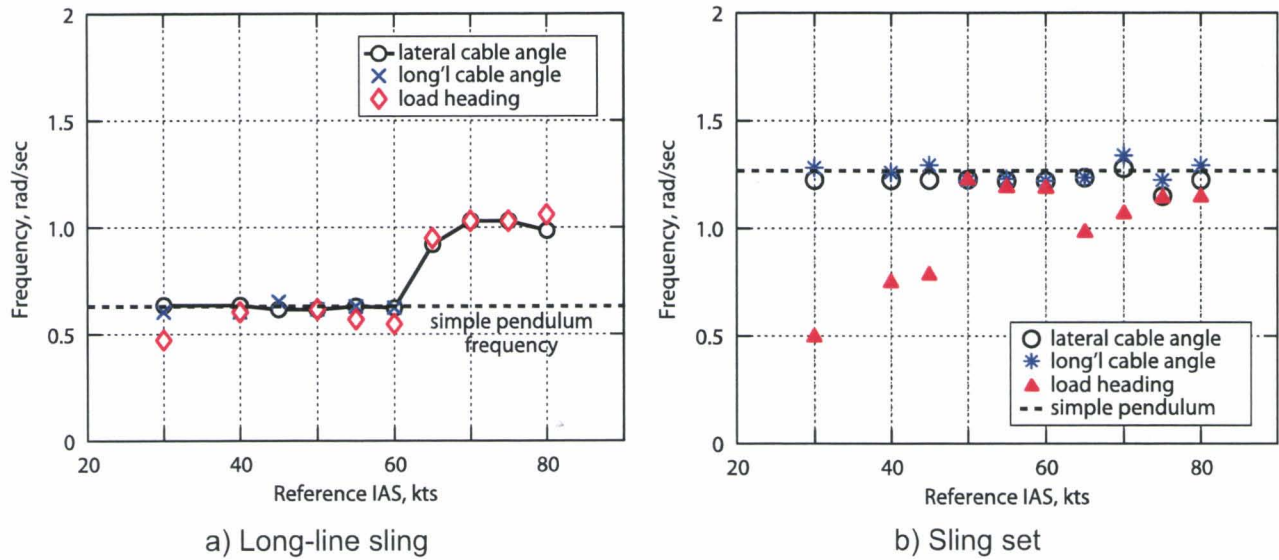


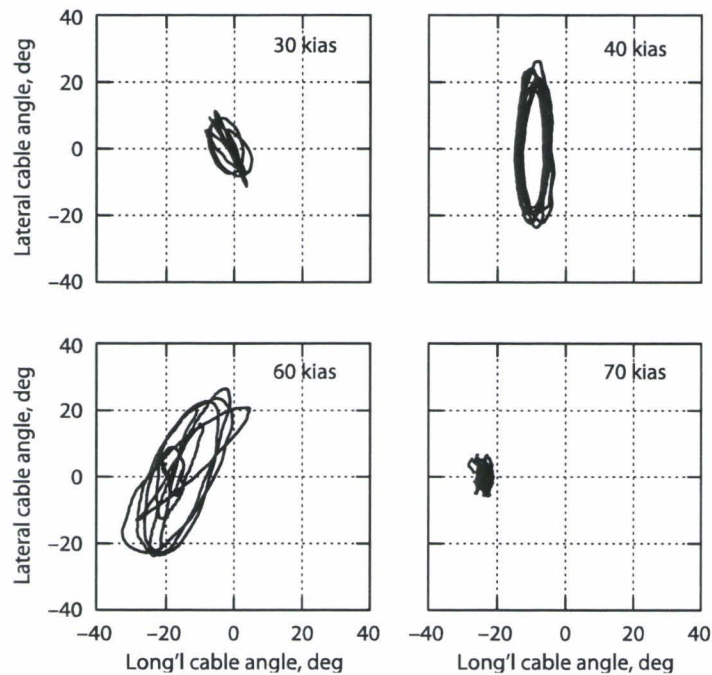
Figure 46. Engine-canister motions: Principal frequencies.

For the sling set (fig. 46(b)) the longitudinal and lateral cable-angle oscillations are very close to the simple pendulum frequency (1.23 rad/sec) at all airspeeds. Yawing frequency is well below the pendulum frequencies at low speeds so that the pendulum and directional motions are not coupled. At 50 kts, where the surge in lateral excursions occurs, the yawing frequency rises to the pendulum frequency and remains at or near the pendulum frequency at all higher airspeeds.

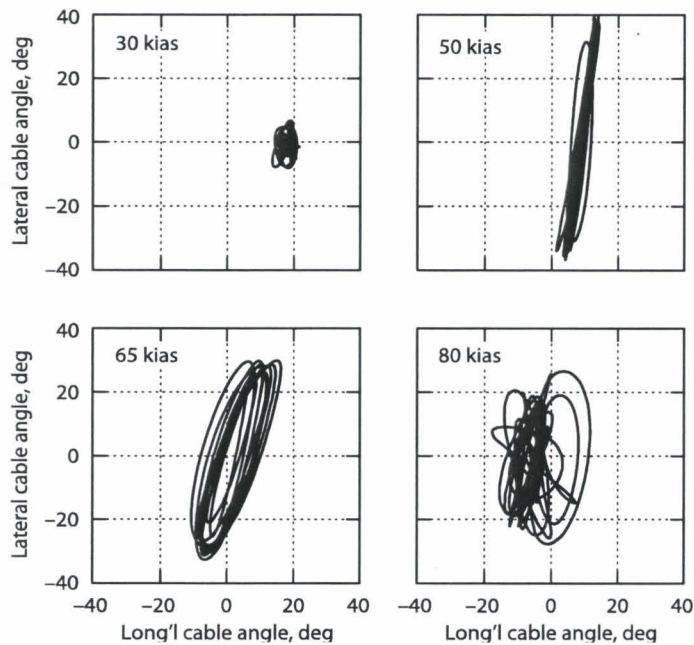
Motion figures. Pendulum loci, $\phi_C(\theta_C)$, for several airspeeds are shown in figure 47. All subplots and axes are at the same scale. For the long-line sling (fig 47(a)) the figure at 40 kts shows coupled motions with dominating lateral cable angle and 90-deg relative phase (maximum ϕ_C at $\theta_C = 0$). The figures at 30 and 60 kts show a less-coherent relationship; lateral cable angle dominates, and at 30 kts the orientation of the long axis of the locus indicates 180-deg relative phase (maximum ϕ_C at minimum θ_C), which shifts to 0 deg at 60 kts. (maximum ϕ_C at maximum θ_C). The figure at 70 kts illustrates the disappearance of significant pendulum motions at high speeds.

For the sling set (fig 47(b)) the subplots show the dramatic increase in lateral pendulum motion at 45 and 50 kts, the large lateral motions at all higher airspeeds and the small magnitude of the longitudinal motion. The orientation of the long axis at 50 and 65 kts indicates 0-deg relative phase. At 80 kts coherent coupling is lost and the relative phase shifts during the record, resulting in random pendulum motion.

Lateral-directional motion loci for two airspeeds are shown in figure 48. For the long-line sling (fig 48(a)), the cases shown at 50 and 70 kts have identical lateral and directional frequencies with a nearly fixed relative phase (180deg). These loci are typical for the two speed ranges with large and small lateral oscillations, respectively. For the sling set (fig 48(b)) the cases at 50 and 60 kts have identical lateral and directional frequencies. The figure at 50 kts shows the dominance of the lateral pendulum motion and a relative phase of 90 deg. At 60 kts, the figure is less coherent and the orientation of the long axis indicates 0-deg relative phase.



a) Long-line sling



b) Sling set

Figure 47. Engine-canister pendulum motions.

Motion summary. The dominant motions are lateral and directional oscillations around the long side to the wind, with little excitation of longitudinal motions. The data indicate varying degrees of coupling among the oscillations of the three degrees of freedom, depending on sling configuration and airspeed.

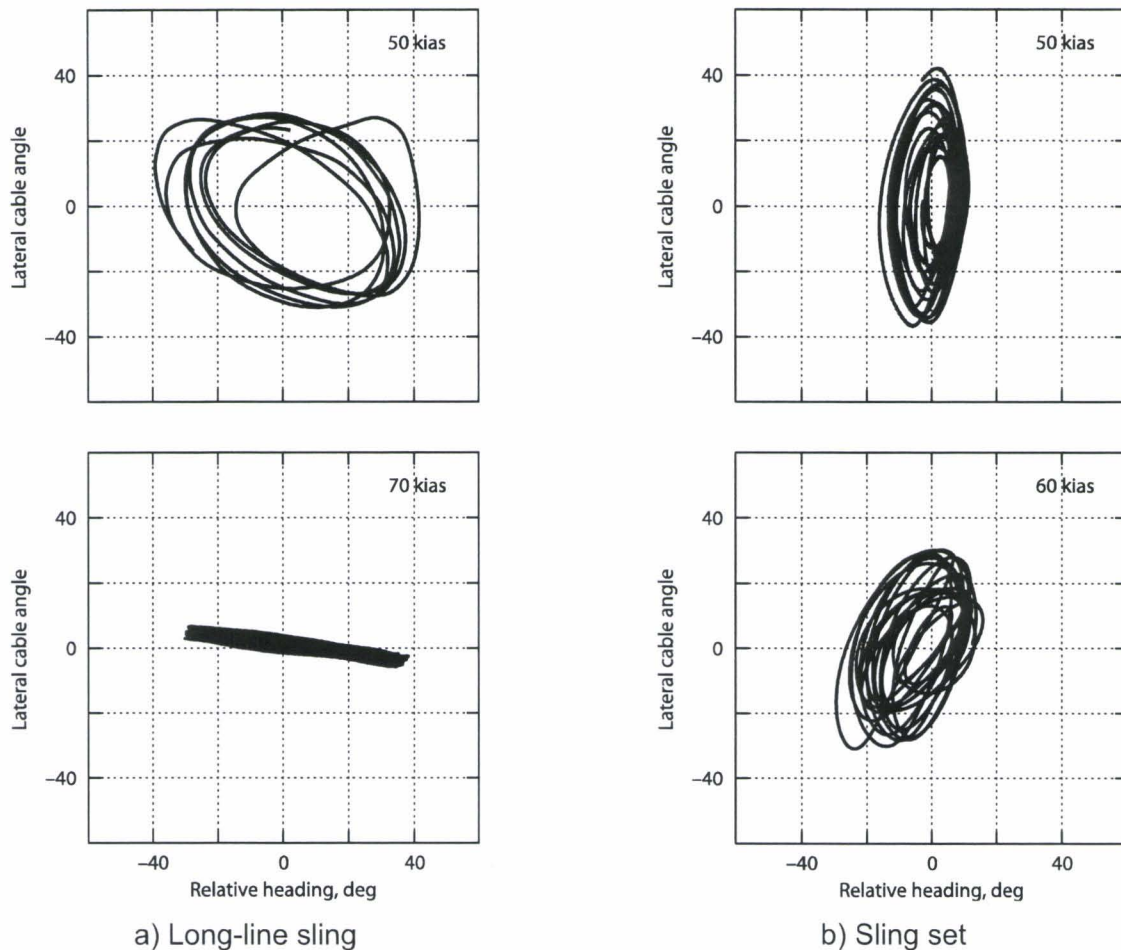


Figure 48. Engine-canister lateral-directional motions.

For the long-line sling, there is a coupled lateral-directional oscillation up to 60 kts at the pendulum frequency (0.63 rad/sec). Above 60 kts, the lateral-directional coupling continues, except that lateral pendulum amplitude is reduced to 5 deg and frequency increases above the simple pendulum frequency. In the high-speed range, the small lateral oscillation is forced by the variation in side force due to the directional oscillation. In the low-speed range the lateral oscillation continues through periods when the load breaks out of its directional oscillation to rotate by $n \times 180$ deg to a new broadside central orientation.

For the sling set, lateral oscillations at the pendulum frequency (1.23 rad/sec) dominate the load motion starting at 50 kts and become excessive. There are irregular directional oscillations in the region around broadside with much lower amplitude than for the long line, and the frequencies of the two oscillations differ. The different pendulum frequencies of the two sling configurations may account for the distinctly different details of the lateral-directional motions.

Trail angle. Data for both suspensions are shown in figure 49(a). Unlike the CONEX, it was found that engine-canister lift was significant, so the effect of lift was included in the approximate expression for trail angle given by (see figure 49(b))

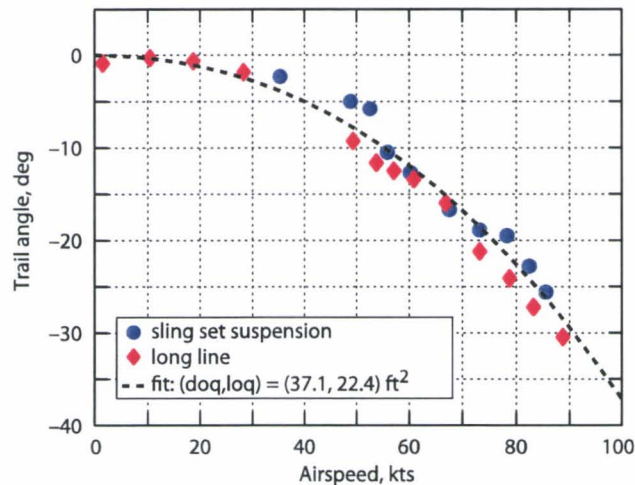
$$\theta_T = \tan^{-1} \left(\frac{D}{W - L} \right)$$

The results of fitting this expression to the flight data in figure 49(a) gave drag and lift parameter values of

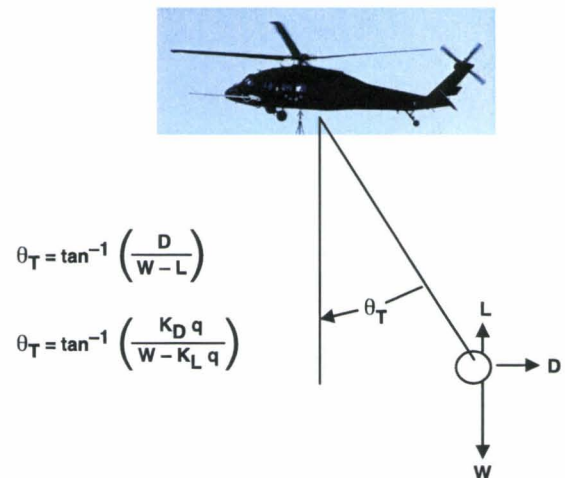
$$D/q = 37.1 \text{ ft}^2$$

$$L/q = 22.4 \text{ ft}^2$$

These values are average values for all the flight records (an average for the attitude history at a given airspeed and then over all airspeeds at different trail angles). These results are consistent with the assumption of significant lift, and both parameter values are within the range of their values obtained in the extracted aerodynamics given in the next section. The corresponding mean specific drag and lift values are shown in figure 50. Lift reaches 20 to 25% of load weight at the limiting true airspeed (85 to 90 kias).



a) Trail angle



b) Trail-angle approximation

Figure 49. Engine-canister trail angle.

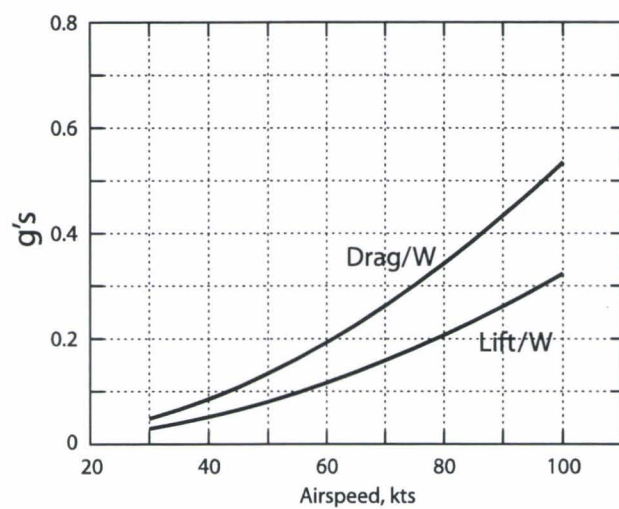


Figure 50. Engine-canister mean specific drag and lift.

ENGINE CANISTER AERODYNAMICS

The engine canister is a 9-ft-long by 5-ft-diameter cylinder with flanges, rings, and skids attached (fig. 3). Its flight motions are primarily oscillations around broadside to the wind, with occasional temporary excursions to small side into the wind and rotations by $n \times 180$ to a new broadside orientation, plus lateral pendulum swing (fig. 45). The frequencies of these motions (fig. 46) are low enough that the aerodynamics obtained from the flight data will be close to the static aerodynamics of a stationary canister. In the following discussion, the engine canister body axes are z positive down and x perpendicular to this axis and perpendicular to the long dimension of the canister. Sideslip angle is zero when the canister is broadside to the wind.

Load cells were present on this load only in flights 91 (trims from 40 to 80 kts) and 107 (climbs, descents, turns, accelerations, and decelerations above 45 kts), both flown with the sling set. The autonomous motions of the engine canister restrict the aerodynamic angles coverage to modest regions around $(\alpha, \beta) = (\theta_T, 0)$. Figure 51(a) shows the coverage obtained in the 50 and 80 kias trim records, and figure 51(b) shows the coverage obtained from all records from both flights merged together. The available coverage is less than 20% of the domain. The flight 107 maneuvers were designed to increase the angle-of-attack coverage and resulted in a modest increase from that given by the trim records, principally adding data at small negative and positive angle-of-attack values to the region around broadside.

The principal aerodynamic components are shown vs. sideslip angle in figure 52 for the 75-kias trim record. Drag has a minimum at small end into the wind (near $\beta = 90$ deg) as expected, and a local minimum at broadside and a maximum for the record at 30 deg. Values are between 22 and 40 ft^2 . Lift ranges from zero at small end to the wind to a maximum of 30 ft^2 at $\beta = 15$ deg. Maximum lift occurs near broadside to the wind and is nearly as large as the drag force. Side force and yaw moment are strongly scattered in magnitude with no well-defined trends in this plot.

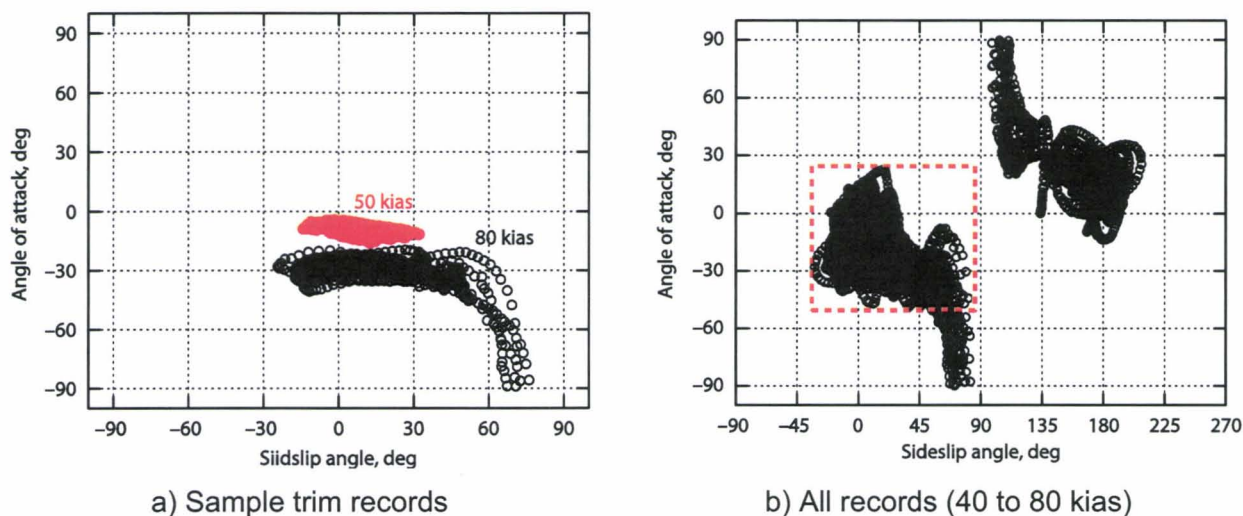


Figure 51. Engine-canister aerodynamic angle coverage in the flight data.

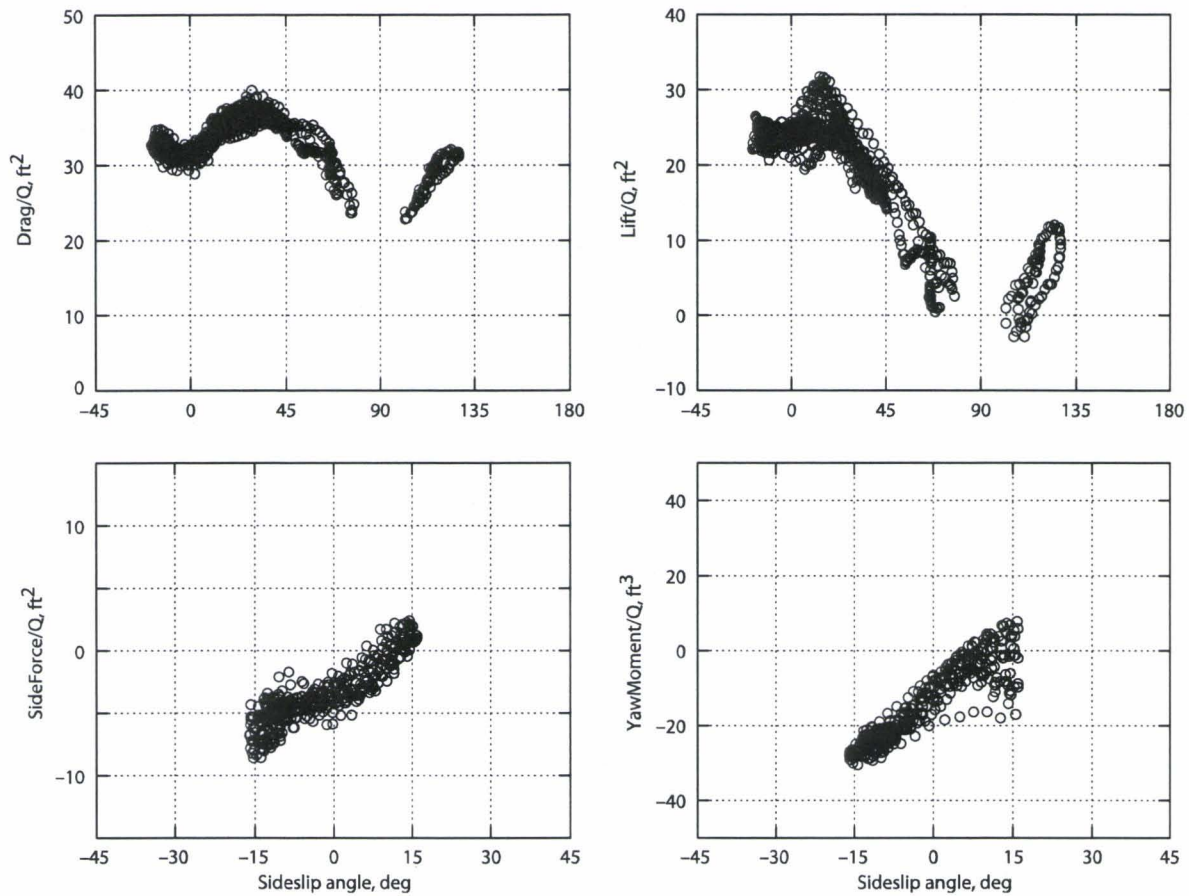
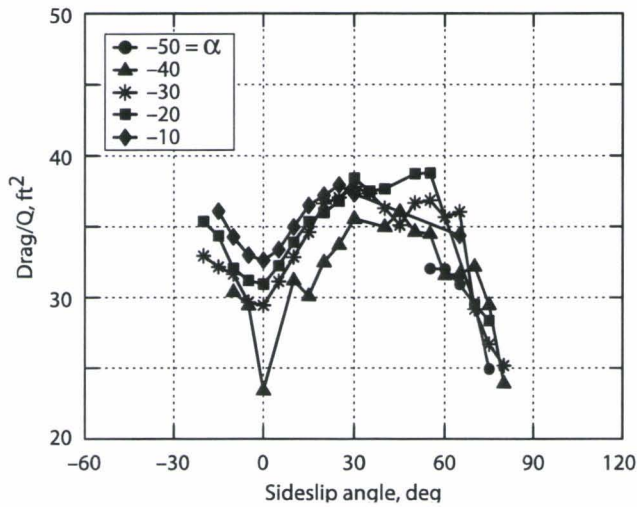


Figure 52. Engine-canister aerodynamics; 75 kias.

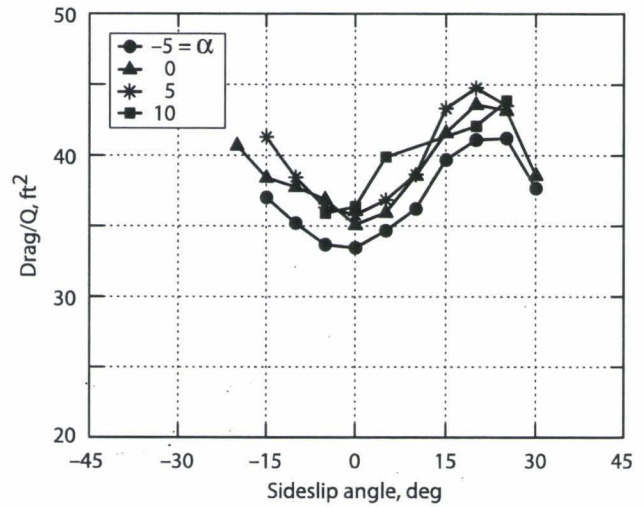
Aerodynamics: In order to obtain the aerodynamics as functions of (α, β) , a grid was defined covering the domain every 5 deg in angle-of-attack and sideslip angle. Values at each grid point were computed as the average of all data points in a (2- x 2-) deg box centered on the grid point. Many of the boxes were empty, and otherwise contained from 1 to more than 500 data points. A table of the aerodynamics for the region outlined by the dashed box in figure 51(b) is given in appendix F. The region above $\beta = 90$ deg with positive α was not included in the table since the engine canister looks physically identical to the flow as it does for $\alpha < 0$ and $|\beta| < 90$ deg and has the same aerodynamics.

Figure 53 presents results for the drag parameter. Table values are in the range $[21, 50] \text{ ft}^2$ and the value extracted from the trail-angle data in the previous section is well inside this range. Figure 53(a) shows the variation with sideslip for fixed negative values of angle of attack. These data extend out to near $\beta = 90$ deg and are consistent with trends seen at 75 kts in figure 52; that is, drag is a minimum at broadside and small side to the wind and a maximum in between. Figure 53(b) shows the available results vs. sideslip for fixed α in $[-5, 10]$ deg. The β range is much smaller but

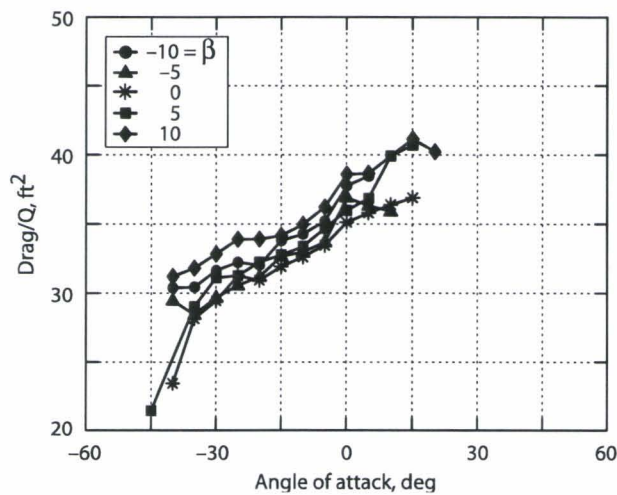
suffices to show a minimum at broadside and a maximum around $\beta = 20$ deg. Figures 53(a) and (b) also show the expected symmetry of drag about $\beta = 0$. A plot vs. α near the broadside orientation (fig. 53(c)) shows that drag increases strongly with angle of attack in this region. Since a simple cylinder would look identical to the flow at all values of α for $\beta = 0$, this trend is evidently the effect of the skids and flange.



a) Drag vs. β ; α in $[-50, -10]$ deg.



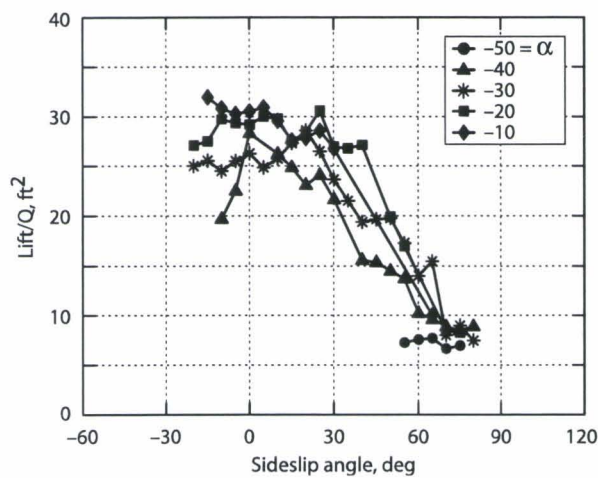
b) Drag vs. β ; α in $[-5, -10]$ deg.



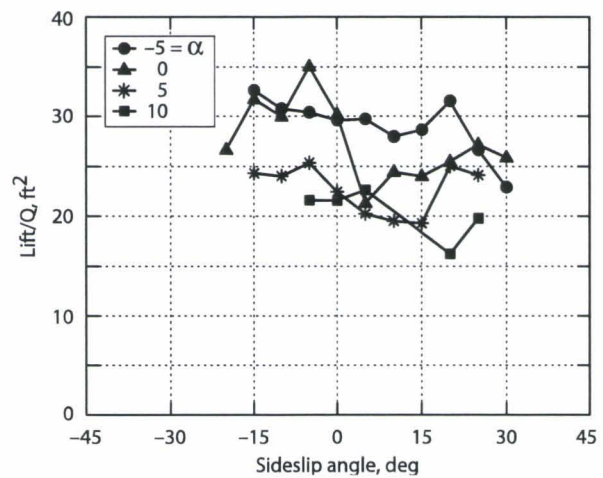
c) Drag vs. α ; β in $[-10, 10]$ deg.

Figure 53. Engine-canister drag.

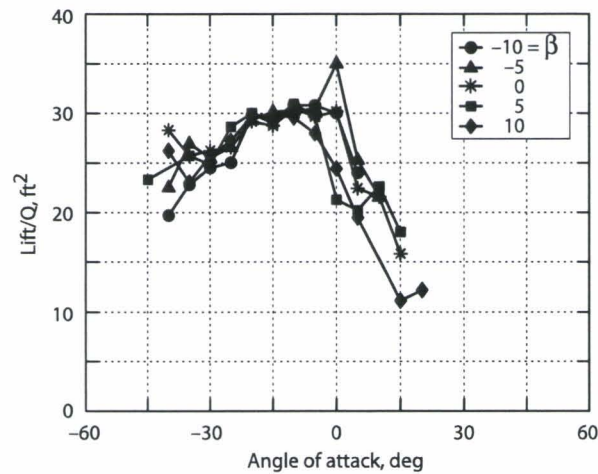
Figure 54 presents results for lift. Table values are in the range $[6.6, 35.0] \text{ ft}^2$ and the value extracted from the trail angle data is well inside this range. Figure 54(a) showing curves for fixed negative angles of attack is similar in trend to figure 52; that is, lift is everywhere positive at all sideslip angles in the available range with a maximum at broadside and a minimum approaching zero at small end into the wind. Data for fixed angle of attack in the range $[-5, 10] \text{ deg}$ is restricted to the region near broadside where lift is near a maximum. A plot vs. α for sideslip angles near the broadside orientation (fig 54(c)) shows a sharp reduction in lift at positive angles of attack. Since a simple cylinder broadside to the wind is expected to generate no lift because of its symmetric geometry, then the nonzero lift at negative α is likely an effect of the skids in creating non-symmetry in the separation points and the pressure distributions.



a) Lift vs. β ; α in $[-50, -10] \text{ deg}$.



b) Lift vs. β ; α in $[-5, -10] \text{ deg}$.



c) Lift vs. α ; β in $[-10, 10] \text{ deg}$.

Figure 54. Engine-canister lift.

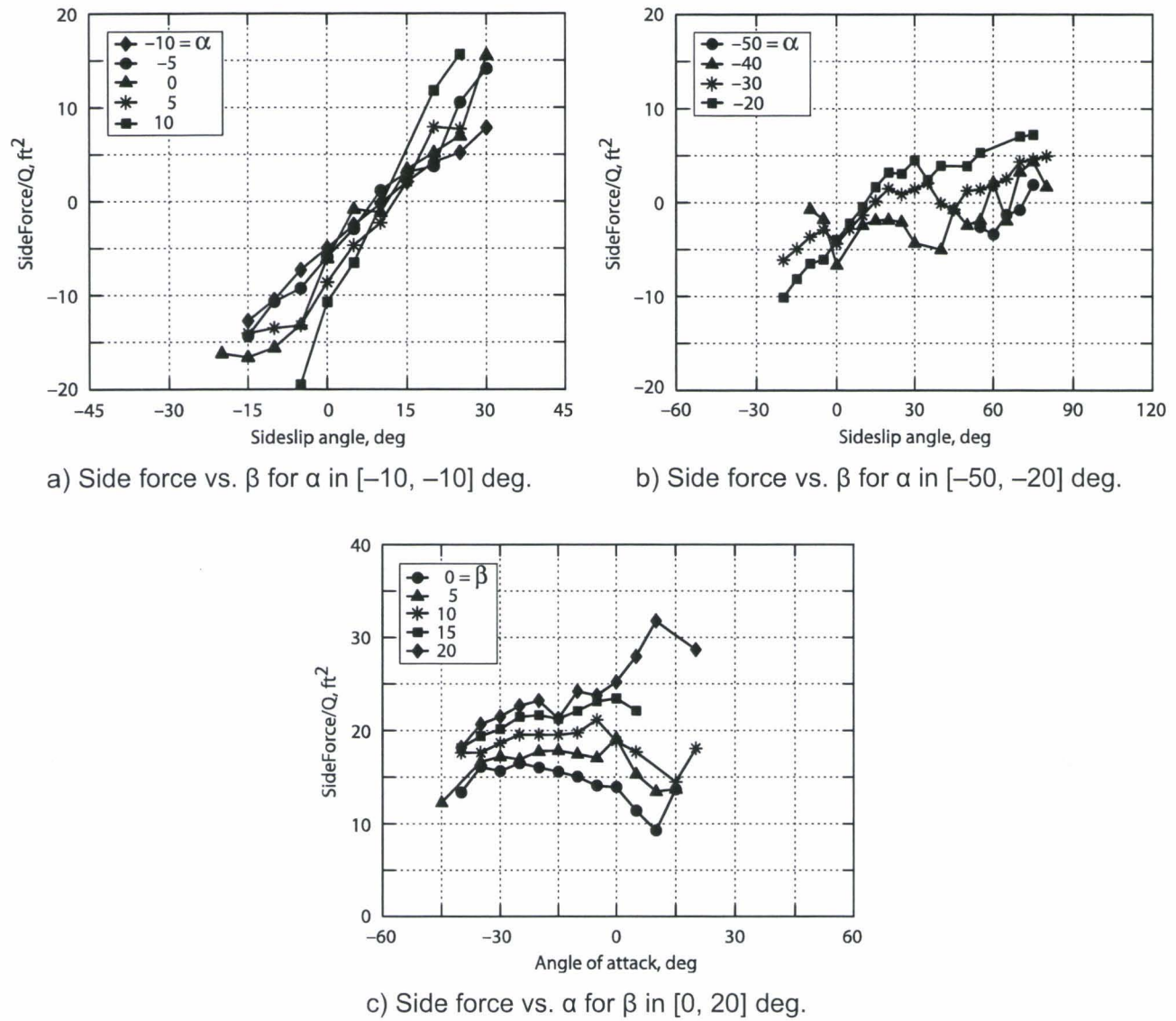
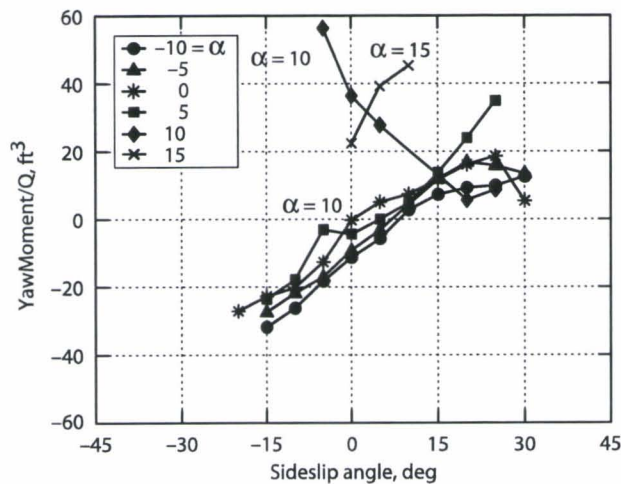
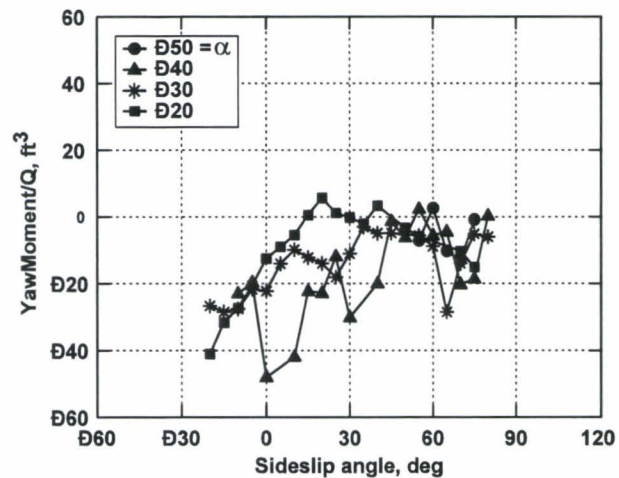


Figure 55. Engine-canister side force.

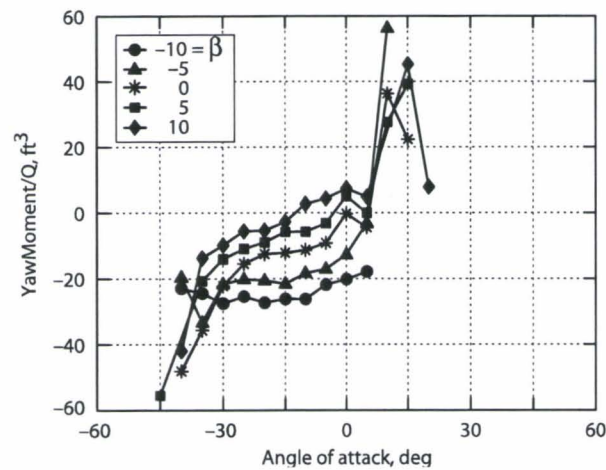
Figure 55 presents results for side force. Table values are in the range $[-19.5, 15.6] \text{ ft}^2$. Figure 55(a) shows results vs. β for fixed α in $[-10, 10]$ deg. In this range of α the available data are restricted to β values in the region around broadside. Side force has a linear trend with positive slope, but offset from anti-symmetry around $(\text{yoq}, \beta) = (0, 0)$. Side force reaches the measured extremes in this region at $\alpha = 10$ deg. Figure 55(b) shows results vs. β for fixed α in $[-50, -20]$ deg. The available data extend out to the small end into the wind without exhibiting a clear trend in that region. The linear trend in the broadside region is present at $\alpha = -20, -30$ deg but breaks up at -40 deg. Results vs. α for fixed sideslip angle in $[0, 20]$ deg are given in figure 55(c). Side force is approximately constant at each β in this range, and this value increases with β .



a) Yaw vs. β for α in $[-10, -15]$ deg.



b) Yaw vs. β for α in $[-50, -20]$ deg.



c) Yaw vs. α for β in $[0, 20]$ deg.

Figure 56. Engine-canister yaw moment.

Figure 56 presents results for yaw moment. Table values are in the range $[-55.5, 56.3]$ ft^3 . These extremes occur near broad side at negative and positive α , respectively. Figure 56(a) shows results for fixed α in the range $[-10, 15]$ deg. A well-defined linear trend with positive slope (statically stable) occurs for α below 10 deg and breaks up abruptly at $\alpha = 10$ deg. This trend line is offset from passing through $(\text{ymoq}, \beta) = (0, 0)$, which, if accurate, would imply a stable point offset from 0 and this is consistent with the offset relative heading seen in fig 4.1b at low airspeeds. Figure 56(b) shows data for fixed negative α in $[-50, -20]$ deg. The linear trend around broadside is present at $\alpha = -20, -30$ deg but breaks up below that. The plot vs. α for fixed sideslip near broadside (fig. 56(c)) shows a coherent variation with α up to $\alpha = 5$ deg, and above that there are abrupt increases in yaw moment. The table extremes occur in this plot. The variation with α for $\beta = 0$ is presumed an effect of departures from the geometry of a simple cylinder.

Aerodynamic summary. The trends in the aerodynamics of the engine canister are what would be expected for a cylinder in some regimes for drag (figs. 53(a) and (b)), side force (fig. 55(a)), and yaw moment (fig. 56(a)). They depart from the expected trends because of the effects of appendages, which produce drag variations with angle of attack (fig. 53(c)), distortion of the nominal trends in side force and yaw moment (figs. 55(b) and 56(b)), and the occurrence of significant lift at all angles of attack in the region of broadside orientation (fig. 54).

Predictability of the engine canister aerodynamics. An important objective of slung-load aerodynamic models is their use in simulation-based airworthiness certification of new loads (ref. 9). The initial concept regarding load aerodynamics in the work of reference 9 was that the literature on wind tunnel results for simple shapes would provide a basis for predicting load static aerodynamics short of requiring wind tunnel data for each load. For the engine canister load, the literature on the aerodynamics of cylinders would be applied; this literature includes references 26–29. Figure 57 shows the results of two prediction efforts for cylindrical loads based on reference 26, both made by simulation engineers. The first prediction produced a formula for drag developed for a cylindrical log carried as a flight test slung load (prediction 1 in fig. 57(a)):

$$CD = 1.1\cos^3\beta + .02$$

A second prediction was made for the engine canister and is given in reference 10 for drag and side force as a function of β . The remaining components were estimated as zero and it was assumed that there is no variation with α . A corrected version of this prediction provided by the author of reference 10 is (prediction 2 in fig. 57):

$$\begin{aligned} CD1 &= 0.45 \cos\beta \\ CD2 &= 0.7 \cos^3\beta + 0.07 \\ CD &= \begin{cases} CD1 & |\beta| \in [0, 33] \text{ deg} \\ CD2 & |\beta| \in (43, 90] \text{ deg} \\ CD1 * \cos^2(\beta_1) + CD2 * \sin^2(\beta_1), & |\beta| \in [33, 43] \text{ deg}, \beta_1 \equiv \frac{\beta - 33}{10} 90 \text{ deg} \end{cases} \\ CY1 &= 0.45 \sin\beta \\ CY2 &= 0.7 \sin\beta \cos^2\beta + 0.07\text{sign}(\beta) \\ CY &= \begin{cases} CY1 & |\beta| \in [0, 20] \text{ deg} \\ CY2 & |\beta| \in (40, 90] \text{ deg} \\ CY1 * \cos^2(\beta_1) + CY2 * \sin^2(\beta_1), & |\beta| \in [20, 40] \text{ deg}, \beta_1 \equiv \frac{\beta - 20}{20} 90 \text{ deg} \end{cases} \end{aligned}$$

The two readings of the literature gave broadside drag estimates that differ by a factor of two, and otherwise the results from both predictions are too inaccurate to adequately predict, for example, load trail angle, which is a factor limiting speed envelope, and could not account for the strong effects of the skids and appendages in modifying the aerodynamics of a simple cylinder. These results indicate that the existing wind tunnel literature on cylinders cannot be successfully applied to near-cylindrical loads.

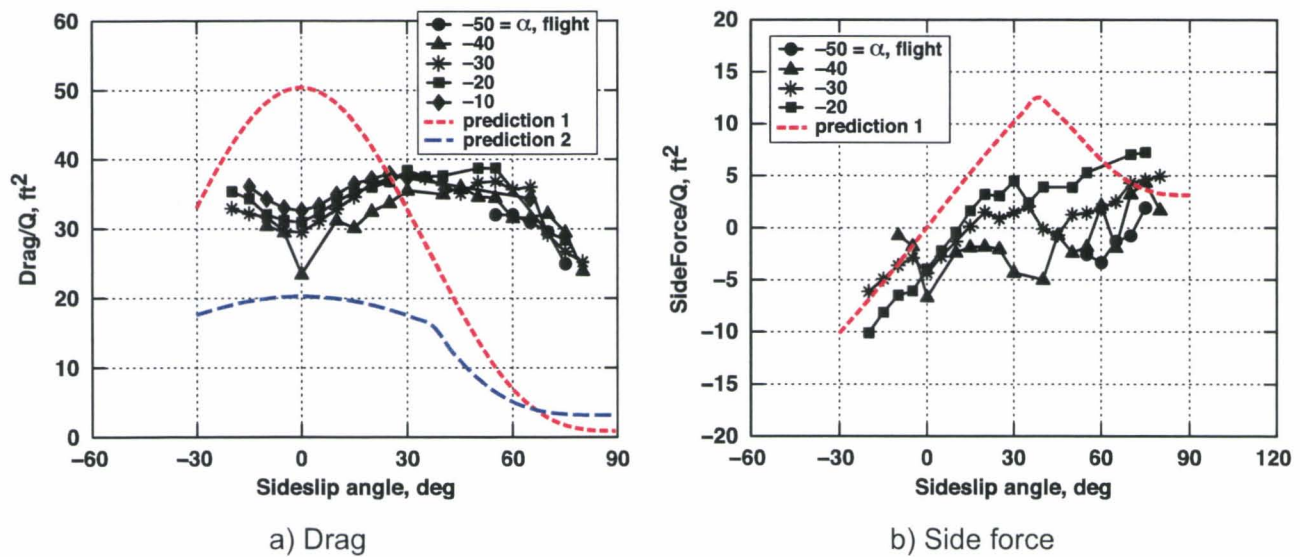


Figure 57. Prediction of engine-canister aerodynamics.

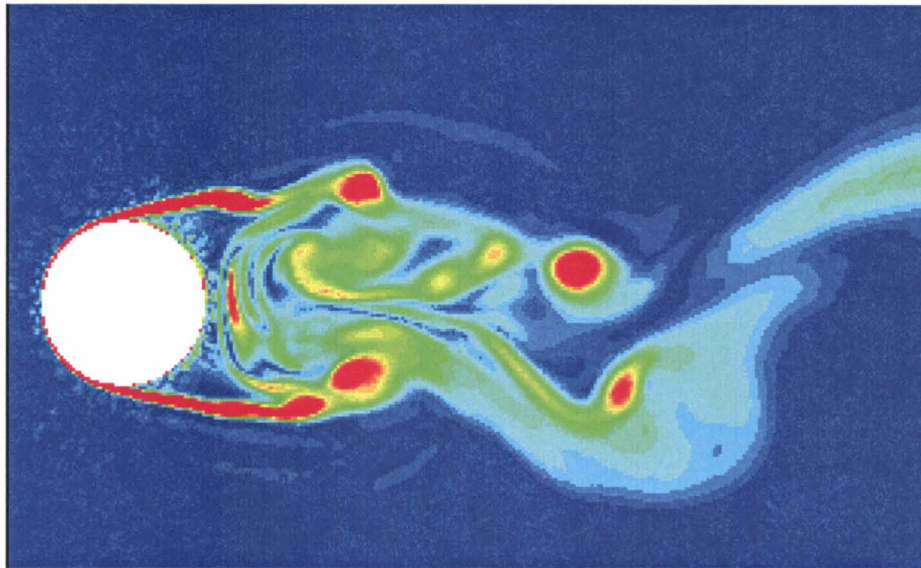
More generally, there are other slung loads close to a simple shape (boxes and flat plates), but most of the standard military loads in reference 22 are general collections of simple shapes attached together in various arrangements. For aerodynamic shapes such as aircraft, superposition of the aerodynamics of its parts is a viable approach to prediction because of the unseparated flow and the small treatable interference effects over wings, fuselage, and tail, but for all except a few slung loads, this approach will not be viable.

Thus scale-model wind tunnel data will be needed for models of the load aerodynamics, even for loads that are close to simple shapes.

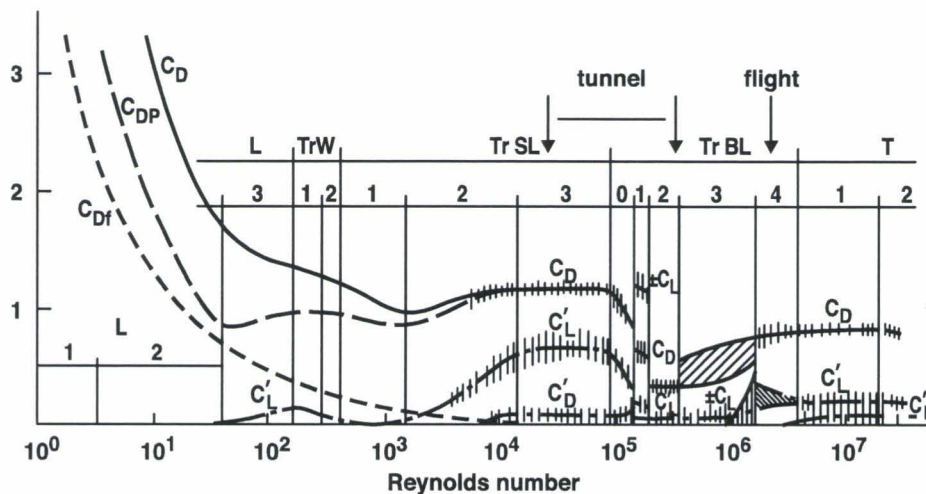
Reynolds number effects. The large majority of slung loads are bluff bodies with massive wakes and highly separated flows, in which case the aerodynamics are independent of Reynolds number, VL/ν , over the range from model scale to full scale. This independence simplifies the task of using wind tunnel data for aerodynamic models of full-scale loads in simulations. This independence has been shown to be the case for the CONEX load in references 5 and 7 based on CFD calculations, and by extension, for cargo containers and the numerous box-shaped loads in the military inventory. However, this may not be the case for cylindrical loads, which are also bluff bodies with large wakes (fig 58(a)).

Figure 58(b) shows data for the drag and lift of a smooth cylinder in undisturbed flow for Reynolds numbers from 10 to 10^7 , taken from reference 27. This reference indicates that the nature of the flow around a cylinder varies with Reynolds number in different primary ranges of the Reynolds number (Re) scale according to the transition-point location (fig. 58(b)). A critical Re exists where the transition point in the shear layer has moved forward to the separation point and into the boundary layer (region TrBL in fig. 58(b)), and above that, the viscous drag is eliminated and the drag reduces significantly. For the engine canister the flight Reynolds numbers are 2 to 4×10^6 , and are in the supercritical range, while the corresponding wind tunnel model-scale Reynolds numbers are 20000 to 400000 and are below the critical Reynolds number.

Figure 58(c) shows the Reynolds numbers for the full-scale flight tests and the corresponding model-scale wind tunnel tests with airspeed scaled by Froude number, V^2/gL . The aerodynamics of realistic cylindrical loads with appendages may have other governing factors besides Re , but this example indicates that it is of interest to determine whether the aerodynamics of a new load are independent of Reynolds number when generating modeling data from wind tunnel tests. This determination can be made, for example, using CFD after validating the CFD with wind tunnel data.

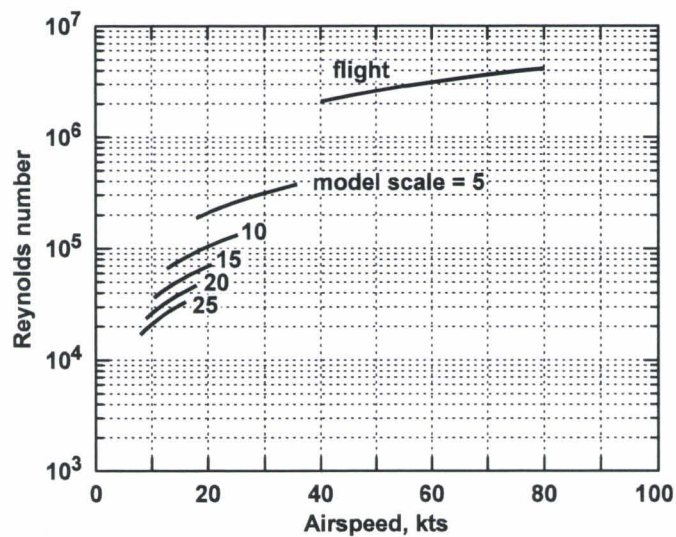


a) Flow around a cylinder: vorticity contours.



b) Drag vs. Reynolds number, cylinders, disturbance-free flow (pg. 17, fig. 1.11 from "Flow Around Circular Cylinders, Vol. I" by Zdravkovich, M. (1997)).

Figure 58. Engine-canister aerodynamics: effects of Reynolds number.



c) Engine-canister Re, flight and wind tunnel

Figure 58. Engine-canister aerodynamics: effects of Reynolds number (continued).

CONCLUSIONS

1. The motions and aerodynamics of the 6- x 6- x 8-ft CONEX cargo container and a 5- x 9-ft engine canister slung load have been documented in flight out to the maximum airspeed limited by excessive pendulum excursions or excessive trail angle or the power limit of the configuration. The CONEX was flown with and without a swivel, with a sling set and with a long-line sling, with centered cg and offset cg, and at three weights. The engine canister was flown with the sling set and with a long-line sling.
2. Without a swivel, the empty CONEX experienced excessive pendulum excursions at 65 kts, consistent with the established operational limit of 60 kts for this load. More generally, the stable speed envelope was extended to the power limit by adding weight, using a swivel to allow the load to spin, or by an extreme offset of the cg. A variety of steady-state yaw motions occurred. Of particular interest, the addition of a swivel resulted in steady spinning of the load that suppressed the pendulum motions. Thus, spin stabilization is a possible approach to stabilizing cargo containers and box-shaped loads.
3. The extraction of load aerodynamics from an instrumented load was demonstrated. Several validation checks indicated that the extracted aerodynamics of the CONEX are sufficiently accurate to measure the effects of spin. Drag was reduced by more than 10% from the corresponding static drag, side force showed strong effects of spin, and yaw moment showed differences that occurred at even harmonics of the spin rate and that varied in phase and amplitude around a rotation. Further, a comparison under nearly static flight conditions showed good agreement between the flight data and the wind tunnel data, thus simultaneously confirming the accuracy of both the flight data and the data from scale-model wind tunnel measurements.
4. Sling-leg tensions and hook-force time histories were also obtained; they revealed significant modal variations that occur continually at all airspeeds and that increase in magnitude with airspeed. For the swiveled sling, sling-leg tensions oscillate at the first four harmonics of the spin rate along with lesser amplitude peaks at the stretching frequencies. The odd harmonics are 180 deg out of phase among pairs of sling legs, and they cancel out when summed into the hook-force history, while the even harmonics are in phase in all legs and are reinforced in the hook force. Without a swivel, sling-leg tensions vary at the period of the sling windup cycle and at the pendulum frequency. Tension variations at the windup period are pair-wise 180 deg out of phase for opposite-corner pairs so that at each extreme of the windup, the tension in one pair of legs is maximized and minimized in the other.
5. The engine canister was a previously untested load. Its aerodynamics were obtained over the range allowed by its autonomous attitude history in flight. A comparison with predictions based on the wind tunnel literature for cylinders showed large differences, owing to the large effects of appendages attached to the cylindrical load for field operations. Thus, scale-model wind tunnel data will be needed for models of the load aerodynamics in slung-load simulations, even for loads that are close to simple shapes.

6. Generally, the aerodynamics of bluff bodies are expected to be independent of Reynolds number from scale-model wind tunnel measurements to full-scale flight conditions. Most slung loads are bluff bodies, including the loads tested here, simplifying the task of generating aerodynamic data for slung loads. For the CONEX, a comparison of full-scale and wind tunnel data for the static aerodynamics as well as related CFD calculations in the literature confirm this independence, and, by extension, all box-shaped slung loads are similarly independent. However, for simple cylinders, the literature indicates a strong effect of Reynolds number in the range between wind tunnel and flight conditions. Wind tunnel data for the engine canister are not yet available to determine if there are Reynolds number effects on nearly cylindrical slung loads.

REFERENCES

- [1] McCoy, A.: Flight Testing and Real-Time System Identification Analysis of a UH-60A Black Hawk Helicopter with an Instrumented External Sling Load. NASA CR-196710, 1998.
- [2] Sahai, R.; Cicolani, L.; Tischler, M.; Blanken, C.; Sullivan, C.; Wei, M.; Ng, Y.S.; and Pierce, L.: Flight-Time Identification of Helicopter Slung-Load Frequency Response Characteristics Using CIPHER. Proceedings, AIAA Atmospheric Flight Mechanics Conference, Portland, Oregon, Aug. 1999.
- [3] Tyson, P.: Simulation Validation and Flight Prediction of UH-60A Black Hawk Helicopter/Slung Load Characteristics. MS Thesis, U.S. Naval Postgraduate School, Monterey, Calif., Mar. 1999. Also: Simulation Prediction and Flight Validation of UH-60A Black Hawk Slung Load Characteristics. 55th Annual Forum of the Am. Helicopter Soc., May 1999.
- [4] Ehlers, G.: High Fidelity Simulation and Prediction of Helicopter Single Point External Load Stabilization. MS Thesis, U.S. Naval Postgraduate School, Monterey, Calif., Sept. 2001. Also: Modeling and Simulation of a Helicopter Slung Load Stabilization Device. 58th Annual Forum of the Am. Helicopter Soc., June 2002.
- [5] da Silva, J.G.A.; Duque, E.P.N.; Cicolani, L.S.; and Tischler, M.B.: Unsteady Aerodynamic Model of a Cargo Container for Slung Load Simulation. 29th European Rotorcraft Forum, Sept. 2003. Also: NASA TP 2004-212817, May 2004. Also: J. Royal Aeron. Soc., July 2004.
- [6] Cone, A.: Simulation of a Cargo Container Slung Load at Speeds with Significant Aerodynamic Effects. MS Thesis, California Polytechnic State University, 2007.
- [7] Theron, J.; Cicolani, L.; and Duque, E.P.N.: A CFD Study of the Aerodynamics of a 6x6x8 ft Cargo Container Suspended Beneath a Helicopter. Part 1: Aerodynamics of the Stationary Container. U.S. Army RDECOM No AFDD/TR-07-001, Oct. 2007.
- [8] Strobe, K.; Gassaway, B.; and Harding, J.: Frequency Domain Verification and Validation of a UH-60A FLIGHTLAB Model with a CONEX Sling Load. 61st Annual Forum of the Am. Helicopter Soc., June 2005.
- [9] Final Report of the Helicopter Sling-Load Working Group T. Thompson, ed., Army Technical Report AMR-AE-06-01, April 2006.
- [10] Gassaway, B.; Strobe, K.; Cicolani, L.; Lusardi, J.; He, C.; and Robinson, D.: Predictive Capabilities of a UH-60 FLIGHTLAB Model with an External Sling Load. Proceedings of the Am. Helicopter Soc. 62nd Annual Forum, May 2006.
- [11] Cicolani, L.; Raz, R.; Rosen, A.; Cone, A.; Theron, J.; Lusardi, J.; and Robinson, D.: Flight Test, Simulation and Passive Stabilization of a Cargo Container Slung Load in Forward Flight. 63d Annual Forum of the Am. Helicopter Soc., May 2007.

- [12] Cicolani, L.; Cone, A.; Theron, J.; Lusardi, J.; Robinson, D.; Raz, R.; and Rosen, A.: Flight Test and Simulation of a Cargo Container Slung Load in Forward Flight. J. Am. Helicopter Soc., vol. 54, no. 3, Aug. 2009.
- [13] Raz, R.; Rosen, A.; Carmeli, A.; Lusardi, J.; Cicolani, L.; and Robinson, D.: Wind Tunnel and Flight Evaluation of the Stability and Passive Stabilization of a Cargo Container Slung Load. 64th Annual Forum of the Am. Helicopter Soc., April 2008. Also: J. Am. Helicopter Soc., vol. 55, no. 2, April 2010.
- [14] Garnett, T.; Smith, J.; and Lane, R.: Design and Flight Test of the Active Arm External Load Stabilization System (AAELSS II). 32nd Annual Forum of the Am. Helicopter Soc., May 1976.
- [15] Watkins, T.; Sincori, J.; and Kesler, D.: Stabilization of Externally Slung Helicopter Loads. USAAMRDL TR 74-42, Aug. 1974.
- [16] Chan D.; Flower, J.; and Simpson, A.: Aerodynamically Induced Motions of Bluff Bodies Suspended Beneath Helicopters. Final Report AD, Univ. of Bristol, Dept. of Aeronautical Engineering, Bristol, UK, Oct. 1975.
- [17] Simpson, A.; and Flower, J.: Unsteady Aerodynamics of Oscillating Containers and Application to the Problem of Dynamic Stability of Helicopter Underslung Loads. AGARD CP-235, Nov. 1978.
- [18] Laub, G.; and Kodani, H.: Wind Tunnel Investigation of Aerodynamic Characteristics of Scale Models of Three Rectangular Shaped Cargo Containers. NASA TM X-62169, 1972.
- [19] Cicolani, L.; and Kanning, G.: A Comprehensive Estimate of the Static Aerodynamics of the 8 by 8 by 20 ft Cargo Container. NASA TM 89433, May 1987.
- [20] Gabel, R.; and Wilson, G.: Test Approaches to External Sling Load Instabilities. J. Am. Helicopter Soc., vol. 13, 1968.
- [21] Cicolani, L.; McCoy, A.; Sahai, R.; Tyson, P.; Tischler, M.; Rosen, A.; and Tucker, G.: Flight Test Identification and Simulation of a UH-60A Helicopter and Slung Load. J. Am. Helicopter Soc., vol. 46, Apr. 2001. Also: NASA TM 2001-209619, Jan. 2001.
- [22] Multiservice Helicopter External Air Transport. Vols. I, II, III. U.S. Army FM-10-450-3,4,5, Sept. 2003.
- [23] Glen Research Center: Lift of a Rotating Cylinder: <http://www.grc.nasa.gov/WWW/K-12/airplane/cyl.html>.
- [24] Rosen A.; Cecutta, S.; and Yaffe, R.: Wind Tunnel Tests of Cube and CONEX Models. Technion Israel Institute of Technology, Faculty of Aerospace Engineering Report TAE 844, Nov. 1999.
- [25] Tischler, M.; and Remple, R.: Aircraft and Rotorcraft System Identification. AIAA Education Series, Schetz, J., ed., 2006.

- [26] Hoerner, S. F.: Fluid Dynamic Drag. S.F. Hoerner, Midland N.J., 1965.
- [27] Zdravkovich, M.M.: Flow around Circular Cylinders. Vol. I: Fundamentals. Oxford University Press, New York, 1997.
- [28] Zdravkovich, M.M.: Flow around Circular Cylinders. Vol. II Applications. Oxford University Press, New York, 2003.
- [29] Humphreys, J.S.: On a Cylinder in a Steady Wind. Ph.D. Thesis, Harvard University, Cambridge, Mass., Aug. 1959.
- [30] Specification for USAF Standard Form, Fit, and Function Medium Accuracy Inertial Navigation Unit. SNU 84-1, Rev D. Sept. 1992.
- [31] Honeywell H-423 Standard Inertial Navigation Unit Technical Description. Sensor and Guidance products, Guidance and Navigation operation, Clearwater, Fla.
- [32] Bach, R.E.: State Estimation Applications in Aircraft Flight Data Analysis. A User's Manual for SMACK. NASA RP 1252, Mar. 1991.
- [33] Cicolani, L.; and Kanning, G.: Equations of Motion of Slung Load Systems, Including Multilift Systems. NASA TP 3280, Nov. 1992.

APPENDIX A. PHYSICAL PROPERTIES OF THE LOADS AND SLINGS

This appendix documents the weight-inertia-center-of-gravity (cg) properties of the load and sling, sling stretching properties, sling geometry, and torsional resistance at the hook with and without a swivel. Units are lb, ft, and sec throughout this appendix. Locations are given in load-body axes relative to the geometric center of the box or cylinder (not including the appendages). Body axes are x perpendicular to a long side, and z is positive down (see fig. 4(b)).

Weight-inertia properties of the load-sling subsystem. Weight and inertia properties for the test loads and sling weights are listed in table A1. Load weights include instrumentation and ballast, and they omit the swivel, load cells, and sling weights, which are listed separately in the table. Inertias are measured about the load cg. The cg coordinates (xcg, ycg, zcg) are given relative to the geometric center of the container box or the engine canister cylinder in load body axes.

TABLE A1. LOAD AND SLING WEIGHT-INERTIA PROPERTIES

Load/sling item	Weight	Ixx	Iyy	Izz	xcg	ycg	zcg
engine can	2271	778	407	836	0.1	0.1	0.4
2K conex	2387	1002	764	933	0.1	0.2	0.4
4K conex	4550	1382	993	1255	0.1	0.1	1.3
4K conex (offset cg)	4608	1696	1066	1604	0.1	-1.5	1.4
6K conex	6176	1782	1260	1880	0.0	0.0	1.8
sling set	52						
swivel	30						
load cells	50						
pendant	103						

Sling stretching properties. The elastic properties of the flight test slings are used to compute the geometry of the loaded sling. A broader discussion of sling characteristics is found in reference 20.

The stretching properties of the 10,000-lb 4-legged sling set used in the flight tests were measured at the Ames Research Center Engineering Evaluation Laboratory (EEL) using a dynamic shaker test. Results (table A2) were given for two weights:

TABLE A2. SLING-SET STRETCHING PROPERTIES

Load weight, lb	701.5	4197
spring constant, lb/ft	22068	38580
spring frequency, rad/sec	30.4	16.0
Damping ratio	0.016	0.027

There is some variation of the spring constant with weight, but the data are insufficient to define it. Nevertheless, its value at the flight weight of the ballasted CONEX has been measured and there is some justification to assume its value at the other test weights is the same. The stretching constant is for all four legs acting together. Individually the stretching constant of the legs is 9645. The results indicate very light damping in stretch, around 2%.

Static stretch tests were performed on the 65-ft standard military polyester round pendant at West Coast Wire, Inc., Seattle, Washington, for weights out to 20,000 lb. The pendant was rated for 21,200-lb load capacity. The data and a linear fit are shown in figure A1. The spring constant (36723 lb/ft) is close to that measured for the sling set at 4197 lb of load, and the data indicate that it is invariant over the range of weights from 2000 to 20,000 lb.

Stretching frequency can be predicted from the equation for a simple spring suspended from an infinite mass as

$$\omega_s = \sqrt{\frac{K_s g}{W_2}}$$

or for a flying dumbbell with connecting spring as

$$\omega_s = \sqrt{K_s g \left(\frac{1}{W_1} + \frac{1}{W_2} \right)}$$

where W_1 , W_2 are the helicopter and load weights, respectively. A plot of stretching frequency vs. load weight is given in figure A2. Using parameter values for the test aircraft and sling set and assuming the stretching constant is independent of weight, then frequency declines with increasing load weight and varies over the range 24 to 14.4 rad/sec for load weights from 2000 to 6000 lb. A general rule (ref. 20) is to keep sling stretching frequencies well above the pilot's input bandwidth (2 Hz) and well below the rotor speed (4.3 Hz for the UH-60 Black Hawk Helicopter).

Sling-set geometry. The hook-force vector is required to derive the load aerodynamics from the flight data. It is given by the vector sum of the cable tensions measured by the load cells taken along the sling-leg directions:

$$F_{c_2} = - \sum_{j=1}^4 \tau_j \mathbf{k} a_j$$

where $\{\mathbf{k} a_j, j = 1, \dots, 4\}$ are the unit direction vectors from the sling apex to lift points 1 to 4. The direction vectors are computed from the sling geometry, which forms a four-sided pyramid (fig. A3) with the geometry of its base fixed by the lift points on the load. For an elastic sling with general lift-point locations and general cg location, the geometry is difficult to calculate. However, the problem is simplified for the present flight loads in that (1) the lift points are in a single plane parallel to the body (x, y) plane and symmetric about the geometric center, (2) the cg is very nearly centered in the body (x,y) plane, (3) a swivel is used to preclude sling windup, and (4) the sling is stiff

enough that variations in sling stretch in general flight conditions is negligible. These properties allow the geometry to be calculated assuming (1) the sling legs are equally loaded and (2) sling geometry in general flight conditions differs negligibly from its geometry in hover.

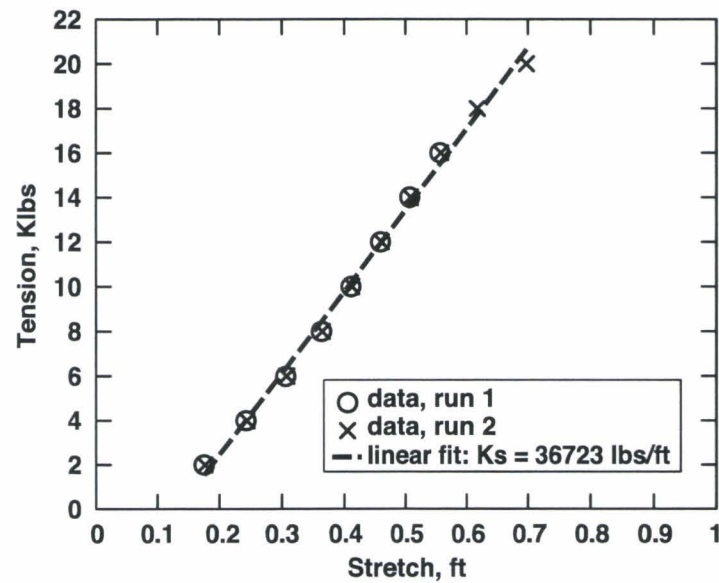


Figure A1. Sling stretch, 65-ft military polyester round sling.

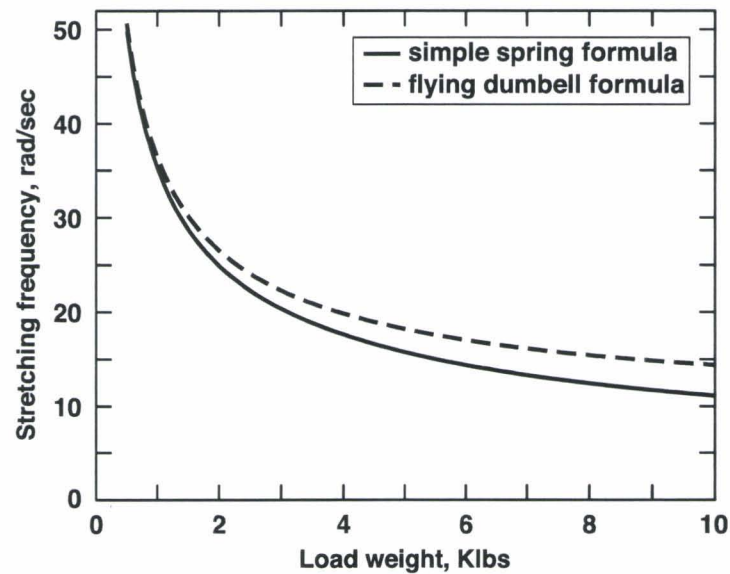


Figure A2. Stretching Frequency vs. load weight; $K_s = 36850$.



Figure A3. Load lift-point geometry.

Sling set stretch is given by $h - h_0 = Fc/K_s$, where h is the pyramid height, h_0 is the height for no load weight, Fc is the hook-force magnitude, and K_s is the stretching constant of the sling set. For $K_s = 38580$ lb/ft the sling set stretches less than 0.2 ft when the sling is loaded with the test-load weights. In forward flight, drag can add about 500 lb to the hook force, and variations in hook force due to load motions and excitation of the stretching modes adds another ± 1000 lb in the flight data. For these variations, sling height differs by less than 0.1 ft from its length at hover. Thus the geometry of the sling set changes very little during flight and can be closely approximated as its hover geometry.

The hover geometry was computed analytically from the unloaded sling-leg length, ℓ_{c_0} ; the lift-point locations; the spring constant for each leg, K_s , and the load weight, W_2 . The unloaded sling-leg length is 16.33 ft, including the load cells. The lift-point locations are shown in figure A3 and their body axes coordinates are given in table A3. The CONEX lift points are set back slightly from the top corners of the container. The engine canister lift points were installed on the outer supports about 3 inches outside the cylinder cross-section and 10 inches back from the ends of the cylinder. In both cases, lift-point numbering matches the sling-leg numbering, with lift points 1 and 2 forward left and right, respectively, and lift points 3 and 4 rear left and right, respectively.

TABLE A3. LIFT-POINT LOCATIONS

ℓ_o	15.833 (16.33 with load cells)					
Ks	38580					
	CONEX			Engine Canister		
lift points	x	y	z	x	y	z
1	2.828	-4.151	-3.205	3.266	-4.146	0
2	2.828	4.151	-3.205	3.266	-4.146	0
3	-2.828	-4.151	-3.205	-3.266	4.146	0
4	-2.828	4.151	-3.205	-3.266	4.146	0

The results for the sling-leg unit direction vectors for the test loads are given in table A4.

TABLE A4. SLING GEOMETRY: SLING-LEG DIRECTION VECTORS
(LOAD-BODY AXES)

sling leg	x	y	z
2K CONEX			
ka1 ₂	0.1787	-0.2623	0.9483
ka2 ₂	0.1787	0.2623	0.9483
ka3 ₂	-0.1787	-0.2623	0.9483
ka4 ₂	-0.1787	0.2623	0.9483
4K CONEX			
ka1 ₂	0.1780	-0.2613	0.9487
ka2 ₂	0.1780	0.2613	0.9487
ka3 ₂	-0.1780	-0.2613	0.9487
ka4 ₂	-0.1780	0.2613	0.9487
Engine Can			
ka1 ₂	-0.2209	-0.2805	0.9341
ka2 ₂	-0.2209	0.2805	0.9341
ka3 ₂	0.2209	-0.2805	0.9341
ka4 ₂	0.2209	0.2805	0.9341

Swivel friction. Torsion is applied to the sling at the hook because of swivel friction if a swivel is used and because of the resistance of the hook to sling windup in the absence of a swivel. In the present work, swivel friction is needed in the extraction of the aerodynamics from the flight data as well as in simulations of the system dynamics.

Friction for the flight test swivel was measured at the Ames Engineering Evaluation Lab (EEL) by suspending a weight from the swivel and rotating the weight at various rates with a selectable-speed motor. Rotation rates and the required torque were measured. Data records were taken for various rotation rates every 20 deg/sec or so up to 200 deg/sec and at three load weights of 1, 2, and 3 tons.

The results indicated that swivel friction was independent of rotation rate and depended only on weight. A linear least-squares fit gave the swivel friction as

$$M_c = .60723 + .00099575 * W_2$$

where W_2 and M_c are in lb and ft-lb. The standard deviation of the residuals for this fit was 0.36 ft-lb. Swivel friction is very small, under 10 ft-lb for the heaviest weight flown.

Sling windup geometry and torsional resistance. Without a swivel the sling winds up against torsional resistance from the hook. Torsional resistance was needed for accuracy in simulating the load yaw degree of freedom without a swivel and was measured at the EEL; the results were previously reported in reference 4 and are repeated here in figure A4. The CONEX was suspended with the sling set from an overhead crane and a motor attached to the bottom of the CONEX to rotate it by fixed angles. Measurements of required torque were made for rotations out to 10 turns. Figure A4 shows torsional resistance vs. windup turns. The variation is nonlinear with starting resistance and hysteresis. Hysteresis can be averaged out for simulation modeling (dashed line in the figure). Resistance is above 100 ft-lb at 5 turns.

The changes in sling geometry due to windup were also measured. The geometry at 5 turns is shown in figure A5, and data are plotted in figure A6 out to 10 turns. At 5 turns the twisted length of sling is over 5 ft or about one-third of the sling length; the twisted length increases to half the sling length at 10 turns. The increase in twisted length per turn declines with successive turns, dropping from 1 ft per turn initially to 0.5 ft per turn. Sling length from the hook to the top of the box decreases by 8 inches at 5 turns and 20 inches at 10 turns.

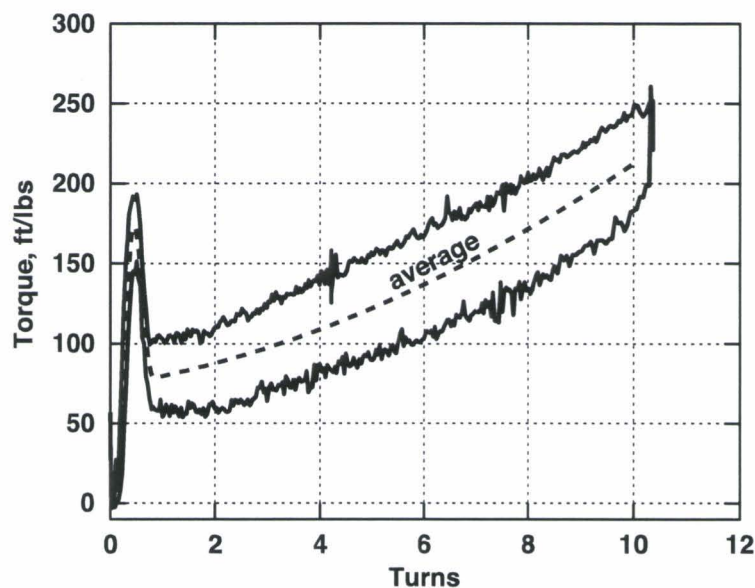


Figure A4. Torsional resistance to sling windup; CONEX, unswiveled sling.

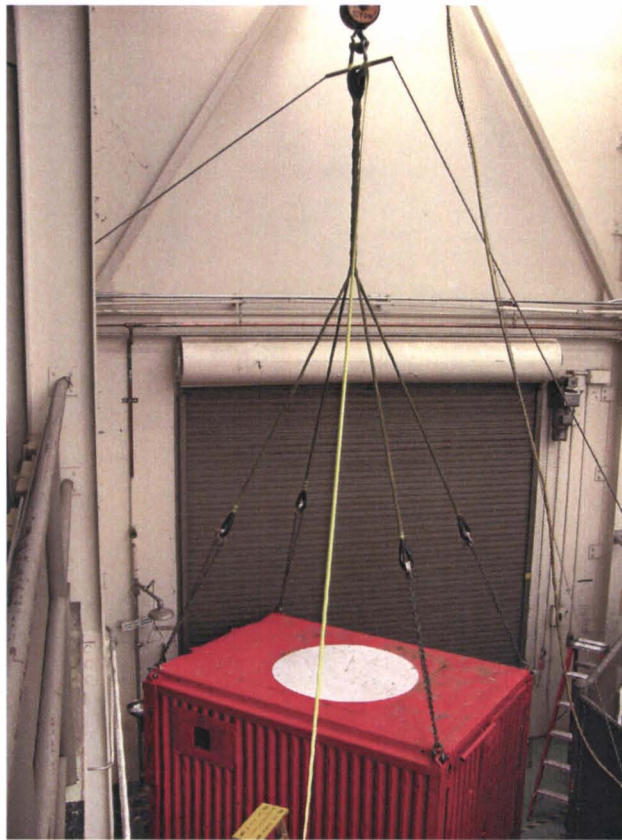


Figure A5. Sling windup geometry; 5 turns.

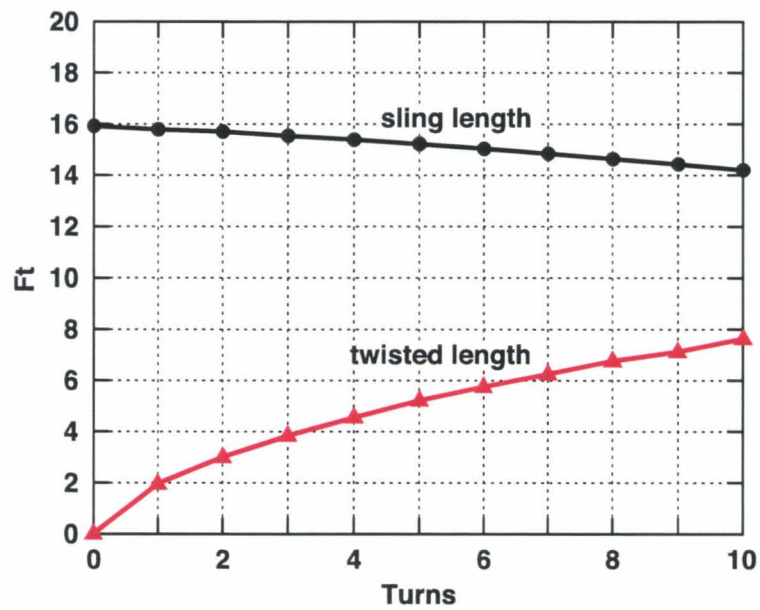


Figure A6. Sling windup geometry.

APPENDIX B. INSTRUMENTATION AND SIGNAL CHARACTERISTICS

Load instrumentation and data acquisition system. The load instrumentation system consists of an embedded GPS/INU (EGI) unit installed in the load, and load cells installed in the four sling legs at the lift points (see figs. 4(b) and 6). The EGI provides accurate measurements of load rigid body dynamics (accelerations, velocities, positions, angular accelerations, angular rates, and attitude), and the load cells provide sling-leg tensions. A photograph of the load data acquisition system (LDAS) is shown in figure 6 and a schematic is shown in figure B1.

The EGI is operated by a Virtual Machine Environment (VME) computer using the VxWorks™ real-time operating system. It merges load cell data with the EGI data, stores the merged data at 100 Hz on a 2-gigabyte solid-state hard drive, and telemeters selected data items up to the aircraft data system at 60 Hz. The load-cell analog data are processed through signal conditioners followed by analog-to-digital (A/D) conversion and processing in a PC computer using C-code software running in the Windows 2000™ operating system. The data are then sent to the VME computer at 65 Hz to be merged into the local data storage and into the up-linked data message to the aircraft. The entire system is operated by four 12-volt marine batteries, and the power distribution is given in red in figure B1. A control panel contains switches for power and INU initialization, connectors for control inputs to the VME and file download from the VME together with status lights.

The EGI satisfies the U.S. Air Force specifications for inertial navigation units of medium accuracy (ref. 30) with outputs in different 1553-formatted data messages at standardized measurement rates variously at 50 or 200 Hz, depending on the message. The unit used is a Honeywell H-423 INU (ref. 31). The signals extracted from these messages and recorded for this project are listed in table B1, along with their measurement rates, ranges, resolutions, and noise characteristics. Velocities and accelerations are given in “navigation axes,” which are local vertical axes related to true North by a wander-angle rotation about the vertical. The wander angle is computed from the EGI variables cn_{xx} , cn_{xy} , as given in reference 30.

The numbers in table B1 for range and resolution of the measurements are from reference 30. The ranges for all variables are more than enough to accommodate the dynamic range of slung load rigid body motions, which is within that of helicopters except that yaw rates up to 200 deg/sec occurred in the current tests. (Yaw rates over 500 deg/sec have been observed in recent tests with a cubic load.) The measurement rates are those at which the EGI refreshes its output messages and are different from the rate of the recording. The load-cell signals are analog with continuous output at the source, but performance limits of the load cell computer reduced its data rate to 65 Hz at the input to the VME. These signals are sampled and stored at 100 Hz in the VME computer. The recorded data frames are stamped with time composed from the 1-Hz UTC time signal from the GPS receiver, and a 64- μ sec counter in the EGI.

Bench tests were conducted with the EGI motionless to review the noise characteristics of the recorded signals. These tests confirmed the resolution data in table B1. The extremes and standard deviations (σ) of the signal variations from a 1000-sec record are listed in table B1. Attitude, angular rates, and accelerometer signal variations are the same order as the truncation intervals, varying over only a few intervals. Angular acceleration and velocity variations were much larger than the

resolution errors. Angular acceleration variations are within $\pm 1.4 \text{ deg/sec}^2$, and accelerometer variations are within $\pm 0.008g$. Time histories and distributions are not presented here, but these signal variations can be characterized as “noise” in that they look like samples of a random variable that are independent from sample to sample, and are distributed symmetrically around the means.

Biases in the angular rate and accelerometer signals were estimated from an analysis of the kinematic consistency of the EGI data in the flight records using the SMACK utility (ref. 32), and the results indicated that biases were negligible, under 0.001 deg/sec and $0.0002g$.

The load cell data were converted to counts in the A/D conversion with a resolution of 0.25 lb. The single-sample raw data had large noise amplitude, of size $\pm 50 \text{ lb}$ ($\sigma = 10 \text{ lb}$), much larger than desired. This problem was treated by averaging 256 samples taken within the 65-Hz output interval of the PC. The averaged signals varied over $\pm 2 \text{ lb}$ with $\sigma = 0.4 \text{ lb}$. Time histories of the single-sample and averaged data are shown in figure B2.

The dynamic responses of the sensors were not evaluated.

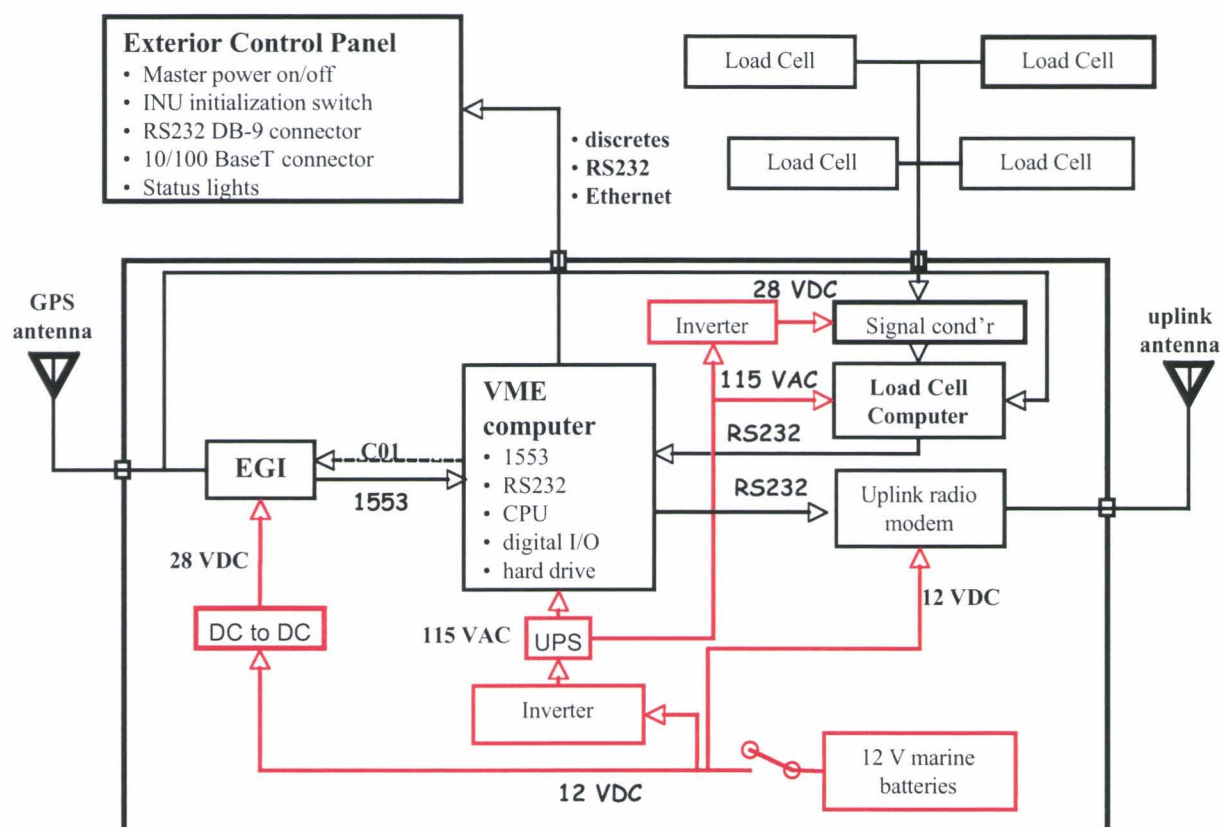


Figure B1. Load data-acquisition system.

TABLE B1. RECORDED LOAD SIGNALS

Name	Description	Units	Range	Resolution	Measurement Rate (Hz)	Bench Test	
EGI						Extremes	σ
dal1	roll	deg	± 180	.0055	200	± 0.011	
dal2	pitch	deg	± 180	.0055	200	± 0.011	
dal3	true heading	deg	± 180	.0055	50	± 0.011	
drl1	roll rate	deg/s	$\pm 4^{\circ}180$.022	200	± 0.044	
drl2	pitch rate	deg/s	$\pm 4^{\circ}180$.022	200	± 0.044	
drl3	roll rate	deg/s	$\pm 4^{\circ}180$.022	200	± 0.044	
dpL	roll ang accln	deg/s ²	$\pm 8^{\circ}180$.044	200	± 1.4	0.3
dqL	pitch ang accln	deg/s ²	$\pm 8^{\circ}180$.044	200	± 1.4	0.3
drL	yaw ang accln	deg/s ²	$\pm 8^{\circ}180$.044	200	± 1.4	0.3
cnexxL			± 1		50		
cnexyL			± 1		50		
cnexzL			± 1		50		
latL	blended latitude	deg	± 90	8e-8	50		
lonL	blended longitude	deg	± 180	8e-8	50		
altL	alt above ellipsoid	ft		.1025	50		
altmslL	alt above mean sea level	ft	-1000 to 80000	4.0	50		
vxnavL	x nav axis velocity	fps	± 3000	.4e-5	200	± 0.012	0.003
vynavL	y nav axis velocity	fps	± 3000	.4e-5	200	± 0.012	0.003
vznavL	z nav axes velocity	fps	± 3000	.4e-5	200	± 0.012	0.003
axnavL	x accel'r, nav axes	fps ²	± 16 g	.03125	50	± 0.25	0.08
aynavL	y accel'r, nav axes	fps ²	± 16 g	.03125	50	± 0.25	0.08
aznavL	z accel'r, nav axes	fps ²	± 16 g	.03125	50	± 0.25	0.08
al01	x-accel'r, body axes	fps ²	± 32 g	.03125	200	± 0.25	0.08
al02	y-accel'r, body axes	fps ²	± 32 g	.03125	200	± 0.25	0.08
al03	z-accel'r, body axes	fps ²	± 32 g	.03125	200	± 0.25	0.08
egimode1	128 = INU aligned				50		
egimode2	160 = gps active				50		
Load Cells							
lc01	Loadcell sling leg 1	lbs	5K lbs	.25	65	± 2	0.42
lc02	Loadcell sling leg 2	lbs	5K lbs	.25	65	± 2	0.42
lc03	Loadcell sling leg 3	lbs	5K lbs	.25	65	± 2	0.42
lc04	Loadcell sling leg 4	lbs	5K lbs	.25	65	± 2	0.42

Aircraft instrumentation and data system. Data are acquired and stored through the PC-based aircraft data system (ADS) installed in the aircraft. A schematic of this system is shown in figure B3.

The data acquisition uses LabView™ software running on Windows NT™ operating system. Data are recorded onboard on a hard drive at approximately 100 Hz and downloaded post-flight via a serial port. The signals are sampled and recorded in groups corresponding to the analog signals from sensors distributed throughout the helicopter, 1553-formatted data messages from the ship's GPS-aided INU, an RS232-formatted data block from the load, and an RS232-formatted data block from the differential GPS. Each of these groups has its own entry port into the PC. A GPS time stamp is added to each group of data as it is stored. The 100-Hz recording has irregular intervals owing to the use of a non-real-time version of LabView™. Measurement rates are variously continuous (analog signals), 50 and 200 Hz (INU messages), 60 Hz (up-linked load data), and 10 Hz (DGPS).

Only a few of the helicopter sensor signals have been used in the present work. A complete listing is included in appendix C, table C2, which lists all the signals archived in the Aeroflightdynamics Directorate flight research data base.

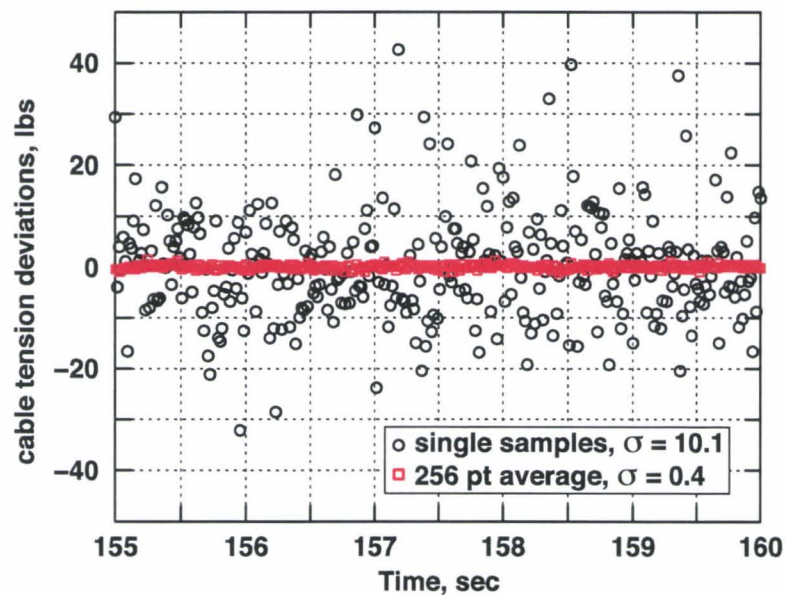


Figure B2. Sample load cell data with and without data averaging.

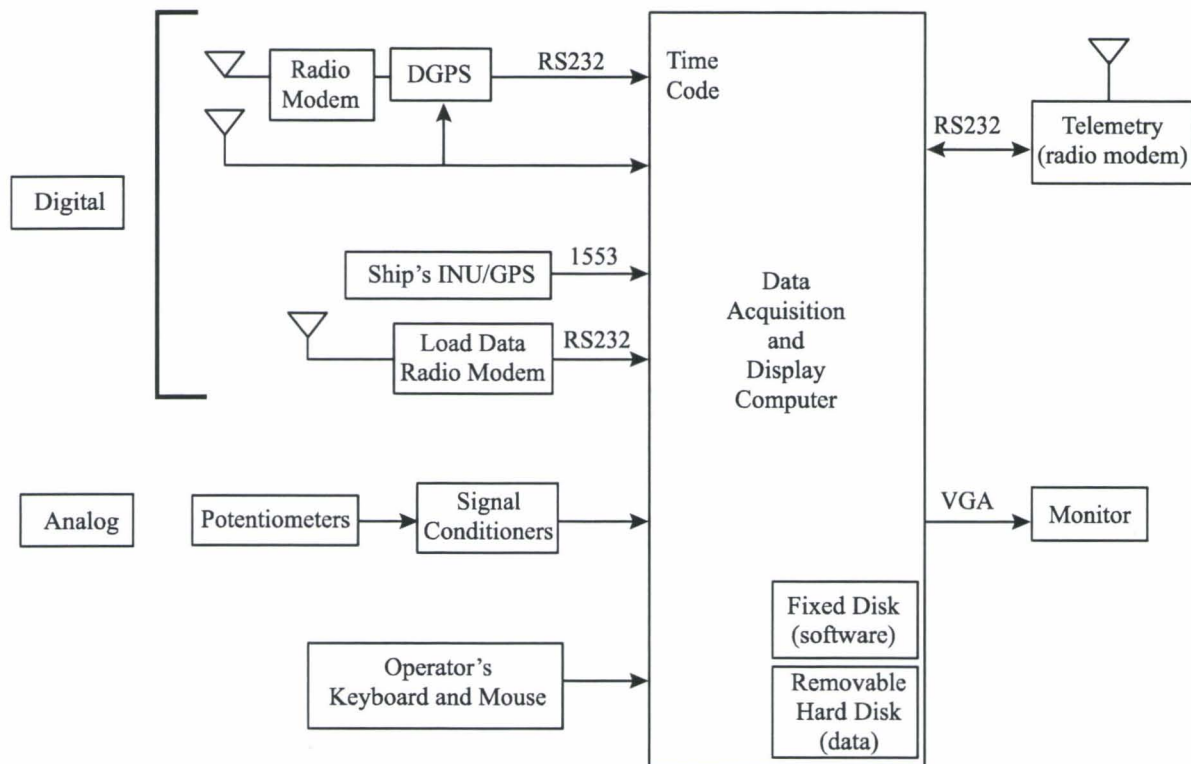


Figure B3. Aircraft data-acquisition system.

APPENDIX C. COMPENDIUM OF EH-60L SLUNG LOAD FLIGHT TESTS

This appendix provides a compendium of slung-load flight test data archived at AFDD in its TRENDS database utility under tail number 657. This appendix contains a summary of flights by load (table C1), a master list of archived sensor signals (table C2) and derived parameters (table C3), and a catalog of records for the flights listed in table 1 of the text (table C4).

Summary of flights by load. Flights are summarized by load in table C1. The table lists the test events and speed range, the number of records, and the sling and cg configurations, and it notes the flights without load-cell data.

Sensor signals. A list of the sensor signals stored in TRENDS is given in table C2. This list is divided into groups by source. The groups are:

AN	Helicopter analog sensor signals (controls, boom data, etc.)
LD	Load sensor signals (EGI, load cells)
I1	Helicopter ship's INU message IO1 signals
I9	Helicopter ship's INU message IO9 signals
H1	Helicopter ship's INU message IH1 signals
AS	Ashtek DGPS signals

Since the signals refresh at various measurement rates from 10 Hz to continuously and are recorded by the non-real-time ADS system at irregular intervals, they have all been interpolated to a common 100-Hz time sequence. The sensor signal names in TRENDS are the same as those listed in table C2 except with the prefix 'I' (e.g., ID100, ID101, ...) to distinguish them from the raw flight data. Angles from the ship's INU are given in pi-radians (multiply by π or 180 to get angles in radians or degrees, respectively). Dynamic pressure from the boom pressure head is subject to increasingly dominating noise at speeds below 30 kts.

Derived parameters. A list of parameters derived from the flight data and stored in TRENDS is given in table C3 and separates into variables derived from the helicopter sensor signals (TRENDS group DH) and those derived from the load sensor signals (group DL). Velocity parameters that depend on the boom dynamic pressure are subject to increasing signal noise below 30 kts (VEB, VICB, VTB, winds, VA2SN, and VA2S2). The movement of the helicopter cg with fuel usage has been accounted for in the cg velocity and acceleration variables. Numerous signals have been filtered to smooth out the noise, and they are denoted with an "s" at the end of the parameter name. A low pass forward-backward 2nd order Butterworth filter was used and is described in reference 32. The filter introduces no phase lag from the raw data and provides derivatives of the smoothed signal. The cutoff frequency was set at 2.5 Hz for all filtered signals, except the loads cells where 1 Hz was used.

Catalog of flight records. A catalog of the flight records stored in TRENDS is given in table C4 for each flight listed in table 1 of the text. Trail angle is noted for all trim records as well as the mean spin rate for trims with a steady state spin.

TABLE C1. TRENDS 657 DATABASE: SUMMARY OF FLIGHTS BY LOAD

Load	Flight	Test Events	Number of Records	Sling	Swivel	Load Cells	CG if Not Centered			
2K CONEX	88	Trims, 40 – 70 kts	22	Sling set	Yes	Yes				
	108	Trims, 0 – 40 kts	8	Sling set						
	109	Trims, 40 – 100 kts	31	Sling set						
	110	Trims, 40 – 70 kts	13	Sling set	No					
	133	Trims, 40 – 100 kts	8	Long line	Yes					
4K CONEX	89	Trims, 40 – 100 kts	30	Sling set						
	90	Sweeps, 0, 30, 60 kts	32	Sling set						
	116	Trims, 40 to 105kts	13	Sling set	No					
	132	Trims. 40 to 107 kts	12	Sling set						
	134	Trims, 80 – 105 kts	9	Sling set						
	135	Trims, 40 – 110kts	10	Sling set						
6K CONEX	85	Sweeps, 0, 50 kts	31	Long line		yes	No			
	86	Trims, 0 – 95 kts	29	Long line						
Engine can	81	Trims, 0 -30 kts	27	Long line					Yes	
	82	Trims, 0 – 80 kts	51	Long line						
	91	Sweeps, 0, 30kts Trims, 0 – 80 kts	52	Sling set						
	107	Maneuvers, 50 – 70kts	43	Sling set						

TABLE C2. TRENDS VARIABLES: SENSOR SIGNALS

Item Name	Description	Units	Measurement Rate	Positive Direction
Helicopter analog sensor signals, TRENDS group AN				
TIME	ADS time stamp analog data	sec	continuous	
AT1	ADS temperature 1	deg F		
AT2	ADS temperature 2	deg F		
D100	longitudinal stick	%		aft stick
D101	lateral stick	%		right stick
D102	pedal	%		rt pedal
D103	collective	%		up
DM00	longitudinal mixer input	%		aft stick
DM01	lateral mixer input	%		right stick
DM02	directional mixer input	%		rt pedal
DP00	forward primary servo	%		
DP01	lateral primary servo	%		
DP03	aft primary servo	%		
DS00	longitudinal SAS output	%		nose up
DS01	lateral SAS output	%		roll right
DS02	directional SAS output	%		nose right
D003	stabulator position	deg		TE down
DAA0	boom angle of attach	deg		nose up
DSS0	boom sideslip angle	deg		nose left
R021	tail rotor imprest pitch	%		nose right
H001	boom static pressure	in Hg		
V001	boom dynamic pressure	in Hg		
T100	Total temperature	deg F		
H003	radar altimeter	ft		
Q1	Engine 1 torque	% of 1414 shp		
Q2	Engine 2 torque	% of 1414 shp		
NR	main rotor RPM	% 257.89 rpm		
Load sensor signals, TRENDS group LD				
AL01	load x accelerometer	g's	60 Hz	fwd
AL02	load y accelerometer	g's		rt wing
AL03	load z accelerometer	g's		down
DAL1	load roll	deg		CW roll
DAL2	load pitch	deg		nose up
DAL3	load magnetic heading	deg		nose right
DRL1	load roll rate	deg/sec		CW roll
DRL2	load pitch rate	deg/sec		nose up
DRL3	load yaw rate	deg/sec		nose right
DPL	load roll angular velocity	deg/sec2		CW roll
DQL	load pitch angular velocity	deg/sec2		nose up
DRL	load yaw angular velocity	deg/sec2		nose right
LC01	Load cell, sling leg 1	lbs		tension
LC02	Load cell, sling leg 2	lbs		tension
LC03	Load cell, sling leg 3	lbs		tension
LC04	Load cell, sling leg 4	lbs		tension
ALTL	Load altitude above the ellipsoid	ft		up
ALTMSLL	Load alt above mean sea level	Ft		up

TABLE C2. TRENDS VARIABLES: SENSOR SIGNALS (cont.)

Item Name	Description	Units	Measurement Rate	Positive Direction
Load sensor signals, TRENDS group LD, cont.				
CNEXXL	Load cnexx		60 Hz	
CNEXYL	Load cnexy			
CNEXZL	Load cnexz			
LATL	Load latitude	Deg		north
LONL	Load longitude	deg		east
VXNAVL	Load nav axes x-velocity			northerly
VYNAVL	Load nav axes y-velocity			westerly
VZNAVL	Load nav axes z-velocity			up
DVXNAVL	Load nav axes x-acceleration	fps2		northerly
DVYNAVL	Load nav axes y-acceleration	fps2		westerly
DVZNAVL	Load nave axes z-acceleration	fps2		up
Ship's INU message IO1, TRENDS group I1				
PHI1	roll angle	pi rad		CW roll
THETA1	pitch angle	pi rad		nose up
PSI1	true heading	pi rad		nose rt
PSIMAG1	magnetic heading	pi rad		nose rt
PB1	roll rate	pi rad /sec		CW roll
QB1	pitch rate	pi rad /sec		nose up
RB1	yaw rate	pi rad /sec		nose rt
VXNAV1	nav axes x-vel @ INU	fps		northerly
VYNAV1	nav axes y-vel @ INU	fps		westerly
VZNAV1	nav axes z-vel @ INU	fps		up
AXNAV1	nav axes x –accelrtr @ INU	fps2		northerly
AYNAV1	nav axes y –accelrtr @ INU	fps2		westerly
AZNAV1	nav axes z –accelrtr @ INU	fps2		up
CNEXX	cnexx			
CNEXY	cnexy			
CNEXZ	cnexz			North
LONINU	longitude	pi rad		East
ALTINU1	altitude above ellipsoid	ft		up
GCE	great crcle steering error	pi rad		
PLATAZ1	platform azimuth	pi rad		
XTILT	x-axis platform tilt	arcsec		
YTILT	y-axis platform tilt	arcsec		
Ship's INU message IO9, TRENDS group I9				
PHI9	roll	pi rad		CW roll
THETA9	pitch	pi rad		nose up
PB9	roll rate	pi rad /sec		roll rt
QB9	pitch rate	pi rad /sec		nose up
RB9	yaw rate	pi rad /sec		nose rt
PBD9	roll angular acceleration	pirad/sec2		CW roll
QBD9	pitch angular acceleration	pirad/sec2		nose up
RBD9	yaw angular acceleration	pirad/sec2		nose rt

TABLE C2. TRENDS VARIABLES: SENSOR SIGNALS (cont.)

Item Name	Description	Units	Hz	Pos. Dir.
Ship's INU message IO9, TRENDS group I9, Cont.				
VXNAV9	nav axes x-velocity at INU	Fps	200 Hz	northerly
VYNAV9	nav axes y-velocity at INU	Fps		westerly
VZNAV9	nav axes z-velocity at INU	Fps		up
AXB	body axes x-acceleration at INU	fps2		forward
AYB	body axes y-acceleration at INU	fps2		rt wing
AZB	body axes z-acceleration at INU	fps2		down
PLATAZ9	platform azimuth	pl rad		
Ship's INU message IH1, TRENDS group H1				
THETAH1	pitch angle	pi rad	200 Hz	nose up
PHIH1	roll angle	pi rad		CW roll
PSIH1	true heading	pi rad		nose rt
VN	north vel @ INU	fps		North
VE	east vel @ INU	fps		East
VD	down vel @ INU	fps		down
VXNAVH1	nav axis x-vel @ INU	fps		northerly
VYNAVH1	nav axis y-vel @ INU	fps		westerly
VZNAVH1	nav axis z-vel @ INU	fps		up
PLTAZH1	platform azimuth	pi rad		
Ashtek DGPS Signals, TRENDS Group AS				
ASHMODE	Standard/Differential position solution ^{1,2}	0—standard 1—diff w/ RTCM 2—diff w/ CPD 3—CPD fixed sol	10 Hz	
ASHSATS	number of satellites used			
ASHLAT	latitude, deg	degrees dd.mm		North
ASHLON	longitude, deg	degrees dd.mm		East
ASHALT	altitude above ellipsoid	ft		Up
ASHTRK	course over ground	deg		CW from N
ASHVGR	ground speed	kts		
ASHZD	vertical velocity	ft/sec		down

1. RTCM–Radio Technical Committee Maritime differential GPS

2. CPD–Carrier Phase Differential GPS

TABLE C3. TRENDS VARIABLES: DERIVED PARAMETERS

(a) Parameters derived from helicopter data, TRENDS group DH

DMIXAIN	lateral mixer input	in
DMIXEIN	longitudinal mixer input	in
DMIXRIN	pedal mixer input	in
DMIXCIN	collective mixer input	in
PSAFTIN	aft primary servo output	in
PSFWDIN	forward primary servo output	in
PSLATIN	lateral primary servo output	in
PSTRIN	tail rotor servo output	in
XABST	lateral boost servo output	in
XEBST	longitudinal boost servo output	in
XPBST	pedal boost servo output	in
XCBST	collective boost servo output	in
XAIN	lateral stick position	in
XBIN	longitudinal stick position	in
XCIN	collective position	in
XPIN	pedal position	in
PBS	filtered roll rate from I09 data	pirad/s
QBS	filtered pitch rate from I09 data	pirad/s
RBS	filtered yaw rate from I09 data	pirad/s
DP	derivative of pbs	pirad/s ²
DQ	derivative of qbs	pirad/s ²
DR	derivative of rbs	pirad/s ²
U1	cg air vel, x body axis, from boom data	fps
V1	cg air vel, y body axis, from boom data	fps
W1	cg air vel, z body axis, from boom data	fps
VCGBX9	cg inertial vel, x body axis, IO9 data	fps
VCGBY9	cg inertial vel, y body axis, IO9 data	fps
VCGBZ9	cg inertial vel, z body axis, IO9 data	fps
VCGNX1	cg inertial vel, x inertial axis, IO1 data	fps
VCGNY1	cg inertial vel, y inertial axis, IO1 data	fps
VCGNZ1	cg inertial vel, z inertial axis, IO1 data	fps
VCGNX9	cg inertial vel, x inertial axis, IO9 data	fps
VCGNY9	cg inertial vel, y inertial axis, IO9 data	fps
VCGNZ9	cg inertial vel, z inertial axis, IO9 data	fps
VCGNXH1	cg inertial vel, x inertial axis, IH1 data	fps
VCGNYH1	cg inertial vel, y inertial axis, IH1 data	fps
VCGNZH1	cg inertial vel, z inertial axis, IH1 data,	fps

TABLE C3. TRENDS VARIABLES: DERIVED PARAMETERS (cont.)

(a) Parameters derived from helicopter data, TRENDS group DH (cont.)

VGR1	ground speed from IO1 data	kts
VGR9	ground speed from IO9 data	kts
VGRH1	ground speed from IH1 data	kts
TRACK1	track angle from IO1 data	deg
TRACK9	track angle from IO9 data	deg
TRACKH1	track angle from IH1 data	deg
VEB	boom equivalent airspeed	kts
VICB	boom indicated airspeed	kts
VTB	boom true airspeed	kts
WANDER	INU wander angle	deg
WINDSPD	estimated wind speed	fps
WINDX	wind - north component	fps
WINDY	wind - east component	fps
WINDZ	wind - vertical component	fps
AMGCGBX	cg accelerometer, x body axis, IO1 data	fps
AMGCGBY	cg accelerometer, y body axis, IO1 data	fps2
AMGCGBZ	cg accelerometer, z body axis, IO1 data	fps2
AMGCGBX9	cg accelerometer, x body axis, IO9 data	ps2
AMGCGBY9	cg accelerometer, y body axis, IO9 data	fps2
AMGCGBZ9	cg accelerometer, z body axis, IO9 data	fps2
AXBS	filtered axb	fps2
AYBS	filtered ayb	fps2
AZBS	filtered azb	fps2
AXNAV1S	filtered axnav1	fps2
AYNAV1S	filtered aynav1	fps2
AZNAV1S	filtered aznav1	fps2
DVCGBX9	cg inertial acceln, x body axis from IO9	fps2
DVCGBY9	cg inertial acceln, y body axis from IO9	fps2
DVCGBZ9	cg inertial acceln, z body axis from IO9	fps2
DVCGNX	cg inertial acceln, x body axis from IO1	fps2
DVCGNY	cg inertial acceln, y body axis from IO1	fps2
DVCGNZ	cg inertial acceln, z body axis from IO1	fps2
HDB	density altitude from boom data	ft
TA	boom ambient temperature	deg C
LATINU	latitude from IO1 data	pirad
XINU ¹	x position from IO1 data	ft
YINU ¹	y position from IO1 data	ft
HINU ¹	altitude from IO1 data	ft
XGPS ¹	x position from Ashtek DGPS data	ft
YGPS ¹	y position from Ashtek DGPS data	ft
HGPS ¹	altitude from Ashtek DGPS data	ft

1. x,y,z position coordinates in local vertical (N, E, D) frame with origin at a runway reference point, Moffett Field.

TABLE C3. TRENDS VARIABLES: DERIVED PARAMETERS (cont.)

(b) Parameters derived from load sensor data: TRENDS group DL

ALFA2	load angle of attack	deg
BETA2	load sideslip angle	deg
DAL3C	continuous load heading	deg
THC	cable pitch angle in HC level heading axes	deg
PHC	cable roll angle in HC level heading axes	deg
DELPHC	cable roll angle in HC body axes	deg
DELTHC	cable pitch angle in HC body axes	deg
P2P	load roll rate in HC heading axes	deg/s
Q2P	load pitch rate in HC heading axes	deg/s
DRL1S	smoothed load roll rate	deg/s
DRL2S	smoothed load pitch rate	deg/s
DRL3S	smoothed load yaw rate	deg/s
DP2	derivative of drl1s	deg/s ²
DQ2	derivative of drl2s	deg/s ²
DR2	derivative of drl3s	deg/s ²
RA2SHX	load cg longitudinal position, HC body axes	ft
RA2SHY	load cg lateral position, HC body axes	ft
TAS2	load airspeed	kts
V2SNX	cg velocity, x inertial axis	fps
V2SNY	cg velocity, y inertial axis	fps
V2SNZ	cg velocity, z inertial axis	fps
VA2S2X	load air velocity, x body axis	fps
VA2S2Y	load air velocity, y body axis	fps
VA2S2Z	load air velocity, z body axis	fps
VA2SNX	load air velocity, x inertial axis	fps
VA2SNY	load air velocity, y inertial axis	fps
VA2SNZ	load air velocity, z inertial axis	fps
AL01S	smoothed load acceleration at EGI, x body axis	g's
AL02S	smoothed load acceleration at EGI, x body axis	g's
AL03S	smoothed load acceleration at EGI, x body axis	g's
A2SNX	load inertial acceleration at cg, x inertial axis	fps ²
A2SNY	load inertial acceleration at cg, x inertial axis	fps ²
A2SNZ	load inertial acceleration at cg, x inertial axis	fps ²
AMG2S2X	load accelerometer at cg, x body axis	fps ²
AMG2S2Y	load accelerometer at cg, y body axis	fps ²
AMG2S2Z	load accelerometer at cg, z body axis	fps ²

TABLE C3. TRENDS VARIABLES: DERIVED PARAMETERS (cont.)

(b) Parameters derived from load sensor data: TRENDS group DL (cont.)

ANGFCK2	angle of hook force vector from load body z axis	deg
SFC	specific hook force, FC/W2	
FC2X	hook force, x load body axis	lbs
FC2Y	hook force, y load body axis	lbs
FC2Z	hook force, z load body axis	lbs
LC01S	filtered cable tension, sling leg 1	lbs
LC02S	filtered cable tension, sling leg 2	lbs
LC03S	filtered cable tension, sling leg 3	lbs
LC04S	filtered cable tension, sling leg 4	lbs
DOQ	drag/dynamic pressure	ft2
LOQ	lift/dynamic pressure	ft2
YOQ	side force/ dynamic pressure	ft2
FA22X	aero force, x load body axes	lbs
FA22Y	aero force, y load body axes	lbs
FA22Z	aero force, z load body axes	lbs
FA22XOQ	fa22x/dynamic pressure	ft2
FA22YOQ	fa22y/dynamic pressure	ft2
FA22ZOQ	fa22z/dynamic pressure	ft2
MA22X	aero moment about cg, x load body axis	ft-lbs
MA22Y	aero moment about cg, y load body axis	ft-lbs
MA22Z	aero moment about cg, z load body axis	ft-lbs
MA22XOQ	ma22x/dynamic pressure	ft3
MA22YOQ	ma22y/dynamic pressure	ft3
MA22ZOQ	ma22z/dynamic pressure	ft3
MAGC2X	aero moment about geom cntr, x load body axis	ft-lbs
MAGC2Y	aero moment about geom cntr, y load body axis	ft-lbs
MAGC2Z	aero moment about geom cntr, z load body axis	ft-lbs
MAGC2XOQ	magc2x/dynamic press	ft3
MAGC2YOQ	magc2y/dynamic press	ft3
MAGC2ZOQ	magc2z/dynamic press	ft3
RMOQ	roll moment about cg/dynamic pressure	ft3
PMOQ	pitch moment about cg/dynamic pressure	ft3
YMOQ	yaw moment about cg/dynamic pressure	ft3
RMGCOQ	roll moment about gc/dynamic pressure	ft3
PMGCOQ	pitch moment about gc/dynamic pressure	ft3
YMGCOQ	yaw moment about gc/dynamic pressure	ft3

TABLE C4. CATALOG OF RECORDS BY FLIGHT NUMBER

Flight No: 81	Date: 8 July 2005
Remarks: engine can, low speed trims and doublets, long line sling + sling set	
Pilot: D. Robinson	
Copilot: R. Watson	
Takeoff Conditions:	
Wind: 4/variable (kts, deg)	SAS on
OAT 30.3 (deg C)	FPS off
Altimeter 29.97 (in Hg)	Stabilator fixed by airspeed
A/C TOGW 16080 (lbs)	Load engine can
XMOMTO 5820.4 e+3 ft lbs	Sling: long line

Record No.	Test Event	Ref IAS (kts)	Start Fuel Weight	Duration (sec)	Spin (deg/sec)	Trail (deg)
1	Trim	hover	2030	24		-3.3
2	Lon doublet		2010	55		
3	Lon doublet		1970	39		
4	Lon doublet		1940	44		
5	Lon doublet		1880	44		
6	Trim	hover	1430	67		0.3
7	Lon doublet		1390	44		
8	Lat doublet		1340	45		
9	Lat doublet		1310	54		
10	Trim	10	1290	76		-1.4
11	Lon doublet		1240	52		
12	Lon doublet		1220	67		
13	Lon doublet		1190	47		
14	Lon doublet		1030	50		
15	Trim	20	1000	64		-4.4
16	Trim		930	70		
17	Lon doublet		900	23		
18	Lon doublet		880	21		
19	Lon doublet		850	33		
20	Lat doublet		830	36		
21	Trim	30	810	43		-7.7
22	Trim		790	62		
23	Lon doublet		730	18		
24	Lon doublet		710	23		
25	aborted					
26	Lon doublet		670	18		
27	Lon doublet		600	35		

TABLE C4. CATALOG OF RECORDS BY FLIGHT NUMBER (cont.)

Flight No: 82	Date: 12 July 2005
Remarks: Engine can, hover to 80kts, trims and doublets, long line + sling set	
Pilot: D. Robinson	
Copilot: R. Watson	
Takeoff Conditions:	
Wind <u>4/variable</u> (kts, deg)	SAS on
OAT <u>16.6</u> (deg C)	FPS off
Altimeter <u>29.97</u> (in Hg)	Stabilator fixed by airspeed
A/C TOGW <u>16080</u> (lbs)	Load Engine can
XMOMTO <u>5820.4 e+3</u> ft lbs	Sling long line

Record No.	Test Event	Ref IAS (kts)	Start Fuel Weight	Duration (sec)	Spin (deg/sec)	Trail (deg)
1	trim	40	2070	85		-1.0
2	aborted					
3	lon doublet		2040	29		
4	lat doublet		2000	28		
5	aborted					
6	lat doublet		1990	40		
7	lat doublet	50	1970	36		
8	trim	45	1950	54		-11.6
9	lon doublet		1930	31		
10	lat doublet		1900	29		
11	Trim	50	1880	74		-12.5
12	lon doublet		1860	20		
13	lon doublet		1840	43		
14	lat doublet		1820	23		
15	lat doublet		1810	27		
16	trim	55	1790	64		-13.4
17	lon doublet		1760	33		
18	lat doublet		1750	29		
19	trim	60	1720	70		-16.0
20	lon doublet		1710	24		
21	lat doublet		1690	27		
22	trim	65	1660	63		-21.2
23	lon doublet		1640	22		
24	lat doublet		1620	25		

TABLE C4. CATALOG OF RECORDS BY FLIGHT NUMBER (cont.)

Flight no 82 cont.

Record No.	Test Event	Ref IAS (kts)	Start Fuel Weight	Duration (sec)	Spin (deg/sec)	Trail (deg)
25	trim	70	1530	58		-24.1
26	aborted					
27	aborted					
28	lon doublet		1500	31		
29	lat doublet		1490	26		
30	trim	75	1450	58		-27.2
31	lon doublet		1450	50		
32	lon doublet		1420	29		
33	lat doublet		1400	24		
34	trim	80	1370	56		-30.5
35	aborted					
36	lon doublet		1330	40		
37	lat doublet		1320	31		
38	trim	Hover	1150	61		-0.9
39	aborted					
40	trim	5	1100	25		-0.3
41	lat doublet		1080	26		
42	trim	10	1040	63		-0.3
43	lon doublet		1010	36		
44	lat doublet		1000	32		
45	trim	20	970	61		-0.6
46	lon doublet		960	33		
47	lat doublet		940	26		
48	trim	30	890	68		-1.8
49	lon doublet		860	22		
50	lon doublet		830	21		
51	lat doublet		800	19		

TABLE C4. CATALOG OF RECORDS BY FLIGHT NUMBER (cont.)

Flight No: 85	Date: 26 July 2005
Remarks: 6K CONEX, lon and lat sweeps at hover and 50 kts, long line + sling set	
Pilot: D. Robinson	
Copilot: R. Watson	
Takeoff Conditions:	
Wind <u>calm</u> (kts, deg)	SAS on
OAT <u>19</u> (deg C)	FPS off
Altimeter <u>29.93</u> (in Hg)	Stabilator fixed by airspeed
A/C TOGW <u>16080</u> (lbs)	Load 6K CONEX
XMOMTO <u>5820.4 e+3</u> ft lbs	Sling long line

Record No.	Test Event	Ref IAS (kts)	Start Fuel Weight	Duration (sec)	Spin (deg/sec)	Trail (deg)
1	aborted	50				
2	lon sweep	50	1930	119		
3	aborted					
4	lon sweep		1890	116		
5	lon sweep		1840	106		
6	lon sweep		1790	111		
7	lon doublet		1740	45		
8	lon doublet		1700	51		
9	lat sweep		1670	102		
10	lat sweep		1630	110		
11	aborted					
12	lat sweep		1560	111		
13	lat doublet		1500	58		
14	lat doublet		1470	42		
15	lat doublet		1450	45		
16	lat doublet		1410	46		
17	aborted					
18	lon sweep	hover	1100	106		
19	lon sweep		1076	112		
20	lon sweep		1020	109		
21	lon sweep		910	105		
22	lat sweep		850	99		
23	lat sweep		800	109		
24	lat sweep		750	115		

TABLE C4. CATALOG OF RECORDS BY FLIGHT NUMBER (cont.)

Flight no 85 cont.

Record No.	Test Event	Ref IAS (kts)	Start Fuel Weight	Duration (sec)	Spin (deg/sec)	Trail (deg)
25	lon doublet	hover	670	46		
26	lon doublet		650	47		
27	lat doublet		620	49		
28	lat doublet		590	53		
29	aborted					
30	lat doublet		520	47		
31	load set down			42		

TABLE C4. CATALOG OF RECORDS BY FLIGHT NUMBER (cont.)

Flight No:	86	Date:	2 August 2005
Remarks:	6K CONEX, trims and doublets, hover to 95 kias, long line + sling set		
PILOT:	D. Robinson		
Copilot:	L. McNelly		
Takeoff Conditions:			
Wind	<u>calm</u>	(kts, deg)	SAS on
OAT	<u>18.3</u>	(deg C)	FPS off
Altimeter	<u>29.84</u>	(in Hg)	Stabilator fixed by airspeed
A/C TOGW	<u>16080</u>	(lbs)	Load 6K CONEX
XMOMTO	<u>5820.4 e+3</u>	ft lbs	Sling long line

Record No.	Test Event	Ref IAS (kts)	Start Fuel Weight (lbs)	Duration (sec)	Spin (deg/sec)	Trail (deg)
1	trim	Hover	1740	65	-17.5	-0.4
2	trim	20	1590	75	-21	-0.8
3	trim	40	1530	120	-76	-3.8
4	lat doublet		1470	35		
5	lon doublet		1440	37		
6	trim	50	1420	26	-119	-6.5
7	trim		1400	68	-133	-5.4
8	lat doublet		1380	33		
9	lon doublet		1360	39		
10	trim	60	1340	87	-153	-8.5
11	lat doublet		1270	42		
12	lon doublet		1230	36		
13	trim	70	1190	75	-184	-11.6
14	lat doublet		1180	40		
15	lon doublet		1150	37		
16	trim	80	1120	70	-193	-13.2
17	lat doublet		1090	31		
18	lon doublet		1070	34		
19	trim	85	1050	80	-185	-15.2
20	lat doublet		1020	27		
21	lon doublet		1000	28		
22	trim	90	960	63	-176	-16.4
23	lat doublet		940	34		
24	lon doublet		920	37		

TABLE C4. CATALOG OF RECORDS BY FLIGHT NUMBER (cont.)

Flight no 86 cont.

Record No.	Test Event	Ref IAS (kts)	Start Fuel Weight (lbs)	Duration (sec)	Spin (deg/sec)	Trail (deg)
25	trim	95	870	64	-163	-18.2
26	lat doublet		820	42		
27	lon doublet		770	28		
28	trim	hover	670	63	-41	-0.2

TABLE C4. CATALOG OF RECORDS BY FLIGHT NUMBER (cont.)

Flight No: 88	Date: 2 August 05
Remarks: 2K CONEX, hover and 40 to 70 kts, trims and doublets, sling set	
PILOT: D. Robinson	
Copilot: R. Watson	
Takeoff Conditions:	
Wind <u>calm</u> (kts, deg)	SAS on
OAT <u>17</u> (deg C)	FPS off
Altimeter <u>29.98</u> (in Hg)	Stabilator fixed by airspeed
A/C TOGW <u>16080</u> (lbs)	Load 2K CONEX
XMOMTO <u>5820.4 e+3</u> ft lbs	Sling sling set

Record No.	Test Event	Ref IAS (kts)	Start Fuel Weight	Duration (sec)	Spin (deg/sec)	Trail (deg)
1	trim	hover	2090	63	-54.5	-0.4
2	trim	40	1990	93	-100	-9.4
3	lat doublet		1950	38		
4	lon doublet		1910	50		
5	trim	50	1870	78	-96.5	-13.4
6	lat doublet		1820	57		
7	aborted			28		
8	lon doublet		1740	42		
9	trim	55	1690	92	-86.5	-15.7
10	lat doublet		1670	49		
11	lon doublet		1630	53		
12	trim	60	1590	91	-70.5	-17.8
13	lat doublet		1540	39		
14	lat doublet		1510	45		
15	lon doublet		1490	44		
16	trim	65	1450	98	-52.5	-21.4
17	lat doublet		1390	65		
18	lon doublet		1360	41		
19	trim	70	1340	93	-52.4	-23.0
20	lat doublet		1310	47		
21	lon doublet		1270	60		
22	load setdown		1100	109		

TABLE C4. CATALOG OF RECORDS BY FLIGHT NUMBER (cont.)

Flight No: 89	Date: 3 September 2005
Remarks: 4K CONEX, hover and 40 to 100 kts, trims and doublets	
PILOT: D. Robinson	
Copilot: R. Watson	
Takeoff Conditions:	
Wind <u>calm</u> (kts, deg)	SAS on
OAT <u>19</u> (deg C)	FPS off
Altimeter <u>29.88</u> (in Hg)	Stabilator fixed by airspeed
A/C TOGW <u>16080</u> (lbs)	Load 4K CONEX
XMOMTO <u>5820.4 e+3</u> ft lbs	Sling sling set

Record No.	Test Event	Ref IAS (kts)	Start Fuel Weight	Duration (sec)	Spin (deg/sec)	Trail (deg)
1	trim	Hover	2130	92	-63.1	-0.7
2	accel	0 to 40		78		
3	trim	40	1990	94	-76	-4.4
4	lat doublet		1940	41		
5	lon doublet		1910	40		
6	trim	50	1880	91	-127	-6.3
7	lat doublet		1860	50		
8	lon doublet		1820	45		
9	trim	60	1790	91	-151	-9.6
10	lat doublet		1740	55		
11	lon doublet		1720	49		
12	trim	70	1670	92	-164	-12.9
13	lat doublet		1640	45		
14	lon doublet		1610	41		
15	trim	75	1590	81	-137	-14.4
16	lat doublet		1540	52		
17	lon doublet		1520	43		
18	trim	80	1500	73	-135	-16.2
19	lat doublet		1460	43		
20	lon doublet		1450	41		
21	trim	85	1390	90	-119	-18.5
22	lat doublet		1350	35		
23	lon doublet		1340	45		
24	trim	90	1300	90	-91.5	-20.1

TABLE C4. CATALOG OF RECORDS BY FLIGHT NUMBER (cont.)

Flight no 89 cont.

Record No.	Test Event	Ref IAS (kts)	Start Fuel Weight	Duration (sec)	Spin (deg/sec)	Trail (deg)
25	lat doublet	90	1280	44		
26	lon doublet		1240	51		
27	trim	95	1170	92	--74.5	-22.5
28	lat doublet		1130	37		
29	lon doublet		1120	41		
30	trim	100	1080	43		-21.0

TABLE C4. CATALOG OF RECORDS BY FLIGHT NUMBER (cont.)

Flight No: 90	Date: 6 October 2005
Remarks: 4K CONEX, lon and lat sweeps and doublets at 0, 30, 50 kts, sling set	
PILOT: D. Robinson	
Copilot: M. Dearing	
Takeoff Conditions:	
Wind <u>calm</u> (kts, deg)	SAS on
OAT <u>18</u> (deg C)	FPS off
Altimeter <u>29.96</u> (in Hg)	Stabilator fixed by airspeed
A/C TOGW <u>16080</u> (lbs)	Load 4K CONEX
XMOMTO <u>5820.4 e+3</u> ft lbs	Sling sling set

Record No.	Test Event	Ref IAS (kts)	Start Fuel Weight	Duration (sec)	Spin (deg/sec)	Trail (deg)
1	trim	50	2080	95	-116	-6.8
2	lon sweep		2020	107		
3	lon sweep		1990	105		
4	lon sweep		1940	115		
5	lat sweep		1910	111		
6	lat sweep		1860	51		
7	lat sweep		1840	101		
8	lat sweep		1800	105		
9	lon doublet		1760	39		
10	lon doublet		1740	43		
11	lat doublet		1710	47		
12	lat doublet		1690	52		
13	Trim	hover	1560	93	-37	-0.4
14	lon sweep		1520	99		
15	lon sweep		1460	105		
16	lon sweep		1410	109		
17	lat sweep		1360	109		
18	lat sweep		1330	96		
19	lat sweep		1260	103		
20	lon doublet		1210	49		
21	lon doublet		1180	44		
22	lat doublet		1150	41		
23	lat doublet		1030	44		
24	trim	30	1090	88	-26	-1.7

TABLE C4. CATALOG OF RECORDS BY FLIGHT NUMBER (cont.)

Flight no 90 cont.

Record No.	Test Event	Ref IAS (kts)	Start Fuel Weight	Duration (sec)	Spin (deg/sec)	Trail (deg)
25	lon sweep	30	1050	93		
26	lon sweep		1030	99		
27	lon sweep		850	123		
28	lat sweep		830	85		
29	lat sweep		780	98		
30	lat sweep		740	94		
31	lon doublet		670	33		
32	lat doublet		650	42		

TABLE C4. CATALOG OF RECORDS BY FLIGHT NUMBER (cont.)

Flight No:	91	Date:	14 October 2009
Remarks:	Engine can, trims at 40 to 80 kts, lon and lat sweeps at 0,30kts, sling set		
PILOT:	D. Robinson		
Copilot:	R. Watson		
Takeoff Conditions:			
Wind	<u>calm</u>	(kts, deg)	SAS on
OAT	<u>16.4</u>	(deg C)	FPS off
Altimeter	<u>29.96</u>	(in Hg)	Stabilator fixed by airspeed
A/C TOGW	<u>16080</u>	(lbs)	Load Engine can
XMOMTO	<u>5820.4 e+3</u>	ft lbs	Sling sling set

Record No.	Test Event	Ref IAS (kts)	Start Fuel Weight (lbs)	Duration (sec)	Spin (deg/sec)	Trail (deg)
1	trim	40	2100	92		-5.0
2	lon doublet		2070	62		
3	lat doublet		2050	43		
4	trim	45	2020	92		-5.8
5	lon doublet		2000	36		
6	lat doublet		1980	44		
7	trim	50	1960	84		-10.5
8	lon doublet		1910	43		
9	lat doublet		1900	42		
10	trim	55	1850	93		-12.7
11	lon doublet		1840	36		
12	lat doublet		1830	44		
13	trim	60	1800	91		-16.7
14	lon doublet		1770	54		
15	lat doublet		1760	47		
16	trim	65	1730	95		-18.9
17	lon doublet		1710	40		
18	lat doublet		1690	53		
19	trim	70	1660	90		-19.5
20	lon doublet		1640	42		
21	lat doublet		1610	69		
22	trim	75	1590	90		-22.8
23	lon doublet		1570	40		
24	lat doublet		1550	50		

TABLE C4. CATALOG OF RECORDS BY FLIGHT NUMBER (cont.)

Flight no 91 cont.

Record No.	Test Event	Ref IAS (kts)	Start Fuel Weight (lbs)	Duration (sec)	Spin (deg/sec)	Trail (deg)
25	Trim	80	1530	90		-25.6
26	lon doublet		1490	22		
27	lon doublet		1480	41		
28	lat doublet		1470	46		
29	Trim	hover	1370	90		-1.1
30	lon sweep		1300	104		
31	lon sweep		1290	103		
32	lon sweep		1230	108		
33	lat sweep		1190	93		
34	lat sweep		1150	96		
35	lat sweep		1100	107		
36	lon doublet		990	41		
37	lon doublet		950	41		
38	lat doublet		930	37		
39	lat doublet		890	41		
40	Trim	30	850	91		-2.3
41	lon sweep		840	65		
42	lon sweep		800	97		
43	lon sweep		760	98		
44	lon sweep		730	97		
45	lat sweep		690	95		
46	lat sweep		650	98		
47	lat sweep		610	94		
48	lon doublet		2270	51		
49	lon doublet		2250	41		
50	lat doublet		2230	37		
51	lat doublet		2220	23		
52	lat doublet		2200	41		

TABLE C4. CATALOG OF RECORDS BY FLIGHT NUMBER (cont.)

Flight No: 107	Date: 16 Feb 2006
Remarks: Engine can, lon and lat sweeps and maneuvers, 50 to 70 kts, sling set	
PILOT: D. Robinson	
Copilot: R. Watson	
Takeoff Conditions:	
Wind _____ (kts, deg)	SAS on
OAT _____ (deg C)	FPS off
Altimeter _____ (in Hg)	Stabilator fixed by airspeed
A/C TOGW 16080 (lbs)	Load Engine can
XMOMTO 5820.4 e+3 ft lbs	Sling sling set

Record No.	Test Event	Ref IAS (kts)	Start Fuel Weight (lbs)	Duration (sec)	Notes
1	climb	45	2170	89	500 ft/min
2	trim	50	2140	99	
3	lon sweep	50	2100	110	
4	lon sweep	50	2060	110	
5	rt turn	50	2030	55	180° turn/15° bank
6	lon sweep	50	2010	111	
7	lat sweep	50	1980	98	
8	lat sweep	50	1950	86	
9	lat sweep	50	1930	110	
10	lon dblt,aft	50	1900	31	
11	lon dblt,aft	50	1880	50	
12	lat dblt, lft	50	1860	41	
13	lat dblt, rt	50	1850	41	
14	trim	50	1840	68	
15	rt turn	50	1820	46	180° turn/15° bank
16	bad record				
17	accel	50-70	1780	53	.07g
18	rt turn	50	1750	66	180° turn/15° bank
19	rt turn	50	1730	46	180° turn/30° bank
20	rt turn	50	1710	46	180° turn/30° bank
21	left turn	50	1690	52	180° turn/15° bank
22	bad record				
23	left turn	50	1650	42	180° turn/30° bank
24	lon sweep	70	1630	106	

TABLE C4. CATALOG OF RECORDS BY FLIGHT NUMBER (cont.)

Flight no 107 cont.

Record No.	Test Event	Ref IAS (kts)	Start Fuel Weight (lbs)	Duration (sec)	notes
25	rt turn	70	1600	59	180° turn/15 ° bank
26	lon sweep	70	1580	111	
27	rt turn	70	1540	53	180° turn/30 ° bank
28	lon sweep	70	1520	105	
29	lat sweep	70	1500	78	
30	lat sweep	70	1480	98	
31	lat sweep	70	1450	115	
32	lon dblt	70	1410	62	
33	lon dblt	70	1390	34	
34	left turn	70	1390	60	180° turn/15 ° bank
35	lat dblt	70	1370	39	
36	lat dblt	70	1350	50	
37	trim	70	1330	112	
38	left turn	70	1300	49	180° turn/30 ° bank
39	lat dblt	70	1290	58	
40	lat dblt	70	1270	39	
41	decel	70-45	1240	48	0.15g
42	descend	45	1190	89	500 ft/min
43	decel	70-50	1150	40	

TABLE C4. CATALOG OF RECORDS BY FLIGHT NUMBER (cont.)

Flight No: 108**Date:** 12 February, 2007**Remarks:** 2K CONEX, low speeds, sling set**PILOT:** D. Robinson**Copilot:** R. Watson**Takeoff Conditions:****Wind** 7/200 (kts, deg)**OAT** 14.2 (deg C)**Altimeter** 30.03 (in Hg)**A/C TOGW** 16080 (lbs)**XMOMTO** 5820.4 e+3 ft lbs**SAS** on**FPS** off**Stabilator** fixed by airspeed**Load** 2K CONEX**Sling** sling set

Record No.	Test Event	Ref Spd (kts)	Start Fuel Weight (lbs)	Duration (sec)	Spin (deg/sec)	Trail (deg)
1	trim	0 INU	2010	63	-11.0	-2.4
2	trim	10 INU	1920	76	0.4	-1.6
3	trim	20 INU	1840	67	10	-3.0
4	trim	25 INU	1820	70	35	-6.0
5	trim	30 INU	1770	63	55	-1.0
6	trim	35 INU	1740	65	65	-7.7
7	trim	40 kias	1720	64	77	-9.8
8	trim	40 kias	1660	65	70	-8.9

TABLE C4. CATALOG OF RECORDS BY FLIGHT NUMBER (cont.)

Flight No:	109	Date:	13 February, 2007
Remarks:	2K CONEX, trims, 40 to 100 kias, sling set		
PILOT:	D. Robinson		
Copilot:	R. Watson		
Takeoff Conditions:			
Wind	<u>9/350</u> (kts, deg)	SAS	on
OAT	_____ (deg C)	FPS	off
Altimeter	<u>30.05</u> (in Hg)	Stabilator	fixed by airspeed
A/C TOGW	<u>16080</u> (lbs)	Load	2K CONEX
XMOMTO	<u>5820.4 e+3</u> ft lbs	Sling	sling set

Record No.	Test Event	Ref IAS (kts)	Start Fuel Weight (lbs)	Duration (sec)	Spin (deg/sec)	Trail (deg)
1	trim	40	1990	101	-40	-8.1
2	lat sinusoid		1960	32		
3	lon sinusoid		1940	61		
4	trim	50	1910	100	-109	-12.9
5	lat sinusoid		1880	50		
6	lon sinusoid		1860	67		
7	trim	60	1836	95	-76	-17.6
8	lat sinusoid		1810	38		
9	lon sinusoid		1770	61		
10	trim	65	1750	71	-69	-19.8
11	lat sinusoid		1730	54		
12	lon sinusoid		1700	53		
13	trim	70	1680	63	-51	-22.6
14	lat sinusoid		1650	61		
15	lon sinusoid		1630	51		
16	trim	75	1610	62	-62	-26.6
17	lat sinusoid		1570	63		
18	lon sinusoid		1550	44		
19	trim	80	1520	63	-55	-27.5
20	lat sinusoid		1500	39		
21	lon sinusoid		1490	51		
22	trim	85	1450	64	-75	-30.7
23	lat sinusoid		1430	40		
24	lon sinusoid		1400	45		

TABLE C4. CATALOG OF RECORDS BY FLIGHT NUMBER (cont.)

Flight no 109 cont.

Record No.	Test Event	Ref IAS (kts)	Start Fuel Weight (lbs)	Duration (sec)	Spin (deg/sec)	Trail (deg)
25	trim	90	1380	65	-76	-32.6
26	lat sinusoid		1350	38		
27	lon sinusoid		1340	45		
28	trim	95	1310	69	-81	-33.7
29	lat sinusoid		1280	38		
30	lon sinusoid		1240	84		
31	trim	100	1190	64	-75	-38.3

TABLE C4. CATALOG OF RECORDS BY FLIGHT NUMBER (cont.)

Flight No:	110	Date:	15 February, 2007
Remarks:	2K CONEX, <u>no swivel</u> , 40 to 70 kias, sling set		
PILOT:	D. Robinson		
Copilot:	M. Dearing		
Takeoff Conditions:			
Wind	<u>8/350</u> (kts, deg)	SAS	on
OAT	<u>15</u> (deg C)	FPS	off
Altimeter	<u>30.51</u> (in Hg)	Stabilator	fixed by airspeed
A/C TOGW	<u>16080</u> (lbs)	Load	2K CONEX
XMOMTO	<u>5820.4 e+3</u> ft lbs	Sling	sling set, no swivel

Record No.	Test Event	Ref IAS (kts)	Start Fuel Weight (lbs)	Duration (sec)	Spin (deg/sec)	Trail (deg)
1	trim	50	1970	62		-14.6
2	lat sinusoid		1950	76		
3	trim	55	1910	62		-14.5
4	lat sinusoid		1900	49		
5	lat sinusoid		1890	72		-17.9
6	trim	60	1840	62		
7	lat sinusoid		1830	72		
8	trim	65	1800	65		-21.0
9	lat sinusoid		1780	72		
10	Trim	70	1760	66		-24.2
11	trim	40	1680	62		-9.1
12	lat sinusoid		1670	71		
13	load set down	hover	1610	46		

TABLE C4. CATALOG OF RECORDS BY FLIGHT NUMBER (cont.)

Flight No:	116	Date:	11 April 2007
Remarks:	4K CONEX, <u>no swivel</u> , 40 to 105 kias, sling set		
PILOT:	D. Robinson		
Copilot:	R. Watson		
Takeoff Conditions:			
Wind	<u>12/310</u>	(kts, deg)	SAS on
OAT		(deg C)	FPS off
Altimeter	<u>30.05</u>	(in Hg)	Stabilator fixed by airspeed
A/C TOGW	<u>16080</u>	(lbs)	Load 4K CONEX
XMOMTO	<u>5820.4 e+3</u>	ft lbs	Sling sling set, no swivel

Record No.	Test Event	Ref IAS (kts)	Start Fuel Weight (lbs)	Duration (sec)	Spin (deg/sec)	Trail (deg)
1						
2	trim	40	1820	64		-3.1
3	trim	50	1790	79		-5.0
4	trim	60	1760	68		-9.0
5	trim	65	1730	66		-10.0
6	trim	70	1700	68		-11.9
7	trim	75	1680	64		-13.3
8	trim	80	1660	64		-15.1
9	trim	85	1620	63		-16.4
10	trim	90	1580	65		-18.7
11	trim	95	1550	65		-20.7
12	trim	100	1510	63		-23.1
13	trim	105	1460	63		-24.9

TABLE C4. CATALOG OF RECORDS BY FLIGHT NUMBER (cont.)

Flight No:	132	Date:	13 August, 2007
Remarks:	4K CONEX, 40 to 107 kias, sling set		
PILOT:	D. Robinson		
Copilot:	R. Watson		
Takeoff Conditions:			
Wind	<u>calm</u>	(kts, deg)	SAS on
OAT	<u>18</u>	(deg C)	FPS off
Altimeter	<u>30.09</u>	(in Hg)	Stabilator fixed by airspeed
A/C TOGW	<u>16080</u>	(lbs)	Load 4K CONEX
XMOMTO	<u>5820.4 e+3</u>	ft lbs	Sling Sling set

Record No.	Test Event	Ref IAS (kts)	Start Fuel Weight (lbs)	Duration (sec)	Spin (deg/sec)	Trail (deg)
1	trim	40	2220	65	-91	-4.3
2	trim	50	2180	64	-127	-6.4
3	trim	60	2130	63	-160	-10.4
4	trim	70	2100	65	-167	-12.9
5	trim	80	2070	64	-160	-16.3
6	trim	80	2030	63	-153	-16.1
7	trim	85	1980	64	-145	-18.5
8	trim	90	1920	62	-128	-19.6
9	trim	95	1880	62	-97	-22.0
10	trim	98 – 100	1840	170	-90	-23.3
11	trim	105 -107	1750	199	-76	-26.7
12	trim	40	1660	63	-102	-4..6

TABLE C4. CATALOG OF RECORDS BY FLIGHT NUMBER (cont.)

Flight No:	133	Date:	7 November 2007
Remarks:	2K CONEX, trims at 40 to 100 kts, long line + sling set, trims,		
PILOT:	D. Robinson		
Copilot:	R. Watson		
Takeoff Conditions:			
Wind	<u>5/340</u> (kts, deg)	SAS	on
OAT	<u>15</u> (deg C)	FPS	off
Altimeter	<u>30.03</u> (in Hg)	Stabilator	fixed by airspeed
A/C TOGW	<u>16080</u> (lbs)	Load	2K CONEX
XMOMTO	<u>5820.4 e+3</u> ft lbs	Sling	long line + sling set

Record No.	Test Event	Ref IAS (kts)	Start Fuel Weight (lbs)	Duration (sec)	Spin (deg/sec)	Trail (deg)
1	trim	40	2260	95	-103	-11.0
2	trim	50	2260	64	-132	-13.8
3	trim	60	2200	62	-111	-20.2
4	trim	70	2160	62	-67	-25.4
5	trim	80	2130	62	-54	-29.0
6	trim	90	2090	63	-46	-37.5
7	trim	95	2020	63		-39.0
8	trim	100	1970	95		-43.3

TABLE C4. CATALOG OF RECORDS BY FLIGHT NUMBER (cont.)

Flight No:	134	Date:	7 November 2007
Remarks:	4K CONEX, sling set, high speed trims		
PILOT:	D. Robinson		
Copilot:	R. Watson		
Takeoff Conditions:			
Wind	<u>6/340</u> (kts, deg)	SAS	on
OAT	<u>16</u> (deg C)	FPS	off
Altimeter	<u>30.03</u> (in Hg)	Stabilator	fixed by airspeed
A/C TOGW	<u>16080</u> (lbs)	Load	4K CONEX
XMOMTO	<u>5820.4 e+3</u> ft lbs	Sling	sling set

Record No.	Test Event	Ref IAS (kts)	Start Fuel Weight (lbs)	Duration (sec)	Spin (deg/sec)	Trail (deg)
1	trim	90	1570	63	-110	-20..5
2	trim	95	1510	62	-111	-21.6
3	trim	97.5	1430	86	-90	-23.2
4	trim	100	1380	74	-75	-23.4
5	trim	100	1340	108	-58	-24.4
6	turn	80	1290	53	-127	-16.9
7	trim	102	1180	134		-24.5
8	trim	105	1100	104		-25.1
9	trim	80	1050	65	100	-16.1

TABLE C4. CATALOG OF RECORDS BY FLIGHT NUMBER (cont.)

Flight No:	135	Date:	21 January 2008
Remarks:	4K CONEX, <u>offset cg</u> , 20 to 110 kias , sling set.		
PILOT:	D. Robinson		
Copilot:	R. Watson		
Takeoff Conditions:			
Wind	<u>6/120</u> (kts, deg)	SAS	on
OAT	<u>9</u> (deg C)	FPS	off
Altimeter	<u>30.26</u> (in Hg)	Stabilator	fixed by airspeed
A/C TOGW	<u>16080</u> (lbs)	Load	4K CONEX
XMOMTO	<u>5820.4 e+3</u> ft lbs	Sling	sling set

Record No.	Test Event	Ref IAS (kts)	Start Fuel Weight (lbs)	Duration (sec)	Spin (deg/sec)	Trail (deg)
1	trim	20	2190	122		-2.8
2	trim	30	2140	127		-2.5
3	trim	40	2080	75		-5.7
4	trim	50	2050	62		-7.4
5	trim	60	2030	62		-9.9
6	trim	70	2000	66		-11.5
7	lat doublet	70	1960	63		-11.9
8	lat doublet	70	1950	62		-12.5
9	trim	80	1930	67		-14.7
10	lat doublet	80	1890	67		-14.7

APPENDIX D. EQUATIONS FOR CABLE ANGLES AND LOAD AERODYNAMICS AND AN ANALYSIS OF ERRORS

This appendix lists the equations used in the data-processing code for this work to derive the cable angles and load aerodynamics from the flight data. In addition, the errors inherent in the derived aerodynamic forces are estimated.

Notation

The notation used throughout this appendix follows the notation given in reference 33 for multi-body slung load systems. Three-dimensional vector mechanics is used throughout. Boldface symbols indicate physical vectors given independent of any reference frame (\mathbf{R} , \mathbf{V} , ...), and vectors given by their coordinates in a frame are in lightface with a subscript to indicate the axes (R_N , V_N , V_1 , V_2 , ...). The subscript can be any of {N, h, 1, 2, w} for inertial, level heading, helicopter body axes, load body axes, and load wind axes, respectively. The inertial axes are the commonly used local vertical axes (North, East, Down axes; Newton's law applies locally). Level heading axes are local vertical axes aligned with the direction of flight. The bodies in the two-body system are enumerated 1, 2 for the helicopter and load, respectively, with corresponding body axes subscripts 1, 2. Also the body number is appended to the natural vectors to indicate the body (e.g., $\mathbf{V1}$, $\mathbf{V2}$, $\omega\mathbf{1}$, $\omega\mathbf{2}$, etc). Units are ft, lb, sec, and rad throughout.

a2s, aegi	inertial acceleration at the load cg and EGI
amg2s, amgegi	accelerometer readings ($\mathbf{a} - \mathbf{g}$) at the cg and EGI
D, Y, L	wind-axes forces: drag, side force, lift
$E_1(\cdot)$, $E_2(\cdot)$, $E_3(\cdot)$	single axis rotation matrices about the x, y, z axes, respectively (ref. 33)
FA2	load aerodynamic force
fax, fay, faz	x, y, z components of $\mathbf{FA2}$
FC	hook force vector
gc	geometric center
g, g	gravity vector and magnitude, 32.17 ft/sec ²
ia, ja, ka	unit axes vectors for frame a, where a is any of {N,h,1,2,w}
I	3- x 3-unit matrix
J2	load inertia about the cg
kc	hook-to-load-cg unit direction vector; positive down
kcj , j = 1,2,3,4	sling-leg unit direction vectors; positive down
ksp	spin axis (direction of FC)
ℓ_{cj}	sling-leg length; j = 1, 2, 3, 4
MA2^{cg} , MA2^{gc}	load aerodynamic moment about the cg or the geometric center
MC	resistance moment at the hook
MCz	resistance at the hook about the spin axis (about ksp)
p, q, r	body-axes components of rigid-body angular velocity
rab	line segment from point a to point b in the configuration
raj , j = 1,2,3,4	sling-leg line segments from hook to lift point j
ra2p	hook-to-load-cg line segment

r2p2s	load-gc-to-load-cg line segment
r2pegi, r2segi	line segments from the load gc and cg to the EGI location
$T_{a,b}$	transformation from vectors in frame b to vectors in frame a
$S(x,y,z)$	skew symmetric matrix in the vector $[x,y,z]^T$ (ref 33)
$u2, v2, w2$	load-body axes velocity components
V_a	airspeed of the load
V2s, Vegi	load inertial velocity at the cg and EGI
$W2$	load weight
W	mean wind vector
α	angle of attack
β	sideslip angle
$\delta(.)$	variation of (.)
$\phi1, \theta1, \psi1$	helicopter Euler attitude angles
$\phi2, \theta2, \psi2$	load Euler attitude angles
ϕ_c, θ_c	cable angles relative to level heading axes
$\Delta\phi_c, \Delta\theta_c$	cable angles relative to helicopter body axes
$\tau_j, j = 1,..,4$	cable tensions, sling legs 1, 2, 3, 4
$\omega2$	load inertial angular velocity
ψ_v	velocity vector heading angle
Ω_{sp}	angular rate around the spin axis, ksp

Cable Angles

Cable angles for the multi-cable sling are the direction angles of the hook-to-load-cg line segment. This direction aligns with gravity in windless hover and with the apparent load (the vector sum of forces due to weight, aerodynamics, and acceleration supported by the hook) in forward flight. The direction angles can be measured in level heading axes (termed cable angles) or in helicopter body axes (termed relative cable angles). Level heading axes are local vertical axes aligned with the direction of flight. These angles are illustrated in figure D1(a) and (b). The order of rotation from the reference frame to the cable direction is pitch first about the reference frame lateral axis and then roll.

The equations to compute cable angles from the flight data are given in figure D2. The sketch in figure D1(c) shows the load-sling geometry and identifies the hook attachment point a, the load geometric center at point 2' (or 2p), and the cg at point 2* (or 2s). The hook-to-load-cg line segment is a fixed direction in load-body axes, $ra2s_2$, and is known from the a priori measurement of the sling geometry, $ra2p_2$, and the cg coordinates of the load, $r2p2s_2$ (eq. 1 in fig. D2). The corresponding unit direction vector is kc_2 (eq. 2). The flight data provide the helicopter and load Euler angles, $\phi_1, \theta_1, \psi_1, \phi_2, \theta_2, \psi_2$, and the flight direction heading, ψ_v . In that case, the direction vector, kc_2 , can be transformed to inertial axes, kc_N , and then to level heading axes, kc_h (eqs. 3 and 4). This direction vector can be expressed in terms of the cable angles, ϕ_c, θ_c , and these expressions can be solved for the cable angles in terms of the components of the direction vector (eq. 4). The solution assumes the

cable-angle magnitudes are less than 90 deg. The relative cable angles, $\Delta\phi_c$, $\Delta\theta_c$, are obtained by transforming kc_2 to helicopter body axes, kc_1 , and a similar solution for these angles can be given (eq. 5).

Load Aerodynamics from Flight Data

Forces, moments, and body axes components. The aerodynamics are extracted from the flight data using the Newton–Euler force and moment balance equations for the load-sling subsystem. This subsystem and the applied forces and moments on it are illustrated in figure D3. They are weight, load aerodynamic force and moment about the cg, hook force, and rotational resistance at the hook due to swivel friction. The present work on load aerodynamics is limited to flight data with the swiveled sling since that simplifies the motion context in which to understand the aerodynamics as those of a steadily spinning body. It also avoids accounting for the variable-sling geometry due to sling windup and periodic yaw rate that occurs without a swivel.

Figure D4 gives the equations used to extract the load aerodynamics from the flight data. It first lists all the required inputs given by (1) a priori measurements of parameters and (2) the flight data signals. The parameters include the load weight and inertia, the hook-to-gc line-segment coordinates, the EGI and cg coordinates relative to the load geometric center, the sling-leg unit direction vectors, $\{kc_{j2}, j = 1 \text{ to } 4\}$, and the swivel torsional friction couple, MC_z . The sling-leg direction vectors are computed a priori from the geometry of the loaded sling. Sling-leg lengths vary during flight, but these variations are under 0.1 ft, they have negligible effect on the direction vectors, and they are neglected in the data processing. The swivel friction is modeled even though it is only a few ft-lb because it accounts for the mean spin rate of the swiveled sling. The required dynamic signals are the body axes components of acceleration at the EGI, a_{egi2} , load angular velocity, ω_{22} , and the sling leg tensions, $\{\tau_j, j = 1, \dots, 4\}$. The desired outputs are the load aerodynamic force and the aerodynamic moment about the geometric center.

The Newton–Euler equations of the load-sling subsystem have been arranged in figure D4, equations 1 and 2, with the aerodynamics on the left and the remaining terms to be evaluated from the flight data and a priori measurements on the right. The Euler equation gives moments about the cg, and they are translated to moments about the gc (eq. 3), which is the commonly used reference point in wind tunnel reports of cargo-container aerodynamics. The right-hand-side variables in equations 1–3 are calculated from the given data as follows: EGI accelerations, a_{egi} , are translated to cg accelerations, a_{2s} , in equation 4, where the cg-to-EGI line-segment coordinates are fixed by the given geometry (eq. 5). The hook-force vector, FC_2 , is reconstructed from the sling-leg tensions measured by load cells installed at the lift points $\{\tau_j\}$, and the sling-leg direction vectors, $\{kc_{j2}, j = 1, 2, 3, 4\}$ in equation 6. The hook moment, MC_2 , is given by swivel friction torsional resistance, MC_z , about the spin axis, k_{sp2} , and signed by the spin angular rate, Ω_{sp} (eqs. 7–10 in fig. D4). The swivel necessarily aligns with the hook force vector, FC , which is therefore the axis of spin.

The angular acceleration required in equations 2 and 4 in figure D4 is measured by the EGI. However, a reliable post-flight method to extract the low-frequency content of the angular acceleration is to filter the angular velocity records with the backward/forward 2nd order Butterworth filter described in reference 32, which gives the derivative as an output. A cutoff frequency of 2.5 Hz was

used for the filtering. This method can be used in the absence of reliable angular-acceleration measurements.

Angle of attack and sideslip angle. The load aerodynamic angles, α , β , are the direction angles of the load air-velocity vector relative to body axes, and they are required in order to compute the wind-axes components of the load aerodynamics. The inertial velocity at the load cg is computed from the inertial velocity measured at the EGI and accounting for the EGI-cg offset (fig. D4, eq. 11). This velocity is corrected with the mean wind vector, W_N , to get the air-velocity vector at the load cg, and transformed to load body axes to get the velocity components, u_2 , v_2 , w_2 (eq. 12), and then the aerodynamic angles can be computed (eqs. 13 and 14). In the present work, sideslip is taken in the range $[-180, 180]$ deg and angle of attack is restricted within ± 90 deg. In the data processing, the wind vector was obtained from the helicopter boom air data (pressure head, temperature, and α , β vanes) and INU inertial velocity. Some data processing is needed to get true airspeed from the air data and to account for the separation between boom and INU (equations omitted).

Forces and moments, wind axes components. Wind axes are defined with its x-axis along the air-velocity vector pointing forward and its z-axis is perpendicular to this axis in the load body axes x-z plane. The body-axes force and moment components are transformed to wind axes as shown in figure D4, equations 15 and 16. The sign changes necessary to get drag and lift are noted in equation 15. The transformation from body to wind axes is given from α , β as rotations about \mathbf{j}_2 and \mathbf{k}_w , respectively.

Summary remarks. The equations developed here to extract the aerodynamics are applicable to any load suspended from any helicopter by a swiveled sling set from a single point, and they are valid for any dynamic load motion. The equation set assumes that the sling is sufficiently stiff in stretch that variations in sling geometry due to cable stretch under all dynamic conditions are negligible. Otherwise, their successful application depends on accurate a priori measurements of load geometric and inertial parameters and on accurate flight-time measurements of the load dynamics, sling leg tensions, and the wind vector.

In the absence of a swivel it would be necessary to account for the changing sling geometry due to sling windup and for torsional resistance to windup at the hook (fig. A4). If a long line were used, the line would be subject to catenary effects, but the equations still apply to the sling set and load subsystem at the end of the long line. The general approach can be applied to two-point suspensions, but a different treatment of the sling geometry is required due to the varying sling geometry in load body axes.

Error Analysis, Aerodynamic Force

It is of interest to determine the accuracy of the derived aerodynamics and whether or not the numerous error sources in the data processing will result in numbers that are mostly error. This section considers the body-axes components of force. Errors in the moments and aerodynamic angles are not analyzed. The EGI measurement errors were discussed in appendix B, and the results obtained in this section indicate these measurements are sufficiently accurate that there is little error in the derived aerodynamic force due to these sources. The errors in the parameter values measured a

priori—particularly weight, cg location, and sling-leg geometry—are less well-known, but working estimates for these errors indicate moderate corresponding force errors. There is, in fact, other evidence that the derived aerodynamics were sufficiently accurate to measure the difference between the static aerodynamics and the aerodynamics of the spinning CONEX.

The following text describes each error source, including the sensitivity of force to the error, and evaluates the sensitivities on a typical flight record (flight 89, record 9: 4000-lb CONEX, 60 kias, -151-deg/sec spin, -9.6-deg trail angle). A summary of the gradients is given at the end.

The equation for body-axes aerodynamic force is repeated in figure D5, eqs. 1–4, and given in terms of the independent a priori and flight-time measurements. The vector **amg** refers to the accelerometer measurements (acceleration minus gravity) and (**raj**, $j = 1,2,3,4$) are the sling-leg line segments. There are 16 scalar parameters ($W2$, $r2segi_2$, (raj_2 , $j = 1,2,3,4$)) and 13 scalar measurements ($amgegi_2$, $\omega 2_2$, $d\omega 2_2/dt$, (τ_j , $j = 1,2,3,4$)).

The aerodynamic force variation is given in terms of variations of the independent measurement quantities in eqs. 5–8, and then the force gradients with respect to the independently measured quantities can be listed (eqs. 9–15).

Weight-error effects. Weight was measured with a load cell with 20-lb resolution. Unknown load cell calibration errors and small load weight changes between weighings add to the uncertainty of the estimated weight in the present work. The gradient is the cg accelerometer reading in g's. The result is predominantly and pound-for-pound a bias error in *faz* with secondary periodic errors in *fax*, *fay* determined by trail angle and spin. Figure D6(a) shows a plot of this gradient for the 60-kias sample record.

EGI accelerometer-error effects. Accelerometer errors are 0.03125 ft/sec^2 truncation with noise variations to 0.25 ft/sec^2 (appendix B, table B1). The noise is filtered out in post-flight data processing, and the truncation error is scaled by mass (fig. D5, eq. 10) to give 4 lb of random force error in all three force components for the 4000-lb CONEX. An estimate of accelerometer biases based on an analysis of kinematic consistency in the data using the SMACK software (ref. 32) indicated accelerometer biases well below the truncation error.

EGI position-error effects. The EGI accelerometer position relative to the cg, $r2segi_2$, is composed of independent measurements of the EGI and load cg locations relative to a reference point in the CONEX (fig. D5, eq. 7). EGI accelerometer signals are referenced to the geometric center of the EGI box, which can be located in the CONEX to a small fraction of an inch. The load cg location was computed from lumped mass analysis of the empty CONEX, the ballast, the instrumentation pallets, and the objects mounted on the pallets. Each component was weighed and its cg located in the CONEX, and the results were combined to estimate the load cg location. In these calculations, the cg location of each component was assigned to the geometric center of the component, equivalent to assuming uniform or symmetric mass distribution. The ballast was composed of 100-lb sandbags arranged on pallets in what was collectively very close to a solid box with uniform mass distribution. The combined errors are due to multiple weight-, location-, and mass-distribution errors and are unknown. A deeper analysis of these errors is omitted here in favor of a working guess of 1 or 2 inches of error.

EGI position errors create a coriolis acceleration error dependent on angular velocity and angular acceleration, and scaled by load mass (fig. D5, eq. 11). The angular velocity term dominates, and it in turn is dominated by the nearly fixed spin rate of the CONEX suspended with a swiveled sling. This gradient is plotted in figure D6(b) for the sample flight record. The result shows that the dominant effects are nearly identical sensitivities in f_{ax} due to x position error and f_{ay} due to y position error at the rate of 6 to 8 lb per inch of error. These errors are proportional to and change with the spin rate, r . Thus, this error source results in approximately fixed errors in f_{ax} , f_{ay} of size 15 lb for the sample case with 151-deg/sec spin rate.

Angular velocity errors. EGI angular rate errors are 0.022 deg/sec truncation with noise variations to 0.044 deg/sec (appendix B, table B1). The noise variations are filtered out post-flight, and an analysis of kinematic consistency indicated rate gyro biases well below the truncation error.

The gradient (fig. D5, eq. 12) is proportional to products of angular rates and $r2segi_2$ coordinates and is scaled by mass. The line segment, $r2segi_2$, is dominated by its z -coordinate. A plot of the gradients in figure D6c for the sample flight record shows maximum sensitivities at 8 to 10 lb per deg/sec error in f_{ax} due to errors in p and in f_{ay} due to errors in q . Force errors due to angular rate truncation errors are less than 1 lb.

Angular acceleration errors. EGI angular-acceleration errors are 0.044-deg/sec² truncation error with noise variations to 1.4 deg/sec². The gradient (eq. 13) is fixed by mass and EGI location (fig. D5, eq. 13), with maximum sensitivities of 3 lb per deg/sec² error. Force errors due to the truncation errors in this signal are under 1 lb.

Sling-geometry errors. Sling-geometry errors are errors in determining the body-axes coordinates of the sling leg line segments, $\{raj_2, j = 1,2,3,4\}$. These vectors were determined from the lift-point geometry and the sling-apex location. Accuracy of the x , y coordinates depends on surveying the lift-point geometry, which can be done to a fraction of an inch distributed among the 4 sling legs. Accuracy of the z -coordinate depends on locating the sling apex. This was done analytically based on the unloaded sling leg length, the load weight, the stretching constant, and the lift point geometry. There are additional uncertainties in modeling the apex as a single point (see the apex assembly in fig. 4(a)) and from neglecting small variations in sling stretch, under 0.1 ft, which occur during the flight. However, the gradient indicates that the derived force is insensitive to errors in the z -coordinate.

The gradient (fig. D5, eq. 14) is similar for all sling legs. The gradients depend on fixed sling geometry elements, kc_j , lc_j , and the cable tension, τ_j . Cable tension varies periodically around a mean value as the load rotates, and its magnitude depends on load weight. A plot of these gradients for one sling leg for the sample 4000-lb CONEX record is shown in figure D6(d). The largest gradients are 6 lb of x and y force error per inch of error in the sling leg x - and y -coordinates, respectively. Force errors are much less sensitive to z -coordinate errors because of the insensitivity of the sling leg direction to this coordinate. The collective effect of sling leg geometry errors is of size 10 lb in f_{ax} , f_{ay} .

Cable tension errors. Cable tensions are measured by load cells with analog signals whose variations are equivalent to 20 lb of noise amplitude around a mean value. The cells were calibrated from long-term averages with residual calibration errors under 1.5 lb due to nonlinearities. The recorded flight data were obtained by averaging 256 samples in the interval between 65-Hz outputs; this reduces noise to within 1.5-lb amplitude. Thus cable-tension measurement errors are under 3 lb each leg.

The force gradient is the fixed sling leg unit direction vector (fig. D5, eq. 15). This direction is within 10 deg of the z-axis, so the effect of cable tension errors is lb-for-lb an error in f_{az} with secondary effects on f_{ax} , f_{ay} .

Summary of errors for body-axes forces. The quantitative results discussed here are summarized in table D1. Results for the gradient magnitudes apply to the 60-kt, 4000-lb CONEX sample record. The magnitude ranges of the force components for this record are noted for comparison with error sizes. The largest error effects in f_{az} are in excess of 20 lb because of weight-measurement error and up to 12 lb net error because of sling-leg-tension errors. The largest error effects in f_{ax} , f_{ay} are up to 15 lb because of cg location errors in the EGI coordinates, and up to 10 lb net error because of sling-geometry errors. Except for cable tension errors, all of these principal measurement errors are fixed and their contributions to body axes force errors are approximately fixed. Smaller, random errors result from accelerometer and rate gyro-truncation errors.

TABLE D1. SUMMARY OF AERODYNAMIC-FORCE ERROR SOURCES AND SENSITIVITIES:
4000-LB CONEX; 60 KIAS; -151-DEG/SEC SPIN RATE; -9.6-DEG TRAIL ANGLE

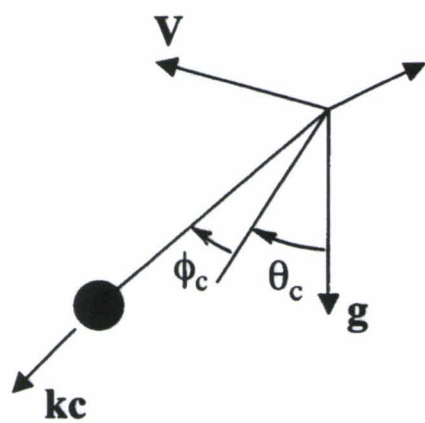
Component	f_{ax}	f_{ay}	f_{az}	Units	Error Source	Dominant Force
Flight Range	± 1000	± 700	-100 to 600	lb	Description	Error
Error source						
W2	± 0.2	± 0.2	1.0	lb per lb	fixed error, > 20 lbs	f_{az} > 20 lbs
amgegi ₂ x	138	0	0	lb per ft/s ²	truncation 0.03 fps ²	f_{ax}, f_{ay}, f_{az} 5 lbs
y	0	138	0			
z	0	0	138			
r2segi ₂ x	7	0	0	lb per inch	fixed error, 1-2 in	f_{ax}, f_{ay} < 15 lbs
y	0	7	0			
z	0	0	0			
ω_{2_2} p	-8	0	0	lb per deg/s	truncation, 0.022 deg/s	f_{ax}, f_{ay} < 1 lb
q	0	-8	-4			
r	0	2	0			
$d\omega_{2_2}/dt$ dp	0	3.1	0.7	lb per deg/s ²	truncation, 0.044 deg/s ²	f_{ax}, f_{ay} < 1 lb
dq	-3.1	0	0			
dr	-0.7	0	0			
ral ₂ x	6.0	0.3	-1.1	lb per inch	x < 0.5 in total y < 0.5 in total z 1-2 in	f_{ax}, f_{ay} < 10 lbs
y	0.3	7.4	1.6			
z	-1.1	1.6	0.7			
τ_j	0.2	0.3	1.0	lb per lb	fixed + noise, < 3 lbs per leg	f_{az} < 12 lbs net

Wind-axes force errors. The transformation of the aerodynamic force from body to wind axes is given in figure D4 and repeated in figure D5 as equation 16, and its variation is given in equation 17 in terms of errors in the aerodynamic angles and the combined body axes force error. The expression for the transformation gradient follows after showing that the gradient of $E_3(\beta)$ is $S(\mathbf{k}_w)$ and the gradient of $E_2(\alpha)$ is $S(\mathbf{j}_2)$, where \mathbf{k}_w , \mathbf{j}_2 are the axes of rotation of the angles β , α , respectively. The gradients are the coefficients of the variations in (α, β) and the variations in the combined body axes force, $FA2_2$, in figure D5, equation 17.

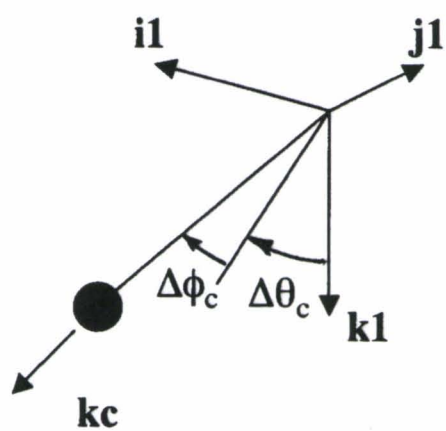
In the gradient with (α, β) , $\mathbf{FA2}$ is dominated by drag so that the cross product, $\mathbf{FA2} \otimes \mathbf{j}_2$, is predominantly in the direction of lift and varies from positive to negative as the \mathbf{j}_2 axis rotates, and $\mathbf{FA2} \otimes \mathbf{k}_w$ is predominantly in the direction of side force and fixed. These properties can be seen in the sample case plots in figure D7(a) and (b). The gradients are given for force divided by dynamic pressure since this normalization gives results that are independent of airspeed. The principal effects are under 1 ft^2 per deg of error, and they occur in lift due to α error and side force due to β error. These effects are small compared to the maximum values of Y/q previously seen in figure 35, so that the wind axes force components are relatively insensitive to errors in estimating α , β . Trail angle has an airspeed-related effect on the secondary gradients, but these effects are small and the sample case results in figure D7(a) and (b) are typical of all flight test airspeeds.

Sensitivity to the combined body axes force errors is given by the transformation to wind axes. Results for the sample case $\alpha(t)$, $\beta(t)$ histories are shown in figures D7(c) to (e). Taken together, errors in f_{ax} , f_{ay} are mostly distributed to drag and side-force errors with little effect on lift, and the distribution is, at most, 1 lb per lb of error. The errors in lift come from f_{az} errors, with no effect from f_{ay} errors and secondary effect from f_{ax} errors.

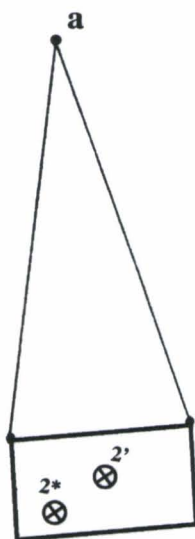
Moment errors. An analysis of moment errors is omitted. The x and y components act only on the load, and with little effect. Only the z-moment, which accounts for the directional degree of freedom of the load, is important. There is evidence in the text that this moment has been accurately derived from the flight data. For records with low spin rate, the derived aerodynamics are close to the corresponding static aerodynamics (e.g., the fig. 37 record at 95 kias and figs. 42 and 43), and for other records with large spin rate the flight aerodynamics have been modeled and used in a simulation with the result that the motion obtained in the simulation agreed in detail with the directional motions of the load (refs. 6 and 12).



(a) Cable angles.



(b) Relative cable angles.



(c) Load-sling geometry.

Figure D1. Cable angles and load-sling geometry.

Given: $ra2p_2, r2p2s_2, \phi_2, \theta_2, \psi_2, \phi_1, \theta_1, \psi_1, \psi_V$

Find: $\phi_c, \theta_c, \Delta\phi_c, \Delta\theta_c$

$$ra2s_2 = ra2p_2 + r2p2s_2 \quad (1)$$

$$kc_2 = \frac{ra2s_2}{|ra2s_2|} \quad (2)$$

$$kc_N = T_{N,2}(\phi_2, \theta_2, \psi_2) kc_2 \quad (3)$$

$$\begin{aligned} kc_h &= E_3(\psi_V) kc_N = (\cos\phi_C \sin\theta_C, -\sin\phi_C, \cos\phi_C \cos\theta_C)^T \\ \phi_C &= -\sin^{-1}(kc_h(2)) \\ \theta_C &= \tan^{-1}\left(\frac{kc_h(1)}{kc_h(3)}\right) \end{aligned} \quad (4)$$

$$\begin{aligned} kc_1 &= T_{1,N}(\phi_2, \theta_2, \psi_2) kc_N = (\cos\Delta\phi_C \sin\Delta\theta_C, -\sin\Delta\phi_C, \cos\Delta\phi_C \cos\Delta\theta_C)^T \\ \Delta\phi_C &= -\sin^{-1}(kc_1(2)) \\ \Delta\theta_C &= \tan^{-1}\left(\frac{kc_1(1)}{kc_1(3)}\right) \end{aligned} \quad (5)$$

where

$$T_{2,N} = E_1(\phi_2) E_2(\theta_2) E_3(\psi_2)$$

$$T_{N,2} = T_{2,N}^T$$

$$T_{1,N} = E_1(\phi_1) E_2(\theta_1) E_3(\psi_1)$$

Figure D2. Equations for the computation of cable angles.

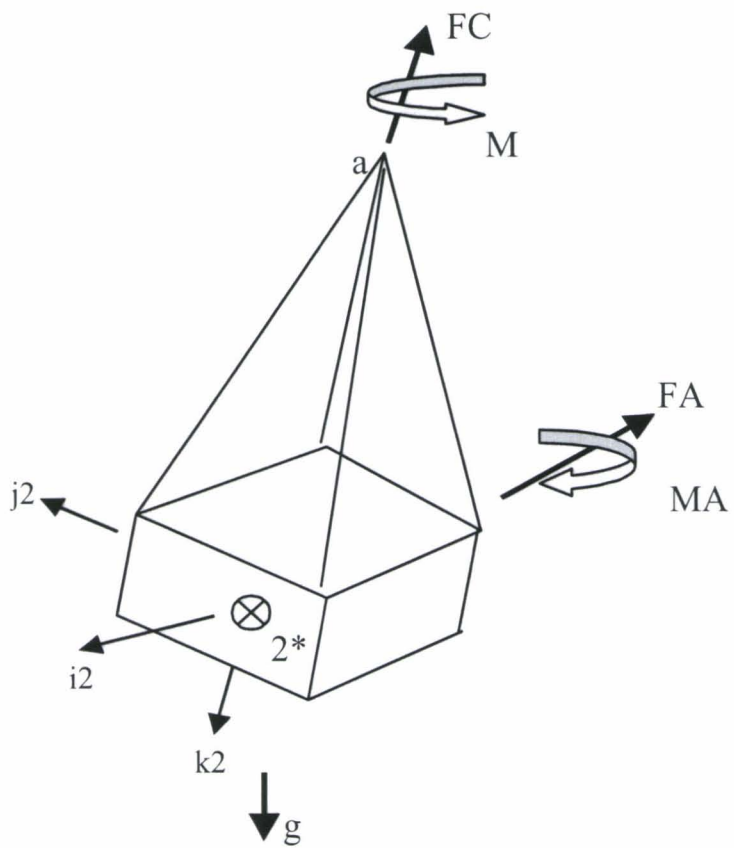


Figure D3. Load-sling subsystem forces and moments.

Load Aerodynamics, Body Axes Components

Given: $W_2, J_2, r_{2p2}, r_{2p2s_2}, r_{2pegi_2}, MC_z, \{kcj_2, j = 1, 2, 3, 4\}$

and; $a_{egi_2}, \omega_{2_2}, \overset{o}{\omega}_{2_2} \{\tau_j, j = 1, 2, 3, 4\}$

Find: $FA_{2_2}, MA_{2_2}^{gc}$

$$FA_{2_2} = m_2 (a_{2s_2} - g_2) - FC_2 \quad (1)$$

$$MA_{2_2}^{cg} = J_2 \overset{o}{\omega}_{2_2} + S(\omega_{2_2}) J_2 \omega_{2_2} + S(r_{2p2s_2}) FC_2 - MC_2 \quad (2)$$

$$MA_{2_2}^{gc} = MA_{2_2}^{cg} + S(r_{2p2s_2}) FA_{2_2} \quad (3)$$

where

$$a_{2s_2} = a_{egi_2} - \left[S(\omega_{2_2}) S(\omega_{2_2}) + S(\overset{o}{\omega}_{2_2}) \right] r_{2segi_2} \quad (4)$$

$$r_{2segi_2} = r_{2pegi_2} - r_{2p2s_2} \quad (5)$$

$$FC_2 = \sum_{j=1}^4 kcj_2 \tau_j \quad (6)$$

$$MC_2 = MC_z ksp_2 \quad (7)$$

$$ksp_2 = FC_2 / |FC_2| \quad (8)$$

where

$$MC_z = -(0.607 + 0.00096 W_2) \text{sign}(\Omega_{sp}) \quad (9)$$

$$\Omega_{sp} = \omega_{2_2}^T ksp_2 \quad (10)$$

Aerodynamic Angles

Given: $\phi_2, \theta_2, \psi_2, \omega_{2_2}, V_{egi_N}, W_N, r_{2pegi_2}, r_{2p2s_2}$

Find: α, β

$$V_{2s_N} = V_{egi_N} - T_{N,2} S(\omega_{2_2}) r_{2segi_2} \quad (11)$$

$$\begin{pmatrix} u_2 \\ v_2 \\ w_2 \end{pmatrix} = T_{2,N}(\phi_2, \theta_2, \psi_2) (V_{2s_N} - W_N) \quad (12)$$

$$\alpha = \tan^{-1} \left(\frac{w_2}{u_2} \right) \in [-90, 90] \text{ deg} \quad (13)$$

$$\sin \beta = \left(\frac{v_2}{V_a} \right), \cos \beta = \frac{u_2}{V_a \cos \alpha}, \beta \in [-180, 180] \text{ deg} \quad (14)$$

where:

$$T_{2,N} = E_1(\phi_2) * E_2(\theta_2) * E_3(\psi_2)$$

$$T_{N,2} = T_{2,N}^T$$

Figure D4. Equations for computation of load aerodynamics.

Load Aerodynamics, Wind Axes Components

$$FA_w = T_{w,2} * FA_2 = (-\text{Drag, Side force, - Lift})^T \quad (15)$$

$$MA2_w^{gc} = T_{w,2} * MA2_w^{gc} = (\text{Roll, Pitch, Yaw})^T \quad (16)$$

where:

$$T_{w,2} = E_3(\beta) * E_2(-\alpha)$$

Figure D4. Equations for computation of load aerodynamics (continued).

Nonlinear Force Equation

$$FA2_2 = \frac{W2}{g} \text{amg}2s_2 - FC_2 \quad (1)$$

$$\text{amg}2s_2 = \text{amgegi}_2 - \left[S(\omega 2_2) S(\omega 2_2) + S(\overset{\circ}{\omega 2_2}) \right] r2segi_2 \quad (2)$$

$$r2segi_2 = r2pegi_2 - r2p2s_2 \quad (3)$$

$$FC_2 = \sum_{j=1}^4 kc_{j2} \tau_j = \sum_{j=1}^4 \frac{raj_2}{\ell c_j} \tau_j \quad (4)$$

Variations

$$\delta FA2_2 = \text{amg}2s_2 \delta m2 + m2 \delta \text{amg}2s_2 - \delta FC_2 \quad (5)$$

$$\delta \text{amg}2s_2 = \delta \text{amgegi}_2 - \left[S(\omega 2_2) S(\omega 2_2) + S(\overset{\circ}{\omega 2_2}) \right] \delta r2segi_2 + \quad (6)$$

$$\left[S(\omega 2_2) S(r2segi_2) + S(S(\omega 2_2) r2segi_2) \right] \delta \omega 2_2 + S(r2segi_2) \delta \overset{\circ}{\omega 2_2}$$

$$\delta r2segi_2 = \delta r2pegi_2 - \delta r2p2s_2 \quad (7)$$

$$\delta FC_2 = \sum_{j=1}^4 \left(\left[I - kc_{j2} kc_{j2}^T \right] \frac{\tau_j}{\ell c_j} \delta raj_2 + kc_{j2} \delta \tau_j \right) \quad (8)$$

Sensitivities

$$\frac{\partial FA2_2}{\partial W2} = \frac{\text{amg}2s_2}{g} \quad (9)$$

$$\frac{\partial FA2_2}{\partial \text{amgegi}_2} = m2 I \quad (10)$$

$$\frac{\partial FA2_2}{\partial r2segi_2} = -m2 \left[S(\omega 2_2) S(\omega 2_2) + S(\overset{\circ}{\omega 2_2}) \right] \quad (11)$$

$$\frac{\partial FA2_2}{\partial \omega 2_2} = -m2 \left[S(\omega 2_2) S(r2segi_2) + S(S(\omega 2_2) r2segi_2) \right] \quad (12)$$

$$\frac{\partial FA2_2}{\partial \overset{\circ}{\omega 2_2}} = -m2 S(r2segi_2) \quad (13)$$

$$\frac{\partial FA2_2}{\partial raj_2} = \left[I - kc_{j2} kc_{j2}^T \right] \frac{\tau_j}{\ell c_j}, j = 1, 2, 3, 4 \quad (14)$$

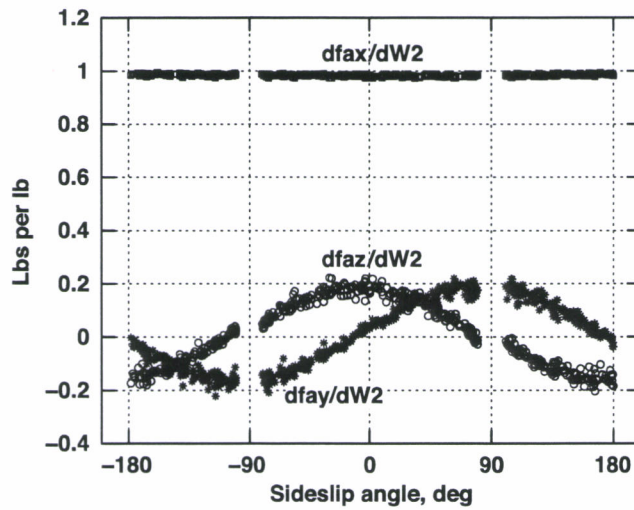
$$\frac{\partial FA2_2}{\partial \tau_j} = kc_{j2}, j = 1, 2, 3, 4 \quad (15)$$

Wind Axes Force Components and Variations

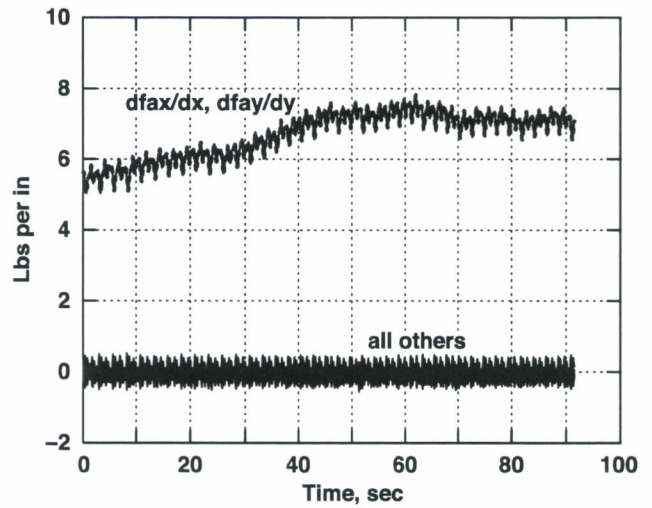
$$FA_w = T_{w,2} * FA2_2 = (-D, Y, -L)^T \quad (16)$$

$$\delta FA2_w = -T_{w,2} S(FA2_2) \begin{bmatrix} j2_2 & kw_2 \end{bmatrix} \begin{pmatrix} \delta \alpha \\ \delta \beta \end{pmatrix} + T_{w,2} \delta FA2_2 \quad (17)$$

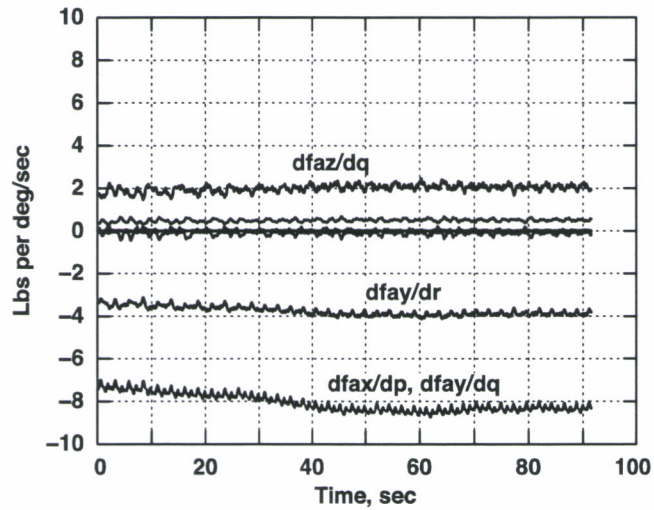
Figure D5. Error sensitivities, body-axes forces.



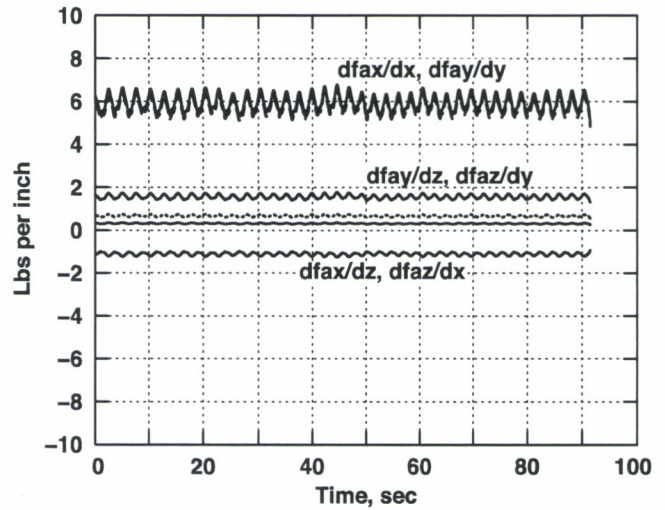
a) Gradients with weight, W_2



b) Gradients with EGI position, r_{2seg12}

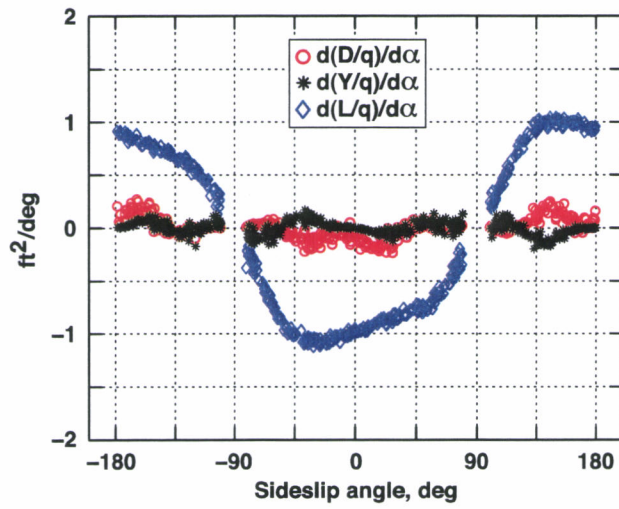


c) Gradients with angular velocity

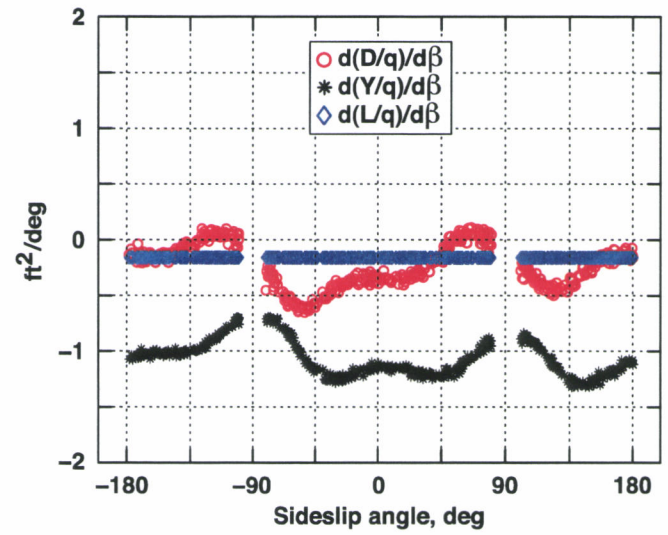


d) Gradients with sling-leg geometry, ra_{12}

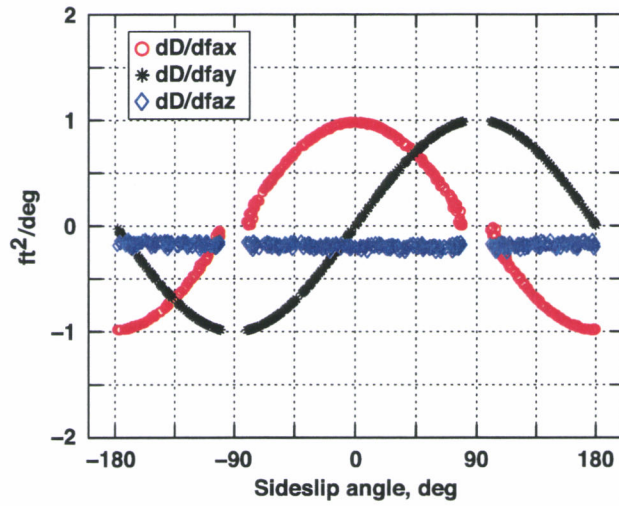
Figure D6. Aerodynamic-force sensitivities to measurement errors: 4000-lb CONEX; 60 kts; swiveled sling.



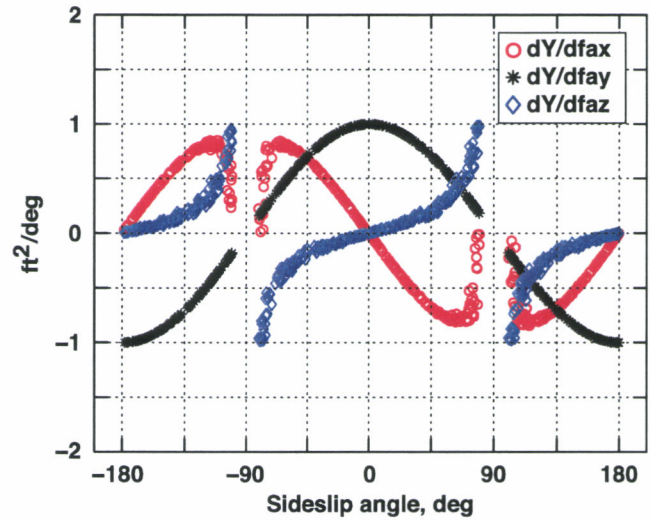
a) Gradients with angle of attack



b) Gradients with sideslip angle

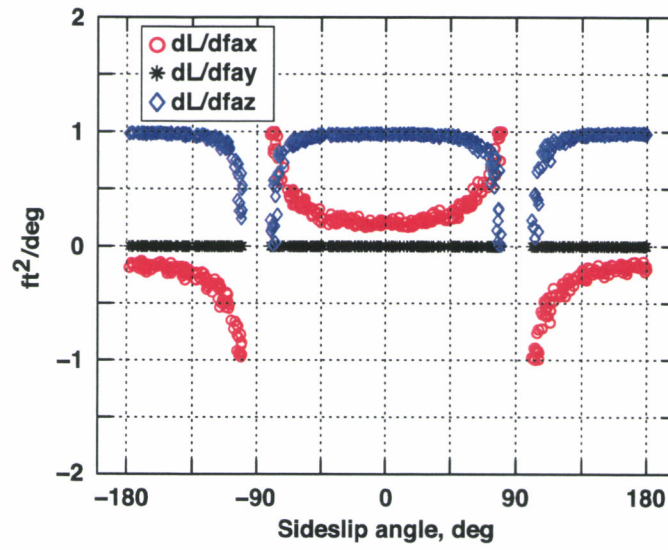


c) Wind axes force gradients with respect to body-axes forces: drag



d) Wind axes force gradients with respect to body axes forces: side force

Figure D7. Error sensitivities, wind-axes forces.



e) Wind axes force gradients with respect to body axes forces: lift

Figure D7. Error sensitivities, wind-axes forces (continued).

APPENDIX E. CONEX STATIC AERODYNAMICS

This appendix provides tables of wind tunnel data for the CONEX static aerodynamics every 5 deg in α over $[-90, 90]$ and β over $[0, 180]$. Broadside and small side into the wind correspond to $\beta = \pm (n \times 180)$ and $90 \pm (n \times 180)$, respectively. Originally published in reference 24, these data are available as electronic files from the Aerospace Faculty, Technion Israel Institute of Technology (IIT), Haifa, Israel. The data are repeated here for completeness.

The data were obtained at Technion IIT in a 1- x 1-m open tunnel with a 1/17 scale model that included skids and corrugations, and with the tunnel running at 20 m/sec (ref. 24). Generally the aerodynamics of bluff bodies are nearly invariant with Reynolds number and Mach number from tunnel model scale to full scale. CFD calculations have verified this for the CONEX for speeds and dimensions in the range of interest from tunnel model scale to full scale (refs. 5 and 7).

The tunnel measurements were taken over the sideslip range $[-180, 180]$. These data were treated to impose symmetry properties about $\beta = 0$ on all components that are either symmetric (drag, lift, pitching moment) or anti-symmetric (side force, roll, and yaw moments). This symmetry occurs for a simple box and is not affected by the skids. Zeros were also imposed at $\beta = \pm 180$ deg on the anti-symmetric functions consistent with the same anti-symmetry about $\beta = 0$. In addition, drag at small end into the wind was averaged to a single value consistent with the invariant geometry facing the wind independent of rotation around the y-axis ($\beta = \pm 90$ deg, all α). Departures of the tunnel measurements from these imposed rules were very small.

Data are given in tables E1 to E6 for the wind axes components of force and moment divided by dynamic pressure. Body axes components are not tabulated here, but they can be generated via the transformation

$$\begin{aligned} FA_b &= T_{b,w} FA_w \\ MA_b &= T_{b,w} MA_w \end{aligned}$$

where

$$FA_w = \begin{bmatrix} -\text{drag} \\ \text{side force} \\ -\text{lift} \end{bmatrix} \quad MA_w = \begin{bmatrix} \text{roll moment} \\ \text{pitch moment} \\ \text{yaw moment} \end{bmatrix}$$

$$T_{b,w} = E_1(\alpha) E_3(-\beta)$$

Figures E1 to E3 provide a graphical overview of the components of principal interest in the load motions: drag, side force, and yaw moment.

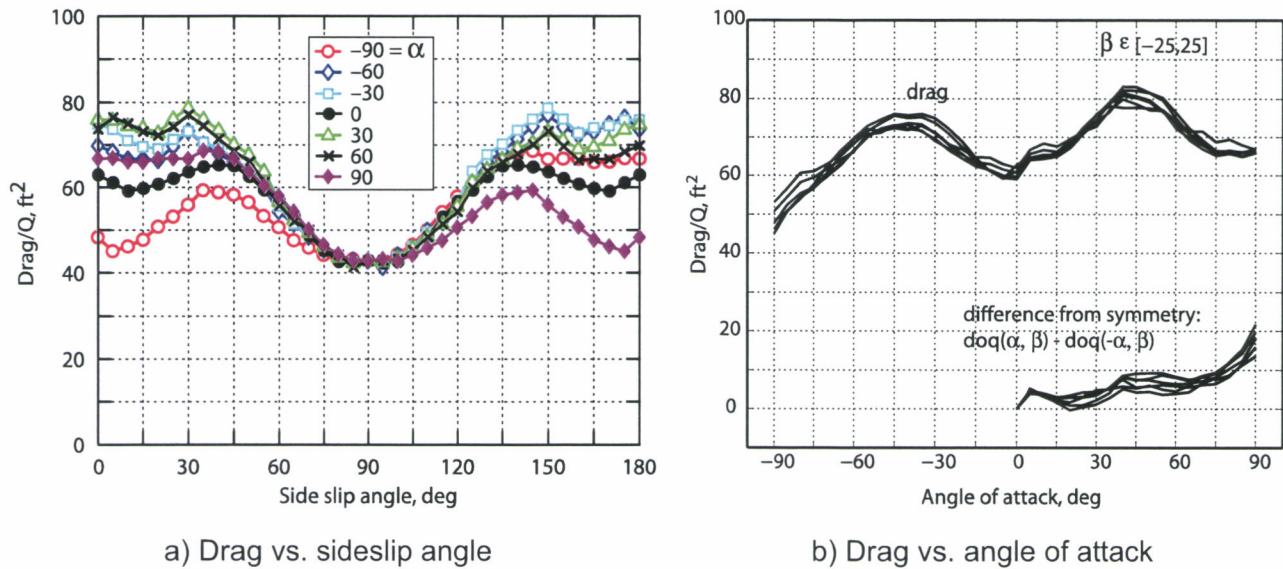


Figure E1. CONEX static aerodynamics: drag.

Drag. Drag vs. sideslip angle is shown in figure E1(a) for every 30 deg in angle of attack (AOA). Drag is the dominant force, and the drag parameter is in the range from 40 to 80 ft². Minimum drag occurs at small side into the wind as expected, and it is identical at all angles of attack there. Maximum drag occurs in the sideslip angle range of 30 to 45 deg from broadside to the wind in the region of maximum frontal area.

The effect of the skids on drag is visible in figure E1(b), where drag is plotted vs. AOA for all sideslip values within 25 deg of broadside to the wind. The drag of a simple box would be symmetric about $\alpha = 0$. The skids face into the wind for positive AOA and away from the wind for negative AOA, and this accounts for the larger drag of the nose-up CONEX. The difference in drag, $doq(\alpha, \beta) - doq(-\alpha, \beta)$, is included in figure E1(b). Over most of the range it is under 10 ft² (12% of maximum drag) and rises to 15–20 ft² at 90 deg, where it is the difference between full forward skids and full aft. Thus the skids result in a moderate departure from the symmetry of drag about $\alpha = 0$ that occurs for a simple box.

Side force. Side force vs. sideslip angle is shown in figure E2 for every 30 deg in AOA. The gross variation is similar at all values of AOA, with zeros every 90 deg in β and at an interior point in each quadrant. Maximum magnitude is 20 ft², one-fourth of the maximum drag. Side force is anti-symmetric in beta every 90 deg, where a side faces into the wind and has positive slope in a region around these points.

Yaw moment. Yaw moment vs. sideslip angle is shown in figure E3 for all values in the AOA grid. There is no significant variation with AOA. Similar to side force, yaw moment has two zero crossings every 90 deg where a side is facing into the wind and at an interior point in each quadrant. Yaw moment is statically stable in beta around the zeros corresponding to a side facing the wind, and the interior zeros are statically unstable. The mean value taken over side slip angle is very nearly zero for all AOA.

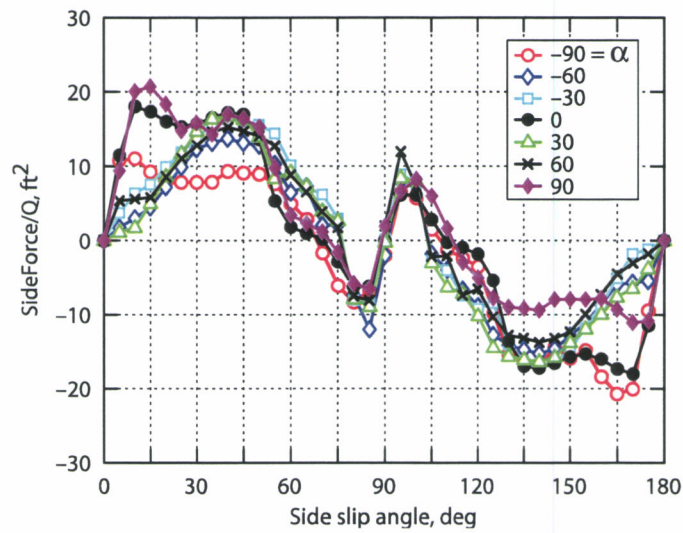


Figure E2. CONEX aerodynamics: side force.

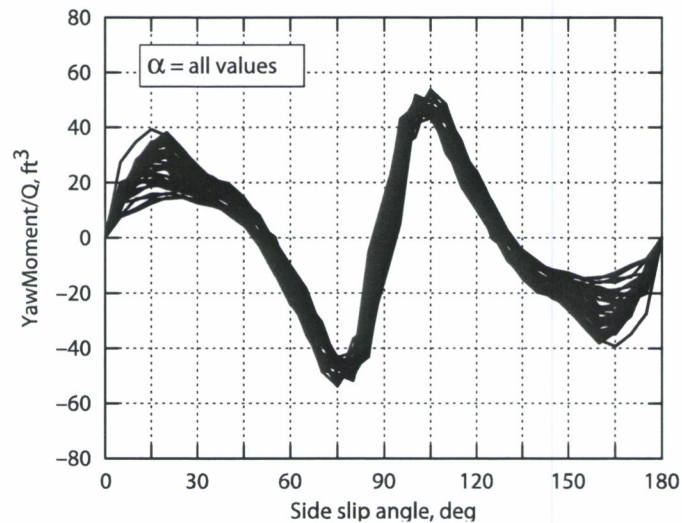
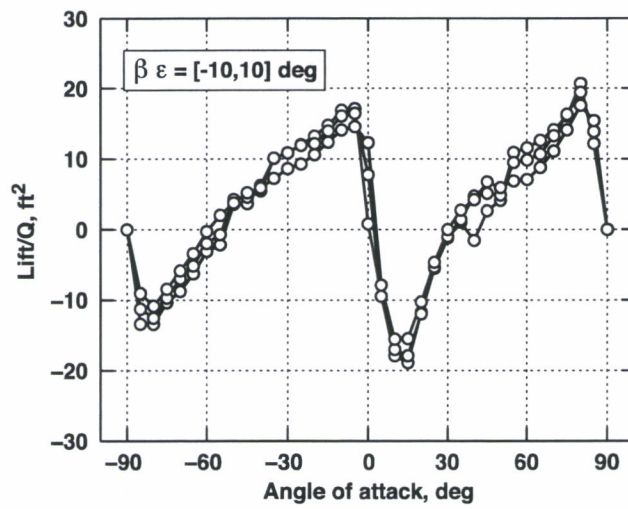
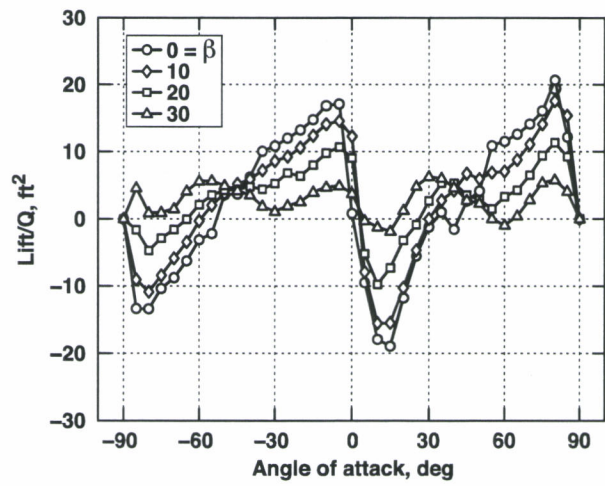


Figure E3. CONEX aerodynamics: yaw moment.

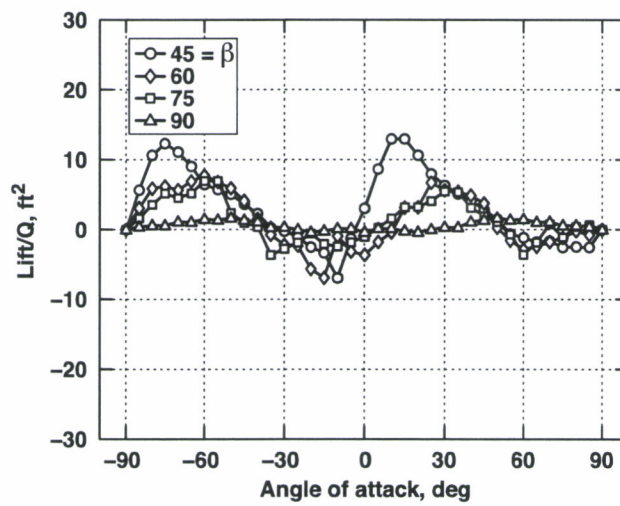
Lift and pitching moment. A graphical overview of lift and pitching moment is given in figures E4 and E5, respectively. Lift variation with AOA for the broadside CONEX (fig. E4(a)) has regions of positive and negative lift separated by zeros at $\text{AOA} = -90, 0, 90$ and an interior point in each 90-deg quadrant. In the region between the interior zeros, skids pointing backward give positive lift and skids pointing forward give negative lift; the slope through $\text{AOA} = 0$ is negative, unlike aerodynamic shapes. The skids introduce some departure from the anti-symmetry of lift about $\text{AOA} = 0$ for a simple box, particularly in the location of the interior zeros. The lift variation with AOA seen at $\beta = 0$ persists for fixed sideslip angles out to 25 deg but with attenuating extremes, and at 30 deg the pattern breaks up (fig. E4(b)). At $\beta = 45$ deg the pattern reverses, and at higher sideslip angles the extremes of lift attenuate to near zero at small side into the wind (fig. E4(c)).



a) Broadside CONEX



b) Variation for β in $[0, 30]$ deg



c) Variation for β in $[45, 90]$ deg

Figure E4. CONEX static aerodynamics: lift.

Figure E5 shows pitching moment vs. AOA. For a simple box, pitching moment would be anti-symmetric about AOA = 0. Because of the skids, pitching moment is biased low by -24 ft^3 at AOA = 0 and the anti-symmetry is distorted. The variation with AOA seen at broadside is similar to the variation of yaw moment with β at AOA = 0, and the two have a similar range of values between minimum and maximum. The broadside variation persists out to at $\beta = 30 \text{ deg}$, but with attenuating extremes. At $\beta = 45 \text{ deg}$ and above, pitching moment reduces to near zero for all values of AOA.

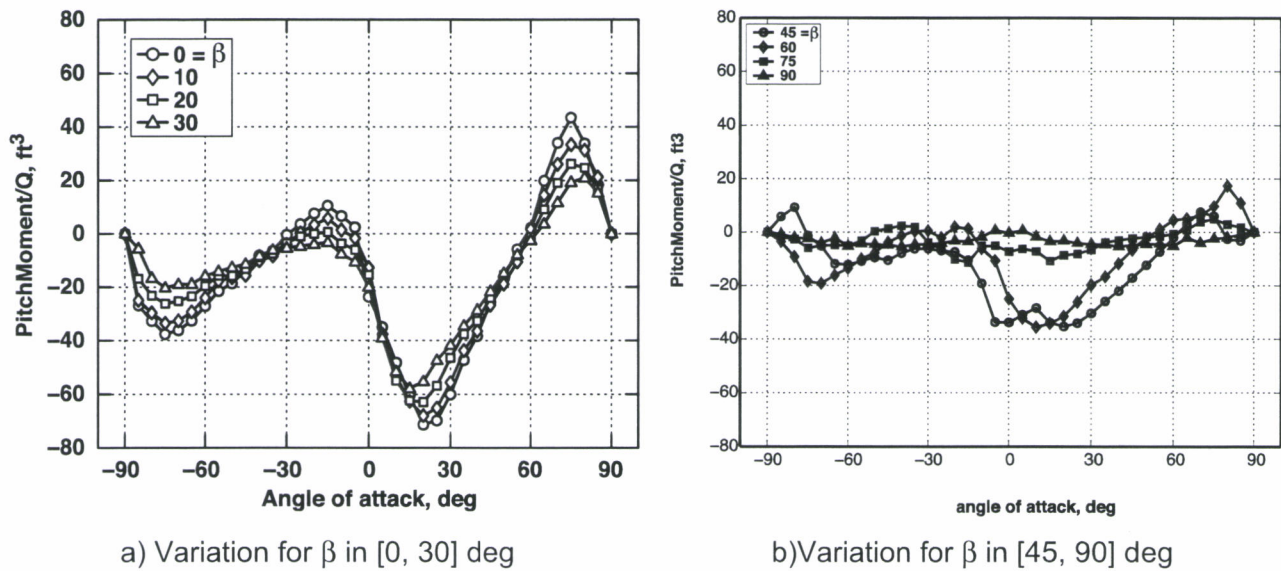


Figure E5. CONEX static aerodynamics: pitching moment.

TABLE E1. CONEX DRAG

DRAG/Q										
beta	0	5	10	15	20	25	30	35	40	45
alpha										
-90	66.76	66.87	66.02	65.93	66.76	66.81	66.69	68.69	68.37	66.7
-85	65.99	66.19	65.17	64.86	66.04	67.94	68.17	69.35	68.86	66.66
-80	66.23	66.39	66.16	65.78	66.65	69.44	68.76	72.23	70.9	68.28
-75	65.78	66.49	65.89	65.19	66.03	68.74	67.28	73.58	70.54	68.07
-70	69.08	69.27	68.2	66.92	68.02	71.45	68.99	74.75	71.38	68.49
-65	70.91	72.34	70.78	69.25	69.79	71.51	72.73	73.74	70.61	68.31
-60	73.71	76.47	74.98	73.11	72.24	74.25	77.05	74.39	71.34	68.46
-55	76.56	80.21	79.58	76.86	76.87	77.09	77.01	76.09	73.41	70.4
-50	79	81.48	81.46	79.65	77.03	77.53	77.35	76.51	75	72.47
-45	80.24	82.98	82.03	80.64	78.6	77.68	77.64	77.32	75.61	73.32
-40	80.75	83.05	82.19	81.44	79.76	77.63	78.42	77.4	75.09	72.23
-35	78.85	79.27	78.81	76.61	77.06	78.08	78.77	77.49	74.94	71.29
-30	75.98	75.83	74.51	74.03	72.79	76.12	78.72	76.05	73.49	70.19
-25	72.61	71.94	71.05	70.89	71.42	71.31	75.04	75.39	73.51	70.18
-20	68.47	68.28	67.26	67.75	68.98	69.63	70.47	75.64	73.78	71.18
-15	66.15	65.45	64.97	65.38	66.29	67.6	69.24	72.52	72.86	69.48
-10	64.7	64.5	64.4	65.46	66.68	68.37	69.9	70.9	69.99	67.47
-5	64.43	64.63	64.07	64.65	65.6	66.77	67.54	67.92	66.54	65.44
0	62.92	61.13	59.13	59.72	60.77	62.07	63.64	64.8	65.24	65
5	59.2	59.8	59.39	60.01	61.58	62.95	63.8	64.83	65.67	65.37
10	61.22	61.35	61.31	61.48	63.06	64.72	65.52	66.49	66.8	66.09
15	64.59	63.77	62.78	62.31	63.44	64.79	64.69	67.16	67.22	65.8
20	68.86	67.42	65.61	64.43	65.49	66.75	66.48	68.91	68.19	66.9
25	72.16	70.98	68.1	66.62	67.12	68.19	69.24	70.37	68.49	66.67
30	74.86	73.64	71.04	69.57	69.07	71.24	73.22	70.59	69.28	66.65
35	76.02	75.16	73.27	71.49	71.64	72.95	73.09	72.66	70.13	67.45
40	75.64	74.92	73.59	73.17	72.19	71.84	72.99	72.9	71.55	69.15
45	76.02	75.56	72.89	73.07	73.06	72.35	73.55	73.14	71.95	69.25
50	74.55	73.65	72.19	72.24	71.16	71.51	72.76	72.32	70.76	68.14
55	72.92	71.51	70.31	70.06	70.76	72.12	73.49	72.26	69.67	67.35
60	69.82	68.39	66.63	66.67	66.35	69.65	73.21	70.12	67.9	65.92
65	66.58	65.12	63.17	62.72	64.17	65.51	67.91	69.1	67.54	65.58
70	62.45	60.68	60.07	59.71	61.81	63.06	63.85	71.3	67.4	65.71
75	57.85	57.1	56.82	57.01	59.55	61.17	62.54	69.11	65.3	63.2
80	54.17	54.36	54.49	55.47	58.32	60.73	62.15	64.76	62.58	61.15
85	50.83	50.78	50.93	52.45	54.56	56.66	58	60.6	59.73	59.14
90	48.33	45.09	46.2	47.74	50.86	53.2	55.96	59.36	58.85	58.28

TABLE E1. CONEX DRAG (cont.)

DRAG/Q										
beta	50	55	60	65	70	75	80	85	90	95
alpha										
-90	63.71	60.45	57.93	54.3	50.14	46.54	44.38	42.84	42.82	43.29
-85	63.88	60.64	53.84	50.33	47.25	44.61	44.8	41.88	42.82	43.97
-80	65.43	59.23	57.6	53.22	49.5	44.62	45.24	41.77	42.82	43.92
-75	64.87	62.44	58.59	51.94	49.4	46.68	44.92	41.6	42.82	43.35
-70	65.64	61.44	57.83	54.97	48.47	46.16	44.97	41.87	42.82	43.04
-65	65.78	60.3	58.25	53.71	51.04	45.14	44.72	42.03	42.82	42.51
-60	65.98	61.2	55.77	52.06	50.03	45.05	44.19	41.3	42.82	42.94
-55	67.11	60.65	57.26	52.13	46.96	47.35	44.11	41.86	42.82	42.97
-50	69.21	63.35	57.52	51.92	47.9	45.44	43.16	42.48	42.82	42.93
-45	68.61	61.06	56.25	54.27	48.75	45.12	43.83	42.55	42.82	42.97
-40	69.16	64.68	58.15	51.83	48.56	45.36	42.97	42.48	42.82	42.87
-35	68.28	62.11	58.51	52.73	47.6	47.23	43.79	42.95	42.82	42.81
-30	67.76	63.81	56.7	52.51	49.5	46.24	43.7	42.37	42.82	42.66
-25	68.38	61.69	59.42	53.35	50.54	45.05	44.02	42.33	42.82	42.89
-20	66.67	63.27	57.87	54.92	48.48	44.78	44.12	42.8	42.82	42.79
-15	65.18	62.28	58.49	52.3	48.12	45.7	44.09	42.86	42.82	43.1
-10	64.65	58.62	56.83	53.13	48.46	43.53	44.17	42.84	42.82	43.28
-5	62.92	60.18	54.49	51.74	46.93	43.64	43.57	43.5	42.82	43.25
0	62.49	59.32	56.73	53.18	48.61	45.19	42.58	42.28	42.82	42.28
5	63.06	59.89	53.48	50.48	46.6	43.74	43.31	43.25	42.82	43.5
10	63.79	58.22	56.95	52.99	48.64	43.97	43.51	43.28	42.82	42.84
15	62.64	60.75	57.5	52.26	48.44	45.77	44.03	43.1	42.82	42.86
20	64.11	61.1	56.71	53.85	48.46	45.07	44.15	42.79	42.82	42.8
25	65.14	60.15	57.7	52.57	50.01	45.11	43.56	42.89	42.82	42.33
30	64.33	61.38	55.57	51.48	48.57	45.83	43.43	42.66	42.82	42.37
35	64.36	60.42	57.13	51.48	46.64	45.65	43.41	42.81	42.82	42.95
40	66.36	61.78	57.08	51.26	48.23	43.9	43.57	42.87	42.82	42.48
45	65.64	59.53	55.13	53.4	48.57	43.85	43.41	42.97	42.82	42.55
50	66.21	62.1	56.26	51.84	48.14	44.31	43.07	42.93	42.82	42.48
55	64.57	59.76	55.76	51.78	46.61	46.3	43.27	42.97	42.82	41.86
60	63.81	59.93	54.34	51.43	48.42	45.3	43.2	42.94	42.82	41.3
65	63.64	57.92	56.2	50.98	49.17	44.22	43.36	42.51	42.82	42.03
70	62.22	58.31	54.42	52.26	47.42	44.17	43.12	43.04	42.82	41.87
75	59.91	57.5	54.66	48.73	46.69	44.73	42.68	43.35	42.82	41.6
80	59.21	53.35	52.26	49.51	47.01	43.35	43.35	43.92	42.82	41.77
85	57.36	54.67	50.12	47.35	45.73	42.77	43.07	43.97	42.82	41.88
90	56.56	53.34	50.69	47.6	45.89	44.21	42.78	43.29	42.82	42.84

TABLE E1. CONEX DRAG (cont.)

DRAG/Q										
beta	100	105	110	115	120	125	130	135	140	145
alpha										
-90	42.78	44.21	45.89	47.6	50.69	53.34	56.56	58.28	58.85	59.36
-85	43.07	42.77	45.73	47.35	50.12	54.67	57.36	59.14	59.73	60.6
-80	43.35	43.35	47.01	49.51	52.26	53.35	59.21	61.15	62.58	64.76
-75	42.68	44.73	46.69	48.73	54.66	57.5	59.91	63.2	65.3	69.11
-70	43.12	44.17	47.42	52.26	54.42	58.31	62.22	65.71	67.4	71.3
-65	43.36	44.22	49.17	50.98	56.2	57.92	63.64	65.58	67.54	69.1
-60	43.2	45.3	48.42	51.43	54.34	59.93	63.81	65.92	67.9	70.12
-55	43.27	46.3	46.61	51.78	55.76	59.76	64.57	67.35	69.67	72.26
-50	43.07	44.31	48.14	51.84	56.26	62.1	66.21	68.14	70.76	72.32
-45	43.41	43.85	48.57	53.4	55.13	59.53	65.64	69.25	71.95	73.14
-40	43.57	43.9	48.23	51.26	57.08	61.78	66.36	69.15	71.55	72.9
-35	43.41	45.65	46.64	51.48	57.13	60.42	64.36	67.45	70.13	72.66
-30	43.43	45.83	48.57	51.48	55.57	61.38	64.33	66.65	69.28	70.59
-25	43.56	45.11	50.01	52.57	57.7	60.15	65.14	66.67	68.49	70.37
-20	44.15	45.07	48.46	53.85	56.71	61.1	64.11	66.9	68.19	68.91
-15	44.03	45.77	48.44	52.26	57.5	60.75	62.64	65.8	67.22	67.16
-10	43.51	43.97	48.64	52.99	56.95	58.22	63.79	66.09	66.8	66.49
-5	43.31	43.74	46.6	50.48	53.48	59.89	63.06	65.37	65.67	64.83
0	42.58	45.19	48.61	53.18	56.73	59.32	62.49	65	65.24	64.8
5	43.57	43.64	46.93	51.74	54.49	60.18	62.92	65.44	66.54	67.92
10	44.17	43.53	48.46	53.13	56.83	58.62	64.65	67.47	69.99	70.9
15	44.09	45.7	48.12	52.3	58.49	62.28	65.18	69.48	72.86	72.52
20	44.12	44.78	48.48	54.92	57.87	63.27	66.67	71.18	73.78	75.64
25	44.02	45.05	50.54	53.35	59.42	61.69	68.38	70.18	73.51	75.39
30	43.7	46.24	49.5	52.51	56.7	63.81	67.76	70.19	73.49	76.05
35	43.79	47.23	47.6	52.73	58.51	62.11	68.28	71.29	74.94	77.49
40	42.97	45.36	48.56	51.83	58.15	64.68	69.16	72.23	75.09	77.4
45	43.83	45.12	48.75	54.27	56.25	61.06	68.61	73.32	75.61	77.32
50	43.16	45.44	47.9	51.92	57.52	63.35	69.21	72.47	75	76.51
55	44.11	47.35	46.96	52.13	57.26	60.65	67.11	70.4	73.41	76.09
60	44.19	45.05	50.03	52.06	55.77	61.2	65.98	68.46	71.34	74.39
65	44.72	45.14	51.04	53.71	58.25	60.3	65.78	68.31	70.61	73.74
70	44.97	46.16	48.47	54.97	57.83	61.44	65.64	68.49	71.38	74.75
75	44.92	46.68	49.4	51.94	58.59	62.44	64.87	68.07	70.54	73.58
80	45.24	44.62	49.5	53.22	57.6	59.23	65.43	68.28	70.9	72.23
85	44.8	44.61	47.25	50.33	53.84	60.64	63.88	66.66	68.86	69.35
90	44.38	46.54	50.14	54.3	57.93	60.45	63.71	66.7	68.37	68.69

TABLE E1. CONEX DRAG (cont.)

DRAG/Q							
beta	150	155	160	165	170	175	180
alpha							
-90	55.96	53.2	50.86	47.74	46.2	45.09	48.33
-85	58	56.66	54.56	52.45	50.93	50.78	50.83
-80	62.15	60.73	58.32	55.47	54.49	54.36	54.17
-75	62.54	61.17	59.55	57.01	56.82	57.1	57.85
-70	63.85	63.06	61.81	59.71	60.07	60.68	62.45
-65	67.91	65.51	64.17	62.72	63.17	65.12	66.58
-60	73.21	69.65	66.35	66.67	66.63	68.39	69.82
-55	73.49	72.12	70.76	70.06	70.31	71.51	72.92
-50	72.76	71.51	71.16	72.24	72.19	73.65	74.55
-45	73.55	72.35	73.06	73.07	72.89	75.56	76.02
-40	72.99	71.84	72.19	73.17	73.59	74.92	75.64
-35	73.09	72.95	71.64	71.49	73.27	75.16	76.02
-30	73.22	71.24	69.07	69.57	71.04	73.64	74.86
-25	69.24	68.19	67.12	66.62	68.1	70.98	72.16
-20	66.48	66.75	65.49	64.43	65.61	67.42	68.86
-15	64.69	64.79	63.44	62.31	62.78	63.77	64.59
-10	65.52	64.72	63.06	61.48	61.31	61.35	61.22
-5	63.8	62.95	61.58	60.01	59.39	59.8	59.2
0	63.64	62.07	60.77	59.72	59.13	61.13	62.92
5	67.54	66.77	65.6	64.65	64.07	64.63	64.43
10	69.9	68.37	66.68	65.46	64.4	64.5	64.7
15	69.24	67.6	66.29	65.38	64.97	65.45	66.15
20	70.47	69.63	68.98	67.75	67.26	68.28	68.47
25	75.04	71.31	71.42	70.89	71.05	71.94	72.61
30	78.72	76.12	72.79	74.03	74.51	75.83	75.98
35	78.77	78.08	77.06	76.61	78.81	79.27	78.85
40	78.42	77.63	79.76	81.44	82.19	83.05	80.75
45	77.64	77.68	78.6	80.64	82.03	82.98	80.24
50	77.35	77.53	77.03	79.65	81.46	81.48	79
55	77.01	77.09	76.87	76.86	79.58	80.21	76.56
60	77.05	74.25	72.24	73.11	74.98	76.47	73.71
65	72.73	71.51	69.79	69.25	70.78	72.34	70.91
70	68.99	71.45	68.02	66.92	68.2	69.27	69.08
75	67.28	68.74	66.03	65.19	65.89	66.49	65.78
80	68.76	69.44	66.65	65.78	66.16	66.39	66.23
85	68.17	67.94	66.04	64.86	65.17	66.19	65.99
90	66.69	66.81	66.76	65.93	66.02	66.87	66.76

TABLE E2. CONEX SIDE FORCE

SIDE FORCE/Q										
beta	0	5	10	15	20	25	30	35	40	45
alpha										
-90	3.06	9.4	20.05	20.69	18.36	14.78	15.87	14.34	17.01	16.43
-85	1.97	10.21	19.72	20.01	17.91	15.76	15.41	14.36	16.07	15.51
-80	3.08	11.34	17.53	18.06	16.79	15.53	14.99	14.34	15.56	15.12
-75	1.27	10.15	14.4	15.21	14.53	13.9	13.79	14.36	14.48	14.57
-70	2.27	8.68	11.8	12.31	12.21	12.73	12.84	13.82	13.75	13.82
-65	2.17	6.69	8.18	8.75	10.17	12.84	13.25	14.12	14.16	14.14
-60	2.04	5.41	5.63	5.88	8.61	11.08	12.83	14.61	15.27	14.73
-55	1.11	4.36	4.04	4.52	6.17	9.05	10.58	14.84	15.94	16.02
-50	0.01	1.16	2.39	3.14	6.59	9.6	11.56	15	16.73	16.66
-45	0.06	0.72	1.8	3.74	6.9	9.54	12.1	15.45	17.94	17.09
-40	-1.1	0.57	0.59	2.99	7.2	8.24	11.76	15.15	17.15	16.75
-35	-0.57	0.69	1.35	4.14	7.36	9.56	12.85	16.16	16.79	16.68
-30	-0.24	1.16	1.77	5.03	8.64	11.77	14.72	16.39	16.76	16.32
-25	0.5	2.05	5.58	8.77	10.12	11.8	14.57	16.17	17	16.18
-20	0.35	5.41	10.36	10.97	10.9	12.03	13.65	16.2	17.52	17.1
-15	0.07	10.16	14.27	13.99	12.77	13.33	15.29	17.32	18.01	15.78
-10	1.05	11.81	16.61	16.43	15.79	16.08	17.76	18.57	16.29	13.94
-5	0.51	9.74	17.76	17.67	16.76	16.52	17.23	17.28	16.58	14.8
0	0.73	11.48	18.03	17.36	16	15.29	15.72	16.55	17.21	16.97
5	1.07	11.68	16.29	16.27	15.06	14.72	15.01	15.37	15.86	17.38
10	0.79	10.35	14.96	15.13	14.78	14.92	15.45	15.38	15.66	16.15
15	1.12	9.74	12.99	14.03	14.01	14.17	15.06	15.4	15.58	15.59
20	1.07	8.25	11.65	12.66	13.37	13.85	14.77	15.75	16.24	16.65
25	0.37	6.37	8.77	9.68	11.15	12.76	14.52	16.09	16.35	16.55
30	0.48	3.73	6.4	7.59	9.92	11.9	13.74	15.71	16.32	16.06
35	0.29	1.66	5.28	6.79	8.21	9.42	11.93	15.24	16.06	15.93
40	-0.95	0.29	3.87	5.41	7.74	9.55	11.43	14.59	16.29	15.98
45	-0.95	0.49	3.92	5.51	7.3	9.52	12.17	14.8	16.88	15.96
50	-0.86	-0.1	3.05	4.94	7.06	8.6	11.19	14.19	15.53	14.87
55	-0.83	0.83	2.78	4.55	6.66	8.51	10.86	14.31	14.47	14.15
60	-0.37	1.76	3.01	4.48	7.24	9.92	12.31	13.17	13.74	13.16
65	-0.23	4.4	5.83	6.57	7.12	9.98	11.33	12.57	13.01	12.76
70	0.21	6.53	8.64	8.52	9.15	9.96	10.56	12.62	13.01	13.39
75	0.61	9.46	11.33	10.74	9.72	10.15	10.76	12.65	12	10.97
80	0.26	11.18	13.26	11.78	10.49	10.14	10.45	9.6	8.89	7.86
85	0.92	11.61	13.48	11.8	9.65	8.93	8.87	7.91	8.95	8.37
90	-0.48	10.82	11.04	9.26	7.8	7.9	7.88	7.93	9.36	9.13

TABLE E2. CONEX SIDE FORCE (cont.)

SIDE_FORCE/Q, ft2										
beta	50	55	60	65	70	75	80	85	90	95
alpha										
-90	15.29	9.81	3.46	2.35	1.2	-1.55	-5.77	-6.49	1.95	6.72
-85	14.36	10.06	7	6.29	3.8	-2.03	-6.7	-7.44	1.93	11.3
-80	13.93	8.7	5.02	6.23	2.51	-2.33	-7.35	-7.54	1.41	10.36
-75	13.96	11.54	9.93	8.25	3.82	0.23	-7.72	-7.68	1.36	10.39
-70	14.05	12.63	10.82	8.78	5.84	-3.31	-7.63	-8.09	1.53	11.16
-65	13.8	11.98	10.91	7.81	5.74	-0.42	-7.02	-8.51	0.83	10.16
-60	14.07	12.73	8.85	6.61	3.9	1.76	-7.5	-8.08	1.96	11.99
-55	14.62	12.29	9.99	6.16	2.37	0.23	-7.81	-8.91	1.22	11.34
-50	15.69	13.45	10.35	6.46	3.99	-3.24	-9.66	-9.77	0.94	11.65
-45	15.74	12.47	9.66	8.34	3.93	-3.96	-6.64	-9.33	0.6	10.53
-40	15.9	12.76	10.39	6.21	3.59	-3.22	-10.39	-9.35	0.5	10.34
-35	15.16	10.5	10.7	6.9	2.33	0.61	-8.4	-9.87	-0.63	8.61
-30	14	8.42	9.21	7.42	4	2.7	-7.87	-8.91	-0.21	8.5
-25	12.95	4.4	4.43	5.84	5.14	-0.19	-6.97	-7.88	-0.14	7.6
-20	12.7	5.89	1.7	2.87	5.4	-1.27	-7.89	-8.16	-0.6	6.96
-15	11.08	4.61	2.75	6.05	1.99	0.73	-8.26	-7.78	-0.44	6.9
-10	11.29	4.96	2.21	1.07	2.25	0.03	-7.98	-7.16	-0.01	7.13
-5	12.88	6.05	2.33	0.68	2.99	0.14	-6.99	-6.32	0.39	7.11
0	13.61	5.35	1.82	0.97	0.22	-2.84	-6.18	-6.19	0	6.19
5	13.74	7.03	6.22	6.25	3.3	0.59	-6.32	-7.11	-0.39	6.32
10	15.9	8.24	4.5	3.9	3.51	0.34	-7.24	-7.13	0.01	7.16
15	14.41	13.22	11.22	8.2	3	1.33	-7.82	-6.9	0.44	7.78
20	15.78	14.42	11.86	10.81	5.96	-1.57	-7.65	-6.96	0.6	8.16
25	16.54	14.24	12.51	9.68	7.58	-0.24	-6.78	-7.6	0.14	7.88
30	15.61	14.43	10.14	7.12	6.27	2.96	-8.04	-8.5	0.21	8.91
35	15.31	13.09	11.09	6.57	4.33	3.59	-8.71	-8.61	0.63	9.87
40	15.21	13.88	10.88	6.81	4.99	-1.43	-11.92	-10.34	-0.5	9.35
45	15.04	11.83	9.48	8.4	4.83	-3.45	-6.99	-10.53	-0.6	9.33
50	14.43	13.57	9.55	7	4.33	-3.13	-9.73	-11.65	-0.94	9.77
55	13.65	10.08	8.45	7.46	1.45	-1.19	-7	-11.34	-1.22	8.91
60	12.79	10.3	6.52	7.37	2.06	2.11	-7.36	-11.99	-1.96	8.08
65	12.34	5.99	1.84	1.74	3.64	-1.58	-6.98	-10.16	-0.83	8.51
70	10.66	8.33	0.79	-0.24	3.64	-3.72	-5.02	-11.16	-1.53	8.09
75	7.99	3.47	2.54	2.68	0.75	-1.72	-4.83	-10.39	-1.36	7.68
80	7.05	5.89	4.54	1.45	1.63	-1.82	-5.66	-10.36	-1.41	7.54
85	8	6.99	4.71	2.31	0.6	-2.4	-5.22	-11.3	-1.93	7.44
90	8.95	7.71	4.99	2.91	-1.67	-6.08	-8.3	-6.72	-1.95	6.49

TABLE E2. CONEX SIDE FORCE (cont.)

SIDE_FORCE/Q, ft2										
beta	100	105	110	115	120	125	130	135	140	145
alpha										
-90	8.3	6.08	1.67	-2.91	-4.99	-7.71	-8.95	-9.13	-9.36	-7.93
-85	5.22	2.4	-0.6	-2.31	-4.71	-6.99	-8	-8.37	-8.95	-7.91
-80	5.66	1.82	-1.63	-1.45	-4.54	-5.89	-7.05	-7.86	-8.89	-9.6
-75	4.83	1.72	-0.75	-2.68	-2.54	-3.47	-7.99	-10.97	-12	-12.65
-70	5.02	3.72	-3.64	0.24	-0.79	-8.33	-10.66	-13.39	-13.01	-12.62
-65	6.98	1.58	-3.64	-1.74	-1.84	-5.99	-12.34	-12.76	-13.01	-12.57
-60	7.36	-2.11	-2.06	-7.37	-6.52	-10.3	-12.79	-13.16	-13.74	-13.17
-55	7	1.19	-1.45	-7.46	-8.45	-10.08	-13.65	-14.15	-14.47	-14.31
-50	9.73	3.13	-4.33	-7	-9.55	-13.57	-14.43	-14.87	-15.53	-14.19
-45	6.99	3.45	-4.83	-8.4	-9.48	-11.83	-15.04	-15.96	-16.88	-14.8
-40	11.92	1.43	-4.99	-6.81	-10.88	-13.88	-15.21	-15.98	-16.29	-14.59
-35	8.71	-3.59	-4.33	-6.57	-11.09	-13.09	-15.31	-15.93	-16.06	-15.24
-30	8.04	-2.96	-6.27	-7.12	-10.14	-14.43	-15.61	-16.06	-16.32	-15.71
-25	6.78	0.24	-7.58	-9.68	-12.51	-14.24	-16.54	-16.55	-16.35	-16.09
-20	7.65	1.57	-5.96	-10.81	-11.86	-14.42	-15.78	-16.65	-16.24	-15.75
-15	7.82	-1.33	-3	-8.2	-11.22	-13.22	-14.41	-15.59	-15.58	-15.4
-10	7.24	-0.34	-3.51	-3.9	-4.5	-8.24	-15.9	-16.15	-15.66	-15.38
-5	6.32	-0.59	-3.3	-6.25	-6.22	-7.03	-13.74	-17.38	-15.86	-15.37
0	6.18	2.84	-0.22	-0.97	-1.82	-5.35	-13.61	-16.97	-17.21	-16.55
5	6.99	-0.14	-2.99	-0.68	-2.33	-6.05	-12.88	-14.8	-16.58	-17.28
10	7.98	-0.03	-2.25	-1.07	-2.21	-4.96	-11.29	-13.94	-16.29	-18.57
15	8.26	-0.73	-1.99	-6.05	-2.75	-4.61	-11.08	-15.78	-18.01	-17.32
20	7.89	1.27	-5.4	-2.87	-1.7	-5.89	-12.7	-17.1	-17.52	-16.2
25	6.97	0.19	-5.14	-5.84	-4.43	-4.4	-12.95	-16.18	-17	-16.17
30	7.87	-2.7	-4	-7.42	-9.21	-8.42	-14	-16.32	-16.76	-16.39
35	8.4	-0.61	-2.33	-6.9	-10.7	-10.5	-15.16	-16.68	-16.79	-16.16
40	10.39	3.22	-3.59	-6.21	-10.39	-12.76	-15.9	-16.75	-17.15	-15.15
45	6.64	3.96	-3.93	-8.34	-9.66	-12.47	-15.74	-17.09	-17.94	-15.45
50	9.66	3.24	-3.99	-6.46	-10.35	-13.45	-15.69	-16.66	-16.73	-15
55	7.81	-0.23	-2.37	-6.16	-9.99	-12.29	-14.62	-16.02	-15.94	-14.84
60	7.5	-1.76	-3.9	-6.61	-8.85	-12.73	-14.07	-14.73	-15.27	-14.61
65	7.02	0.42	-5.74	-7.81	-10.91	-11.98	-13.8	-14.14	-14.16	-14.12
70	7.63	3.31	-5.84	-8.78	-10.82	-12.63	-14.05	-13.82	-13.75	-13.82
75	7.72	-0.23	-3.82	-8.25	-9.93	-11.54	-13.96	-14.57	-14.48	-14.36
80	7.35	2.33	-2.51	-6.23	-5.02	-8.7	-13.93	-15.12	-15.56	-14.34
85	6.7	2.03	-3.8	-6.29	-7	-10.06	-14.36	-15.51	-16.07	-14.36
90	5.77	1.55	-1.2	-2.35	-3.46	-9.81	-15.29	-16.43	-17.01	-14.34

TABLE E2. CONEX SIDE FORCE (cont.)

SIDE_FORCE/Q, ft2							
beta	150	155	160	165	170	175	180
alpha							
-90	-7.88	-7.9	-7.8	-9.26	-11.04	-10.82	0
-85	-8.87	-8.93	-9.65	-11.8	-13.48	-11.61	0
-80	-10.45	-10.14	-10.49	-11.78	-13.26	-11.18	0
-75	-10.76	-10.15	-9.72	-10.74	-11.33	-9.46	0
-70	-10.56	-9.96	-9.15	-8.52	-8.64	-6.53	0
-65	-11.33	-9.98	-7.12	-6.57	-5.83	-4.4	0
-60	-12.31	-9.92	-7.24	-4.48	-3.01	-1.76	0
-55	-10.86	-8.51	-6.66	-4.55	-2.78	-0.83	0
-50	-11.19	-8.6	-7.06	-4.94	-3.05	0.1	0
-45	-12.17	-9.52	-7.3	-5.51	-3.92	-0.49	0
-40	-11.43	-9.55	-7.74	-5.41	-3.87	-0.29	0
-35	-11.93	-9.42	-8.21	-6.79	-5.28	-1.66	0
-30	-13.74	-11.9	-9.92	-7.59	-6.4	-3.73	0
-25	-14.52	-12.76	-11.15	-9.68	-8.77	-6.37	0
-20	-14.77	-13.85	-13.37	-12.66	-11.65	-8.25	0
-15	-15.06	-14.17	-14.01	-14.03	-12.99	-9.74	0
-10	-15.45	-14.92	-14.78	-15.13	-14.96	-10.35	0
-5	-15.01	-14.72	-15.06	-16.27	-16.29	-11.68	0
0	-15.72	-15.29	-16	-17.36	-18.03	-11.48	0
5	-17.23	-16.52	-16.76	-17.67	-17.76	-9.74	0
10	-17.76	-16.08	-15.79	-16.43	-16.61	-11.81	0
15	-15.29	-13.33	-12.77	-13.99	-14.27	-10.16	0
20	-13.65	-12.03	-10.9	-10.97	-10.36	-5.41	0
25	-14.57	-11.8	-10.12	-8.77	-5.58	-2.05	0
30	-14.72	-11.77	-8.64	-5.03	-1.77	-1.16	0
35	-12.85	-9.56	-7.36	-4.14	-1.35	-0.69	0
40	-11.76	-8.24	-7.2	-2.99	-0.59	-0.57	0
45	-12.1	-9.54	-6.9	-3.74	-1.8	-0.72	0
50	-11.56	-9.6	-6.59	-3.14	-2.39	-1.16	0
55	-10.58	-9.05	-6.17	-4.52	-4.04	-4.36	0
60	-12.83	-11.08	-8.61	-5.88	-5.63	-5.41	0
65	-13.25	-12.84	-10.17	-8.75	-8.18	-6.69	0
70	-12.84	-12.73	-12.21	-12.31	-11.8	-8.68	0
75	-13.79	-13.9	-14.53	-15.21	-14.4	-10.15	0
80	-14.99	-15.53	-16.79	-18.06	-17.53	-11.34	0
85	-15.41	-15.76	-17.91	-20.01	-19.72	-10.21	0
90	-15.87	-14.78	-18.36	-20.69	-20.05	-9.4	0

TABLE E3. CONEX LIFT

LIFT/Q, ft ²										
beta	0	5	10	15	20	25	30	35	40	45
alpha										
-90	0	0	0	0	0	0	0	0	0	0
-85	12.17	13.87	15.4	13.17	9.26	6.64	4.09	0.9	-0.94	-2.56
-80	20.7	19.45	17.59	14.46	11.36	7.72	5.81	0.3	-1.38	-2.47
-75	16.08	16.33	14.11	12.22	9.44	4.06	5.37	-2.5	-1.71	-2.53
-70	14.12	13.29	11.11	9.09	6.49	2.66	2.88	-2.44	-1.23	-1.66
-65	12.62	10.69	8.8	6.09	4.24	1.7	0.44	-1.05	-1.13	-1.77
-60	11.57	9.86	7.06	3.47	3.28	1.17	-0.93	-0.41	-0.55	-1.16
-55	10.91	9.5	6.87	2.86	1.49	1.66	0.04	0.02	0.49	-0.62
-50	4.1	4.86	5.94	2.75	2.82	2.58	2.33	2.1	1.74	1.49
-45	2.64	5.09	6.72	4.55	3.53	2.67	2.77	2.53	2.32	2.84
-40	-1.58	4.73	4.2	5.63	5.33	4.37	4.65	4.01	3.85	4.2
-35	1	1.36	2.73	4.19	5.28	5.54	6.02	5.22	5.29	5.11
-30	-1.19	-1	-0.02	2.42	2.69	4.3	6.3	6.21	6.19	6.33
-25	-5.54	-5.37	-4.68	-2.19	-0.87	1.38	4.87	7.37	8.35	7.99
-20	-11.76	-11.96	-10.26	-6.65	-3.21	-0.51	1.26	9.49	11.11	10.65
-15	-18.9	-17.88	-15.45	-11.55	-7.3	-4.34	-1.84	6.71	12.28	13
-10	-17.88	-16.98	-15.51	-12.9	-9.75	-5.58	-1.22	2.61	11.2	12.99
-5	-9.52	-9.46	-7.92	-8.39	-5.22	-2.92	-0.26	2.5	7.87	8.68
0	0.82	7.74	12.28	11.02	9.07	5.6	3.78	4	2.89	3.05
5	17.13	16.46	14.56	13.3	10.7	7.52	4.89	3.41	-0.18	-1.27
10	16.89	16.08	14.11	12.47	9.82	7	4.73	3.4	-4.89	-6.92
15	14.79	13.98	12.38	11.1	8.03	5.56	3.96	1.52	-2.78	-3.33
20	13.22	12.17	10.61	9.21	6.38	4.31	2.53	0.17	-1.97	-2.5
25	11.99	11.94	9.27	8.48	6.83	4.35	1.95	0.32	-0.63	-1.12
30	10.85	10.88	8.63	6.75	5.25	2.77	1.12	1.13	0.01	-0.21
35	10.08	10.14	7.22	4.98	4.41	2.51	1.9	1.85	1.57	0.27
40	6.26	5.45	5.88	5.04	4.76	4.46	3.54	3.21	2.95	2.31
45	3.67	4.59	5.19	4.6	4.41	4.5	4.21	3.38	3.55	3.62
50	3.58	4.23	3.75	3.94	4.24	4.21	4.96	3.85	4.34	5.04
55	-2.19	-0.73	2	2.65	3.53	4.86	5.67	4.49	4.93	5.74
60	-3.12	-1.99	-0.3	1.4	2.12	3.94	5.61	5.4	5.64	6.47
65	-6.29	-5.18	-3.42	-0.75	-0.06	2.06	4.13	6.83	8.33	9.06
70	-8.78	-7	-5.88	-3.52	-1.59	0.32	1.53	11.78	10.05	11.11
75	-10.36	-9.72	-8.44	-5.48	-2.88	-0.83	0.97	11.53	10.77	12.35
80	-13.39	-12.52	-10.87	-8.32	-4.73	-2.12	0.89	5.09	10.14	10.64
85	-13.37	-11.26	-9.05	-6.26	-1.63	1.86	4.61	7.12	5.96	5.67
90	0	0	0	0	0	0	0	0	0	0

TABLE E3. CONEX LIFT (cont.)

LIFT/Q, ft2										
beta	50	55	60	65	70	75	80	85	90	95
alpha										
-90	0	0	0	0	0	0	0	0	0	0
-85	-2.97	-2.65	-0.78	-0.85	-0.82	0.65	1.65	0.86	0.41	-0.04
-80	-2.49	-1.04	-0.24	-1.37	-0.55	0.43	3.69	0.88	0.58	0.28
-75	-2.54	-2.04	-1.19	-1.53	-1.8	-1.13	3.78	0.66	0.59	0.52
-70	-2.97	-2.2	-1.75	-2.76	-3.17	0.77	3.31	1.34	1.13	0.93
-65	-2.04	-2.5	-2.44	-3.08	-3.21	-1.82	2.22	1.14	1.06	0.98
-60	-1.46	-1.72	-2.85	-2.93	-2.91	-3.58	2.06	1	1.51	2.01
-55	-1.13	-1.3	-1.57	-1.81	-1.49	-0.68	1.78	0.86	1.39	1.92
-50	0.96	-0.26	0.25	1.01	0.48	1.09	1.31	1.09	1.7	2.3
-45	3.15	3.63	3.75	3.99	2.07	1.95	1.18	0.41	1.37	2.33
-40	4.59	8.16	4.88	4.2	3.75	3.14	-0.25	-0.02	1.13	2.3
-35	7.34	7.83	5.42	5.36	5.3	5.39	0.62	-0.78	0.32	1.43
-30	8.18	11.07	5.65	5.69	5.8	5.47	0.21	-0.94	0.37	1.68
-25	11.65	8.86	6.75	4.18	4.9	4.09	0.5	-1.44	0.01	1.46
-20	11.02	9.89	3.2	2.64	4.15	3.22	-0.19	-1.95	-0.36	1.23
-15	9.82	6.15	3.15	2.48	2.29	3.21	-1	-1.4	-0.19	1
-10	10.47	2.8	-0.42	-0.33	1.66	1.6	-1.04	-0.7	0.13	0.96
-5	7.15	3.39	-1.78	-2.38	0.69	0.3	-1.01	-0.55	0.17	0.88
0	2.08	-1.2	-3.63	-3	-1.62	-1.05	-1.09	-0.9	-0.36	-0.9
5	-1.66	-2.12	-3.15	-2.6	-2.37	-1.84	-0.42	0.88	0.17	-0.55
10	-7	-3.12	-0.96	-0.48	-0.86	-2.44	-0.98	0.96	0.13	-0.7
15	-4.39	-8.14	-6.91	-2.75	-1.3	-2.08	0.28	1	-0.19	-1.4
20	-2.57	-2.44	-5.67	-5.48	-3.57	-0.57	1.06	1.23	-0.36	-1.95
25	-2.09	-2.15	-2.33	-5.88	-5.36	-1.88	1.98	1.46	0.01	-1.44
30	-0.54	-1.92	-2.23	-1.83	-5.91	-2.75	2.62	1.68	0.37	-0.94
35	0.1	-1.09	-0.75	-1.34	-2.12	-3.63	2.75	1.43	0.32	-0.78
40	1.56	0.45	1.53	1.22	2.56	0.39	3.51	2.3	1.13	-0.02
45	3.61	4.33	4.11	4.39	4.59	0.99	1.66	2.33	1.37	0.41
50	5.57	6.54	5.94	6.41	6.4	2.4	0.84	2.3	1.7	1.09
55	6.39	8.84	6.84	7.77	7.38	6.98	-0.16	1.92	1.39	0.86
60	6.9	9.06	7.77	7.56	7.39	6.96	-0.17	2.01	1.51	1
65	9.44	7.92	6.91	6.11	6.69	5.21	0.17	0.98	1.06	1.14
70	11.56	9.29	5.69	4.67	5.2	4.5	-0.76	0.93	1.13	1.34
75	10.67	7.81	6.2	5.68	5.66	5.21	-0.37	0.52	0.59	0.66
80	9.45	6.79	5.87	5.2	4.63	3.56	-0.7	0.28	0.58	0.88
85	5.27	5.73	3.07	2.71	2.18	1.63	-0.36	-0.04	0.41	0.86
90	0	0	0	0	0	0	0	0	0	0

TABLE E3. CONEX LIFT (cont.)

LIFT/Q, ft2										
beta	100	105	110	115	120	125	130	135	140	145
alpha										
-90	0	0	0	0	0	0	0	0	0	0
-85	-0.36	1.63	2.18	2.71	3.07	5.73	5.27	5.67	5.96	7.12
-80	-0.7	3.56	4.63	5.2	5.87	6.79	9.45	10.64	10.14	5.09
-75	-0.37	5.21	5.66	5.68	6.2	7.81	10.67	12.35	10.77	11.53
-70	-0.76	4.5	5.2	4.67	5.69	9.29	11.56	11.11	10.05	11.78
-65	0.17	5.21	6.69	6.11	6.91	7.92	9.44	9.06	8.33	6.83
-60	-0.17	6.96	7.39	7.56	7.77	9.06	6.9	6.47	5.64	5.4
-55	-0.16	6.98	7.38	7.77	6.84	8.84	6.39	5.74	4.93	4.49
-50	0.84	2.4	6.4	6.41	5.94	6.54	5.57	5.04	4.34	3.85
-45	1.66	0.99	4.59	4.39	4.11	4.33	3.61	3.62	3.55	3.38
-40	3.51	0.39	2.56	1.22	1.53	0.45	1.56	2.31	2.95	3.21
-35	2.75	-3.63	-2.12	-1.34	-0.75	-1.09	0.1	0.27	1.57	1.85
-30	2.62	-2.75	-5.91	-1.83	-2.23	-1.92	-0.54	-0.21	0.01	1.13
-25	1.98	-1.88	-5.36	-5.88	-2.33	-2.15	-2.09	-1.12	-0.63	0.32
-20	1.06	-0.57	-3.57	-5.48	-5.67	-2.44	-2.57	-2.5	-1.97	0.17
-15	0.28	-2.08	-1.3	-2.75	-6.91	-8.14	-4.39	-3.33	-2.78	1.52
-10	-0.98	-2.44	-0.86	-0.48	-0.96	-3.12	-7	-6.92	-4.89	3.4
-5	-0.42	-1.84	-2.37	-2.6	-3.15	-2.12	-1.66	-1.27	-0.18	3.41
0	-1.09	-1.05	-1.62	-3	-3.63	-1.2	2.08	3.05	2.89	4
5	-1.01	0.3	0.69	-2.38	-1.78	3.39	7.15	8.68	7.87	2.5
10	-1.04	1.6	1.66	-0.33	-0.42	2.8	10.47	12.99	11.2	2.61
15	-1	3.21	2.29	2.48	3.15	6.15	9.82	13	12.28	6.71
20	-0.19	3.22	4.15	2.64	3.2	9.89	11.02	10.65	11.11	9.49
25	0.5	4.09	4.9	4.18	6.75	8.86	11.65	7.99	8.35	7.37
30	0.21	5.47	5.8	5.69	5.65	11.07	8.18	6.33	6.19	6.21
35	0.62	5.39	5.3	5.36	5.42	7.83	7.34	5.11	5.29	5.22
40	-0.25	3.14	3.75	4.2	4.88	8.16	4.59	4.2	3.85	4.01
45	1.18	1.95	2.07	3.99	3.75	3.63	3.15	2.84	2.32	2.53
50	1.31	1.09	0.48	1.01	0.25	-0.26	0.96	1.49	1.74	2.1
55	1.78	-0.68	-1.49	-1.81	-1.57	-1.3	-1.13	-0.62	0.49	0.02
60	2.06	-3.58	-2.91	-2.93	-2.85	-1.72	-1.46	-1.16	-0.55	-0.41
65	2.22	-1.82	-3.21	-3.08	-2.44	-2.5	-2.04	-1.77	-1.13	-1.05
70	3.31	0.77	-3.17	-2.76	-1.75	-2.2	-2.97	-1.66	-1.23	-2.44
75	3.78	-1.13	-1.8	-1.53	-1.19	-2.04	-2.54	-2.53	-1.71	-2.5
80	3.69	0.43	-0.55	-1.37	-0.24	-1.04	-2.49	-2.47	-1.38	0.3
85	1.65	0.65	-0.82	-0.85	-0.78	-2.65	-2.97	-2.56	-0.94	0.9
90	0	0	0	0	0	0	0	0	0	0

TABLE E3. CONEX LIFT (cont.)

LIFT/Q, ft ²							
beta	150	155	160	165	170	175	180
alpha							
-90	0	0	0	0	0	0	0
-85	4.61	1.86	-1.63	-6.26	-9.05	-11.26	-13.37
-80	0.89	-2.12	-4.73	-8.32	-10.87	-12.52	-13.39
-75	0.97	-0.83	-2.88	-5.48	-8.44	-9.72	-10.36
-70	1.53	0.32	-1.59	-3.52	-5.88	-7	-8.78
-65	4.13	2.06	-0.06	-0.75	-3.42	-5.18	-6.29
-60	5.61	3.94	2.12	1.4	-0.3	-1.99	-3.12
-55	5.67	4.86	3.53	2.65	2	-0.73	-2.19
-50	4.96	4.21	4.24	3.94	3.75	4.23	3.58
-45	4.21	4.5	4.41	4.6	5.19	4.59	3.67
-40	3.54	4.46	4.76	5.04	5.88	5.45	6.26
-35	1.9	2.51	4.41	4.98	7.22	10.14	10.08
-30	1.12	2.77	5.25	6.75	8.63	10.88	10.85
-25	1.95	4.35	6.83	8.48	9.27	11.94	11.99
-20	2.53	4.31	6.38	9.21	10.61	12.17	13.22
-15	3.96	5.56	8.03	11.1	12.38	13.98	14.79
-10	4.73	7	9.82	12.47	14.11	16.08	16.89
-5	4.89	7.52	10.7	13.3	14.56	16.46	17.13
0	3.78	5.6	9.07	11.02	12.28	7.74	0.82
5	-0.26	-2.92	-5.22	-8.39	-7.92	-9.46	-9.52
10	-1.22	-5.58	-9.75	-12.9	-15.51	-16.98	-17.88
15	-1.84	-4.34	-7.3	-11.55	-15.45	-17.88	-18.9
20	1.26	-0.51	-3.21	-6.65	-10.26	-11.96	-11.76
25	4.87	1.38	-0.87	-2.19	-4.68	-5.37	-5.54
30	6.3	4.3	2.69	2.42	-0.02	-1	-1.19
35	6.02	5.54	5.28	4.19	2.73	1.36	1
40	4.65	4.37	5.33	5.63	4.2	4.73	-1.58
45	2.77	2.67	3.53	4.55	6.72	5.09	2.64
50	2.33	2.58	2.82	2.75	5.94	4.86	4.1
55	0.04	1.66	1.49	2.86	6.87	9.5	10.91
60	-0.93	1.17	3.28	3.47	7.06	9.86	11.57
65	0.44	1.7	4.24	6.09	8.8	10.69	12.62
70	2.88	2.66	6.49	9.09	11.11	13.29	14.12
75	5.37	4.06	9.44	12.22	14.11	16.33	16.08
80	5.81	7.72	11.36	14.46	17.59	19.45	20.7
85	4.09	6.64	9.26	13.17	15.4	13.87	12.17
90	0	0	0	0	0	0	0

TABLE E4. CONEX ROLL MOMENT

ROLL_MOMENT/Q, ft3										
beta	0	5	10	15	20	25	30	35	40	45
alpha										
-90	0	0	0	0	0	0	0	0	0	0
-85	1.33	3.39	4.92	4.68	2.59	3.85	4.32	7.34	3.59	2.16
-80	1.63	4.28	5.35	4.85	3.85	3.49	3.09	4.68	5.18	3.65
-75	2.09	2.33	2.69	3.59	3.02	6.24	1.76	1.73	-0.07	-0.1
-70	1.66	0.73	-0.1	1.03	0.4	2.09	-0.5	-1.86	-3.75	-5.98
-65	2.03	-0.86	-1.83	-1.66	-2.36	-3.32	-2.69	-4.55	-7.17	-9.33
-60	2.06	-2.16	-3.95	-3.09	-4.48	-5.68	-5.71	-7.71	-9.67	-11.66
-55	1.83	-2.56	-4.62	-4.65	-6.21	-7.37	-9.33	-9.17	-11.13	-12.65
-50	0.43	-1.43	-4.95	-7.11	-8.24	-8.8	-11.36	-12.56	-13.45	-14.12
-45	0.03	-2.13	-5.51	-7.31	-9.5	-11.09	-13.75	-15.68	-15.91	-15.94
-40	0.73	-2.06	-4.65	-8.54	-10.4	-13.25	-15.98	-18.07	-18.1	-17.77
-35	0.9	0.17	-3.89	-8.7	-11.96	-15.68	-18.83	-21.02	-20.93	-18.9
-30	1.2	-0.37	-4.12	-7.71	-14.25	-18.73	-23.15	-24.15	-23.22	-19.16
-25	0.66	-1.89	-6.48	-9.86	-14.61	-20.33	-24.91	-26.67	-24.41	-20.29
-20	0.3	-3.85	-9.23	-14.15	-18.53	-23.62	-24.81	-28.9	-29.03	-25.11
-15	0.23	-4.95	-9.93	-16.64	-21.92	-25.87	-27.47	-31.55	-34.24	-27.6
-10	-0.4	-3.75	-7.37	-15.08	-21.06	-26.57	-30.06	-32.78	-33.81	-28.17
-5	0.03	-2.79	-3.65	-9.6	-14.98	-20.46	-24.21	-28.13	-29.53	-27.63
0	-0.03	-0.13	-0.56	-2.66	-6.11	-12.72	-18.67	-22.52	-25.67	-25.91
5	0.17	-0.1	-0.8	-2.13	-3.99	-7.71	-11.43	-15.35	-17.6	-18.73
10	0.27	0.33	-0.9	-2.36	-4.52	-7.27	-9.57	-11.53	-17.17	-18.37
15	-0.07	-1.36	-1.83	-3.32	-5.02	-6.74	-7.81	-9.5	-10.79	-11.82
20	-0.23	-2.19	-2.76	-4.68	-5.75	-5.81	-7.24	-7.94	-9.37	-10.7
25	-0.47	-2.33	-3.12	-4.85	-5.68	-5.81	-7.01	-7.84	-8.9	-10.4
30	-1.26	-3.92	-3.82	-4.78	-5.95	-7.04	-7.04	-8.04	-9.8	-10.96
35	-0.8	-3.79	-2.72	-4.92	-5.51	-5.78	-6.88	-7.44	-9	-10.6
40	-0.53	-2.72	-2.69	-5.38	-6.05	-7.34	-7.44	-7.61	-8.74	-10.36
45	-0.13	-1.4	-2.19	-4.02	-5.05	-7.61	-7.37	-7.84	-8.97	-9.63
50	-0.03	-1.13	-1.56	-1.93	-4.55	-6.58	-6.78	-7.74	-7.67	-6.88
55	0.76	-1.3	-1.96	-2.16	-4.98	-6.08	-6.74	-7.97	-7.31	-5.65
60	0.66	-1.53	-2.03	-2.23	-4.72	-6.78	-8.7	-7.94	-6.81	-5.25
65	0.63	-1.4	-1.83	-2.19	-3.26	-6.48	-8.07	-8.04	-7.84	-5.91
70	0.37	-1.4	-2.23	-2.29	-3.55	-5.08	-6.14	-12.19	-10.5	-9.13
75	0.33	-1.86	-3.06	-3.89	-4.19	-4.82	-6.68	-15.05	-11.79	-7.54
80	-0.03	-2.86	-3.95	-4.38	-4.52	-5.68	-8.04	-10.03	-7.41	-5.68
85	-0.4	-3.52	-4.92	-5.12	-4.75	-4.48	-4.78	-6.08	-3.89	-3.62
90	0	0	0	0	0	0	0	0	0	0

TABLE E4. CONEX ROLL MOMENT (cont.)

ROLL_MOMENT/Q, ft3										
beta	50	55	60	65	70	75	80	85	90	95
alpha										
-90	0	0	0	0	0	0	0	0	0	0
-85	0.13	-3.69	-2.52	-1.2	-0.86	-0.76	-0.37	0.5	0.07	-0.37
-80	1.03	-3.52	-5.85	-3.69	-2.13	-1.76	-1.1	0.8	0.17	-0.47
-75	-0.47	-4.28	-4.95	-2.66	-2.72	-2.86	-1.06	0.8	0.07	-0.63
-70	-6.14	-7.54	-5.38	-5.75	-2.89	-2.72	-1.23	1.13	-0.1	-1.33
-65	-9.47	-9.5	-9.1	-6.48	-5.38	-2.66	-2.06	1.36	0	-1.36
-60	-11.99	-10.93	-9.73	-8.57	-5.12	-3.42	-1.69	0.9	-0.47	-1.86
-55	-13.22	-11.92	-10.89	-9.07	-4.78	-3.99	-1.36	1.26	-0.37	-1.96
-50	-13.75	-13.09	-11.26	-8.37	-6.84	-3.16	0.33	1.36	-0.4	-2.16
-45	-14.75	-12.52	-10	-8.97	-6.84	-2.86	-0.9	1.06	-0.4	-1.89
-40	-16.57	-12.36	-10.96	-7.91	-6.14	-2.86	1.26	1.66	-0.1	-1.86
-35	-15.91	-11.56	-11.13	-8.54	-5.65	-4.52	0.27	2.33	0.33	-1.63
-30	-15.74	-9.93	-11.13	-9.47	-6.91	-5.88	0.27	2.79	0.66	-1.49
-25	-14.91	-8.84	-8.6	-9.53	-8.44	-4.15	-0.23	2.49	0.47	-1.53
-20	-16.94	-9.53	-9.23	-9.2	-8.34	-3.92	1.13	2.86	0.8	-1.26
-15	-18	-11.56	-10.36	-11.06	-6.34	-5.02	1.73	2.69	0.47	-1.79
-10	-20.63	-13.45	-11.39	-8.54	-6.91	-4.58	2.26	2.03	0.23	-1.56
-5	-23.42	-15.78	-11.16	-8.34	-6.61	-4.38	1.96	1.56	0.03	-1.46
0	-22.88	-17.8	-12.32	-8.7	-5.08	-2.26	1.3	2.13	0	-2.13
5	-16.04	-11.49	-10.7	-9.5	-4.98	-2.49	1.06	1.46	-0.03	-1.56
10	-17.04	-10.56	-8.67	-5.65	-3.59	-1.86	1.2	1.56	-0.23	-2.03
15	-13.05	-14.12	-11.96	-6.88	-1.79	-0.63	0.47	1.79	-0.47	-2.69
20	-10.66	-9.23	-10.86	-9.57	-4.98	0.03	-0.33	1.26	-0.8	-2.86
25	-11.36	-9.57	-9.07	-8.87	-7.57	-1.2	0.33	1.53	-0.47	-2.49
30	-10.6	-10.23	-8.5	-7.44	-6.21	-2.69	0.3	1.49	-0.66	-2.79
35	-9.43	-9.5	-8.77	-6.44	-4.02	-4.15	0.4	1.63	-0.33	-2.33
40	-9.13	-8	-7.47	-5.51	-3.35	-2.26	1.99	1.86	0.1	-1.66
45	-8.04	-6.64	-5.68	-5.15	-3.29	-0.9	0.5	1.89	0.4	-1.06
50	-5.98	-7.17	-4.45	-4.09	-3.09	-0.47	1.59	2.16	0.4	-1.36
55	-6.64	-4.52	-3.09	-4.02	-2.69	-1.56	1.13	1.96	0.37	-1.26
60	-5.15	-3.62	-1.66	-3.85	-2.46	-2.66	1.4	1.86	0.47	-0.9
65	-5.48	0.8	2.76	-0.76	-2.46	-1.03	1.36	1.36	0	-1.36
70	-3.59	-0.96	1.73	0.8	-1.79	-0.2	1.16	1.33	0.1	-1.13
75	-2.29	1.93	1.06	-1.03	-0.66	-0.73	1.3	0.63	-0.07	-0.8
80	-2.69	-0.13	-0.17	-0.1	-0.93	-0.7	1.13	0.47	-0.17	-0.8
85	-2.69	-0.9	-0.83	-0.43	-0.53	-0.33	0.56	0.37	-0.07	-0.5
90	0	0	0	0	0	0	0	0	0	0

TABLE E4. CONEX ROLL MOMENT (cont.)

ROLL_MOMENT/Q, ft3										
beta	100	105	110	115	120	125	130	135	140	145
alpha										
-90	0	0	0	0	0	0	0	0	0	0
-85	-0.56	0.33	0.53	0.43	0.83	0.9	2.69	3.62	3.89	6.08
-80	-1.13	0.7	0.93	0.1	0.17	0.13	2.69	5.68	7.41	10.03
-75	-1.3	0.73	0.66	1.03	-1.06	-1.93	2.29	7.54	11.79	15.05
-70	-1.16	0.2	1.79	-0.8	-1.73	0.96	3.59	9.13	10.5	12.19
-65	-1.36	1.03	2.46	0.76	-2.76	-0.8	5.48	5.91	7.84	8.04
-60	-1.4	2.66	2.46	3.85	1.66	3.62	5.15	5.25	6.81	7.94
-55	-1.13	1.56	2.69	4.02	3.09	4.52	6.64	5.65	7.31	7.97
-50	-1.59	0.47	3.09	4.09	4.45	7.17	5.98	6.88	7.67	7.74
-45	-0.5	0.9	3.29	5.15	5.68	6.64	8.04	9.63	8.97	7.84
-40	-1.99	2.26	3.35	5.51	7.47	8	9.13	10.36	8.74	7.61
-35	-0.4	4.15	4.02	6.44	8.77	9.5	9.43	10.6	9	7.44
-30	-0.3	2.69	6.21	7.44	8.5	10.23	10.6	10.96	9.8	8.04
-25	-0.33	1.2	7.57	8.87	9.07	9.57	11.36	10.4	8.9	7.84
-20	0.33	-0.03	4.98	9.57	10.86	9.23	10.66	10.7	9.37	7.94
-15	-0.47	0.63	1.79	6.88	11.96	14.12	13.05	11.82	10.79	9.5
-10	-1.2	1.86	3.59	5.65	8.67	10.56	17.04	18.37	17.17	11.53
-5	-1.06	2.49	4.98	9.5	10.7	11.49	16.04	18.73	17.6	15.35
0	-1.3	2.26	5.08	8.7	12.32	17.8	22.88	25.91	25.67	22.52
5	-1.96	4.38	6.61	8.34	11.16	15.78	23.42	27.63	29.53	28.13
10	-2.26	4.58	6.91	8.54	11.39	13.45	20.63	28.17	33.81	32.78
15	-1.73	5.02	6.34	11.06	10.36	11.56	18	27.6	34.24	31.55
20	-1.13	3.92	8.34	9.2	9.23	9.53	16.94	25.11	29.03	28.9
25	0.23	4.15	8.44	9.53	8.6	8.84	14.91	20.29	24.41	26.67
30	-0.27	5.88	6.91	9.47	11.13	9.93	15.74	19.16	23.22	24.15
35	-0.27	4.52	5.65	8.54	11.13	11.56	15.91	18.9	20.93	21.02
40	-1.26	2.86	6.14	7.91	10.96	12.36	16.57	17.77	18.1	18.07
45	0.9	2.86	6.84	8.97	10	12.52	14.75	15.94	15.91	15.68
50	-0.33	3.16	6.84	8.37	11.26	13.09	13.75	14.12	13.45	12.56
55	1.36	3.99	4.78	9.07	10.89	11.92	13.22	12.65	11.13	9.17
60	1.69	3.42	5.12	8.57	9.73	10.93	11.99	11.66	9.67	7.71
65	2.06	2.66	5.38	6.48	9.1	9.5	9.47	9.33	7.17	4.55
70	1.23	2.72	2.89	5.75	5.38	7.54	6.14	5.98	3.75	1.86
75	1.06	2.86	2.72	2.66	4.95	4.28	0.47	0.1	0.07	-1.73
80	1.1	1.76	2.13	3.69	5.85	3.52	-1.03	-3.65	-5.18	-4.68
85	0.37	0.76	0.86	1.2	2.52	3.69	-0.13	-2.16	-3.59	-7.34
90	0	0	0	0	0	0	0	0	0	0

TABLE E4. CONEX ROLL MOMENT (cont.)

ROLL_MOMENT/Q, ft3							
beta	150	155	160	165	170	175	180
alpha							
-90	0	0	0	0	0	0	0
-85	4.78	4.48	4.75	5.12	4.92	3.52	0
-80	8.04	5.68	4.52	4.38	3.95	2.86	0
-75	6.68	4.82	4.19	3.89	3.06	1.86	0
-70	6.14	5.08	3.55	2.29	2.23	1.4	0
-65	8.07	6.48	3.26	2.19	1.83	1.4	0
-60	8.7	6.78	4.72	2.23	2.03	1.53	0
-55	6.74	6.08	4.98	2.16	1.96	1.3	0
-50	6.78	6.58	4.55	1.93	1.56	1.13	0
-45	7.37	7.61	5.05	4.02	2.19	1.4	0
-40	7.44	7.34	6.05	5.38	2.69	2.72	0
-35	6.88	5.78	5.51	4.92	2.72	3.79	0
-30	7.04	7.04	5.95	4.78	3.82	3.92	0
-25	7.01	5.81	5.68	4.85	3.12	2.33	0
-20	7.24	5.81	5.75	4.68	2.76	2.19	0
-15	7.81	6.74	5.02	3.32	1.83	1.36	0
-10	9.57	7.27	4.52	2.36	0.9	-0.33	0
-5	11.43	7.71	3.99	2.13	0.8	0.1	0
0	18.67	12.72	6.11	2.66	0.56	0.13	0
5	24.21	20.46	14.98	9.6	3.65	2.79	0
10	30.06	26.57	21.06	15.08	7.37	3.75	0
15	27.47	25.87	21.92	16.64	9.93	4.95	0
20	24.81	23.62	18.53	14.15	9.23	3.85	0
25	24.91	20.33	14.61	9.86	6.48	1.89	0
30	23.15	18.73	14.25	7.71	4.12	0.37	0
35	18.83	15.68	11.96	8.7	3.89	-0.17	0
40	15.98	13.25	10.4	8.54	4.65	2.06	0
45	13.75	11.09	9.5	7.31	5.51	2.13	0
50	11.36	8.8	8.24	7.11	4.95	1.43	0
55	9.33	7.37	6.21	4.65	4.62	2.56	0
60	5.71	5.68	4.48	3.09	3.95	2.16	0
65	2.69	3.32	2.36	1.66	1.83	0.86	0
70	0.5	-2.09	-0.4	-1.03	0.1	-0.73	0
75	-1.76	-6.24	-3.02	-3.59	-2.69	-2.33	0
80	-3.09	-3.49	-3.85	-4.85	-5.35	-4.28	0
85	-4.32	-3.85	-2.59	-4.68	-4.92	-3.39	0
90	0	0	0	0	0	0	0

TABLE E5. CONEX PITCHING MOMENT

PITCH_MOMENT/Q, ft3										
beta	0	5	10	15	20	25	30	35	40	45
alpha										
-90	0	0	0	0	0	0	0	0	0	0
-85	18.37	19.03	21.36	19	16.81	16.94	15.38	9.7	1.96	-3.16
-80	33.88	33.98	31.32	27.93	24.74	22.12	21.02	13.25	3.62	-2.59
-75	43.48	35.97	33.41	30.13	26.24	25.34	19.36	11.99	11.46	5.91
-70	34.14	28.56	26.11	22.88	19.13	15.71	11.79	7.67	8.17	7.54
-65	19.93	16.97	14.55	11.76	9.13	1.69	3.69	2.49	2.96	3.12
-60	2.26	3.09	1.59	-0.96	-1.13	-2.59	-2.46	-4.42	-3.35	-2.06
-55	-5.78	-9.17	-10.56	-10.5	-8.07	-8.6	-7.84	-10.3	-9.33	-7.34
-50	-16.67	-18.83	-18.83	-16.77	-15.38	-16.01	-14.75	-15.11	-14.68	-12.39
-45	-25.71	-28.33	-26.77	-26.34	-24.05	-22.69	-21.59	-20.36	-19.56	-17.14
-40	-38.3	-36.6	-36.4	-33.88	-32.62	-30.09	-28.53	-26.04	-24.18	-22.05
-35	-47.26	-47.5	-43.74	-40.75	-37.53	-38	-34.44	-31.35	-28.56	-25.84
-30	-60.19	-59.45	-55.67	-50.82	-46.5	-44.24	-41.72	-37.3	-33.25	-30.36
-25	-69.82	-68.65	-65.2	-61.48	-56.9	-49.92	-47.4	-42.75	-38.03	-33.98
-20	-71.35	-71.05	-68.02	-65.8	-62.94	-58.72	-55.3	-48.06	-41.15	-35.27
-15	-60.58	-62.44	-62.74	-63.07	-62.44	-60.09	-57.89	-51.28	-41.35	-33.85
-10	-48.23	-50.12	-53.38	-55.5	-54.97	-54.54	-51.52	-48.26	-37.1	-28.4
-5	-34.94	-35.91	-37.6	-40.16	-38.76	-39.59	-38.93	-37.17	-31.32	-30.92
0	-23.78	-17.97	-12.75	-14.98	-15.35	-18.83	-20.06	-21.39	-29	-33.78
5	2.39	0.03	-1.73	-4.55	-6.01	-8.9	-10.53	-13.19	-24.45	-33.65
10	6.64	3.59	1.36	-1	-3.65	-5.28	-7.57	-10.7	-16.04	-19.23
15	10.53	7.64	5.65	2.92	0.6	-1.56	-3.19	-5.68	-9	-10.5
20	7.57	4.88	3.29	0.76	-0.03	-1.76	-3.95	-5.75	-6.28	-7.37
25	3.55	0.76	0.33	-0.23	-1.03	-3.12	-4.62	-4.62	-6.24	-6.88
30	-0.5	-3.22	-3.99	-3.52	-3.49	-5.98	-5.31	-5.85	-6.14	-6.31
35	-6.44	-9	-8.4	-7.01	-7.54	-6.21	-6.14	-7.11	-7.34	-6.24
40	-8.27	-9.53	-10.2	-7.91	-8.84	-10.43	-8.3	-8.8	-8.74	-7.87
45	-13.75	-14.81	-15.71	-14.61	-13.22	-14.12	-11.43	-10.96	-10.6	-10.46
50	-18.67	-18.37	-16.54	-16.28	-15.84	-13.95	-12.62	-11.09	-9.8	-9.47
55	-21.56	-20.06	-17.77	-16.31	-15.71	-15.31	-14.15	-11.99	-10.53	-10.79
60	-27.14	-26.37	-24.08	-21.12	-19.56	-17.6	-15.81	-14.15	-12.69	-12.16
65	-32.58	-31.59	-29.26	-26.34	-23.48	-20.66	-18.83	-15.91	-12.82	-11.82
70	-36.1	-35.04	-32.58	-28.43	-25.21	-21.76	-18.97	-11.99	-10	-5.21
75	-37.6	-36.1	-33.48	-29.33	-26.24	-23.05	-20.26	-8.77	-4.38	-1.4
80	-32.72	-31.26	-29.63	-25.94	-23.22	-20.76	-16.61	-6.31	5.68	9.37
85	-26.87	-27.07	-24.98	-21.59	-16.84	-12.02	-5.58	3.35	5.25	5.81
90	0	0	0	0	0	0	0	0	0	0

TABLE E5. CONEX PITCHING MOMENT (cont.)

PITCH_MOMENT/Q, ft3										
beta	50	55	60	65	70	75	80	85	90	95
alpha										
-90	0	0	0	0	0	0	0	0	0	0
-85	-2.89	9.2	10.93	8	3.79	1.69	1.36	0.4	-0.73	-1.83
-80	-1.96	12.32	17.4	11.92	6.31	2.89	5.31	-1.76	-2.03	-2.29
-75	1.83	8.84	9.7	7.64	6.28	4.82	4.02	-1.86	-2.42	-2.99
-70	4.75	7.77	6.08	6.38	5.38	3.82	2.86	-2.69	-4.02	-5.31
-65	3.79	6.31	5.05	6.05	4.92	0.86	1.89	-1.79	-2.06	-2.36
-60	-0.27	2.13	4.48	4.78	1.93	-0.7	0.37	-3.89	-5.25	-6.58
-55	-4.32	-0.17	1.03	3.39	0.2	-1.49	-0.83	-3.59	-4.35	-5.12
-50	-10.2	-5.71	-2.06	0.37	0.33	-1.76	-3.35	-4.88	-4.48	-4.09
-45	-12.75	-8.4	-6.64	-5.38	-2.19	-2.33	-3.99	-5.65	-4.78	-3.89
-40	-18.43	-13.62	-11.76	-9.43	-5.12	-3.02	-6.34	-7.67	-5.41	-3.16
-35	-21.02	-18.53	-16.67	-12.99	-5.78	-3.82	-7.27	-8	-4.58	-1.13
-30	-26.04	-21.82	-19.8	-15.64	-10.6	-6.64	-8.07	-9.37	-4.52	0.33
-25	-28.83	-28.53	-26.14	-21.99	-17.04	-8.07	-8.54	-6.88	-4.12	-1.33
-20	-32.42	-33.25	-31.45	-27	-20.36	-8.6	-10.93	-7.64	-3.26	1.16
-15	-36.27	-38	-34.14	-28.03	-18.47	-10.76	-11.03	-6.54	-3.49	-0.43
-10	-31.85	-39.39	-35.54	-28.7	-20.29	-7.21	-10.73	-3.79	-1.76	0.27
-5	-27.8	-36.74	-32.19	-24.48	-13.98	-6.24	-10.23	0.6	0.6	0.56
0	-30.23	-26.11	-25.04	-18.33	-12.42	-7.24	-9	-5.38	-0.37	-5.38
5	-31.32	-17.11	-10.7	-4.22	-6.71	-5.15	-6.98	0.56	0.6	0.6
10	-16.84	-12.29	-6.11	-4.09	-5.45	-5.12	-5.78	0.27	-1.76	-3.79
15	-7.74	-2.46	1.23	-0.83	-9.23	-11.43	-2.86	-0.43	-3.49	-6.54
20	-7.37	-6.34	1.89	2.62	-1.2	-10.13	-1.43	1.16	-3.26	-7.64
25	-5.21	-4.15	-2.13	2.72	3.22	-6.31	-6.44	-1.33	-4.12	-6.88
30	-5.02	-2.33	0.5	2.33	3.49	-3.95	-5.95	0.33	-4.52	-9.37
35	-5.75	-1.53	0.23	1.59	0.03	1.93	-5.08	-1.13	-4.58	-8
40	-7.41	-4.65	-1.33	-0.07	-1.96	2.36	-6.21	-3.16	-5.41	-7.67
45	-8.3	-5.05	-3.79	-3.72	-4.02	1.36	-1.26	-3.89	-4.78	-5.65
50	-8.54	-5.95	-7.74	-7.94	-5.78	0.27	-2.46	-4.09	-4.48	-4.88
55	-8.9	-6.91	-10	-10.3	-4.95	-3.22	-1.83	-5.12	-4.35	-3.59
60	-11.43	-9.23	-13.52	-11.59	-8.67	-5.08	-2.03	-6.58	-5.25	-3.89
65	-10.96	-14.75	-16.18	-16.31	-12.59	-4.82	-2.99	-2.36	-2.06	-1.79
70	-7.77	-14.12	-19.2	-18.47	-12.85	-5.05	-2.16	-5.31	-4.02	-2.69
75	-6.08	-16.77	-18.47	-14.81	-9.83	-5.88	-2.49	-2.99	-2.42	-1.86
80	2.72	-5.91	-9.17	-11.89	-7.97	-2.62	-1	-2.29	-2.03	-1.76
85	5.05	1.73	-3.52	-3.72	-2.29	-1.69	-0.93	-1.83	-0.73	0.4
90	0	0	0	0	0	0	0	0	0	0

TABLE E5. CONEX PITCHING MOMENT (cont.)

PITCH_MOMENT/Q, ft3										
beta	100	105	110	115	120	125	130	135	140	145
alpha										
-90	0	0	0	0	0	0	0	0	0	0
-85	-0.93	-1.69	-2.29	-3.72	-3.52	1.73	5.05	5.81	5.25	3.35
-80	-1	-2.62	-7.97	-11.89	-9.17	-5.91	2.72	9.37	5.68	-6.31
-75	-2.49	-5.88	-9.83	-14.81	-18.47	-16.77	-6.08	-1.4	-4.38	-8.77
-70	-2.16	-5.05	-12.85	-18.47	-19.2	-14.12	-7.77	-5.21	-10	-11.99
-65	-2.99	-4.82	-12.59	-16.31	-16.18	-14.75	-10.96	-11.82	-12.82	-15.91
-60	-2.03	-5.08	-8.67	-11.59	-13.52	-9.23	-11.43	-12.16	-12.69	-14.15
-55	-1.83	-3.22	-4.95	-10.3	-10	-6.91	-8.9	-10.79	-10.53	-11.99
-50	-2.46	0.27	-5.78	-7.94	-7.74	-5.95	-8.54	-9.47	-9.8	-11.09
-45	-1.26	1.36	-4.02	-3.72	-3.79	-5.05	-8.3	-10.46	-10.6	-10.96
-40	-6.21	2.36	-1.96	-0.07	-1.33	-4.65	-7.41	-7.87	-8.74	-8.8
-35	-5.08	1.93	0.03	1.59	0.23	-1.53	-5.75	-6.24	-7.34	-7.11
-30	-5.95	-3.95	3.49	2.33	0.5	-2.33	-5.02	-6.31	-6.14	-5.85
-25	-6.44	-6.31	3.22	2.72	-2.13	-4.15	-5.21	-6.88	-6.24	-4.62
-20	-1.43	-10.13	-1.2	2.62	1.89	-6.34	-7.37	-7.37	-6.28	-5.75
-15	-2.86	-11.43	-9.23	-0.83	1.23	-2.46	-7.74	-10.5	-9	-5.68
-10	-5.78	-5.12	-5.45	-4.09	-6.11	-12.29	-16.84	-19.23	-16.04	-10.7
-5	-6.98	-5.15	-6.71	-4.22	-10.7	-17.11	-31.32	-33.65	-24.45	-13.19
0	-9	-7.24	-12.42	-18.33	-25.04	-26.11	-30.23	-33.78	-29	-21.39
5	-10.23	-6.24	-13.98	-24.48	-32.19	-36.74	-27.8	-30.92	-31.32	-37.17
10	-10.73	-7.21	-20.29	-28.7	-35.54	-39.39	-31.85	-28.4	-37.1	-48.26
15	-11.03	-10.76	-18.47	-28.03	-34.14	-38	-36.27	-33.85	-41.35	-51.28
20	-10.93	-8.6	-20.36	-27	-31.45	-33.25	-32.42	-35.27	-41.15	-48.06
25	-8.54	-8.07	-17.04	-21.99	-26.14	-28.53	-28.83	-33.98	-38.03	-42.75
30	-8.07	-6.64	-10.6	-15.64	-19.8	-21.82	-26.04	-30.36	-33.25	-37.3
35	-7.27	-3.82	-5.78	-12.99	-16.67	-18.53	-21.02	-25.84	-28.56	-31.35
40	-6.34	-3.02	-5.12	-9.43	-11.76	-13.62	-18.43	-22.05	-24.18	-26.04
45	-3.99	-2.33	-2.19	-5.38	-6.64	-8.4	-12.75	-17.14	-19.56	-20.36
50	-3.35	-1.76	0.33	0.37	-2.06	-5.71	-10.2	-12.39	-14.68	-15.11
55	-0.83	-1.49	0.2	3.39	1.03	-0.17	-4.32	-7.34	-9.33	-10.3
60	0.37	-0.7	1.93	4.78	4.48	2.13	-0.27	-2.06	-3.35	-4.42
65	1.89	0.86	4.92	6.05	5.05	6.31	3.79	3.12	2.96	2.49
70	2.86	3.82	5.38	6.38	6.08	7.77	4.75	7.54	8.17	7.67
75	4.02	4.82	6.28	7.64	9.7	8.84	1.83	5.91	11.46	11.99
80	5.31	2.89	6.31	11.92	17.4	12.32	-1.96	-2.59	3.62	13.25
85	1.36	1.69	3.79	8	10.93	9.2	-2.89	-3.16	1.96	9.7
90	0	0	0	0	0	0	0	0	0	0

TABLE E5. CONEX PITCHING MOMENT (cont.)

PITCH_MOMEN/Q, ft3							
beta	150	155	160	165	170	175	180
alpha							
-90	0	0	0	0	0	0	0
-85	-5.58	-12.02	-16.84	-21.59	-24.98	-27.07	-26.87
-80	-16.61	-20.76	-23.22	-25.94	-29.63	-31.26	-32.72
-75	-20.26	-23.05	-26.24	-29.33	-33.48	-36.1	-37.6
-70	-18.97	-21.76	-25.21	-28.43	-32.58	-35.04	-36.1
-65	-18.83	-20.66	-23.48	-26.34	-29.26	-31.59	-32.58
-60	-15.81	-17.6	-19.56	-21.12	-24.08	-26.37	-27.14
-55	-14.15	-15.31	-15.71	-16.31	-17.77	-20.06	-21.56
-50	-12.62	-13.95	-15.84	-16.28	-16.54	-18.37	-18.67
-45	-11.43	-14.12	-13.22	-14.61	-15.71	-14.81	-13.75
-40	-8.3	-10.43	-8.84	-7.91	-10.2	-9.53	-8.27
-35	-6.14	-6.21	-7.54	-7.01	-8.4	-9	-6.44
-30	-5.31	-5.98	-3.49	-3.52	-3.99	-3.22	-0.5
-25	-4.62	-3.12	-1.03	-0.23	0.33	0.76	3.55
-20	-3.95	-1.76	-0.03	0.76	3.29	4.88	7.57
-15	-3.19	-1.56	0.6	2.92	5.65	7.64	10.53
-10	-7.57	-5.28	-3.65	-1	1.36	3.59	6.64
-5	-10.53	-8.9	-6.01	-4.55	-1.73	0.03	2.39
0	-20.06	-18.83	-15.35	-14.98	-12.75	-17.97	-23.78
5	-38.93	-39.59	-38.76	-40.16	-37.6	-35.91	-34.94
10	-51.52	-54.54	-54.97	-55.5	-53.38	-50.12	-48.23
15	-57.89	-60.09	-62.44	-63.07	-62.74	-62.44	-60.58
20	-55.3	-58.72	-62.94	-65.8	-68.02	-71.05	-71.35
25	-47.4	-49.92	-56.9	-61.48	-65.2	-68.65	-69.82
30	-41.72	-44.24	-46.5	-50.82	-55.67	-59.45	-60.19
35	-34.44	-38	-37.53	-40.75	-43.74	-47.5	-47.26
40	-28.53	-30.09	-32.62	-33.88	-36.4	-36.6	-38.3
45	-21.59	-22.69	-24.05	-26.34	-26.77	-28.33	-25.71
50	-14.75	-16.01	-15.38	-16.77	-18.83	-18.83	-16.67
55	-7.84	-8.6	-8.07	-10.5	-10.56	-9.17	-5.78
60	-2.46	-2.59	-1.13	-0.96	1.59	3.09	2.26
65	3.69	1.69	9.13	11.76	14.55	16.97	19.93
70	11.79	15.71	19.13	22.88	26.11	28.56	34.14
75	19.36	25.34	26.24	30.13	33.41	35.97	43.48
80	21.02	22.12	24.74	27.93	31.32	33.98	33.88
85	15.38	16.94	16.81	19	21.36	19.03	18.37
90	0	0	0	0	0	0	0

TABLE E6. CONEX YAW MOMENT

YAW_MOMENT/Q, ft3										
beta	0	5	10	15	20	25	30	35	40	45
alpha										
-90	-0.76	11.82	25.77	34.21	38.2	32.22	25.94	21.09	19.73	14.68
-85	-2.82	9.77	23.52	31.55	35.84	31.02	24.81	19.26	18.3	13.82
-80	-2.06	11.03	21.76	28	32.35	27.14	20.89	15.41	16.87	13.42
-75	-3.65	12.65	23.48	27	31.02	23.62	18.43	16.14	13.88	10.7
-70	0.17	11.79	23.81	27.24	29.43	23.22	16.97	15.74	12.75	8.07
-65	-2.72	11.82	21.22	24.21	25.14	16.64	15.98	13.25	9.3	4.98
-60	-0.47	12.56	19.46	20.99	22.49	17.17	18	12.69	8.47	4.35
-55	-1.2	12.65	17.5	18.7	19.16	16.37	15.08	13.78	9.67	5.08
-50	-1.13	7.97	14.18	14.75	16.18	15.18	13.02	12.36	9.67	5.98
-45	-0.8	7.91	10.63	13.85	14.18	14.58	12.59	11.53	9.5	6.11
-40	-0.47	7.57	9.77	12.46	14.58	14.55	14.05	11.86	9.03	4.82
-35	1.46	12.75	13.62	16.01	15.78	17.37	15.21	13.52	9.4	6.14
-30	3.92	12.99	16.01	19.66	19.2	18	16.97	12.26	9.07	4.75
-25	2.19	16.44	22.09	24.48	26.9	20.19	17.37	14.28	9.96	5.02
-20	1.2	17.04	25.48	29.99	31.29	23.72	21.92	17.3	14.81	9
-15	0.93	15.25	25.24	32.15	33.51	26.14	23.62	20.23	17.44	10.13
-10	0.73	14.32	26.94	33.48	34.68	28.7	23.52	18.67	16.87	10.03
-5	0.4	12.39	26.9	34.41	36.24	31.92	26.24	20.93	16.87	12.29
0	0.33	13.68	28.27	32.95	33.48	29.66	24.35	21.95	18.2	13.25
5	0.37	14.08	26.6	29.79	31.52	26.77	21.95	20.46	18.3	13.55
10	0.17	12.72	23.58	28.53	29.13	24.48	18.43	16.84	15.01	10.03
15	2.42	17.04	25.31	29.63	29.96	24.98	19.13	17.64	14.25	9.6
20	1.79	15.64	23.81	27.73	27.2	22.39	18.23	16.01	12.69	8
25	1.79	15.28	22.88	26.01	24.68	20.53	17.8	14.42	10.89	6.54
30	3.59	18.27	24.05	23.65	22.25	19.7	18.63	13.65	9.73	6.68
35	4.42	20.06	22.49	22.49	19.4	19.36	17.64	14.91	10.2	7.14
40	1.93	15.18	20.99	19.96	18.17	17.87	16.51	13.62	11.16	7.24
45	1.26	15.01	20.39	19.83	17.7	17.11	14.75	12.29	10.96	5.98
50	2.26	13.02	20.79	20.76	18.8	17.87	15.01	12.75	10.76	6.68
55	2.69	14.42	19.8	20.69	19.73	18.4	16.11	13.92	9.57	6.31
60	2.16	13.85	19	23.05	20.63	18.37	18.67	12.65	8.93	5.31
65	1.63	12.99	20.93	26.24	25.91	19.56	16.34	13.52	10.86	6.84
70	2.09	13.42	21.95	29.69	28.86	22.09	17.21	17.64	15.68	12.46
75	2.69	15.51	24.28	31.12	31.06	23.75	18.67	19.26	17.87	11.66
80	1.56	14.81	23.91	31.45	31.65	26.01	20.46	17.7	16.41	11.49
85	1.1	16.21	27.4	34.84	35.04	28.8	21.89	17.54	15.28	11.29
90	0.03	27.4	34.81	39.23	36.93	29.63	23.58	17.44	16.08	11.82

TABLE E6. CONEX YAW MOMENT (cont.)

YAW_MOMENT/Q, ft3										
beta	50	55	60	65	70	75	80	85	90	95
alpha										
-90	7.01	-3.39	-11.36	-21.89	-34.38	-43.84	-47.23	-33.51	-0.07	18.33
-85	6.61	-3.29	-11.09	-21.42	-34.41	-45.01	-47.26	-35.51	-15.28	4.95
-80	7.17	-4.88	-14.12	-24.55	-33.08	-45.14	-47.63	-36.7	-14.05	8.57
-75	5.88	-4.42	-10.73	-20	-37.37	-45.17	-47.56	-35.21	-12.46	10.33
-70	4.42	-2.49	-13.52	-21.95	-33.05	-47.07	-48.13	-37	-11.79	13.42
-65	0.9	-7.11	-12.72	-27.53	-35.91	-46.67	-50.19	-36.2	-7.21	21.82
-60	-0.4	-7.67	-20.53	-31.16	-42.45	-45.17	-49.86	-40.59	-11.63	17.34
-55	-0.47	-9.1	-18.1	-33.55	-47	-49.72	-48.86	-39.63	-7.24	25.14
-50	0.7	-6.94	-19.56	-35.11	-44.64	-51.75	-44.94	-42.32	-7.74	26.84
-45	-1.3	-12.95	-24.18	-29.23	-44.28	-52.38	-47.7	-43.05	-3.92	35.17
-40	-0.13	-9.03	-21.06	-34.74	-45.14	-52.51	-43.74	-41.75	-4.68	32.38
-35	-2.82	-13.42	-19.86	-33.12	-47.86	-49.49	-48.96	-38.23	-2.23	33.81
-30	-2.89	-12.69	-23.72	-31.79	-43.41	-47.3	-50.92	-36.37	-3.62	29.13
-25	-2.56	-13.32	-19.2	-32.98	-37.7	-49.39	-51.81	-30.03	0.63	31.29
-20	1.53	-8.57	-20.53	-28.46	-35.11	-49.95	-49.02	-30.23	-2.59	25.04
-15	1.36	-7.71	-15.74	-25.18	-38.7	-46.14	-47.76	-26.24	-0.96	24.28
-10	4.12	-6.68	-14.95	-26.24	-33.91	-46.3	-48.09	-23.88	-1	21.89
-5	6.78	-2.92	-13.65	-22.75	-32.58	-46.7	-47.63	-23.38	0.63	24.65
0	8.14	-2.52	-12.29	-22.98	-35.57	-45.84	-46.07	-23.32	0	23.32
5	7.64	-1.73	-12.56	-21.52	-32.42	-46.37	-46.14	-24.65	-0.63	23.38
10	5.68	-3.59	-12.16	-23.08	-30.52	-46.6	-44.31	-21.89	1	23.88
15	4.22	-4.88	-12.06	-20.23	-34.84	-43.48	-44.81	-24.28	0.96	26.24
20	4.45	0.2	-15.31	-23.15	-31.95	-46.14	-45.14	-25.04	2.59	30.23
25	1.86	-5.25	-11.29	-28.56	-36.17	-46.23	-46.73	-31.29	-0.63	30.03
30	2.09	-6.24	-18.7	-29.16	-45.11	-46.67	-44.91	-29.13	3.62	36.37
35	1.03	-8.4	-17.07	-30.96	-48.43	-53.71	-43.48	-33.81	2.23	38.23
40	1.1	-4.62	-18.4	-32.55	-43.61	-53.77	-36.47	-32.38	4.68	41.75
45	-1.13	-11.49	-22.55	-26.87	-41.75	-53.87	-44.54	-35.17	3.92	43.05
50	1	-5.12	-17.4	-32.45	-42.61	-53.08	-40.42	-26.84	7.74	42.32
55	0.27	-9.93	-17.14	-30.33	-45.01	-47.8	-49.19	-25.14	7.24	39.63
60	0.4	-9.03	-20.89	-29.93	-41.65	-45.14	-48.29	-17.34	11.63	40.59
65	1.93	-9.96	-16.67	-29.86	-35.94	-46.37	-49.26	-21.82	7.21	36.2
70	4.25	-4.65	-17.17	-24.91	-35.01	-46.53	-51.15	-13.42	11.79	37
75	3.89	-5.68	-13.25	-21.42	-36.07	-43.91	-49.82	-10.33	12.46	35.21
80	6.05	-3.85	-11.63	-22.72	-32.98	-44.04	-48.03	-8.57	14.05	36.7
85	6.11	-1.3	-10.06	-18.43	-33.28	-43.78	-46.97	-4.95	15.28	35.51
90	6.24	-2.13	-10.56	-20.53	-34.51	-43.31	-41.42	-18.33	0.07	33.51

TABLE E6. CONEX YAW MOMENT (cont.)

YAW_MOMENT/Q, ft3										
beta	100	105	110	115	120	125	130	135	140	145
alpha										
-90	41.42	43.31	34.51	20.53	10.56	2.13	-6.24	-11.82	-16.08	-17.44
-85	46.97	43.78	33.28	18.43	10.06	1.3	-6.11	-11.29	-15.28	-17.54
-80	48.03	44.04	32.98	22.72	11.63	3.85	-6.05	-11.49	-16.41	-17.7
-75	49.82	43.91	36.07	21.42	13.25	5.68	-3.89	-11.66	-17.87	-19.26
-70	51.15	46.53	35.01	24.91	17.17	4.65	-4.25	-12.46	-15.68	-17.64
-65	49.26	46.37	35.94	29.86	16.67	9.96	-1.93	-6.84	-10.86	-13.52
-60	48.29	45.14	41.65	29.93	20.89	9.03	-0.4	-5.31	-8.93	-12.65
-55	49.19	47.8	45.01	30.33	17.14	9.93	-0.27	-6.31	-9.57	-13.92
-50	40.42	53.08	42.61	32.45	17.4	5.12	-1	-6.68	-10.76	-12.75
-45	44.54	53.87	41.75	26.87	22.55	11.49	1.13	-5.98	-10.96	-12.29
-40	36.47	53.77	43.61	32.55	18.4	4.62	-1.1	-7.24	-11.16	-13.62
-35	43.48	53.71	48.43	30.96	17.07	8.4	-1.03	-7.14	-10.2	-14.91
-30	44.91	46.67	45.11	29.16	18.7	6.24	-2.09	-6.68	-9.73	-13.65
-25	46.73	46.23	36.17	28.56	11.29	5.25	-1.86	-6.54	-10.89	-14.42
-20	45.14	46.14	31.95	23.15	15.31	-0.2	-4.45	-8	-12.69	-16.01
-15	44.81	43.48	34.84	20.23	12.06	4.88	-4.22	-9.6	-14.25	-17.64
-10	44.31	46.6	30.52	23.08	12.16	3.59	-5.68	-10.03	-15.01	-16.84
-5	46.14	46.37	32.42	21.52	12.56	1.73	-7.64	-13.55	-18.3	-20.46
0	46.07	45.84	35.57	22.98	12.29	2.52	-8.14	-13.25	-18.2	-21.95
5	47.63	46.7	32.58	22.75	13.65	2.92	-6.78	-12.29	-16.87	-20.93
10	48.09	46.3	33.91	26.24	14.95	6.68	-4.12	-10.03	-16.87	-18.67
15	47.76	46.14	38.7	25.18	15.74	7.71	-1.36	-10.13	-17.44	-20.23
20	49.02	49.95	35.11	28.46	20.53	8.57	-1.53	-9	-14.81	-17.3
25	51.81	49.39	37.7	32.98	19.2	13.32	2.56	-5.02	-9.96	-14.28
30	50.92	47.3	43.41	31.79	23.72	12.69	2.89	-4.75	-9.07	-12.26
35	48.96	49.49	47.86	33.12	19.86	13.42	2.82	-6.14	-9.4	-13.52
40	43.74	52.51	45.14	34.74	21.06	9.03	0.13	-4.82	-9.03	-11.86
45	47.7	52.38	44.28	29.23	24.18	12.95	1.3	-6.11	-9.5	-11.53
50	44.94	51.75	44.64	35.11	19.56	6.94	-0.7	-5.98	-9.67	-12.36
55	48.86	49.72	47	33.55	18.1	9.1	0.47	-5.08	-9.67	-13.78
60	49.86	45.17	42.45	31.16	20.53	7.67	0.4	-4.35	-8.47	-12.69
65	50.19	46.67	35.91	27.53	12.72	7.11	-0.9	-4.98	-9.3	-13.25
70	48.13	47.07	33.05	21.95	13.52	2.49	-4.42	-8.07	-12.75	-15.74
75	47.56	45.17	37.37	20	10.73	4.42	-5.88	-10.7	-13.88	-16.14
80	47.63	45.14	33.08	24.55	14.12	4.88	-7.17	-13.42	-16.87	-15.41
85	47.26	45.01	34.41	21.42	11.09	3.29	-6.61	-13.82	-18.3	-19.26
90	47.23	43.84	34.38	21.89	11.36	3.39	-7.01	-14.68	-19.73	-21.09

TABLE E6. CONEX YAW MOMENT (cont.)

YAW_MOMENT/Q, ft3							
beta	150	155	160	165	170	175	180
alpha							
-90	-23.58	-29.63	-36.93	-39.23	-34.81	-27.4	0
-85	-21.89	-28.8	-35.04	-34.84	-27.4	-16.21	0
-80	-20.46	-26.01	-31.65	-31.45	-23.91	-14.81	0
-75	-18.67	-23.75	-31.06	-31.12	-24.28	-15.51	0
-70	-17.21	-22.09	-28.86	-29.69	-21.95	-13.42	0
-65	-16.34	-19.56	-25.91	-26.24	-20.93	-12.99	0
-60	-18.67	-18.37	-20.63	-23.05	-19	-13.85	0
-55	-16.11	-18.4	-19.73	-20.69	-19.8	-14.42	0
-50	-15.01	-17.87	-18.8	-20.76	-20.79	-13.02	0
-45	-14.75	-17.11	-17.7	-19.83	-20.39	-15.01	0
-40	-16.51	-17.87	-18.17	-19.96	-20.99	-15.18	0
-35	-17.64	-19.36	-19.4	-22.49	-22.49	-20.06	0
-30	-18.63	-19.7	-22.25	-23.65	-24.05	-18.27	0
-25	-17.8	-20.53	-24.68	-26.01	-22.88	-15.28	0
-20	-18.23	-22.39	-27.2	-27.73	-23.81	-15.64	0
-15	-19.13	-24.98	-29.96	-29.63	-25.31	-17.04	0
-10	-18.43	-24.48	-29.13	-28.53	-23.58	-12.72	0
-5	-21.95	-26.77	-31.52	-29.79	-26.6	-14.08	0
0	-24.35	-29.66	-33.48	-32.95	-28.27	-13.68	0
5	-26.24	-31.92	-36.24	-34.41	-26.9	-12.39	0
10	-23.52	-28.7	-34.68	-33.48	-26.94	-14.32	0
15	-23.62	-26.14	-33.51	-32.15	-25.24	-15.25	0
20	-21.92	-23.72	-31.29	-29.99	-25.48	-17.04	0
25	-17.37	-20.19	-26.9	-24.48	-22.09	-16.44	0
30	-16.97	-18	-19.2	-19.66	-16.01	-12.99	0
35	-15.21	-17.37	-15.78	-16.01	-13.62	-12.75	0
40	-14.05	-14.55	-14.58	-12.46	-9.77	-7.57	0
45	-12.59	-14.58	-14.18	-13.85	-10.63	-7.91	0
50	-13.02	-15.18	-16.18	-14.75	-14.18	-7.97	0
55	-15.08	-16.37	-19.16	-18.7	-17.5	-12.65	0
60	-18	-17.17	-22.49	-20.99	-19.46	-12.56	0
65	-15.98	-16.64	-25.14	-24.21	-21.22	-11.82	0
70	-16.97	-23.22	-29.43	-27.24	-23.81	-11.79	0
75	-18.43	-23.62	-31.02	-27	-23.48	-12.65	0
80	-20.89	-27.14	-32.35	-28	-21.76	-11.03	0
85	-24.81	-31.02	-35.84	-31.55	-23.52	-9.77	0
90	-25.94	-32.22	-38.2	-34.21	-25.77	-11.82	0

APPENDIX F. ENGINE-CANISTER AERODYNAMIC TABLES

This appendix presents the numerical results for the engine canister aerodynamics derived from the available flight test data (flights 91 and 107) as tables of drag, side force, lift, and yaw moment divided by dynamic pressure (tables F1 to F4, respectively). Plots and analysis were given the text in the section "Engine-Canister Aerodynamics." The table grid is every 5 deg in angle of attack and sideslip angle. Values were computed by averaging the data in a 2- x 2-deg box centered on each grid point. The table domain is limited to $(\alpha, \beta) \in [-50, 20] \otimes [-30, 80]$ which is about 13% of the complete domain, $[-90, 90] \otimes [-180, 180]$. Values were obtained at 50% of the grid points within the table domain.

Some extension in coverage is possible, based principally on the geometric symmetry of the engine canister about the y-z and the x-z center planes, but this topic is outside the scope of the present report.

Table F5 shows the number of data points averaged at each grid point to get the tabulated aerodynamics. The number of data points ranges from 1 to 564. Standard deviations were calculated and, stated briefly, almost all values for drag, side force, lift, and yaw moment were, respectively, below 6, 20, 15, and 27% of the table maximum magnitude.

TABLE F1. ENGINE CANISTER DRAG/Q (FT²)

$\alpha \downarrow \beta \rightarrow$	-30.00	-25.00	-20.00	-15.00	-10.00	-5.00	0.00	5.00	10.00	15.00	20.00
-50.00											
-45.00								21.44			
-40.00					30.41	29.46	23.43		31.22	30.12	32.50
-35.00		30.56		30.96	30.45	28.43	28.14	29.01	31.82	32.98	35.08
-30.00			32.93	32.16	31.65	29.68	29.45	31.13	32.84	34.60	36.62
-25.00	35.00		34.06	32.76	32.24	30.58	31.28	31.28	33.89	35.06	35.82
-20.00			35.36	34.34	32.04	31.19	30.94	32.24	33.90	35.33	35.99
-15.00			37.63	33.88	33.80	32.65	31.93	32.77	34.15	35.11	36.80
-10.00				36.08	34.26	32.98	32.62	33.36	34.96	36.48	37.19
-5.00				37.02	35.20	33.69	33.46	34.67	36.21	39.71	41.11
0.00			40.72	38.43	37.76	36.90	35.10	35.96	38.58	41.62	43.60
5.00				41.30	38.44	36.31	35.79	36.84	38.65	43.31	44.78
10.00						35.90	36.38	39.90			42.08
15.00							36.88	40.69	41.13		
20.00									40.21		49.67

$\alpha \downarrow \beta \rightarrow$	25.00	30.00	35.00	40.00	45.00	50.00	55.00	60.00	65.0	70.0	75.0	80.0
-50.00							32.03	32.00	30.93	29.53	24.94	
-45.00			32.81	33.87	33.83	34.20	33.72	32.60	32.25	30.33	25.74	
-40.00	33.73	35.55		34.98	36.05	34.64	34.50	31.58	31.66	32.19	29.49	23.93
-35.00	35.81	36.56	37.13	35.76	34.21	36.79	34.68		32.54	32.97		24.49
-30.00	37.04	37.79	37.33	36.28	35.11	36.67	36.84	35.66	36.04	29.17	26.69	25.18
-25.00	37.64	38.16	37.12	37.56	37.83	37.67	35.93	36.51				
-20.00	36.79	38.42	37.49	37.65		38.73	38.77			29.52	28.36	
-15.00	38.18	39.94	38.49					37.24		31.24		
-10.00	37.93	37.31							34.37			
-5.00	41.23	37.67										
0.00	43.18	38.60										
5.00	43.52											
10.00	43.86											
15.00												
20.00												

TABLE F2. ENGINE CANISTER SIDE FORCE (FT²)

$\alpha \downarrow \beta \rightarrow$	-30.00	-25.00	-20.00	-15.00	-10.00	-5.00	0.00	5.00	10.00	15.00	20.00
-50.00											
-45.00								-7.75			
-40.00					-0.71	-1.77	-6.66		-2.40	-1.88	-1.83
-35.00		-4.53		-3.48	-1.27	-3.49	-3.92	-3.38	-2.36	-0.59	0.65
-30.00			-6.14	-4.93	-3.64	-2.91	-4.37	-2.78	-1.34	0.13	1.48
-25.00	-7.60		-8.05	-6.75	-5.42	-4.61	-3.52	-3.11	-0.45	1.46	2.65
-20.00			-10.12	-8.13	-6.50	-6.08	-3.98	-2.22	-0.45	1.65	3.20
-15.00			-10.61	-10.17	-8.32	-6.72	-4.45	-2.15	-0.48	1.23	1.27
-10.00				-12.75	-10.51	-7.32	-4.97	-2.54	-0.26	2.10	4.18
-5.00				-14.34	-10.71	-9.28	-5.94	-2.94	1.13	3.11	3.75
0.00			-16.22	-16.62	-15.59	-13.16	-6.08	-0.84	-1.16	3.43	5.19
5.00				-14.06	-13.53	-13.23	-8.62	-4.70	-2.31	2.10	7.92
10.00						-19.52	-10.74	-6.55			11.78
15.00							-6.35	-6.31	-5.54		
20.00									-1.93		8.65

$\alpha \downarrow \beta \rightarrow$	25.00	30.00	35.00	40.00	45.00	50.00	55.00	60.00	65.00	70.00	75.00	80.00
-50.00							-2.59	-3.37	-1.30	-0.78	1.90	
-45.00			-4.65	-7.63	-5.47	-3.32	-1.80	1.23	-1.46	1.29	2.57	
-40.00	-2.06	-4.32		-5.01	-0.74	-2.41	-1.84	2.15	-1.93	3.26	4.37	1.69
-35.00	-0.37	-0.24	-0.90	-1.53	-1.41	-0.98	-0.19		2.99	3.56		3.60
-30.00	0.87	1.45	2.06	-0.13	-0.73	1.27	1.42	1.88	2.52	4.32	4.61	4.95
-25.00	3.16	2.60	2.97	2.14	2.95	1.10	0.93	0.65				
-20.00	3.07	4.49	2.40	3.92		3.88	5.31			7.04	7.24	
-15.00	4.70	5.39	2.89					5.42		7.98		
-10.00	5.21	7.85							7.91			
-5.00	10.54	14.09										
0.00	7.00	15.54										
5.00	7.71											
10.00	15.64											
15.00												
20.00												

TABLE F3. ENGINE CANISTER LIFT/Q (FT²)

$\alpha \downarrow \beta \rightarrow$	-30.00	-25.00	-20.00	-15.00	-10.00	-5.00	0.00	5.00	10.00	15.00	20.00
-50.00											
-45.00								23.31			
-40.00					19.71	22.54	28.29		26.23	24.88	23.11
-35.00		25.22		20.60	22.80	26.96	25.74	25.71	23.03	28.70	26.60
-30.00			25.01	25.55	24.51	25.52	26.25	24.88	25.75	27.31	28.59
-25.00	26.13		27.18	25.62	25.03	26.59	26.57	28.62	27.21	26.26	25.71
-20.00			27.08	27.48	29.73	29.32	29.18	30.01	29.76	27.46	28.44
-15.00			27.90	32.10	29.50	30.16	28.72	28.93	29.83	28.49	31.59
-10.00				31.93	30.82	30.26	30.50	30.93	29.55	27.55	27.83
-5.00				32.61	30.78	30.41	29.62	29.74	27.96	28.65	31.55
0.00			26.64	31.72	30.01	35.00	30.19	21.28	24.41	23.99	25.47
5.00				24.30	24.02	25.33	22.43	20.22	19.49	19.28	25.01
10.00						21.59	21.57	22.61			16.21
15.00							15.83	18.04	11.15		
20.00									12.20		12.70

$\alpha \downarrow \beta \rightarrow$	25.00	30.00	35.00	40.00	45.00	50.00	55.00	60.00	65.00	70.00	75.00	80.00
-50.00							7.25	7.56	7.69	6.62	6.95	
-45.00			14.86	15.81	13.13	11.51	10.60	8.91	10.62	8.49	7.08	
-40.00	24.12	21.66		15.57	15.34	14.49	13.68	10.24	9.62	8.88	8.46	8.91
-35.00	24.61	21.28	18.90	16.74	17.43	18.56	15.62		8.99	11.77		8.11
-30.00	26.49	23.66	21.51	19.38	19.64	19.77	17.26	13.98	15.45	8.01	8.96	7.45
-25.00	25.32	26.39	23.18	23.03	20.86	19.82	16.35	17.11				
-20.00	30.57	26.93	26.79	27.12		19.90	16.95			8.43	8.25	
-15.00	28.51	27.44	27.41					14.27		9.12		
-10.00	28.56	26.76							10.00			
-5.00	26.62	22.90										
0.00	27.15	25.85										
5.00	24.11											
10.00	19.77											
15.00												
20.00												

TABLE F4. ENGINE CANISTER: YAW MOMENT/Q (FT³)

$\alpha \downarrow \beta \rightarrow$	-30.00	-25.00	-20.00	-15.00	-10.00	-5.00	0.00	5.00	10.00	15.00	20.00
-50.00											
-45.00								-55.51			
-40.00					-23.00	-19.66	-48.06		-41.93	-22.27	-22.81
-35.00		-28.70		-24.43	-24.51	-33.40	-35.69	-20.78	-13.85	-19.81	-13.47
-30.00			-26.71	-28.49	-27.58	-21.67	-22.27	-14.08	-9.92	-12.31	-14.04
-25.00	-23.17		-32.89	-28.73	-25.44	-20.19	-15.54	-11.06	-5.61	-0.46	0.85
-20.00			-41.09	-31.72	-27.34	-20.56	-12.59	-9.00	-5.44	0.57	5.69
-15.00			-31.57	-33.44	-26.23	-21.62	-12.21	-5.84	-2.74	1.24	1.38
-10.00				-31.89	-26.24	-18.34	-11.43	-5.79	2.68	7.27	9.23
-5.00				-27.45	-21.84	-17.08	-9.26	-3.21	4.30	11.81	16.77
0.00			-27.17	-22.81	-20.22	-12.76	-0.29	5.03	7.38	11.72	16.03
5.00				-23.62	-17.88	-3.13	-4.45	-0.09	4.83	13.62	23.92
10.00						56.35	36.33	27.66			5.61
15.00							22.37	39.17	45.26		
20.00									7.82		16.56

$\alpha \downarrow \beta \rightarrow$	25.00	30.00	35.00	40.00	45.00	50.00	55.00	60.00	65.00	70.00	75.00	80.00
-50.00							-7.12	2.63	-10.34	-13.18	-0.84	
-45.00			-18.40	-23.35	-9.94	-9.70	-3.30	-13.88	-12.73	-26.03	-5.02	
-40.00	-11.93	-30.18		-20.02	-1.32	-6.29	2.32	-5.58	-4.45	-20.24	-18.59	0.29
-35.00	-19.33	-14.87	-13.18	-7.64	-3.74	-9.39	-5.83		-12.67	-34.83		-2.88
-30.00	-18.12	-11.12	-3.05	-4.94	-4.86	-5.31	-5.63	-8.91	-28.49	-14.01	-5.16	-6.03
-25.00	0.13	-8.37	-1.92	-1.77	-2.63	-9.96	-11.33	-19.35				
-20.00	1.15	-0.19	-2.11	3.32		-3.30	-5.82			-10.35	-15.12	
-15.00	5.39	4.20	3.61					-10.94		-11.19		
-10.00	9.89	12.56							-8.83			
-5.00	15.71	13.38										
0.00	18.49	5.33										
5.00	34.84											
10.00	8.67											
15.00												
20.00												

TABLE F5. NUMBER OF DATA POINTS AVERAGED

$\alpha \downarrow \beta \rightarrow$	-30	-25	-20	-15	-10	-5	0	5	10	15	20
-50											
-45								6			
-40					12	1	2		7	9	5
-35		6		24	17	35	60	62	113	59	28
-30			13	36	73	79	153	153	172	141	96
-25	1		55	161	262	355	215	219	248	301	341
-20			72	153	273	372	246	279	334	288	184
-15			24	263	263	210	327	219	316	395	322
-10				139	524	466	564	497	546	392	505
-5				137	446	319	268	155	125	144	332
0			55	134	52	59	21	17	174	198	148
5				8	79	180	133	209	206	66	13
10						16	26	24			19
15							25	29	5		
20									10		13

$\alpha \downarrow \beta \rightarrow$	25	30	35	40	45	50	55	60	65	70	75	80
-50							54	29	23	13	2	
-45			2	6	13	14	19	6	14	2	1	
-40	32	9		54	7	65	5	7	2	1	3	1
-35	68	66	103	221	26	18	27		16	9		1
-30	93	142	123	70	32	18	18	28	2	5	2	2
-25	147	122	152	61	45	18	20	12				
-20	426	204	145	19		16	33			2	6	
-15	254	138	70					1		2		
-10	257	70							3			
-5	64	5										
0	47	1										
5	43											
10	19											
15												
20												

INITIAL DISTRIBUTION LIST

		<u>Copies</u>
Weapon Systems Technology Information Analysis Center Alion Science and Technology 201 Mill Street Rome, NY 13440	Ms. Perry E. Onderdonk ponderdonk@alionscience.com	Electronic
Defense Technical Information Center 8725 John J. Kingman Rd., Suite 0944 Fort Belvoir, VA 22060-6218	Mr. Jack L. Rike jrike@dtic.mil	Electronic
AMSAM-LI,	Ms. Anne C. Lanteigne anne.lanteigne@us.army.mil	Electronic
RDMR		Electronic
RDMR-CSI		Electronic